BIOSAR 2007
Technical Assistance for the Development of Airborne SAR and Geophysical Measurements during the BioSAR 2007 Experiment

Final Report without Synthesis

Prepared for

European Space Agency

Prepared by

German Aerospace Center

Microwaves and Radar Institute (HR)

Oberpfaffenhofen, Germany

and

Department of Radar Systems

Swedish Defence Research Agency FOI

Linköping, Sweden

and

Politecnico di Milano POLIMI

Miland, Italy

26. February 2008
Version 3

ESA STUDY CONTRACT REPORT -SPECIMEN

ESA Contract No.:	Subject:	Contractor:
20755/07/NL/CB	**Technical Assistance for the Development of Airborne SAR and Geophysical Measurements during the BioSAR 2007 Experiment**	**German Aerospace Center**
ESA CR() No:	No.of Volume: 1 This is Volume No.: 1	Contractors References: Final Report

Abstract:

The understanding of processes occurring in Boreal forests and observation of changes over the huge areas of Boreal regions can efficiently be carried out using satellite instruments, which provide sustained, consistent observations over a longer time period. In order to monitor parameters important for detecting environmental changes that affect Earth's climate, several different sensor systems are needed that are capable of measuring different physical parameters with a sufficient spatial and temporal resolution as well as the required spatial and temporal coverage. The BIOSAR project acquired airborne SAR data at longer wavelength in L- and P-band using polarimetric and polarimetric SAR interferometry modes with temporal and spatial baselines varying from 15 min to 60 min within one day and in repeat pass after 36 and 56 days; the spatial baseline variation is ranging from 0 m to 80 m, respectively. The consolidated test site Remmingstorp with the boreal like forest type is located in shouthern Sweden and represents a managed mixed forest with trees having biomass values up to 400 t/ha. The SAR acquisitions were done simultanouly to the ground measurements. First order data quality checks of the SAR data and ground measurements are provided. Further first analysis with respect to temporal decorrelation in L- and P-band, forest height inversion, temporal baseline SAR Tomography and 6Mhz bandwith forest height inversion at P-band are presented and discussed.

Name of authors: Editor Irena Hajnsek (DLR) – Complete authors name next page!

Name of ESA study manager: Malcolm Davidson Div: Mission Science Division Directorate: Earth Observation Program	ESA Budget Heading:

Contract:

ESA contract No.: 20755/07/NL/CB

ESA study manager:

Malcolm Davidson

Prepared by:

Irena Hajnsek, Rolf Scheiber (Prime Contractor)

Microwaves and Radar Institute (DLR-HR),

German Aerospace Center (DLR),

PO BOX 1116, 82234 Wessling, Germany

Lars Ulander, Anders Gustavsson, (Subcontractor of DLR)

FOI, Division of Sensor Systems
P.O. Box 1165, SE-58111 Linköping, Sweden

Gustaf Sandberg (Subcontractor of FOI)

Radar Remote Sensing Group (RRS)
Department of Radio and Space Science
Chalmers University of Technology
SE-412 96 Göteborg Sweden

Stefano Tebaldini, Andrea Monte Guarnieri,
Fabio Rocca (Subcontractor of DLR)

Politecnica di Milano (Polimi)
Dipartimento di Elettronica e Informazione
Piazza Leonardo da Vinci 32, Milano, Italy

Fabrizio Bombardini, Matteo Pardini (Subcontractor of Polimi)

University of Pisa, Italy

Version date changes:

1.0 12/12/2007 Draft version provided to ESA

2.0 25/02/2008 Final version provided to ESA

3.0 26/02/2008 Update of final version provided to ESA

The authorship of this report is listed in the table below:

Chapter	Authors
2. Introduction	DLR
3. Description of the Study Area	FOI
4. BIOSAR Time Schedule	DLR
5. Airborne Data Acquisition	DLR
6. Ground Measurements	FOI
7. Data Base	DLR
8. BIOSAR Data Analysis	DLR / FOI / POLIMI
9 / 10 Summary & Recommendation	DLR / FOI / POLIMI
9. Appendix	University of PISA

1 CONTENTS

2 INTRODUCTION

This document describes the BIOSAR campaign carried out from the 8th of March to the 3rd of May 2007. In the following the main objectives of the BIOSAR campaign are summarised and a description of the test site, the acquired airborne data and ground data, as well as the data quality and preliminary analysis with the acquired data are given.

In the frame of its Earth Observation Envelope Programme of the European Space Agency (ESA), BIOSAR aims to support geophysical algorithm development, calibration/validation and the simulation of future spaceborne Earth Observation missions.

The next generation of ESA Earth Observation satellites includes a series of innovative satellites dedicated to a specific application. BIOSAR supports the current selected candidate Earth Explorer Mission BIOMASS. The main objective of BIOMASS is the estimation of forest biomass in order to support carbon modelling using longer wavelength SAR measurements.

2.1 Campaign Objectives

The BIOSAR 2007 campaign aimed to collect in-situ coordinated from FOI and airborne SAR data coordinated from DLR-HR in support of decisions being taken on satellite instrument configurations for the BIOMASS satellite mission. In addition it aims to provide an important database for the study of longer term mission concepts.

The BioSAR 2007 campaign addresses important specific programmatic needs of the selected candidate ESA’s Earth Explorer Mission BIOMASS:

- To asses the potential of BIOMASS for biomass estimation in boreal forest
- To investigate temporal decorrelation at L- and P-band for revisit times compatible with spaceborne mission concepts
- To explore the influence of resolution (6 MHz) at 350 MHz center frequency in P-band

BioSAR 2007 is aiming primarily at the investigation of radar signatures of boreal forest which are consistent with the concept of future ESA mission.

2.2 Campaign Institutions

BIOSAR involved in total 27 people from 5 different institutes coming from 4 different countries, participating during the ground measurements and SAR data acquisition periods.

Participants included the German team from DLR-HR, the Swedish team from FOI, CTH and SLU and one person from RSAC.

AIRBORNE TEAM:

German Aerospace Center (DLR), Microwaves and Radar Institute (HR)

P.O. Box 11 16, D-82230 Wessling, Germany
in the following referred to as **DLR-HR**

German Aerospace Center (DLR), Flight Operations (FB)

P.O. Box 11 16, D-82230 Wessling, Germany
in the following referred to as **DLR-FB**

GROUND TEAM:

Chalmers University of Technology

in the following referred as **CTH**

Swedish Defence Research Agency

in the following referred as **FOI**

Swedish University of Agricultural Sciences

in the following referred as **SLU**

2.3 Campaign Participants

ORGANISATION Team:

ESA	Malcolm Davidson
RSAC	Mike Wooding
DLR-HR	Irena Hajnsek
FOI	Lars Ulander

AIRBORNE Team:

DLR-FB	Andrea Hausold Philip Weber Stefan Grillenbeck Klaus Dietl Roland Welser Michael Grossrubatscher Emil Sauer Helmut Kirner Siegfried Judt Roman Koch Frank Schirmer
DLR-HR	Ralf Horn Bernd Gabler Peter Hackenberg

GROUND Team:

CTH	Leif Eriksson Klas Folkesson Gustaf Sandberg
FOI	Björn Flood Anders Gustavsson Olle Nyström Lars Ulander
SLU	Johan Fransson Mattias Magnusson

3 DESCRIPTION OF THE TEST SITE

The Remningstorp test site used for the BioSAR 2007 experiment is located in southern Sweden (58°28´N, 13°38´E), see Figure 3.1. The test site has been overlaid in black on a standard road map in Figure 3.2. The two large fresh water lakes Vänern and Vättern can be seen here in blue in the upper left and lower right corner, respectively.

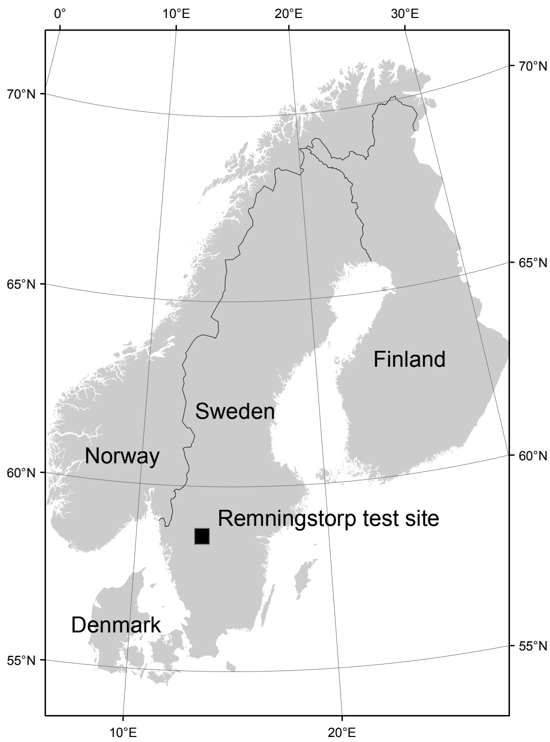

Figure 3.1: The location of the Remningstorp test site in the Sweden.

The estate has about 1200 ha of productive forested land and is managed by the Forestry Society's Estate Management Company. Most of the forestry studies taking place here over the years have been defined and conducted by the Swedish University of Agricultural Sciences (SLU). The forested parts are divided into about 340 forest stands. The topography is fairly flat with some small variations ranging between 120 and 145 m above sea level. Prevailing tree species are Norway spruce (*Picea abies*), Scots pine (*Pinus sylvestris*) and birch (*Betula* spp.), with an annual growth yield of about 9 m^3 ha^{-1} $year^{-1}$. A few forest stands are dominated by oak (*Quercus robur*) and beech (*Fagus sylvatica*). The dominant soil type is till with a field layer, when present, of blueberry (*Vaccinium myrtillus*) and narrow thinned grass (*Deschampsia flexuosa*). Further descriptions of the Remningstorp estate (in Swedish) can be found in [1].

Large efforts have been made in collecting forest inventory data at Remningstorp test site since year 2000 using different inventory designs with varying degree of accuracy. The inventories have been funded by Hildur and Sven Wingquist's Foundation. A vide range of stem volumes exists among all forest stands up to a maximum of about 620 m^3 ha^{-1}. The delineation of the different forest stands are presented in Figure 3.3. A unique number is used to reference a specific forest stand. The outer boundary of the whole area is also found as an overlay in the map of Figure 3.4.

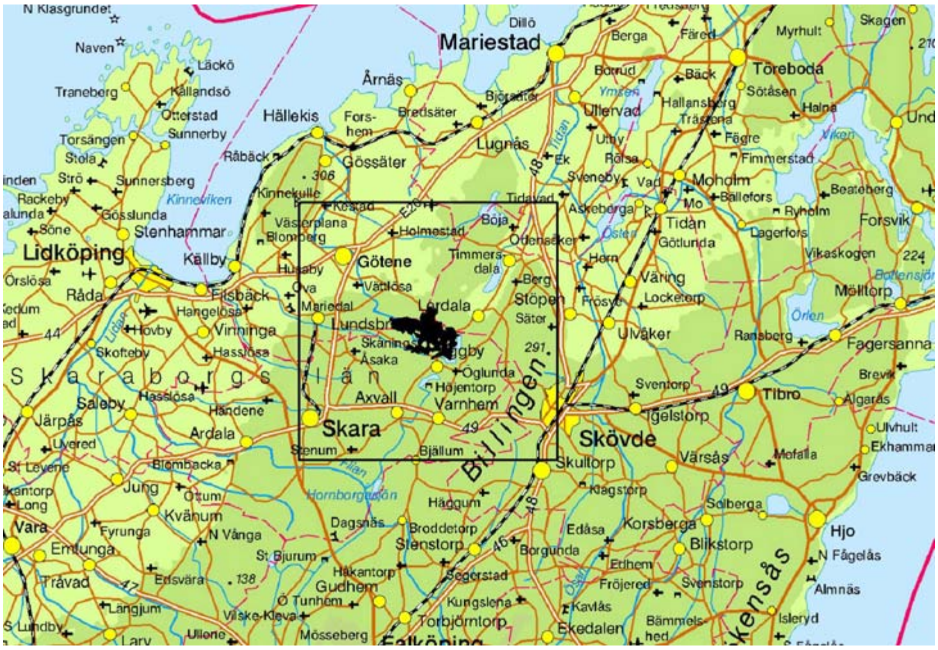

Figure 3.2: Map showing the northern part of the province Västergötland. The properties belonging to Remningstorp can be identified as the dark area in the middle (58º28'N, 13º38'E). The marked area is larger than 1200 ha since it includes not only productive forested land. The drawn square in black has a size of 25 km by 25 km. (© Map: Lantmäteriverket Gävle).

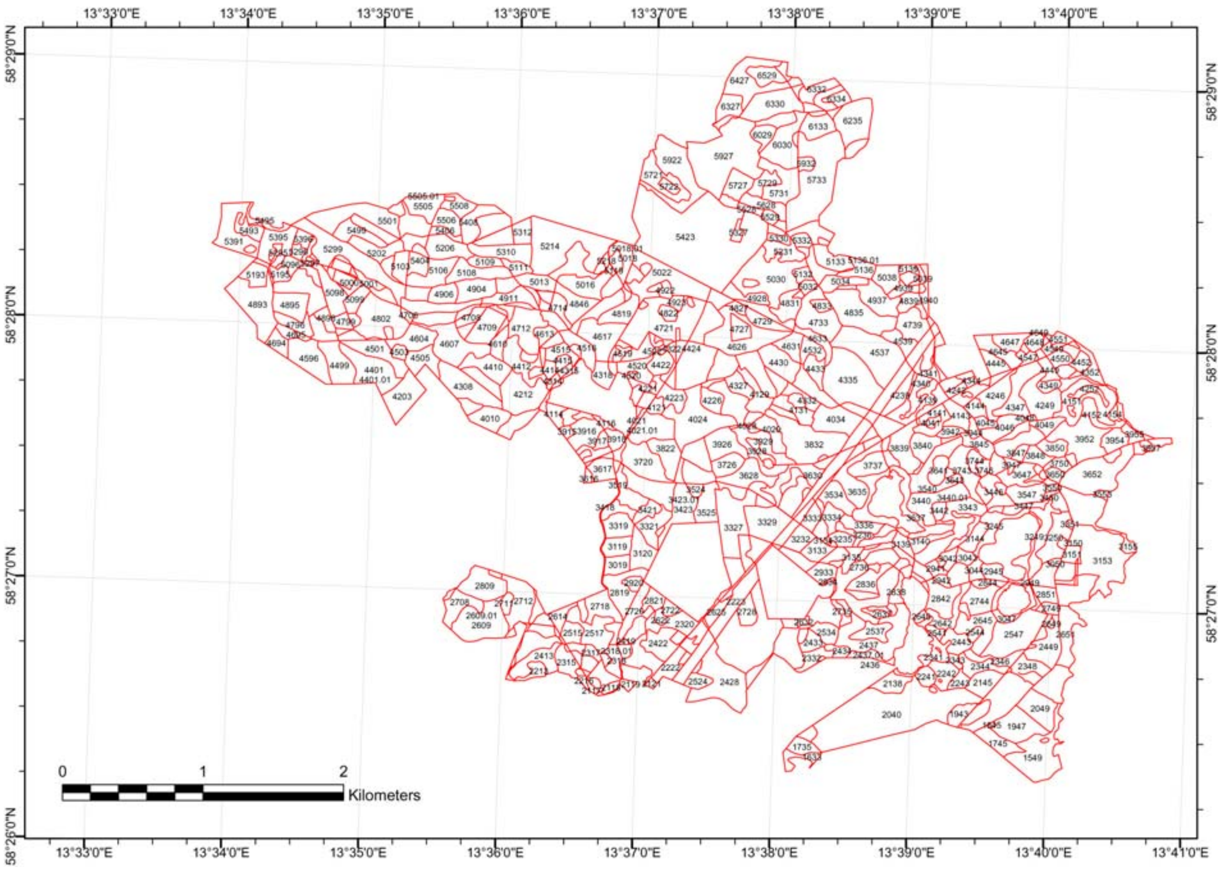

Figure 3.3: The forest stands in Remningstorp with the assigned identification numbers given.

Figure 3.4: The border of the Remmingstorp estate is marked in black on the map. The square grid corresponds to an area size of 1 km by 1 km and is given in the Swedish reference system RT90. (© Map: Lantmäteriverket Gävle).

3.1 Digital Elevation Model of the Study Area

The existing Digital Elevation Model (DEM) of Sweden is fairly coarse, i.e. having a grid size of 50 m by 50 m. The geo-coding of E-SAR slant range imagery results performed by DLR is based on this product since the image formation generates ground scenes that cover parts outside the borders depicted in Figure 3.4. However, DEMs with higher resolution based on helicopterborne lidar measurements are available but are limited to areas within or just outside the Remningstorp estate.

Upon request and specification provided DLR a coarse DEM was obtained from the National Land Survey of Sweden ("Lantmäteriverket", "Lantmäteriet" or "LMV") [2]. This product is commercial and subject to a license agreement. The data set purchased is therefore a single user license with DLR defined as the end-user. In case other research groups working with

BioSAR data are interested in this DEM product they have to order their own data set using the information and point of contacts found at the web site in [2]. The area of interest to be included by the coarse DEM was defined by DLR in UTM Zone33 coordinates according to:

- N 6485000 - E 417000 (Upper left corner, North-West)
- N 6477500 - E 423500 (Lower right corner, South-East)

The lidar based DEMs are available without any commercial restrictions and will be described in Chapter 6.

3.2 Radar Reference Targets Deployed in the Study Area

The Remningstorp area has also been one of the calibration sites for the Japanese Advanced Land Observing Satellite (ALOS). In preparation for the ALOS calibration campaign four large trihedral corner reflectors, labelled 1-4, were deployed in April 2006 and were used throughout the year. During a storm in January 2007, reflector number 2 overturned and got severe damages on some parts of the smooth inner surfaces. The remaining three reflectors could be used for the BioSAR experiment 2007 and the locations of them can be seen in Figure 3.5.

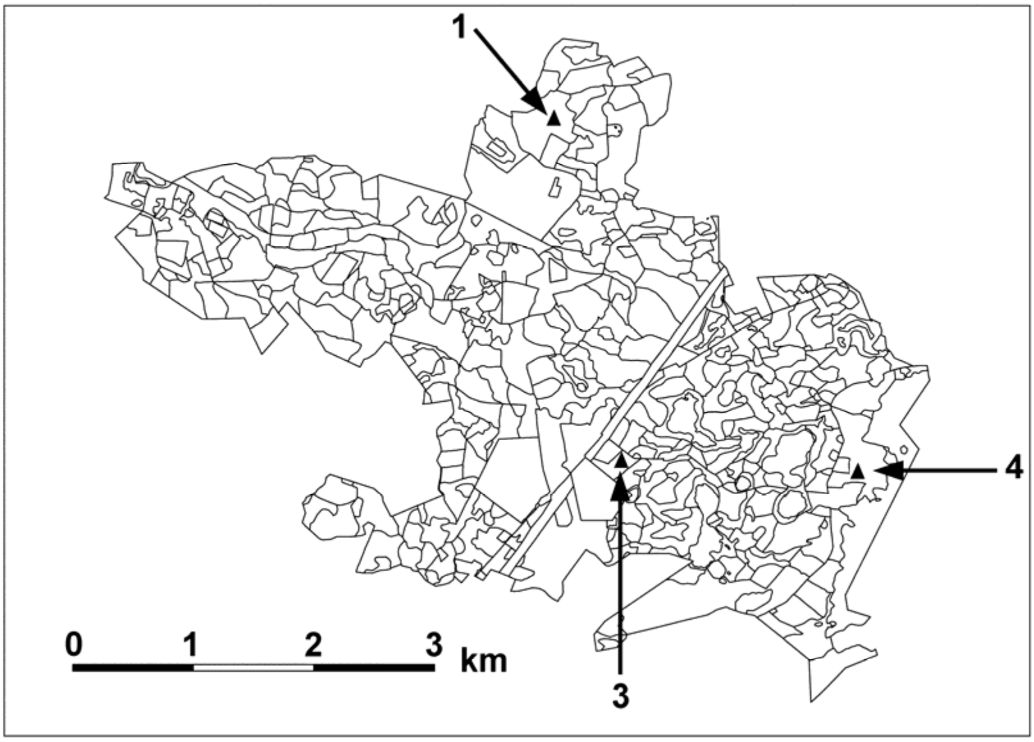

Figure 3.5: The location of the trihedrals (#1, #3 and #4) in Remningstorp used for E-SAR radar imaging.

The trihedral reflectors were originally developed for CARABAS-II, a Swedish airborne VHF SAR system [3]. To be suitable for the ALOS L-band frequencies the inside of the trihedral was covered with metal plates [4]. The size of an assembled trihedral is indicated in Figure 3.6. The reflectors can be rotated 360 degrees and the elevation angles (between horizontal plane and boresight) can be adjusted in the range 35º to 70º. One limitation for the pointing of the reflectors is the requirement for suitable anchor points. For the ALOS calibration campaign six large stones were placed in the ground around each reflector to allow pointing in azimuth and elevation for both ascending and descending orbits. The arrangement is illustrated in Figure 3.7. The locations of these anchor stones were not optimal for the flight directions selected for the BioSAR data acquisitions. As a result, reflector #1 could not be elevated as high as required with respect to the defined E-SAR imaging geometry. Figure 3.8 to Figure 3.10 show the three trihedrals in the fixed orientations used during all BioSAR missions with E-SAR.

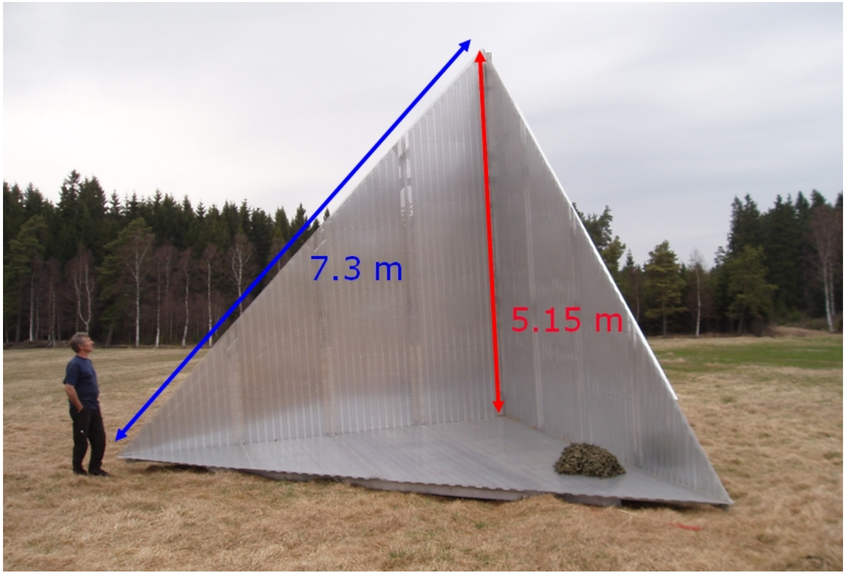

Figure 3.6: Size of the deployed trihedrals in Remningstorp. This is unit #2 that got damaged in a storm and was not in use during BioSAR 2007

Figure 3.7: Trihedral #1 in position and adjusted properly for one of the imaging ALOS orbits.

Figure 3.8: Trihedral #1 in position for BioSAR data acquisitions. Orientation in azimuth: 198º, Azimuth look direction: 288º, Elevation of baseplane: 17º. The elevation should have been 20º but this could not be fulfilled due to limitations in the tilting mechanism optimized for ALOS ascending and descending orbits. Photos captured on 31 March (left) and 2 May (right).

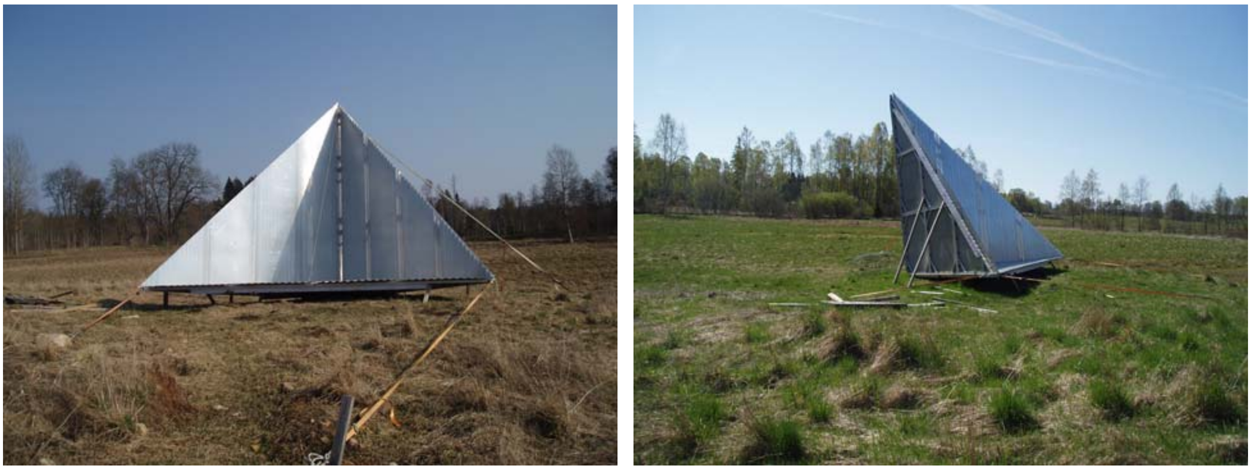

Figure 3.9: Trihedral #3 in position for BioSAR data acquisitions. Orientation in azimuth: 198º, Azimuth look direction: 288º, Elevation of baseplane: 9º. Photos captured on 31 March (left) and 2 May (right).

Figure 3.10: Trihedral #4 in position for BioSAR data acquisitions. Orientation in azimuth: 177º, Azimuth look direction: 267º, Elevation of baseplane: 5º. Photos captured on 31 March.

3.3 References

[1] O. Ahlberg and L. Kardell, “Remningstorp – från herresäte till skogslaboratorium,” Västergötlands Tryckeri AB, Skara, Sweden 1997. (in Swedish).

[2] Lantmäteriet, www.lantmateriet.se.

[3] H. Hellsten, L.M.H. Ulander, A. Gustavsson, and B. Larsson, “Development of VHF CARABAS II SAR,” *Proc. Radar Sensor Technology*, held in Orlando, FL, 8-9 April 1996, SPIE vol. 2747, pp. 48-60, 1996.

[4] L.M.H. Ulander, L. Eriksson, G. Smith-Jonforsen, J.E.S. Fransson, and H. Olsson, “ALOS calibration and validation activities in Sweden,” *Proc. 2006 IEEE International Geoscience and Remote Sensing Symposium & 27th Canadian Symposium on Remote Sensing*, held in Denver, CO, 31 July - 4 August 2006, pp. 336-339, 2006.

4 BIOSAR CAMPAIGN SCHEDULE

The main objectives of the BIOSAR campaign were translated into requirements for the campaign execution including instrument modes, settings and flight parameters. The main requirements include to:

- collect L- and P-band data at three different time periods to estimate temporal decorrelation levels
- acquire data with different spatial baselines in L-band and P-band for Pol-InSAR analysis
- collect spatial data for tomographic analysis at P-band
- acquire P-band data for backscattering analysis

Concerning to these objectives the following flight configuration were planned to be performed:

E-SAR Mode	Frequency	Baselines Spacing	Objectives
Pol-InSAR with 3 Tracks	L-band	8m	• Forest height inversion • Forest height relation to Biomass • Time analysis (temporal coherences)
Pol-InSAR with 4 Track	P-band (100 Mhz @ 350 Mhz center frequency)	10m	• Forest height inversion • Forest height relation to Biomass • Time analysis (temporal coherences)
PolSAR with 1 Track	P-band (6 Mhz @ 350 Mhz center frequency)		• Performance simulation of BIOMASS
PolSAR with 1 Track	P-band (100 Mhz @ 350 Mhz center frequency)		• Performance simulation of BIOMASS for sigma zero analysis (inventory plots in the near range – 25to35 degree – ESAR heading North-South)

Table 4.1: The operation modes of the E-SAR system for the BIOSAR campaign

The following flight stripe has been agreed with ESA to be flown over the Remningstorp forest (Figure 4.2):

- Flight level of the E-SAR system will be 130 corresponding to 3880m over ground.
- There are two flight lines (10 and 20).
    - Line 10: track heading is 200° true North or 198° magnetic (the declination is 2 - 3° east)
    - Line 20: track heading is 179° true North or 177° magnetic

Line 10 indicates flight lines for Pol-InSAR and spatial tomography. Line 20 were flown after a special request of ESA in order to cover the laser area in near range of the radar image. The waypoints 2, 3 and 4 indicate the CR positions.

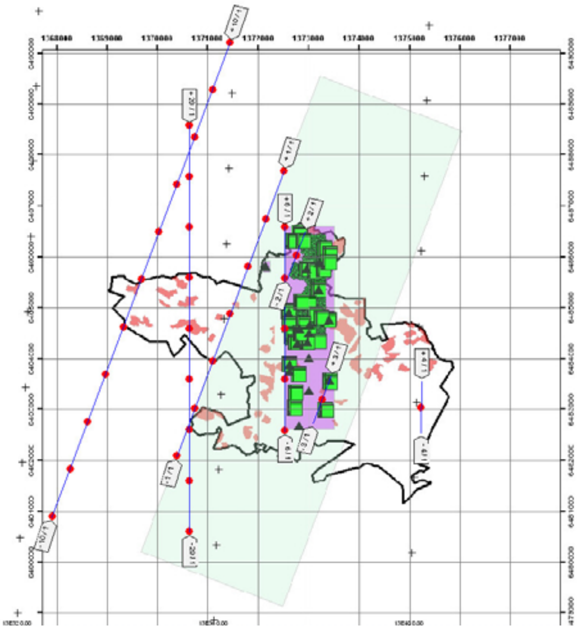

Figure 4.2: Flight lines for the BIOSAR campaign over the Remningstorp forest area. Line 10 for Pol-InSAR and Line 20 for PolSAR data acquisitions.

In order to obtain the highest possible variation of baselines the best strategy was to vary the baselines in time. The reason for it is the limitation of the amount of flight passes which is limited in the range distance of the aircraft in function of the weight of the E-SAR system. For the installation of the L-band and P-band hardware and antennas maximum 9 passes could be flown. Therefore the baseline configurations for the flights were varying during the three campaigns in order to obtain 9 baselines for topographic investigations. For L-band only one constant and one additional baseline could be flown. Line 20 was selected to ensure that the tests sites and associated in-situ and laser height data were acquired at incidence angles compartible with a spaceborne system, typically 25-35 degrees incidence.

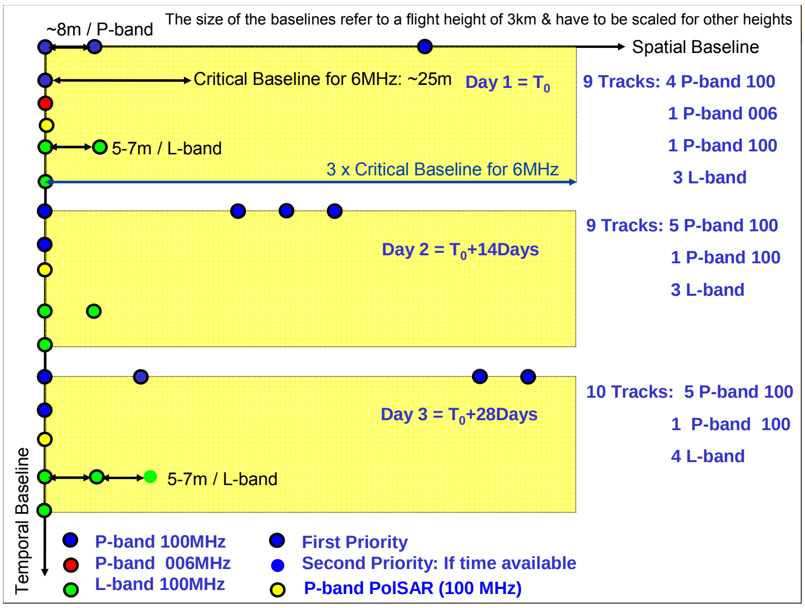

Figure 4.3: Temporal distribution of the baselines at L- and P-band.

5 AIRBORNE DATA ACQUISITION

Overall the data collection during the BIOSAR was successful in terms of logistics and planned data acquisition as stated in the experimental plan. In the following the mission logistics, the calibration for the airborne SAR, measurement campaign execution and data quality are described.

5.1 Mission Logistics

Before the BIOSAR campaign start the E-SAR system was tested. The direct flight to the test site has been performed as defined in the mission planning that is described in the Experimental Plan. The ferry flight of the Do228 took approximately 4 h starting in Oberpfaffenhofen and landing at the airport Lidköping in Sweden. Data acquisition was done over the North-South and the tilted flight track with the heading 179° during one day.

The time table in Figure 5.1 shows the time duration of the three campaigns.

BIOSAR Issue	Duration	Start	End
1. Campaign	**4 Days**	**06/03**	**09/03**
Ferry to ESGL	1 Day	06/03	06/03
Data Acquisition	2 Day	07/03	08/03
Ferry to TOS	1 Day	09/03	09/03
2. Campaign	**6 Days**	**28/03**	**02/04**
Ferry to ESGL	1 Day	28/03	28/03
Data Acquisition	4 Day	29/03	01/04
Ferry to EDMO	1 Day	02/04	02/04
3. Campaign	**5 Days**	**28/04**	**02/05**
Ferry to ESGL	1 Day	28/04	28/04
Data Acquisition	4 Day	29/04	01/05
Ferry to EDMO	1 Day	02/05	02/05

Figure 5.1: Time table for the data acquisition

5.2 Calibration of the E-SAR system

In order to secure high quality E-SAR data, recording of good quality kinematic phase differential GPS measurements a GPS monitoring station has been installed at the airport from FOI. Static DGPS surveying using data of a permanent GPS station at a range of less than 50 km has been performed to determine its geographical position with a relative accuracy of less than 5 cm. The chosen test sites were located not too far from the airport, so that only few reference points needed to be set-up. 3 corner reflectors were selected from 5 for validation purposes. The 3 corner reflectors were fixed for the whole time and have the size of 5 m. The corner reflectors belongi to FOI and their position and stability have been already described in the sections before.

5.3 Main Measurement Campaign

A total of 3 radar campaigns were executed in the period of 08.03 and 03.05.2007 over the Remmningstorp test site in southern Sweden. All data as already described in the Experimental Plan were able to be collected, without any delays or technical problems. The data were recorded on HHDT Tapes and were transcribed to hard disk at the DLR site after the data acquisition . After transcription the radar data processing started, with an integrated radar data quality check.

In Figure 5.2 two photo graphs are presented showing the airport of Lidköping the main base during the three E-SAR flight campaigns and a view out of the aircraft during the first flight campaign.

Figure 5.2: Left the airport of Lidköping the main base for the starting and landing before and after the flight campaign of the E-SAR system. Right view from the aircraft during the first flight over the Remningstorp test site.

Figure 5.3: View out of the aircraft at the second flight E-SAR flight campaign

5.4 Radar Data Acquisition

The test site is divided into two smaller areas of interest:

- t01: Pol-InSAR area of interest (flight direction south-west, look direction left)
- t02: PolSAR area of interest. (flight direction south, look direction left)

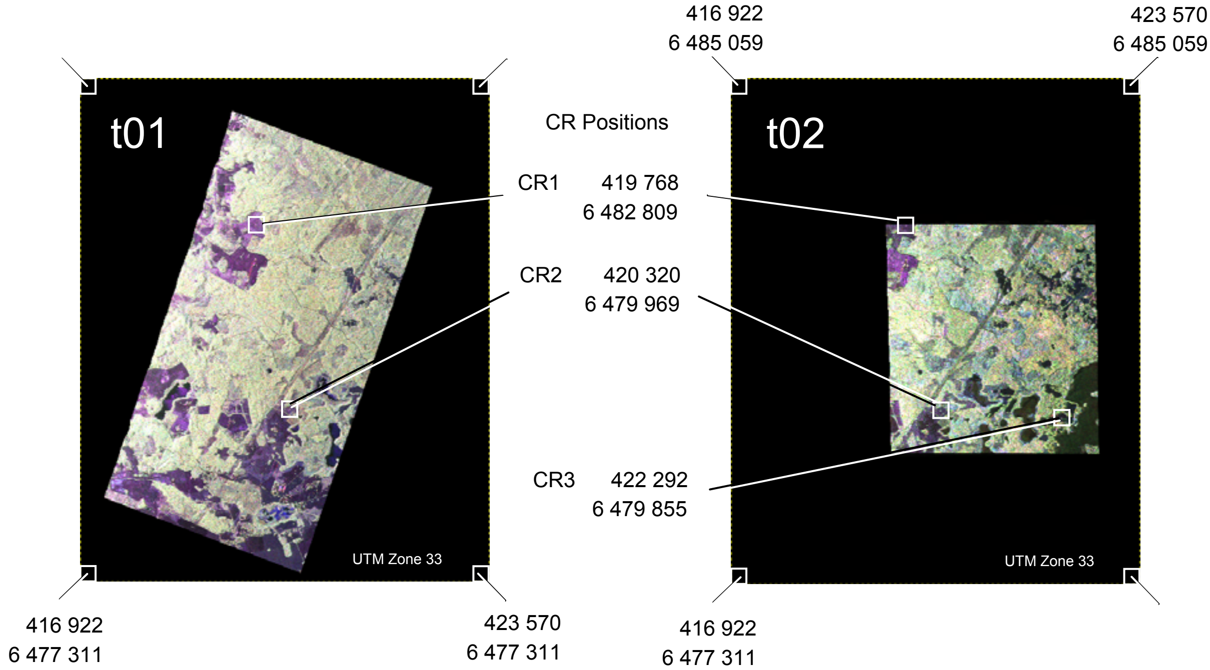

Three airborne SAR data sets have been acquired for BIOSAR:

(1) Pol-InSAR data set in P-band (14 scenes) at Remningstorp t01

(2) Pol-InSAR data set in L-band (9 scenes) at Remningstorp t01

(3) PolSAR data set in P-band (4 scenes) at Remningstorp t02

5.5 SAR Processing

5.5.1 Processing Strategy

The overall strategy in processing the acquired airborne BIOSAR data is to reach a maximum in comparability. Each data set is therefore processed in repeat pass mode, i.e. all scenes within a data set are co registered to each other. In that way it is achieved that corresponding pixels in different images refer to exactly the same position on ground.

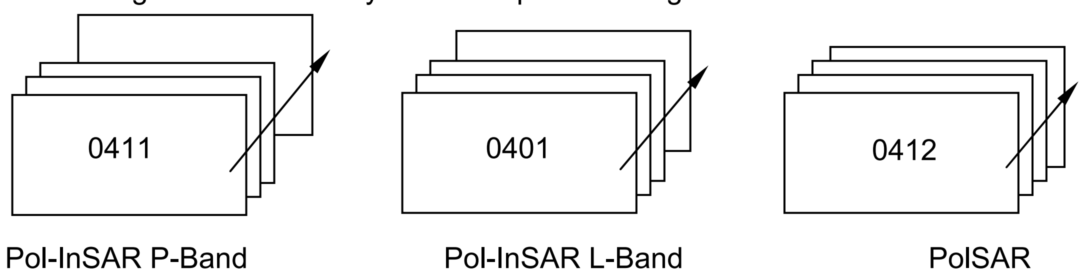

Due to varying wind conditions from scene to scene, each scene is usually imaged in its individual image geometry (its individual flight track, velocity variations and aircraft roll, drift and pitch angles). In contrast to single pass processing, repeat pass processing allows to process scenes according to the image geometry of a reference scene (master).

The master scene in a data set is usually chosen among the nearly ideal flight tracks. For BIOSAR, the following scenes have been chosen as master scenes among InSAR-masters/Slave-0m scenes due to calm wind conditions on May 5, 7007:

- 07biosar0411:Pol-InSAR P-Band Repeat Pass Master
- 07biosar0401:Pol-InSAR L-Band Repeat Pass Master
- 07biosar0412:PolSAR Repeat Pass Master

This processing approach allowed the

- calculation of interferograms (coherency and interferometric phase) and a
- pixel-by-pixel comparison of polarimetric images within data sets.

5.5.2 Digital Elevation Model

In scenes with varying terrain (height differences of more than 50 metres in a scene) it is important to embrace a precise digital elevation model in repeat pass SAR processing. Otherwise, platform motion errors cannot be estimated and corrected properly.

In all BIOSAR repeat pass processing, an external Digital Elevation Model (DEM) ordered from Lantmäteriet, the National Land Survey of Sweden, has been used.

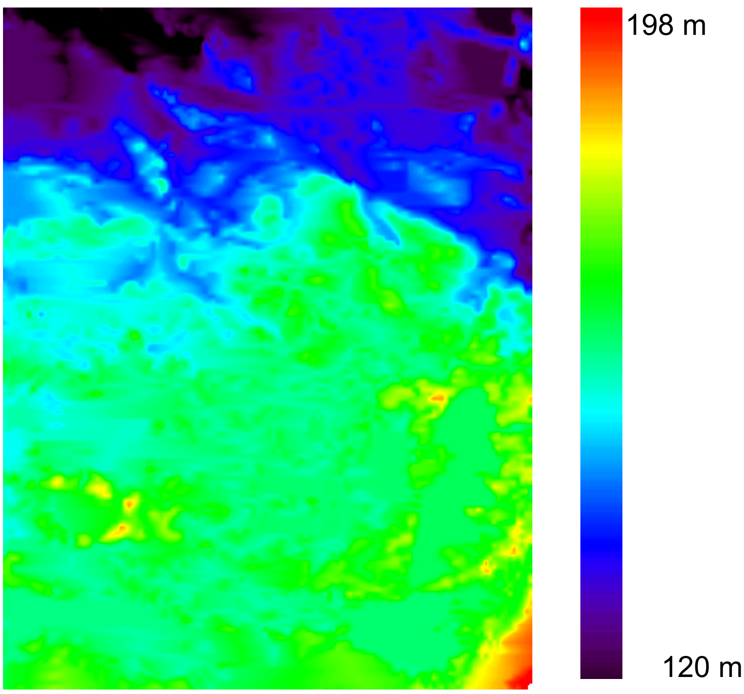

Figure 5.4: DEM Remningstorp in UTM zone 33 projection. (DEM coordinates correspond to the Remningstorp test site locations t01 and t02 given above.

The original DEM was in ASCII code in RT90 projection in pixel spacing of 50 by 50 metres. It had to be converted to UTM zone 33 binary format and pixel spacing 5 by 5 metres for SAR precision processing. It has been, furthermore, converted to pixel spacing 2 by 2 metres in order to allow geo-referencing the processed data (RGI) to Geocoded and Terrain Corrected (GTC) products in a 2 by 2 meters grid.

5.6 Flights and Processing Survey

The following table shows all scene IDs and summarises all data acquisitions in three airborne SAR data sets for BIOSAR:

Time	Pol-InSAR/Tomo P-band (Baseline [m])	Pol-InSAR L-band (Baseline [m])	PolSAR P-band	6MHz P-band
09/03/2007 #Tracks: 9	Master 0105 RGI, GTC 10m 0106 RGI 80m 0107 RGI 0m 0109 RGI, GTC	Master 0101 RGI, GTC 8m 0103 RGI 0m 0104 RGI, GTC	0110 RGI, GTC	0111 RGI, GTC
31/03 - 02/04 #Tracks: 9	Master 0301 RGI, GTC 30m 0302 RGI 40m 0303 RGI 50m 0304 RGI 0m 0306 RGI, GTC	Master 0201 RGI, GTC 8m 0202 RGI 0m 0205 RGI, GTC	0206 RGI, GTC	
02/05 #Tracks: 9	Master 0406 RGI, GTC 20m 0407 RGI 60m 0408 RGI 70m 0409 RGI 0m **0411** RGI, GTC	Master **0401** RGI, GTC 8m 0402 RGI 0m 0405 RGI, GTC	**0412** RGI, GTC	

Pol-InSAR P-Band: RP-Processing Master: 0411, Slaves: 0105, 0106, 0107, 0109, 0301, 0302, 0303, 0304, 0306
Pol-InSAR L-Band: RP-Processing Master: 0401, Slaves: 0101, 0103, 0104, 0201, 0202, 0205, 0402, 0405
PolSAR P-Band: RP-Processing Master: 0412, Slaves: 0110, 0111, 0206

RGI = Radar Geometry Image
GTC = Geocoded Terrain Corrected

Figure 5.5: Acquired BioSAR data at different frequencies and baselines

5.7 Processing Workflow

5.7.1 Single Pass Processing

The acquired airborne BIOSAR data were processed according to E-SAR standard products.

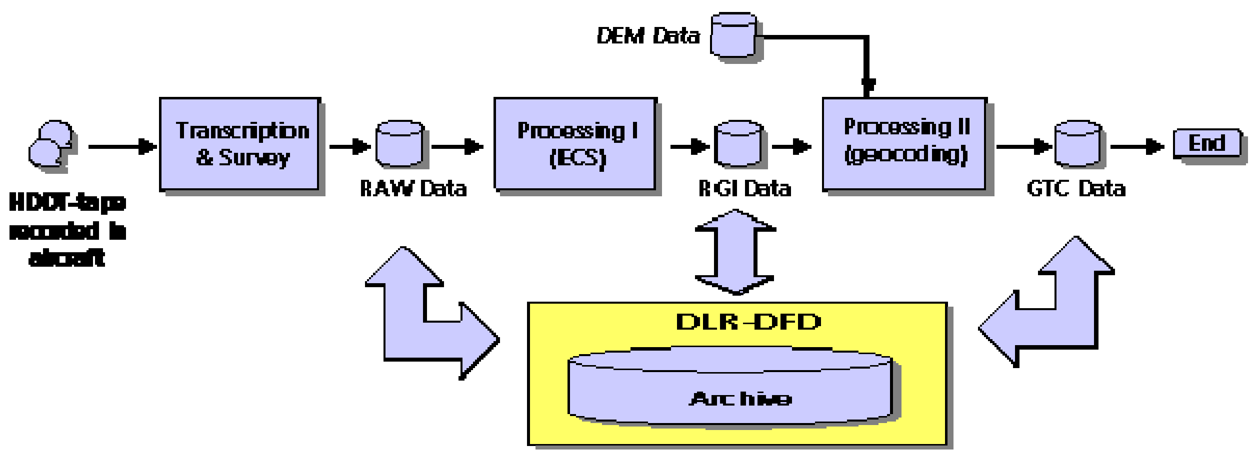

Figure 5.6: E-SAR processing workflow: (1) Transcription, (2) Precision SAR processing, (3) Geocoding

E-SAR products:

RAW …	Raw product (after transcription from tape and survey processing)
RGI …	Radar geometry image product (after precision SAR processing)
GTC …	Geo-coded and terrain corrected product (after geocoding)

Step 1 includes data transcription and channel separation of recorded SAR raw data from tape to hard disc, navigation data processing and a first data screening, i.e. survey processing (quicklook images) and flight track evaluations (e.g. squint variations). Especially, squint variations are investigated prior to precise processing.

Step 2 accomplishes high-precision SAR processing creating fully resolved SAR images in slant range geometry (fix resolution in azimuth and range direction). Additionally, the slant range image is projected to ground range geometry assuming flat terrain. (In that geometry, the image range resolution naturally degrades from far to near range according to steeper incidence angles.)

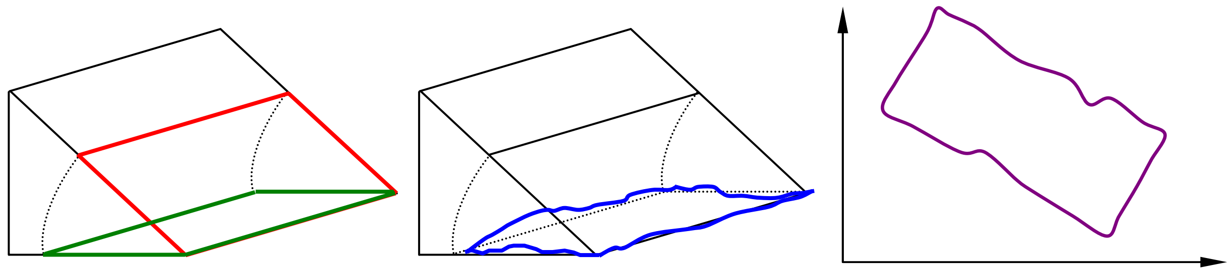

Figure 5.7: SAR data geometries: SLANT range (red), GROUND range (green), GROUND range terrain corrected (blue), GEOCODED and terrain corrected (purple)

Step 3 performs terrain-correction and geocoding which converts slant range data (RGI) into the geometry of a three-dimensional geographic coordinate system (e.g. WGS84 ellipsoid) and its projection onto a projected geographic coordinate system (e.g. UTM). This forms the Geocoded and Terrain Corrected product (GTC).

5.7.2 Repeat Pass Processing

Repeat pass processing performs precision SAR processing (as described above) of a slave scene according to an already calculated master scene. The slave scene start and stop times are chosen such that they match those of the master scene. Furthermore, the slave scene is fully co -registered during processing to the master scene. Up to three iterations of the Multi-squint technique are used to estimate and eliminate platform motion errors. Finally, an interferogram is calculated (coherency and interferometric phase).

5.8 Geocoding

The Universal Transverse Mercator System (UTM), zone 33 (ellipsoid WGS84) has been used for BIOSAR data projections because of its common global use and popularity. A pixel spacing of two metres in east and north direction adapts well to the processed resolutions.

Geocoding Features:

Ellipsoid:	*WGS 84*
UTM zone	*33*
Matrix dimension (east x north):	*3325 x 3875*
Easting coordinates:	*416922 … 423570*
Northing coordinates:	*6477311 … 6485059*
Pixel spacing (east x north):	*2m x 2m*

In BIOSAR, we geocoded all master and slave-0m scenes.

Additional geocodings can be done using the delivered geocoding transformation matrices included in GTC products as files

- azimuth_flt<scene ID>_int.dat.gz
- range_flt<scene ID>_int.dat.gz

for multilook geometry conversions and

- azimuth_slc<scene ID>_int.dat.gz
- range_slc<scene ID>_int.dat.gz

for single look complex (SLC) geometry conversions.

ML Data Geocoding (Multi-look)

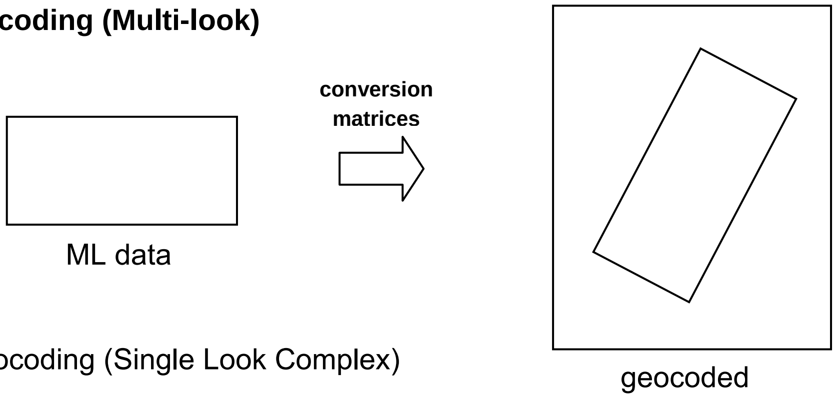

SLC Data Geocoding (Single Look Complex)

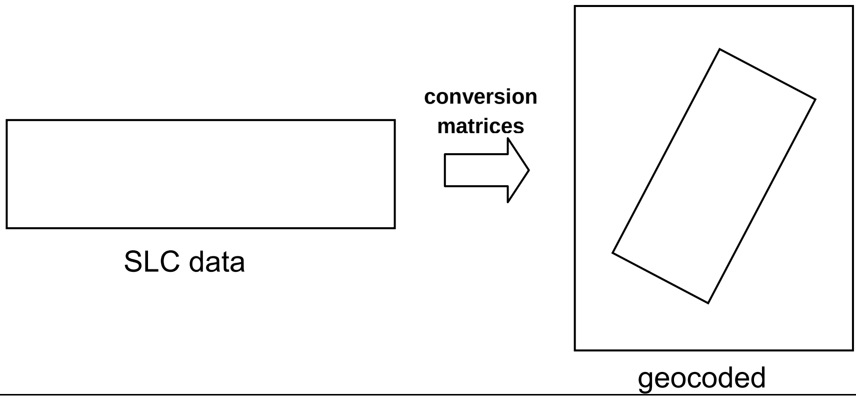

Furthermore, all repeat pass slave scenes in SLC geometry are co-registered to master geometry, i.e. the master conversion matrices azimuth_slc* and range_slc* can be used to geocode slave SLC-geometry data to UTM grid.

The following master GTC products include SLC conversion matrices for the three data sets (Pol-InSAR-L, Pol-InSAR-P, PolSAR):

- Pol-InSAR L-Band Master Scene ID: 07biosar0401x1_t01
- Pol-InSAR P-Band Master Scene ID: 07biosar0411x1_t01
- Pol-SAR Master Scene ID: 07biosar0412x1_t02

The master ML geometry conversion files cannot be used for slave multilook data conversions because slave ML data are not co-registered to master geometry.

Further details about reading the conversion files are explained in the corresponding GTC product <scene ID>_README_GTC.txt file.

5.9 Data Quality

5.9.1 Data Selection

The quality of airborne SAR data strongly depends on platform movements, i.e. wind and weather conditions. Therefore the E-SAR data are acquired with redundancy as far as the financial budget, fuel or other constrains allow the acquisition of additional data takes. The E-SAR operator decides while E-SAR operation during flight whether some tracks must be repeated due to severe fluctuations or intolerable deviations the from nominal flight track.

This strategy secures that bad data takes can be sorted out. For BIOSAR, at least two data takes were repeated: 0102 and 0305 as 0103 and 0306 respectively.

5.9.2 GPS Data Quality

During each data acquisition flight for BIOSAR we had periods of critical GPS satellite constellation. Only flight “biosar04” can be considered uncritical.

In the first three flights (“biosar01”, “biosar02”, “biosar03”) there were occasionally only three GPS satellites above 15° of elevation which results in no solution for the aircraft position. The satellite elevation mask had to be set to 10° elevation to find at least four satellites giving a solution.

Nevertheless, no obvious quality loss due to the critical GPS satellite constellations could found in the processed data.

5.9.3 RFI Filtering

In P-band data acquisitions we had many disturbances from communication channels, mainly occurring in the upper frequency band. As a consequence, we could not use the full range data spectrum. Instead of processing from -45 MHz to +45 MHz we only used frequencies -45 MHz to +25 MHz. This approach eliminated most of the Radio Frequency Interferences (RFI) from communication channels in P-band such that an excellent image quality is achieved in P-band.

Therefore the bandwidth of the full resolution P-band data is reduced from 94 to 70 MHz.

In L-band, no interferences could be noticed.

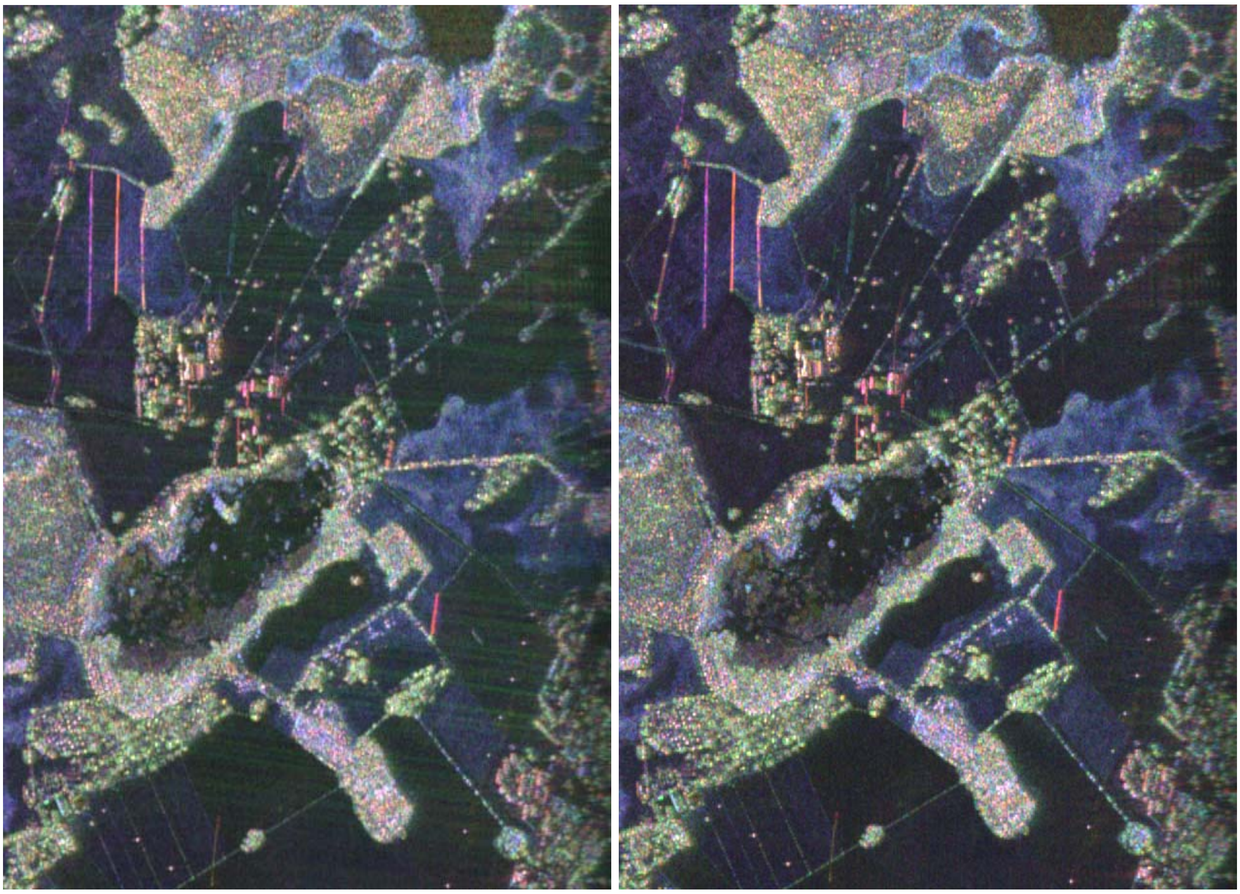

Figure 5.8: P-band data with Radio Frequency Interferences (RFI) left and RFI filtered (right)

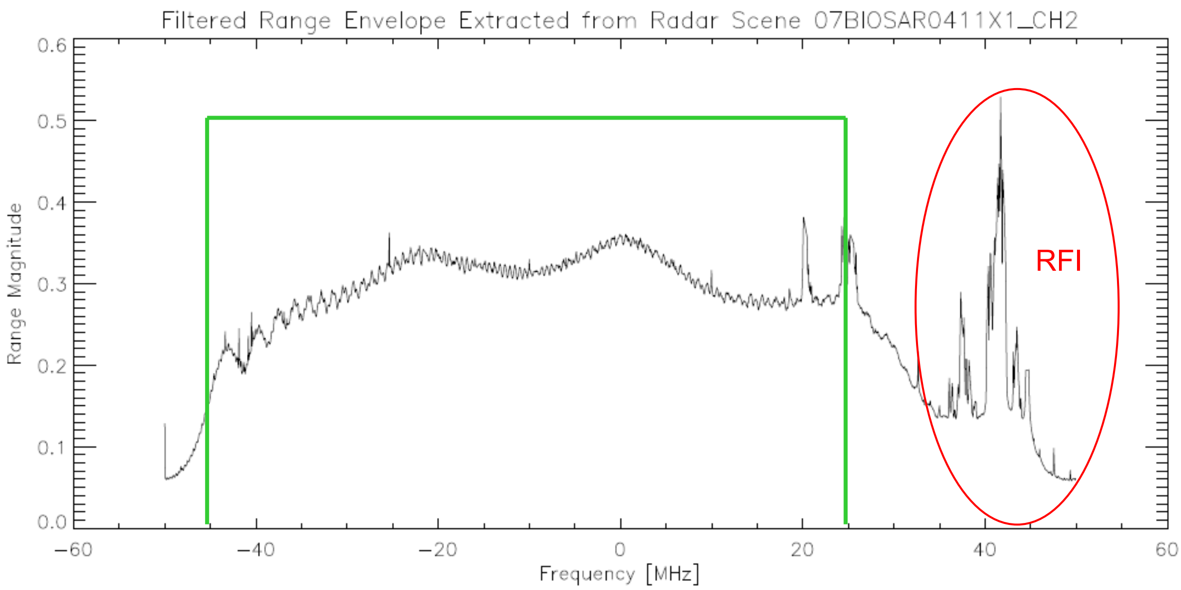

Figure 5.9: P-band raw data spectrum in range, RFI disturbances beyond +25 MHz are removed

5.9.4 Residual Motion Error Correction

An iterative estimation of residual motion errors (variable baseline errors) has been performed in all L-band and P-band repeat pass processing using the multi-squint approach.

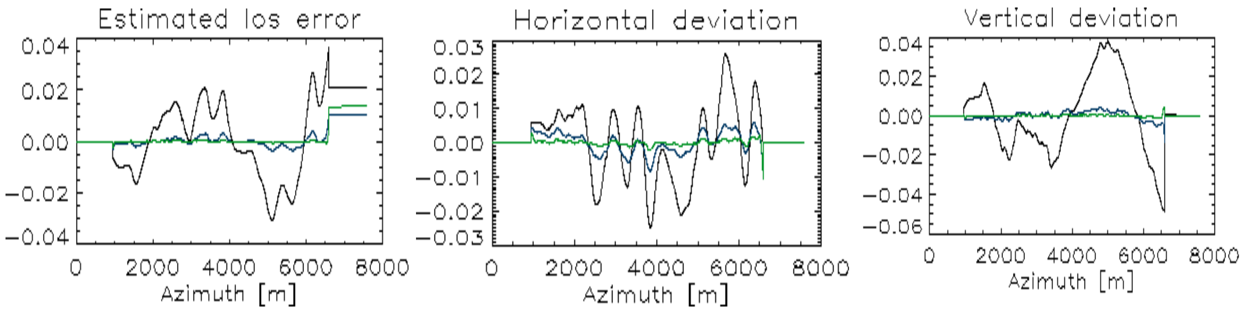

Figure 5.10: L-band residual motion error correction (for example scene 0405 in slave to scene 0401), a line-of-sight (LOS) error of 4 cm is reduced to only millimetres

The accuracy of variable baseline error compensation is in the order of millimetres. All slave data have been iteratively reprocessed to compensate for these residual motion errors. In P-band, the effect of residual motion errors is less severe but has also been compensated (see below).

Only the correction of residual motion errors let Pol-InSAR and tomography techniques become feasible.

5.9.5 Squint and Velocity

Squint and velocity differences between master and slave scenes influence the ability to co-register slave scenes to master scenes. As the slave scene geometry (squint) is forced to that of the master scene, the slave quality might degrade due to the wrong squint angle.

In L- and P-band we can accept up to 5 degrees difference in squint angles between master and slave scenes. Velocity differences between master and slaves are less critical.

In BIOSAR, we matched those requirements and no quality losses in slave scenes due to squint or velocity differences could be noticed.

Pol-InSAR P-Band

Scene ID	Test Site	Track	Band	Pol	Velocity	Common Velocity	Squint	Common Squint
07biosar0105x1	t01	10	P	PM	86.45	92,5	7.09	2.61
07biosar0106x1	t01	11	P	PM	90.24	92,5	6.89	2.61
07biosar0107x1	t01	18	P	PM	90.55	92,5	6.70	2.61
07biosar0109x1	t01	10	P	PM	91.19	92,5	6.57	2.61
07biosar0301x1	t01	10	P	PM	93.09	92,5	6.36	2.61
07biosar0302x1	t01	13	P	PM	91.54	92,5	6.47	2.61
07biosar0303x1	t01	14	P	PM	94.95	92,5	5.52	2.61
07biosar0304x1	t01	15	P	PM	95.14	92,5	5.76	2.61
07biosar0306x1	t01	10	P	PM	91.97	92,5	5.97	2.61
07biosar0406x1	t01	10	P	PM	102.20	92,5	2.31	2.61
07biosar0407x1	t01	12	P	PM	95.49	92,5	3.32	2.61
07biosar0408x1	t01	16	P	PM	95.32	92,5	3.16	2.61
07biosar0409x1	t01	17	P	PM	96.09	92,5	3.24	2.61
07biosar0411x1	t01	10	P	PM	96.84	92,5	2.73	2.61

Pol-InSAR L-Band

Scene ID	Test Site	Track	Band	Pol	Velocity	Common Velocity	Squint	Common Squint
07biosar0101x1	t01	10	L	PM	88.74	92.5	3.64	0.45
07biosar0103x1	t01	11	L	PM	91.01	92.5	4.51	0.45
07biosar0104x1	t01	10	L	PM	90.10	92.5	5.04	0.45
07biosar0201x1	t01	10	L	PM	92.34	92.5	2.10	0.45
07biosar0202x1	t01	11	L	PM	91.70	92.5	2.50	0.45
07biosar0205x1	t01	10	L	PM	92.05	92.5	2.76	0.45
07biosar0401x1	t01	10	L	PM	95.63	92.5	0.78	0.45
07biosar0402x1	t01	11	L	PM	97.45	92.5	1.60	0.45
07biosar0405x1	t01	10	L	PM	96.10	92.5	1.21	0.45

PolSAR

Scene ID	Test Site	Track	Band	Pol	Velocity	Common Velocity	Squint	Common Squint
07biosar0110x1	t02	20	P	PM	88.41	92.5	6.75	1.46
07biosar0111x1	t02	20	P	PM	88.59	92.5	6.63	1.46
07biosar0206x1	t02	20	P	PM	92.19	92.5	5.06	1.46
07biosar0412x1	t02	20	P	PM	95.82	92.5	1.27	1.46

5.10 Calibration

After each mounting of the airborne E-SAR instrument into the aircraft the radar system parameters are checked by dedicated measurements. Thus the system is calibrated before the first SAR data acquisition. During the camapaign acquisitions corner reflectors are not used for system calibration but serve for the following purposes:

- as a check of the radiometric calibration
- as a check of the achieved image resolution and as
- as a reference for the geocoding process.

In Figure 5.11 the same SAR images in L-band are plotted with the position of the corner reflectors. In plot t01 two corner reflectors can be seen: one in near and the other one in far range. In t02 three corner reflectors are visible, one along azimuth, second in near and the third one in far range.

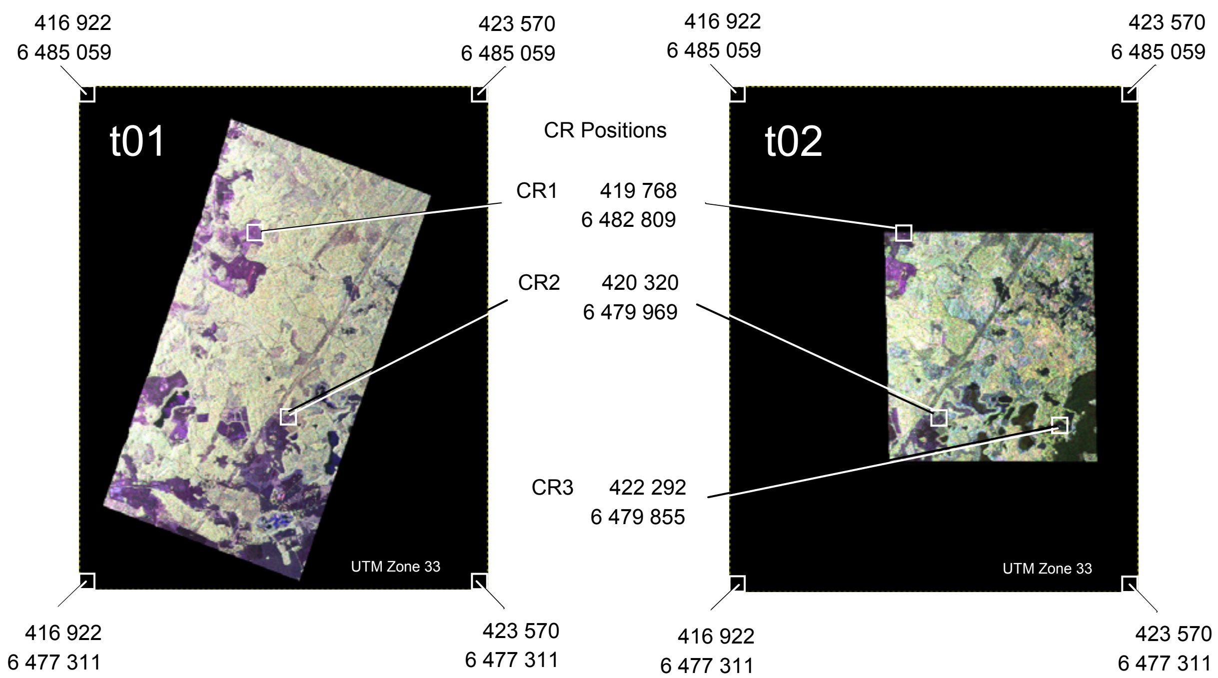

Figure 5.11: Three corner reflectors (CR1 and CR2) were adjusted as displayed in the left and right image

E-SAR uses a fix calibration factor of 1.000.000 for amplifying the backscatter signal intensity in order to allow a 16 bit data representation and hence securing sufficient data dynamics for data evaluation. This determines the E-SAR calibration constant which amounts to 60 dB.

5.10.1 Calibration Requirements

Depending on the complexity of the intended data evaluation, different calibration requirements must be considered. With increasing complexity also the calibration effort is increased, which is summarized in the table below:

Data Evaluation Method	Reflectivity Evaluation	Pol-InSAR	Tomography
Calibration Requirements	**Radiometric calibration** relative gain between different acquisitions (antenna patterns, different receiver gain settings, etc.) absolute radiometric calibration	**Polarimetric & interferometric calibration** cross-talk, imbalance, co-polar phase residual motion errors no absolute phase calibration required.	**Tomographic phase calibration** absolute phase calibration for all data takes required (range dependent because of baseline errors in the order of 5-10 cm)
Corner Reflectors	for validation only	for validation only	mandatory CR use to estimate constant baseline offsets (alternatively DEM)

Absolute tomograpic phase calibration (to properly allow the combination of all P-band data takes) has not been carried out by DLR-HR for BIOSAR. It is left to be performed by the data evaluation groups depending on their needs (for example for SAR tomography).

5.10.2 Radiometric Calibration

The following table summarises the differences between expected (theoretic) and measured radar cross section (RCS) in [dB] on corner reflectors CR1 and CR2 in the L-band scenes. Deviations of +/- 1 dB around the E-SAR calibration constant of 60 dB are tolerated.

Pol-InSAR L-Band – CR1

Scene ID	Try	Freq	Track	CR Name	Scene No.	HH	VV
e07biosar0101x1	t01	L	10	CR1	1	61.2025	61.5933
e07biosar0103x1	t01	L	11	CR1	2	59.4519	59.2052
e07biosar0104x1	t01	L	10	CR1	3	57.7377	58.3047
e07biosar0201x1	t01	L	10	CR1	4	58.2717	58.5594
e07biosar0202x1	t01	L	11	CR1	5	58.2472	58.3812
e07biosar0205x1	t01	L	10	CR1	6	58.2708	58.1742

e07biosar0401x1	t01	L	10	CR1	7	59.2942	59.3523
e07biosar0402x1	t01	L	11	CR1	8	58.6304	58.7622
e07biosar0405x1	t01	L	10	CR1	9	59.0268	59.0864

Pol-InSAR L-Band – CR2

Scene ID	Try	Freq	Track	CR	Scene	HH	VV
				No.	No.		
e07biosar0101x1	t01	L	10	CR2	1	61.2525	60.8241
e07biosar0103x1	t01	L	11	CR2	2	60.0396	59.1842
e07biosar0104x1	t01	L	10	CR2	3	58.6832	58.6179
e07biosar0201x1	t01	L	10	CR2	4	59.8682	59.7553
e07biosar0202x1	t01	L	11	CR2	5	59.7323	59.7478
e07biosar0205x1	t01	L	10	CR2	6	59.6449	59.5742
e07biosar0401x1	t01	L	10	CR2	7	60.3971	60.1866
e07biosar0402x1	t01	L	11	CR2	8	59.7613	59.555
e07biosar0405x1	t01	L	10	CR2	9	60.0888	59.9544

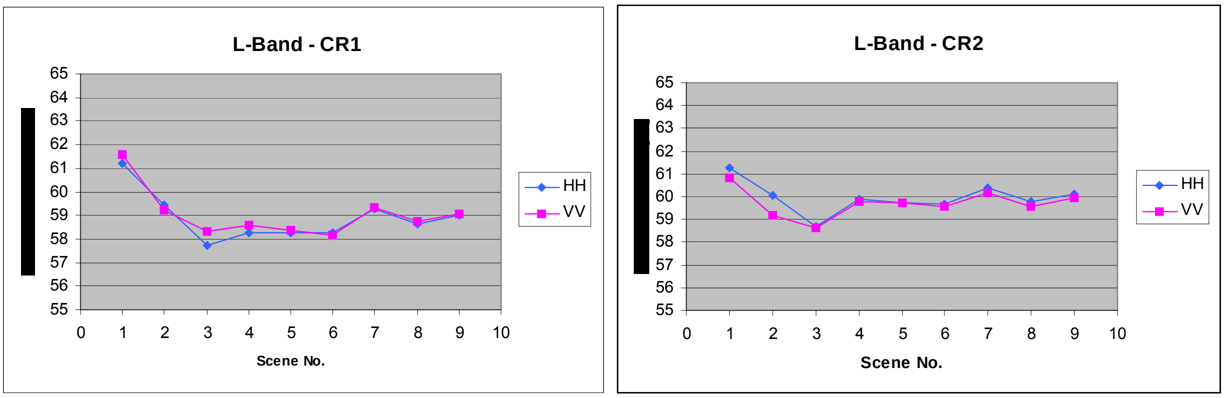

Figure 5.12: Radiometric Calibration in time for the different data acquisitions for CR1 and CR2 at L-band

Calibration check at corner reflectors CR1 and CR2 for L-band: CR1 is 1-2 dB too low (wrong orientation in elevation (17 deg instead of 20) – see also P-band below and section 6.3). The first data acquisition (scene ID biosar0101) is out of specification for both corner reflectors (1-2 dB too high). Probably due to system warm-up, otherwise good temporal stability has been observed. We suggest to rely to the third (0104) L-band acquisition for this first flight period in terms of radiometric calibration.

Pol-InSAR P-Band – CR1

Scene ID	Try	Freq	Track	CR Name	Scene No.	HH	VV
e07biosar0105x1	t01	P	10	CR1	1	58.2103	57.4643
e07biosar0106x1	t01	P	11	CR1	2	58.4358	57.6445
e07biosar0107x1	t01	P	18	CR1	3	58.4742	57.8022
e07biosar0108x1	t01	P	12	CR1	4	58.3033	57.6205
e07biosar0109x1	t01	P	10	CR1	5	58.6942	57.9273
e07biosar0301x1	t01	P	10	CR1	6	57.7878	57.3653
e07biosar0302x1	t01	P	13	CR1	7	57.8118	57.4474
e07biosar0303x1	t01	P	14	CR1	8	57.7125	57.4985
e07biosar0304x1	t01	P	15	CR1	9	57.779	57.4655
e07biosar0306x1	t01	P	10	CR1	10	57.8567	57.3677
e07biosar0307x1	t01	P	12	CR1	11	57.7891	57.3868
e07biosar0406x1	t01	P	10	CR1	12	57.6088	57.0431
e07biosar0407x1	t01	P	12	CR1	13	57.7074	57.2074
e07biosar0408x1	t01	P	16	CR1	14	57.7827	57.3485
e07biosar0409x1	t01	P	17	CR1	15	57.8362	57.352
e07biosar0411x1	t01	P	10	CR1	16	57.7278	57.3402

Pol-InSAR P-Band – CR2

Scene ID	Try	Freq	Track	CR No.	Scene No.	HH	VV
e07biosar0105x1	t01	P	10	CR2	1	59.7866	59.6812
e07biosar0106x1	t01	P	11	CR2	2	60.057	59.8276
e07biosar0107x1	t01	P	18	CR2	3	59.8795	59.8661
e07biosar0108x1	t01	P	12	CR2	4	59.8986	59.776
e07biosar0109x1	t01	P	10	CR2	5	60.1493	59.7489
e07biosar0301x1	t01	P	10	CR2	6	59.5231	59.5717
e07biosar0302x1	t01	P	13	CR2	7	59.4876	59.4055
e07biosar0303x1	t01	P	14	CR2	8	59.5169	59.7387
e07biosar0304x1	t01	P	15	CR2	9	59.5254	59.5715
e07biosar0306x1	t01	P	10	CR2	10	59.4097	59.6278
e07biosar0307x1	t01	P	12	CR2	11	59.5585	59.6323
e07biosar0406x1	t01	P	10	CR2	12	59.4923	59.6398
e07biosar0407x1	t01	P	12	CR2	13	59.6253	59.7818
e07biosar0408x1	t01	P	16	CR2	14	59.4292	59.6072
e07biosar0409x1	t01	P	17	CR2	15	59.524	59.6596
e07biosar0411x1	t01	P	10	CR2	16	59.6701	59.8381

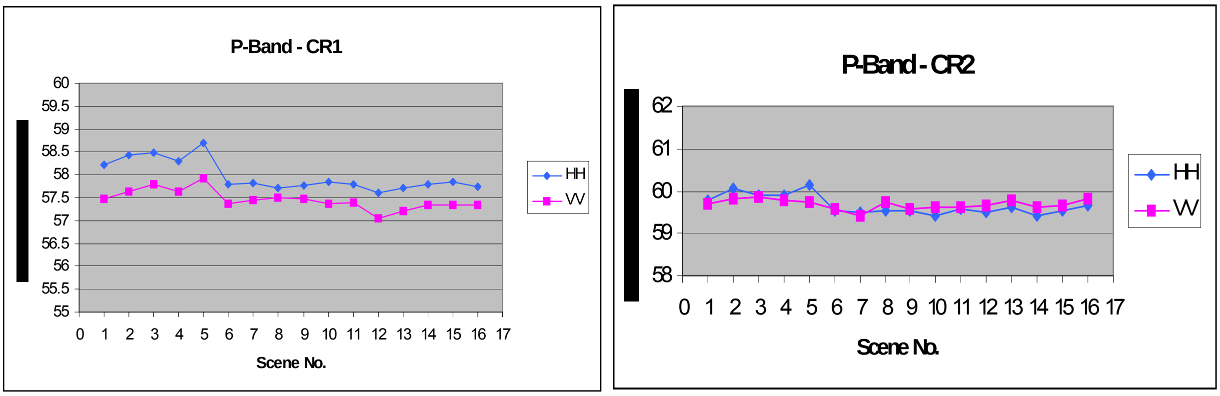

Figure 5.12: Radiometric Calibration in time for the different data acquisitions for CR1 and CR2 at P-band

Calibration check at corner reflectors CR1 and CR2 for P-band: Also here CR1 is 1-2 dB too low (wrong orientation in elevation (17 deg instead of 20) – see also L-band above and section 6.3). Otherwise good temporal stability.

Pol-SAR P-Band – CR3

Scene ID	Try	Freq	Track	CR No.	Scene No.	HH	VV
e07biosar0110x1	t02	P	20	CR3	1	59.8512	59.8683
e07biosar0206x1	t02	P	20	CR3	2	59.7697	59.6114
e07biosar0412x1	t02	P	20	CR3	3	59.7721	59.6508

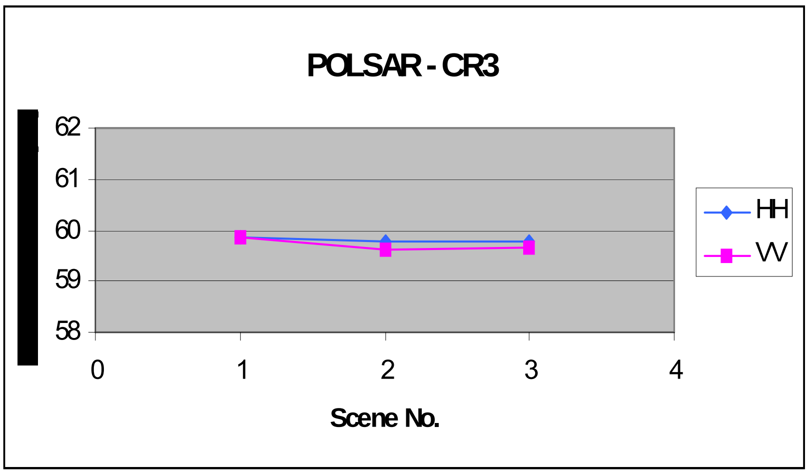

Figure 5.14: Radiometric Calibration in time for the different data acquisitions for CR3 at P-band

Calibration check at corner reflector CR3 for P-band: Corner reflectors CR1 and CR2 cannot be used for radiometric calibration checks in Pol-SAR scenes despite they are seen in the images (orientation is according to t01-flights). Only CR3 is oriented to t02-flights. The three 100MHz-bandwidth scenes (0110, 0206 and 0412) have excellent stability.

The 6MHz scene 0111 has not been considered for calibration check due to less reliable estimation of RCS on the corner reflector (low resolution).

5.10.3 Polarimetric Calibration

Pol-InSAR P-Band

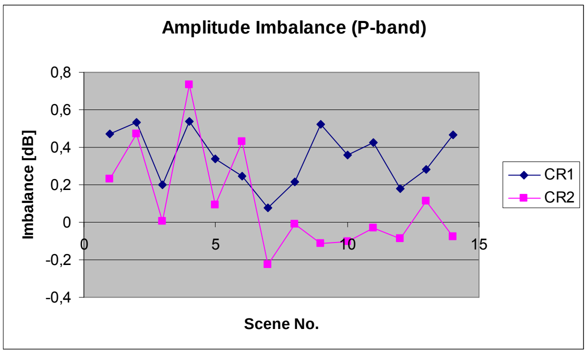

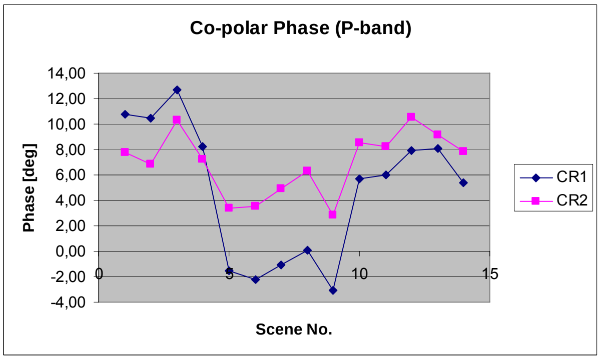

Pol-InSAR L-Band

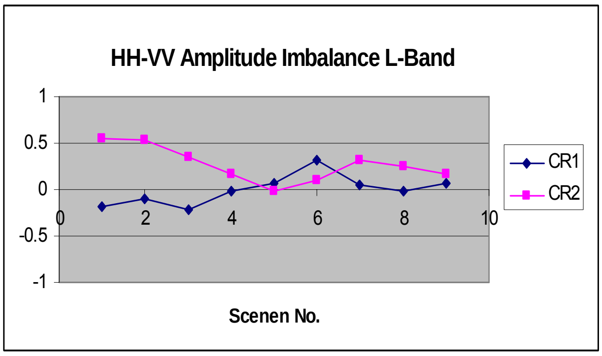

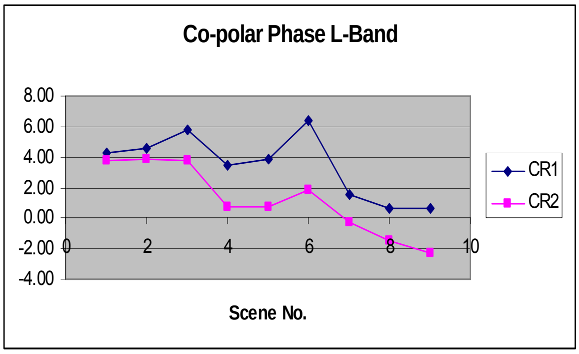

Pol-SAR P-Band

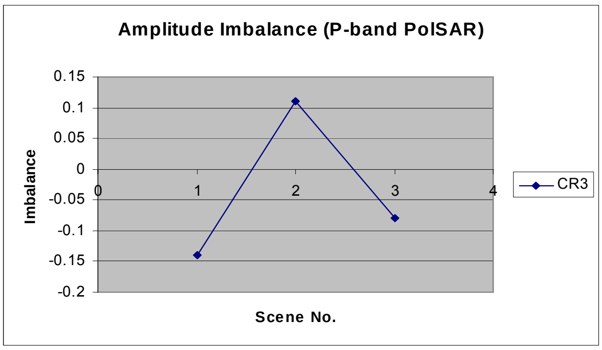

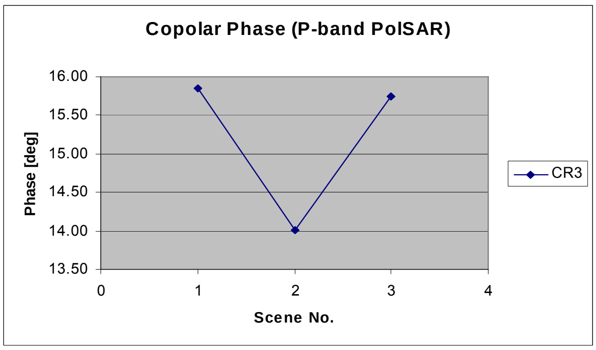

The polarimetric calibration check shows that all three data sets are within specification. We have channel imbalances between HH and VV polarisation of 0.5 to 1 dB which is within the radiometric accuracy. The co-polar phase may lie in the order of 10 to 15 degrees. All three data sets fulfil this requirement. Pol-InSAR P-band data are below 12 degrees and Pol-InSAR L-band is even below 6 degrees.

5.11 E-SAR system performance summary

The data quality analysis performed with the BIOSAR campaign data confirmed the expected performance of the E-SAR data products in terms of absolute and relative radiometric accuracy, polarimetric calibration performance and interferometric phase. The performance parameters are summarized in the table below:

Parameter	Accuracy	Remark
Absolute radiometric accuracy	+/- 1.0 dB	(*)
Relative radiometric accuracy	+/- 0.5 dB	within flight period over the swath(**)
Co-polar amplitude imbalance	+/- 0.5 dB	Absolute within one scene
Co-polar phase	+/- 15 deg (+/- 5 deg)	absolute (within one scene)
Relative interferometric phase	< 10 deg	along azimuth (***)

(*) Mission 1 BIOSAR data acquired in L-band have reduced absolute radiometric accuracy, probably due to system warmup effects.

(**) The good performance benefits also from the INDREX-II campaign data (acquired by E-SAR in 2004), where homogeneous rain forest data was used to evaluate uncertainties in the radiometric calibration of the antenna elevation patterns (which originate mainly from the influence of the antenna fuselage). This analysis improved the relative radiometric accuracy over the swath.

(***) The accuracy of the relative interferometric phase along azimuth is achieved by the use of sophisticated residual motion error estimation and compensation approaches, which improve the solution of the integrated INS/GPS data in a relative sense between master and slaves. Nevertheless, absolute interferometric phase calibration generally NOT performed for E-SAR repeat-pass interferometric data (which usually is range dependent).

GROUND MEASUREMENTS

5.12 Registrations of Reference GPS Data for E-SAR at Lidköping Airport

The DLR Dornier DO 228 aircraft with the E-SAR system onboard used Lidköping airport for the data collection program during the BioSAR 2007 experiment. This is a fairly small airport and it is normally closed during weekends and public holidays. This made it difficult to guarantee a full flexibility for the registration program in case of bad weather conditions or other delays. One exception from this constraint could, however, be arranged with a radar imaging mission undertaken on Saturday 31 March. The hangar space available at the airport was only used during the first visit of the DO 228. Figure 6.1 shows the aircraft at the airport during the last data collection period. Lidköping airport is located approximately 28 km from the centre of Remningstorp test site as illustrated in Figure 6.2. Further details about the airport infrastructure can be found in [1].


Figure 6.1: The DO 228 aircraft parked at Lidköping airport and in operation on the runway on 2 May.

In order to obtain high quality E-SAR data a reference GPS station was deployed at the airport and operated during all radar imaging missions. The equipment used for this purpose was an Ashtech Z-12 receiver unit. The registration frequency of available satellite signals was set to one per second. The time intervals with reference GPS data gathered by the Ashtech system are summarized in Table 6.1. Local time is UTC + 1 hour on 9 March, otherwise UTC + 2 hours.

Date	Start GPS (UTC)	Stop GPS (UTC)	Number of epochs
2007-03-09	07:43:46	11:36:45	13980
2007-03-31	11:27:14	14:22:22	10509
2007-04-02	07:46:01	10:03:48	8268
2007-05-02	09:54:37	13:10:52	11776

Table 6.1: Reference GPS data registered at Lidköping airport during BioSAR 2007.

The location for the GPS antenna mounted on a tripod was at the northeast part of the airfield, fairly close to the runway on its northern side. The photos in Figure 6.3 show the GPS system in operation during the E-SAR flight on 2 May.

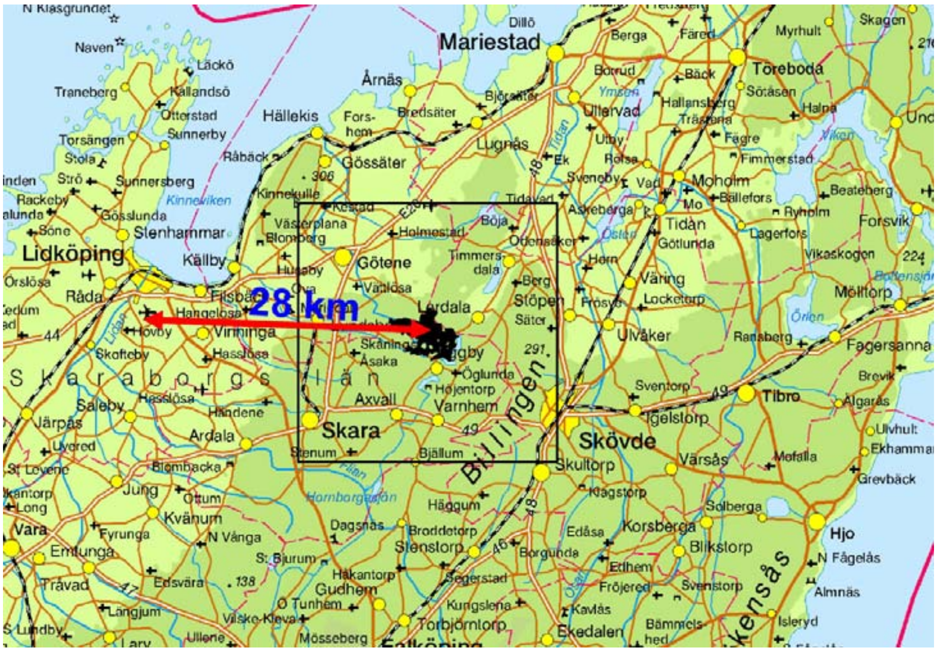

Figure 6.2: Map showing the Remningstorp test site and the Lidköping Hovby airport where the E-SAR system was based during the full BioSAR 2007 program. (© Map: Lantmäteriverket Gävle).

Figure 6.3: The reference GPS system deployed at Lidköping airport. The antenna dish is found 166 cm above the ground with the centre adjusted to line up at the middle point of a reference stake.

5.13 Accurate Positioning of Lidköping GPS Unit Using SWEPOS

In the post-processing to retrieve the detailed flight track of the E-SAR platform the reference GPS data collected in Lidköping are combined with registrations made by the navigation system onboard during the corresponding time interval. As an input parameter in this process it is of importance to have the absolute position of the deployed Ashtech Z-12 GPS antenna given accurately enough. To provide means to achieve that data from the Swedish national GPS network SWEPOS were ordered with margins to cover the time intervals given in Table 6.1.

The SWEPOS system is operated by LMV [2]. The network consists of 21 complete and 100 simplified stations distributed over the whole country of Sweden. To achieve redundancy and secure data access, the complete stations are equipped with two parallel GPS receiving systems and the power supply is also built to handle failures like power outages for a period of up to 48 hours. In addition, the GPS antenna is here mounted on pillars that are made of concrete and are placed on solid bedrock, often at high altitudes where the obstacles are in low elevations. The simplified stations have less redundancy and the antennas often mounted on available buildings with the supporting equipment indoors. Examples of a complete and simplified station in the SWEPOS network are seen in Figure 6.4.

Figure 6.4: The complete SWEPOS GPS station Jönköping is shown to the left whereas the antenna of the simplified station Falköping is found to the right. (Images: http://swepos.lmv.lm.se).

Data from four complete SWEPOS GPS stations and six simplified were provided for all occasions when detailed positioning was needed for the BioSAR activities. The data were made available on a daily subscription basis and could be downloaded from an ftp-server at LMV. The names and the accurate antenna positions for the complete and simplified stations in use are given in Table 6.2 and Table 6.3, respectively. The main criterion to select these stations was to encompass the region of interest, i.e. Remningstorp test site and Lidköping airport.

Station	Latitude (SWEREF 99)	Longitude (SWEREF 99)	Height (ellipsoidal, m)
Borås	57° 42’ 53.841107”	12° 53’ 28.841590”	219.9042
Jönköping	57° 44’ 43.696079”	14° 3’ 34.578991”	260.3517
Karlstad	59° 26’ 38.466738”	13° 30’ 20.237201”	114.2654
Vänersborg	58° 41’ 35.249161”	12° 2’ 5.997716”	169.6638

Table 6.2: Complete SWEPOS GPS stations providing data during BioSAR 2007.

Station	Latitude (SWEREF 99)	Longitude (SWEREF 99)	Height (ellipsoidal, m)
Falköping	58° 10' 11.766935"	13° 33' 21.901151"	259.8677
Hasslerör	58° 44' 56.552728"	13° 56' 15.743475"	97.6886
Hjo	58° 18' 4.761438"	14° 17' 11.431825"	140.2096
Kållandsö	58° 39' 49.053707"	13° 11' 32.995989"	90.0416
Väne-Åsaka	58° 14' 30.154240"	12° 25' 23.066046"	112.6157
Zinkgruvan	58° 49' 9.695595"	15° 5' 19.090206"	231.2269

Table 6.3: Simplified SWEPOS GPS stations providing data during BioSAR 2007.

The reference system SWEREF 99 found in Table 6.2 and Table 6.3 is the Swedish realisation of ETRS 89 (the European Terrestrial Reference System 1989). The maps in Figure 6.5 and Figure 6.6 give an idea of the approximate locations for these SWEPOS stations in relation to both Remningstorp and Lidköping airport, cf. Figure 6.2.

Figure 6.5: Locations of the four complete SWEPOS GPS stations providing data for accurate positioning during BioSAR. (Images: http://swepos.lmv.lm.se).

Figure 6.6: Locations of the six simplified SWEPOS GPS stations providing data for accurate positioning during BioSAR. (Images: http://swepos.lmv.lm.se).

The post-processing to retrieve the Lidköping location accurately was carried out by DLR with the same software package (Novatel Waypoint GrafNet/GrafNav v7.8) as the one used in the next step to calculate the aircraft flight track for each full data collection mission. By using the same software any differences in parameter settings could be avoided and hence reduce the risk to introduce small unintentional errors in the output result.

5.14 Positioning of the Trihedrals in Remningstorp

A few days before the first BioSAR data acquisition took place on March 9 the three trihedrals deployed in Remningstorp were adjusted according to the specifications given by DLR and found in Table 6.4. Trihedral #1 and #3 were aimed at giving support to flight line 10, i.e. the Pol-InSAR measurements.

Trihedral	Baseplane elevation angle	Elevation look angle	Azimuth look angle
#1	20°	55°	288°
#3	8°	43°	288°
#4	5°	40°	267°

Table 6.4: Figures given by DLR for the orientation of the trihedrals in Remningstorp.

The trihedrals were left in the same fixed position during the whole campaign period. To check whether any significant changes in the orientations had occurred measurements of angles were conducted at four different times. The results are summarized in Table 6.5. The noticed variations were considered to be minor and no adjustments of the trihedrals were undertaken. The obvious 3° difference in the baseplane elevation angle of trihedral #1 was caused by the location of the existing anchor stones optimized for ALOS, which prohibited that the required high elevation could be reached in this case.

Date trihedral #1	Baseplane elevation angle	Azimuth look angle	Horizontal
2007-03-06	17°	288°	0.05°
2007-03-20	17°	288°	0.5°
2007-03-31	16.9°	288°	0.5°
2007-05-02	16.8°	287.5°	0.5°
Date trihedral #3	**Baseplane elevation angle**	**Azimuth look angle**	**Horizontal**
2007-03-06	9°	288.5°	0°
2007-03-20	9.1°	288°	0.5°
2007-03-31	9.2°	288.5°	0.4°
2007-05-02	9.1°	288°	0.5°
Date trihedral #4	**Baseplane elevation angle**	**Azimuth look angle**	**Horizontal**
2007-03-06	5°	267°	0.5°
2007-03-20	4.5°	267°	0.8°
2007-03-31	4.9°	267°	0.6°
2007-05-02	4.9°	266°	0.4°

Table 6.5: Measurements made of the orientations for the trihedrals in Remningstorp during the BioSAR 2007 experiment period.

Positioning of the apex for each trihedral was performed after the campaign on 21 June. The same GPS equipment used for the reference registration at Lidköping airport was also operated here, i.e. a Ashtech Z-12 GPS receiver. The location of the apex was observed and marked on the ground before the trihedral was lowered to a non-elevating orientation. To avoid interferences with the trihedral structure during the GPS measurements the antenna was mounted on top of an aluminium rod and raised to be well above the trihedral and thus have any obstacles at low elevations. The other end of the rod was positioned to be in line with the earlier marked position for the apex. The trihedral structure gave support to the rod during the measurements with some ropes attached to keep it in a fixed position. Deviations from a horizontal orientation for the lowered trihedral was also registered with adjustments made to get as close as possible before the measurements could start. Figure 6.7 illustrates the situation during the measurements of trihedral #1. With this procedure it is estimated that the true apex position in elevated mode was correctly located and measured within an uncertainty of 10 cm.

Figure 6.7: GPS measurements in Remningstorp on June 21 of the apex position in elevated mode for trihedral #1, marked on the ground before lowering the reflector structure.

All three trihedral positions were registered with the GPS device during one hour or more. The exact data collection periods are found in Table 6.6 together with the antenna height above the apex point.

Trihedral	Start GPS (UTC)	Stop GPS (UTC)	Antenna height (cm)
#1	16:47:00	17:47:56	538
#3	12:59:55	14:27:00	558
#4	10:01:55	11:01:06	538

Table 6.6: Time intervals of GPS data registered on 21 June for the three trihedrals deployed in Remningstorp. Local time is UTC + 2 hours. The antenna height is the estimated value above the true apex point with the corresponding radar reflector in elevated mode.

The accurate absolute positions were retrieved in the same way as for the GPS location at Lidköping airport. Data from the same set of ten complete and simplified SWEPOS stations were requested from LMV also in this case, with some margins added according to the intervals given in Table 6.6. Since SWEPOS data are delivered in a format covering one full hour of the day in each file this means for example that data for trihedral #1 were made available between 16:00 and 18:00 UTC. The phase differential GPS post-processing were performed at DLR and the results are presented in Table 6.7.

Trihedral	Latitude (WGS 84)	Longitude (WGS 84)	Height (ellipsoidal, m)
#1	58.4785255611°	13.6241788611°	148.0
#3	58.4531219028°	13.6346293306°	161.0
#4	58.4524607667°	13.6684512667°	171.0

Trihedral	Northing UTM Zone 33	Easting UTM Zone 33
#1	6 482 809.50	419 767.61
#3	6 479 969.20	420 319.52
#4	6 479 855.90	422 291.70

Table 6.7: Apex positions of each trihedral deployed in Remningstorp when adjusted for the look directions defined by the BioSAR data collection program.

5.15 Lidar Measurements

A number of helicopter flights with the lidar system TopEye have been performed over Remningstorp since 1997, see Table 6.8. The data gathering is carried out from a fairly low altitude of a few hundred meters as illustrated in Figure 6.8. The efforts to obtain these lidar raw data have been financially supported by Hildur and Sven Wingquist's Foundation.

Year	Data type	Pulse density	Covered area
1997	Points	1 pulse/m^2	Small area
2000	Points	5 pulses/m^2	50% of central part using strips
2003	Points	2 pulses/m^2	Entire Remningstorp estate
2004	Points	50 pulses/m^2	Central part
2007	Points, Waveform	30-50 pulses/m^2	Central part

Table 6.8: Lidar measurements conducted in Remningstorp 1997 - 2007.

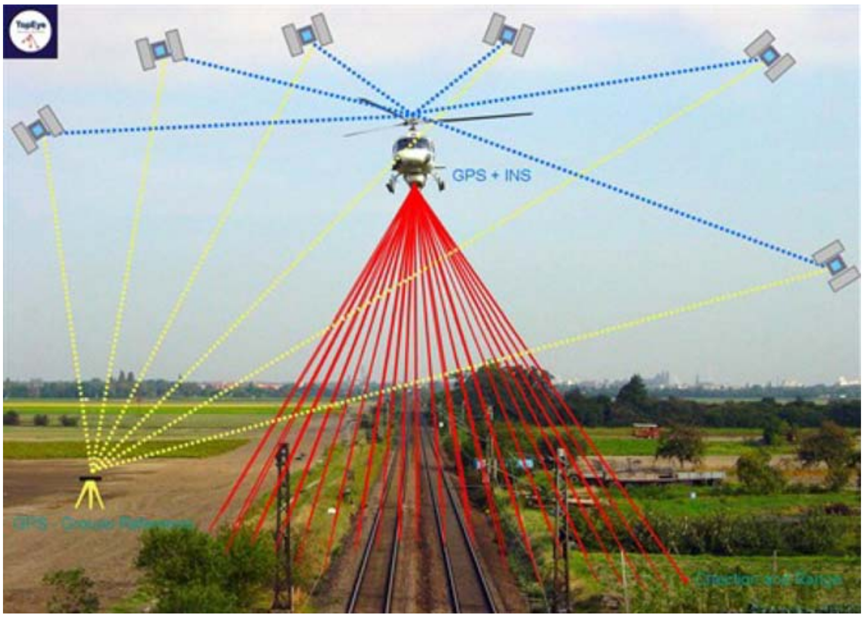

Figure 6.8: Typical imaging geometry of the TopEye lidar system. The imaged swath in cross-track depends on the flight altitude chosen. A combined inertial navigation system (INS) and a phase differential GPS are used to monitor the orientation of the helicopter platform during data registrations. (Image: http://www.topeye.com).

Most of the data collections have been made over smaller areas and there is only one data set from 2003 that covers almost all of the 1200 ha productive forested land found in the entire estate. In this data collection, TopEye collected data with a pulse density of about 2 pulses per m^2 according to Table 6.8. The data have been processed to a digital elevation model of the ground surface with a grid size of 5 m [3]. This data set is available and is represented in the Swedish reference grid system "Rikets Nät" (Datum RT90 2.5 gon W) with the height given as above sea level values according to the Swedish RH70 definition. In this coordinate system the file containing the DEM with the 5 m posting has the following corners:

- N 6487895 - E 1368300 (Upper left corner, North-West)
- N 6481275 - E 1376675 (Lower right corner, South-East)

Most of the Remningstorp estate is covered with height values in this file but there exist some gaps, primarily for small areas close to the border in Figure 3.4. On the other hand, there are parts found outside the estate that are included in the data set.

The most recent lidar data collection was conducted on 24 April 2007. It covered one main area of about 300 ha and four smaller ones as can be seen in Figure 6.9. A pulse density of 30-50 pulses per m^2 was used. The data set includes both points as well as waveform data.

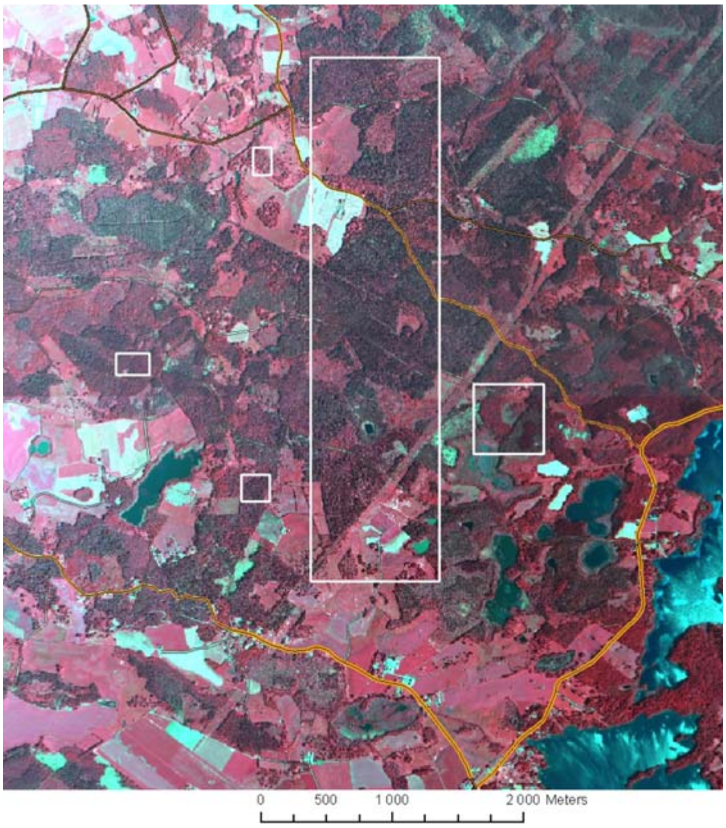

Figure 6.9: The central part of Remningstorp with the areas to be mapped by TopEye in 2007 marked with white rectangles. The existing road system is also overlaid. (© Infrared photo: Lantmäteriverket Gävle).

The much higher pulse density used in this lidar data collection makes it possible to derive a detailed DEM. Processing of the lidar raw data has resulted in height values on a grid has size of

0.25 m by 0.25 m. The full coverage in the Swedish RT90 system for this data set, with values given above sea level (RH70 system), is:

- N 6486909.75 - E 1370590 (Upper left corner, North-West)
- N 6482190 - E 1374609.75 (Lower right corner, South-East)

A sub-sampled version of this file with the height values on a grid of 5 m by 5 m only is shown in Figure 6.10. The five areas of interest defined in Figure 6.9 have been covered with some margins. The minimum value found is 108 m (in RH70) and presented in black. The colorcoding goes from this level to the highest one in red, i.e. 141 m (in RH70). Areas not mapped by the laser are here also represented by black but found as negative numbers in the data set to indicate lack of data. Single pixels of the illuminated part where no laser returns were obtained precluded any height retrieval and are therefore assigned with the same negative value to indicate missing data points.

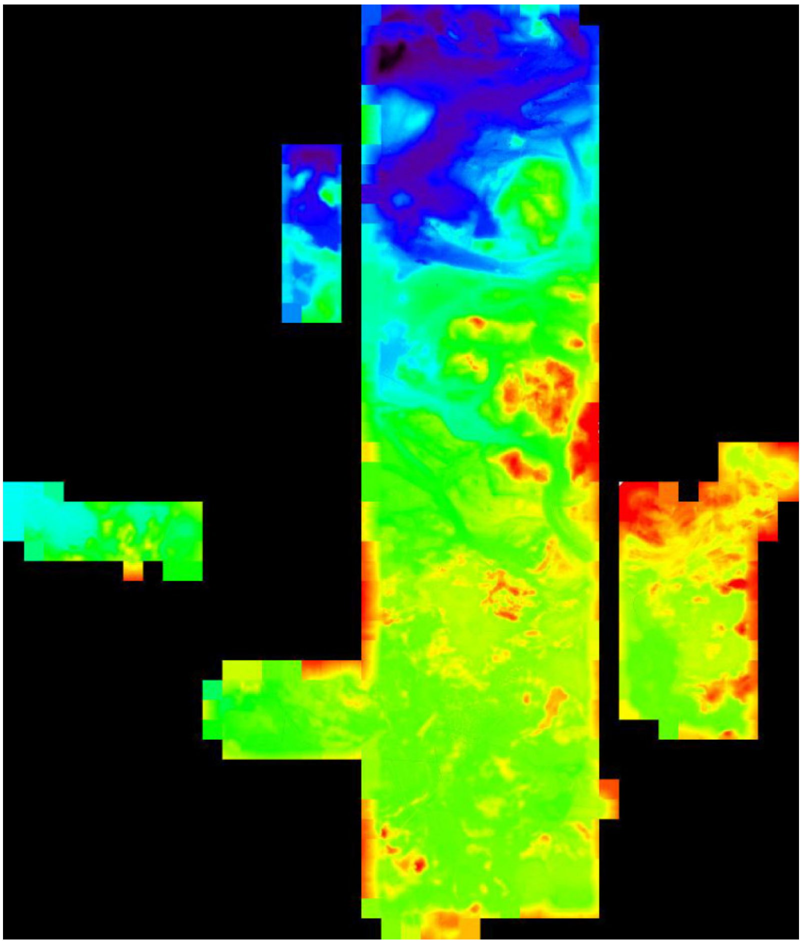

Figure 6.10: The DEM retrieved from the central part of Remningstorp using the laser scanned data gathered on 24 April 2007. The original grid size of 0.25 m by 0.25 m has here been sub-sampled by a factor 20 in both directions.

A second product from the lidar raw data set is a file in which the largest height value has been extracted from the cloud of laser returns present within each singe grid cell of 0.25 m 0.25 m. The obtained values are also adjusted with the retrieved ground level of the corresponding pixels and will thus in some sense reflect the top layer of the illuminated scene. Figure 6.11 shows this result sub-sampled in the same manner as in Figure 6.10. An enlargement of two smaller areas with full pixel spacing is found in Figure 6.12 and Figure 6.13. Both of them cover an area with a size of 265 m by 195 m.

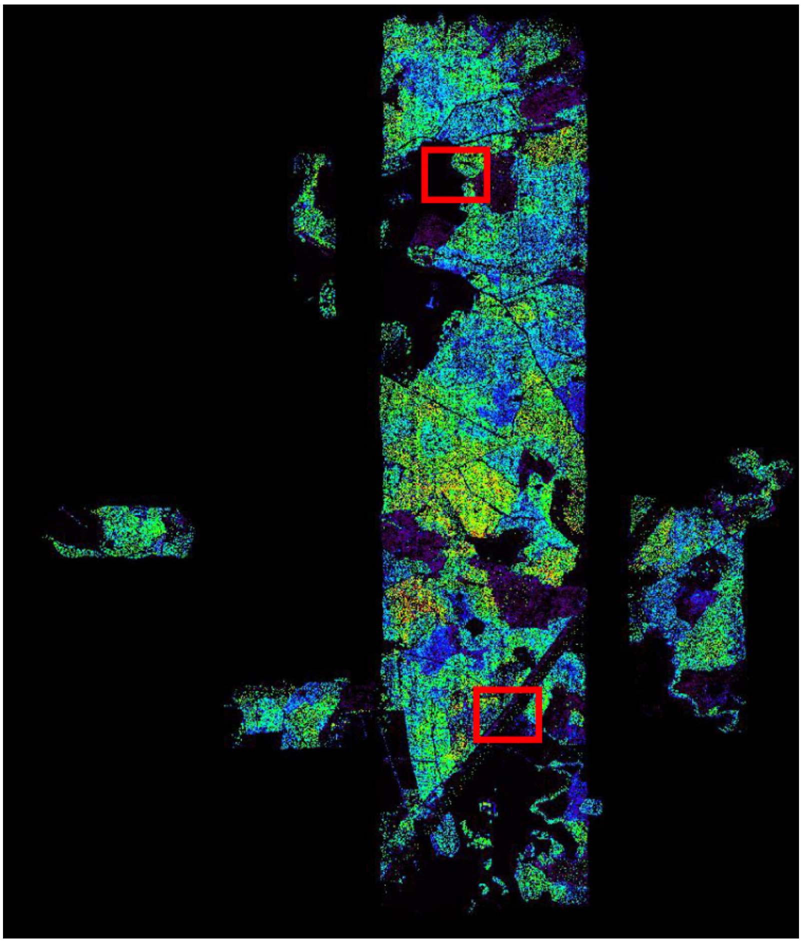

Figure 6.11: The maximum height relative the ground level for the central part of Remningstorp and based on lidar measurements made from a helicopter on 24 April 2007. The original grid size of 0.25 m by 0.25 m has here been sub-sampled by a factor 20 in both directions. The two areas encompassed by a red rectangle are found with the original high resolution in Figure 6.12 (north) and Figure 6.13 (south).

Both the data set containing the DEM and the one with the top layer profile representation have been transformed by DLR into the reference system UTM Zone 33 as well giving the following corners:

- N 6486909.75 - E 1370590 (Upper left corner, North-West)
- N 6482190 - E 1374609.75 (Lower right corner, South-East)

The height values in the DEM are in this case represented by WGS84 ellipsoidal figures.

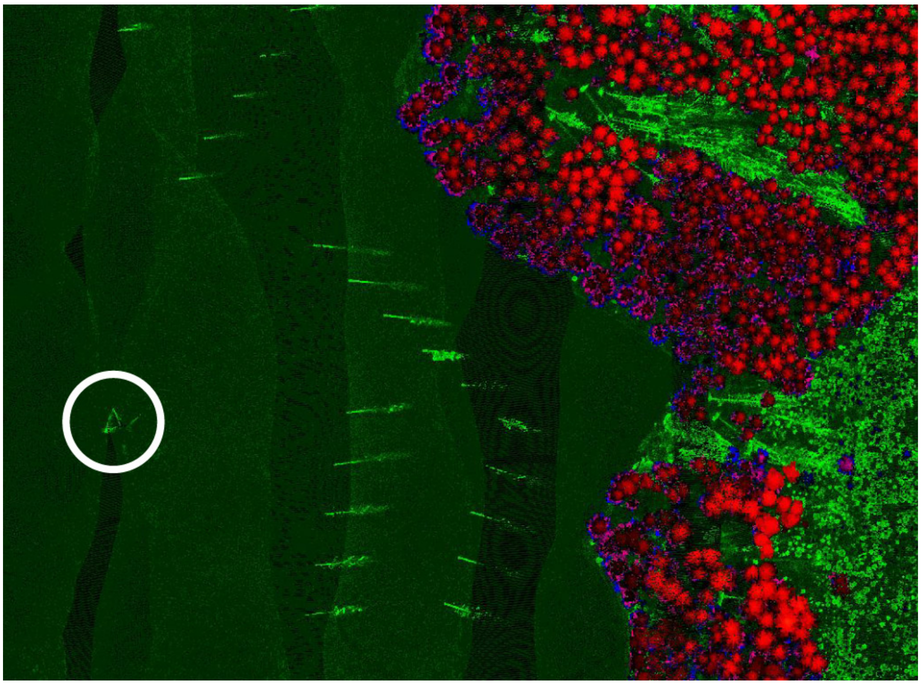

Figure 6.12: On the open field to the left is trihedral #1 deployed. The height profile of this reflector can be seen inside the overlaid circle. On this field are also a large number of spruces placed for studies in storm damage detection using remote sensing instruments. The trunk section with the root is uplifted about 1 m above the ground whereas the tree top is still on ground. Some of the patterns visible on the open field are residual effects from the block processing steps to generate the DEM. The forested areas to the right correspond to forest stand #6029 (north) and #6030 (south).

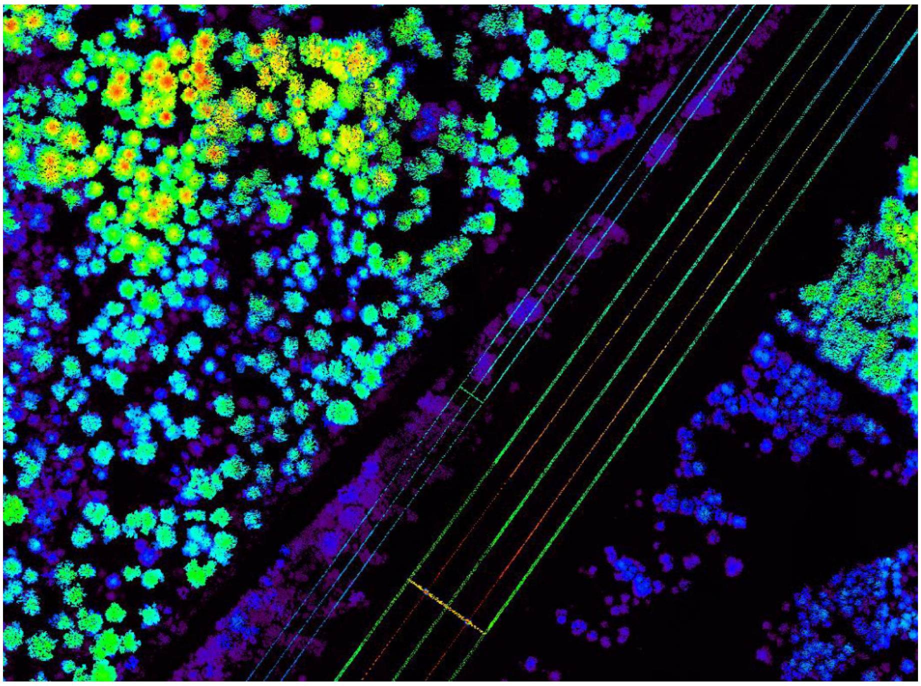

Figure 6.13: The height profile of the big power lines crossing Remningstorp estate in the south-west to north-east direction.

Other algorithms that can be applied on the high resolution lidar raw data set concern detection and measurements on single trees [5, 6]. This has, however, not been carried out within the BioSAR framework.

5.16 Field Observations

A major source of influence on the SAR data collected by E-SAR and other SAR systems is the moisture/wetness conditions on the ground and in the canopy. During the BioSAR campaign objective measurements of soil moisture and temperature were made but the deployed instruments were limited to one an open area and one in a forest stand close by, both located in the vicinity of trihedral #1. To complement the objective observations subjective measurements were acquired. A number of sites were visited three days out of four when E-SAR imaged Remningstorp. The locations of those places in terms of forest stand numbers are summarized in Table 6.9

Date	Forest stands (#)
2007-03-09	2517, 2728, 2836, 3329, 3534, 3726, 3926, 4029, 4626, 4733, 5729 and 5932
2007-03-31	2517, 2728, 3329, 3534, 3726, 3926, 4029, 4327, 4430, 4626, 4733, 5729 and 5932
2007-04-02	None
2007-05-02	2517, 2728, 3329, 3534, 3726, 3926, 4029, 4327, 4430, 4626, 4733, 5729 and 5932

Table 6.9: Overview of forest stands visited during days when E-SAR was collecting BioSAR data.

The measurements were performed by gathering information according a pre-defined protocol. The layout of the protocol with notes taken on 9 March at one of the sites in Remningstorp is shown in Figure 6.14. The information in the protocol provides a description of each site with the date and local time when the observations were made. Identification numbers on photos taken at the site are also noted to enable a correct association with all photos available from the full day. The look direction of the 1 - 3 photos typically captured at each site is also given, measured using a compass built into the camera used. The measured position is based on a single snap-shot from a handheld Garmin GPS device. Hence, the position figures given are less accurate compared to differential measurements, in particular since there was also a considerable amount of foliage obscuration at the site in most cases. The ground and canopy wetness was visually inspected. It was noted whether or not there was standing water and if the ground was frozen or covered in snow. For many sites a general description of the moisture state was also noted. The temperature was taken from the thermometer in a car parked as close as possible to the site. The wind speed and direction was estimated from visual inspection, e.g. moving branches and leaves. Finally, some additional remarks were noted when considered to be of importance. Examples of such notes are “single wind-felled tree” or “water high in ditches along road”. When the no information was found in handwritten protocol this is expressed with the abbreviation “na” in the transcribed digital version, with this acronym corresponding to “not available”.

Site ID (stand #)	2836
Time of day (local)	09:30
Photo ID(s)	11
North pos. (photo) [°]	58,45223
East pos. (photo) [°]	13,64316
Photo direction(s) [°]	190
Slope (%)	0
Growth stage	na
Stratification	pine, some birch
Snow on branches	no
Water droplets	no
Herb layer	moss, blueberry
Litter thickness	<1 cm
Litter type	na
Standing water	no
Snow cover	no
Frozen ground	no
Additional notes on wetness	moist, no visible water, saturated
Air temperature [°C]	3
Wind speed [m/s]	3
Precipitation	no
Wind direction	SW
Other notes	Thin ice cover on small lake

Figure 6.14: Protocol used for the field observations during BioSAR. The example is an excerpt from the work carried out on 9 March and shows the situation in forest stand #2836.

The protocols from each occasion are available in Excel-documents with the file names given as:

- BioSAR_protocol_field_observations_070309.xls
- BioSAR_protocol_field_observations_070331.xls
- BioSAR_protocol_field_observations_070502.xls

The photos captured from each occasion are available in folders with the file names given as:

- BioSAR_Photos_Remningstorp_070309
- BioSAR_Photos_Remningstorp_070331
- BioSAR_Photos_Remningstorp_070502

Figure 6.15 shows the single photo captured at the test site in forest stand #2836 according to the protocol in Figure 6.14. Work in progress on field observations is illustrated in Figure 6.16.

Figure 6.15: Photo captured on 9 March at the test site in forest stand #2836 at about 9:30 local time. Look direction 190°. Position 58.45223° N and 13.64316° E. Filename of photo is “Remningstorp 011.jpg”.

Figure 6.16: Activities in the field carried out on 31 March to the left and 2 May to the right.

5.17 Field Inventory

In situ data of individual trees have been collected to support the BioSAR campaign in Sweden during spring of 2007. Data are consisting of measured and computed forest parameters which are delivered in one Excel-file (Microsoft Office Excel 2003) with the given name:

- Remningstorp forest data 2007-10-17.xls

Details of the parameters found in this document will be described here.

The data were collected within the estate Remningstorp, located in the province of Västergötland, and will be used for analysis of E-SAR data acquired in P- and L-band.

The measurements on individual trees were performed by specialists contracted by SLU during fall 2006 and spring 2007. In total, 17 areas were inventoried and the database consists in total of 4358 trees, see Figure 6.17 and Table 6.10. Due to a severe storm on 14 January 2007 (named “Per”), i.e. between the two inventories, the relevance of the measurements with respect to the E-SAR data can presently only be guaranteed for the spring 2007 inventory consisting of 11 areas. The data delivery therefore only includes the latter part.

All trees, within the measured areas and with a diameter at breast height larger than 5 cm, have been marked with number tags attached to the stem. Each area has a numbering sequence staring from one and ending with the total number of trees in the area. In some cases, i.e. when the numbering was defined for an inventory in the past, certain tree numbers are missing in the sequence since they are no longer present.

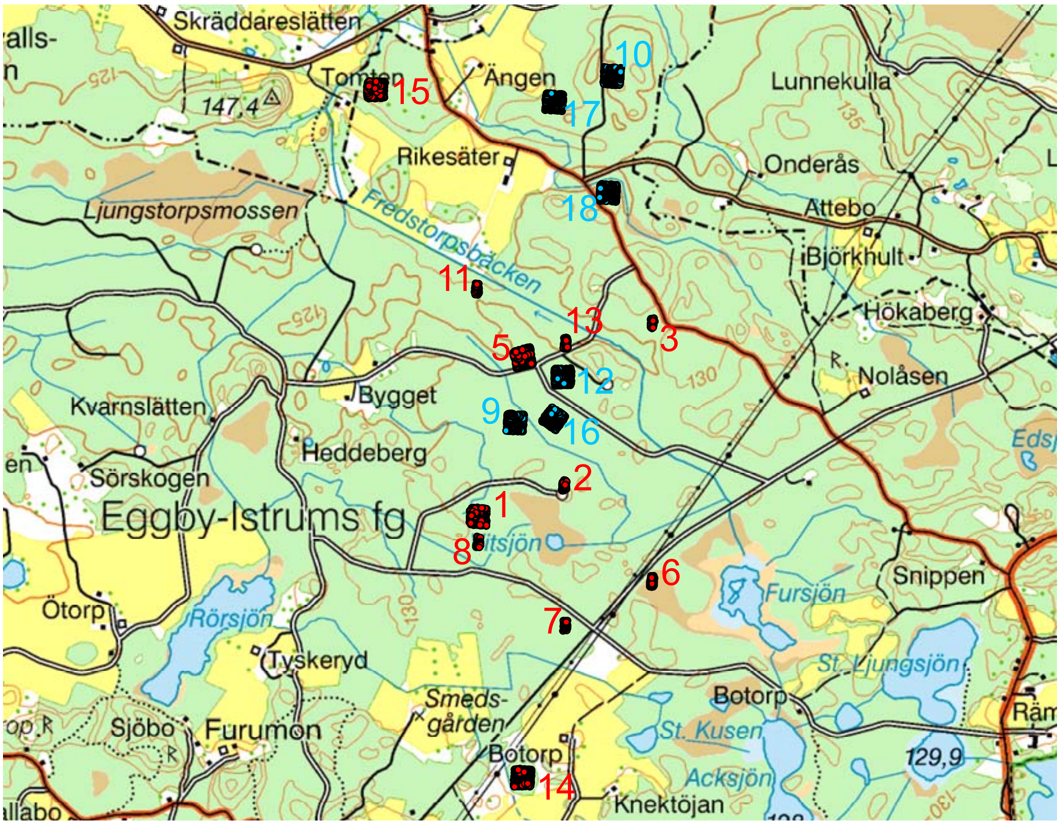

Figure 6.17: Map of inventoried areas in Remningstorp. 6 areas (in blue) were inventoried in fall 2006 and 11 areas (in red) in spring 2007. (© Map: Lantmäteriverket Gävle 2007).

Area	Forest stand #	Size (m)	Number of trees	Time of inventory
1	3926	80 × 80	278	Spring 2007
2	4029	20 × 50	82	Spring 2007
3	4733	20 × 50	42	Spring 2007
5	4626	80 × 80	552	Spring 2007
6	3534	20 × 50	140	Spring 2007
7	3329	20 × 50	29	Spring 2007
8	3726	20 × 50	46	Spring 2007
9	4327	80 × 80	369	Fall 2006
10	5932	80 × 80	424	Fall 2006
11	5022	20 × 50	41	Spring 2007
12	4430	80 × 80	357	Fall 2006
13	4626	20 × 50	107	Spring 2007
14	2728	80 × 80	346	Spring 2007
15	5721	80 × 80	419	Spring 2007
16	4430	80 × 80	410	Fall 2006
17	5729	80 × 80	384	Fall 2006
18	5332	80 × 80	332	Fall 2006

Table 6.10: Stand number, size, number of trees and inventory date for the measured areas.

The Excel-file consists of one row per tree. The columns (text in parentheses is the column heading) include the following information:

- Area number (**Avd**)
- Tree number (**Trad**)
- Tree species code, see below (**KlaTrSl**)
- Stem diameter at breast height (1.3 m) of trees with diameter larger than 5 cm. Two diameters are given in mm which have measured with a separation of 90° (**Dia1** and **Dia2**)
- Average of **Dia1** and **Dia2** in mm (**KlaDim**)
- Tilt of stem in degrees from vertical axis for trees with tilt ≥ 2° (**Lutning**)
- Tilt direction in integer degrees, 0-360°, relative North (**LutRikt**)
- =1 if test tree; =0 otherwise (**Pt**). Note: All trees in this data set are test trees.
- Tree height in dm, only for test trees (**PtHojd**)
- Height to lower limit of crown in dm, only on test trees (**KronGr**)
- Age in years for some of the test trees (**PtAld**). Note: None in this data set.
- Northing in m, “Swedish grid” RT90 (**X_trad_final**)
- Easting in m, “Swedish grid” RT90 (**Y_trad_final**)
- Time of inventory (**Datum**).
- Stem volume in dm^3, see Näslunds functions below (**Volym Stam)**
- Stem biomass in kg, ses Marklunds functions below (**Biomassa Stam**)
- Branch biomass in kg, see Marklunds functions below (**Biomassa Grenar**)
- Needle biomass in kg, see Marklunds functions below (**Biomassa Barr**)
- Easting in m, UTM zone 33 (**Easting_trad_UTM33_final**)
- Northing in m, UTM zone 33 (**Northing_trad_UTM33_final**)

5.17.1 Codes for tree species

The codes used for tree species (**KlaTrSl**) are defined according to: 1 – pine, 2 – spruce, 3 – birch, 4 – aspen, 5 – other deciduous, 6 – lodge pole pine, 7 – bouquet, 8 – dry standing or lying on ground (11 – seed tree pine, 12 – seed tree spruce, 13 – seed tree birch, 14 – seed tree aspen, 15 – seed tree other deciduous, 16 – seed tree lodge pole pine).

5.17.2 Stem volume and biomass

Stem volume and biomass (stem, branch, needle) values have been computed based on the tree measurements using functions described below. Dead trees (tree species code 8) have not been assigned values since the functions are not applicable to dead trees. In addition, 16 living trees (tree species code other than 8) have not been assigned values since they do not conform to the assumptions used to derive the functions. This is due to several reasons, e.g. the tree is broken, the tree consists of multiple stems etc.

5.17.3 Functions according to Näslund (Stem volume)

The stem volume above the stump and including bark was calculated using functions from [6]. The functions have been developed for pine, spruce and birch in southern Sweden. All deciduous trees in the database were considered to be birch, thus generalizing the group deciduous. The following functions were used:

v = 0,1072*d^2 + 0,02427*d^2*h + 0,007315*d*h^2 (pine)

v = 0,1059*d^2 + 0,01968*d^2*h + 0,006168*d^2*k + 0,01468*d*h^2 – 0,04585*h^2 (spruce)

v = 0,1432*d^2 + 0,008561*d^2*h + 0,02180*d*h^2 – 0,0663*h^2 (birch)

where v is the stem volume in dm^3, d is the diameter at breast height in cm, h is the tree height in m, and k is the height to the lower limit of crown in m.

5.17.4 Functions according to Marklund (Biomass)

Functions given in [7] were used to calculate dry biomass. The functions were developed for pine, spruce and birch in Sweden. The stem biomass (**Biomassa Stam**) is the biomass for the stem above the stump including bark. The branch biomass (**Biomassa Grenar**) is the total living branch biomass including needles for coniferous trees but excluding leaves for deciduous trees. The needle biomass (**Biomassa Barr**) has been computed and is given separately. No functions for leaf biomass exist. All deciduous trees were treated as birch in the calculations, thus generalizing the group deciduous.

The following functions for pine were used:

ln(stem) = – 2,6768 + 7,5939*d/(d + 13) + 0,0151*h + 0,8799*ln(h)
ln(branches) = – 2,5413 + 13,3955*d/(d + 10) – 1,1955*ln(h)
ln(needles) = – 3,4781 + 12,1095*d/(d + 7) + 0,0413*h – 1,5650*ln(h)

The following functions for spruce were used:

ln(stem) = – 2,1702 + 7,4690*d/(d + 14) + 0,0289*h + 0,6828*ln(h)
ln(branches) = – 1,2063 + 10,9708*d/(d + 13) – 0,0124*h – 0,4923*ln(h)
ln(needles) = – 1,8551 + 9,7809*d/(d + 12) – 0,4873*ln(h)

The following functions for birch were used:

ln(stem) = – 3,5686 + 8,2827*d/(d + 7) + 0,0393*h + 0,5772*ln(h)
ln(branches) = 0,0432 + 12,7821*d/(d + 10) – 0,8525*ln(h) – 0,0409*NKO,
where NKO is the northing coordinate of the tree in RT90, measured in km*100.

The biomass is measured in kg, d is the diameter at breast height in cm, h is the height of the tree in m, and ln( ) is the natural logarithm function.

5.18 Weather Conditions

Weather data are based on two main sources, i.e. observations taken at an air force base and registrations provided by the Swedish Meteorological and Hydrological Institute (SMHI). In addition, measurements on wind conditions made at a few wind power plants in the vicinity of Remningstorp are also included.

5.18.1 Såtenäs air foce base

Såtenäs air force base is situated about 55 km west of Remningstorp (58°26´N, 12°42´E). In fact, it is has approximately the same location as the Remningstorp area but on the opposite, western side of Lidköping airport. Weather observations are carried out here daily on a regular basis when military activities are going on. This means that the service is in general not in operation during weekends. A summary of the observations made at Såtenäs during the time interval with E-SAR airborne is found in Table 6.11.

Weather parameter	2007-03-09	2007-03-31	2007-04-02	2007-05-02
Time interval (local)	08.30 - 12.30	-	09.30 - 12.00	12.00 - 15.30
Total cloud cover	8/8	-	1/8	1/8 - 2/8
Cloud base [m]	200 - 1200	-	7000	6000
Precipitation	drizzle 11.45 - 12.10	-	no	no
Temperature [° C]	3.3 - 4.9	-	5.7 - 11.6	11.2 - 15.3
Wind direction [°]	190 - 210	-	230 - 240	340 - 30
Wind speed [m/s]	6.4 - 9.7	-	7.4 - 8.6	3.5 - 5.6

Table 6.11: Weather parameters registered at Såtenäs during the E-SAR data collections. The range of variation in parameter values during the corresponding time intervals is presented.

5.18.2 SMHI

Weather data from SMHI originates mainly from the national network of automatic weather stations. The number of parameters measured differs, however, with the location of each facility. In the eastern part of Remningstorp estate one station is available but limited to temperature and precipitation parameters only (58°27´N, 13°40´E). The grid for wind conditions is coarser and in this case the station in Hällum was selected (58°19´N, 13°02´E). Hällum is found about 40 km west-southwest of the area mapped by E-SAR and the landscape in between is mainly an open and flat agricultural district. The cloud information are not based on any *in situ* instrument but retrieved by SMHI using the tool Mesan - an Operational Mesocale Analysis System [8]. This system gives estimates of various meteorological parameters by combining many available sources, e.g. manual observations, automatic weather station data, satellite and radar imagery. The weather data provided by SMHI are summarized in Table 6.12 and for the cloud figures Mesan has generated these estimates at a position on ground corresponding to the automatic weather station in Remningstorp.

Weather parameter	2007-03-09	2007-03-31
Registration time (local)	07.00, 10:00, 13.00	11.00 , 14:00, 17.00
Total cloud cover	8/8, 8/8, 8/8	0, 1/8, 0
Cloud base [m]	470, 630, 340	-, 1600, -
Precipitation 24 h [mm]	0.0	0.0
Temperature [° C], (local time)	2.6 (07:00), 4.8 (19:00)	4.8 (08:00), 7.1 (20:00)
Wind direction [°]	210, 200, 190	120, 340, 20
Wind speed [m/s]	6, 7, 7	2, 2, 2
Weather parameter	**2007-04-02**	**2007-05-02**
Registration time (local)	08.00, 11:00, 14.00	11.00 , 14:00, 17.00
Total cloud cover	0, 0, 0	0, 0, 0
Cloud base [m]	-, -, -	-, -, -
Precipitation 24 h [mm]	0.0	0.0
Temperature [° C], (local time)	6.0 (08:00), 6.5 (20:00)	7.3 (08:00), 13.8 (20:00)
Wind direction [°]	220, 250, 250	30, 10, 10
Wind speed [m/s]	5, 8, 7	1, 3, 3

Table 6.12: Weather parameters registered by SMHI during the four days with E-SAR missions undertaken. Data are collected with certain time intervals and the figures given here cover each SAR measurement period with enough margins. For the temperature, only one value in the morning and one in the evening are available.

5.18.3 Wind power plants at Remningstorp

In close vicinity to Remningstorp there are a number of wind power plants. From three of them wind speed measurements were retrieved during the E-SAR flights. Two of these wind power plants were located southwest of Remningstorp, in Ölanda and Bränningsholm (see Figure 6.18), and one to the west in Lilla Erikstorp. The first two locations can be found on the map in Figure 3.4. Lilla Erikstorp is just outside the western edge of the same map. The power turbines were manufactured by Vestas and the towers have a height of 74 m. The recorded wind speeds were hourly averages that were supplied by the manager of the wind power plants. Only approximate wind directions were given. The wind speeds for the four E-SAR flight days are given in Table 6.13 to 6.16.

Figure 6.18: Two of the wind power plants in the vicinity of Remningstorp, the ones in Bränningsholm (right) and Ölanda (left).

Time interval (local)	Ölanda	Bränningsholm	Lilla Erikstorp
07.00 - 08.00	7.7	7.4	7.7
08.00 - 09.00	7.8	7.5	7.0
09.00 - 10.00	6.6	6.8	6.5
10.00 - 11.00	6.8	7.0	6.8
11.00 - 12.00	6.8	7.6	6.6
12.00 - 13.00	6.8	7.6	6.7

Table 6.13: Average wind speeds registered by wind turbines 2007-03-09. Wind direction: SW.

Time interval (local)	Ölanda	Bränningsholm	Lilla Erikstorp
12.00 - 13.00	1.5	2.1	1.5
13.00 - 14.00	1.8	1.6	2.0
14.00 - 15.00	2.3	2.2	1.3
15.00 - 16.00	1.1	1.9	1.2
16.00 - 17.00	1.2	2.5	1.7

Table 6.14: Average wind speeds registered by wind turbines 2007-03-31. Wind direction: NE.

Time interval (local)	Ölanda	Bränningsholm	Lilla Erikstorp
07.00 - 08.00	9.4	8.4	8.5
08.00 - 09.00	8.3	8.4	7.7
09.00 - 10.00	7.9	7.9	7.4
10.00 - 11.00	8.7	10.1	9.1
11.00 - 12.00	9.6	10.4	9.5
12.00 - 13.00	8.7	10.3	9.3

Table 6.15: Average wind speeds registered by wind turbines 2007-04-02. Wind direction: SW.

Time interval (local)	Ölanda	Bränningsholm	Lilla Erikstorp
11.00 - 12.00	4.9	5.5	4.4
12.00 - 13.00	6.3	7.1	4.5
13.00 - 14.00	5.1	6.4	4.3
14.00 - 15.00	6.2	7.4	4.9
15.00 - 16.00	5.5	5.3	5.4
16.00 - 17.00	5.1	5.8	4.5

Table 6.16: Average wind speeds registered by wind turbines 2007-05-02. Wind direction unknown.

5.19 Soil moisture and soil temperature

In April 2006 two Aquaflex soil moisture sensors were installed at Remningstorp (see Figure 6.19). Both were placed in the vicinity of reflector 1 (see e.g. Figure 3.7), sensor 1 on the same field as the reflector and sensor 2 in an adjacent forest. The Aquaflex soil moisture probe uses a process called Time Domain Transmission (TDT) where an electric pulse is sent along a 3 m long transmission line buried about 15 cm under the surface [10]. The sensor measures the percent volumetric soil moisture and the soil temperature. Measurements are done at predefined intervals and the values are stored in a logger. Both Aquaflex sensors were active during the BioSAR campaign and measurements are shown in Figure 6.20 to 6.23.

Figure 6.19: Installation of an Aquaflex soil moisture sensor.

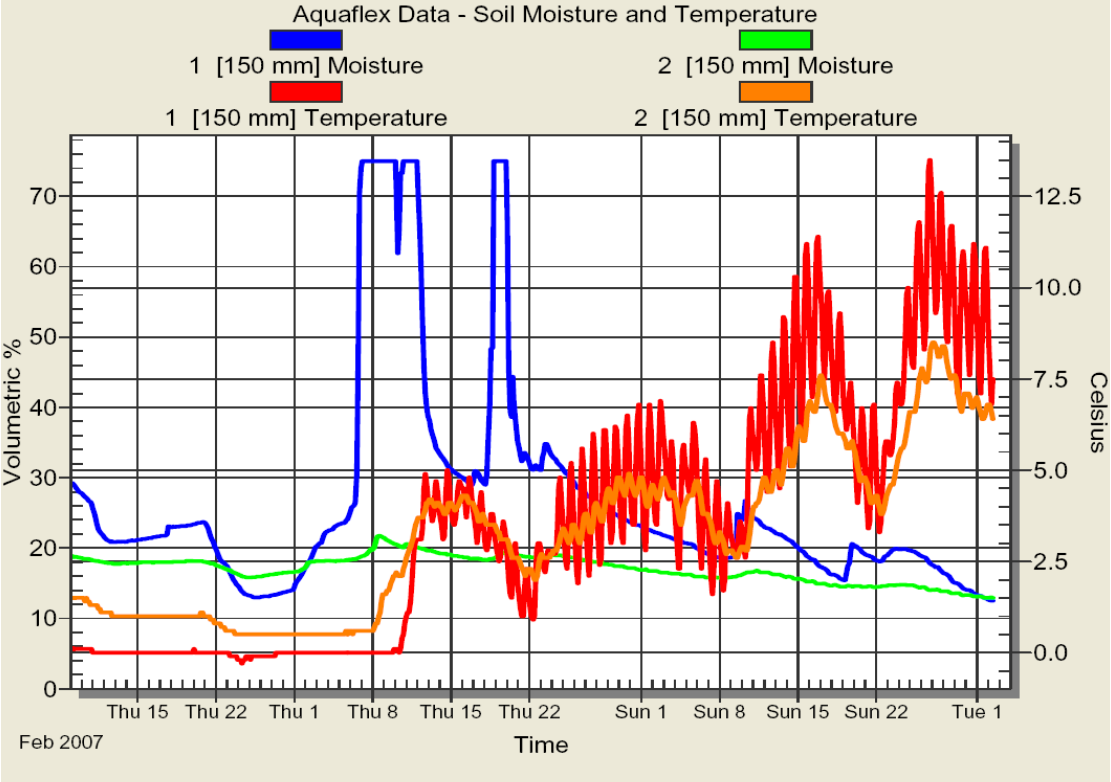

Figure 6.20: Soil moisture and soil temperature from the beginning of February until the beginning of May 2007. Sensor 1 is installed on a field and 2 in forest.

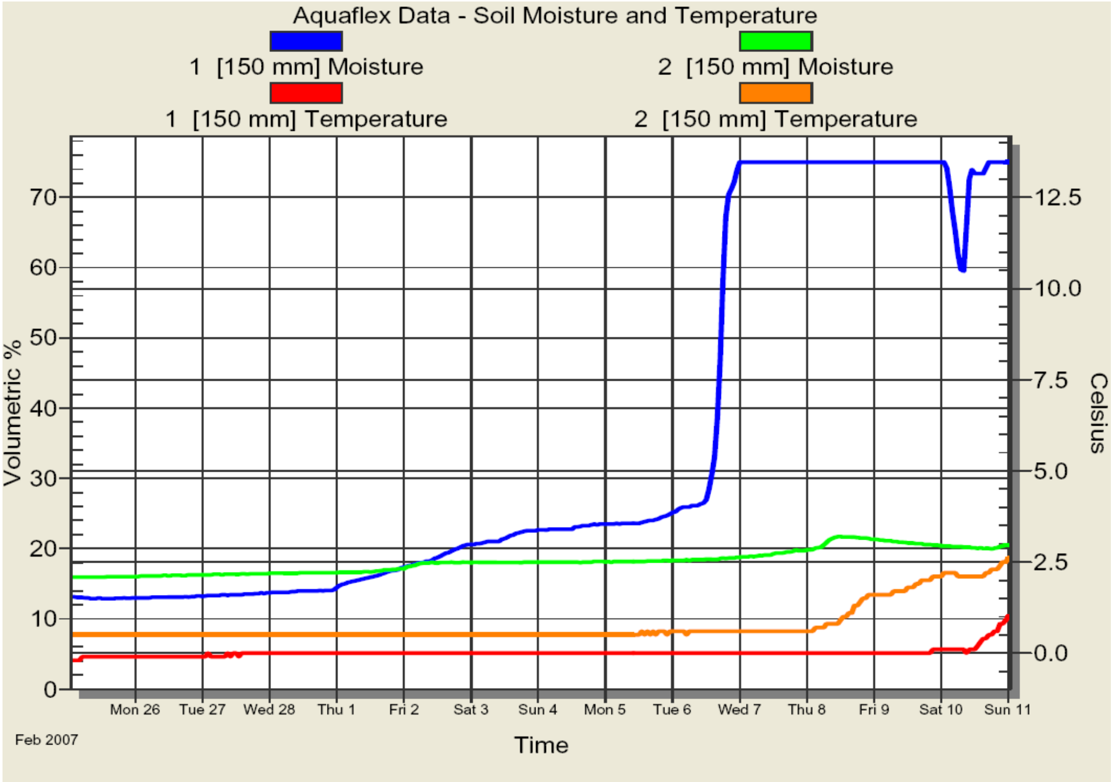

Figure 6.21: Soil moisture and soil temperatures from 2007-02-25 to 2007-03-11.

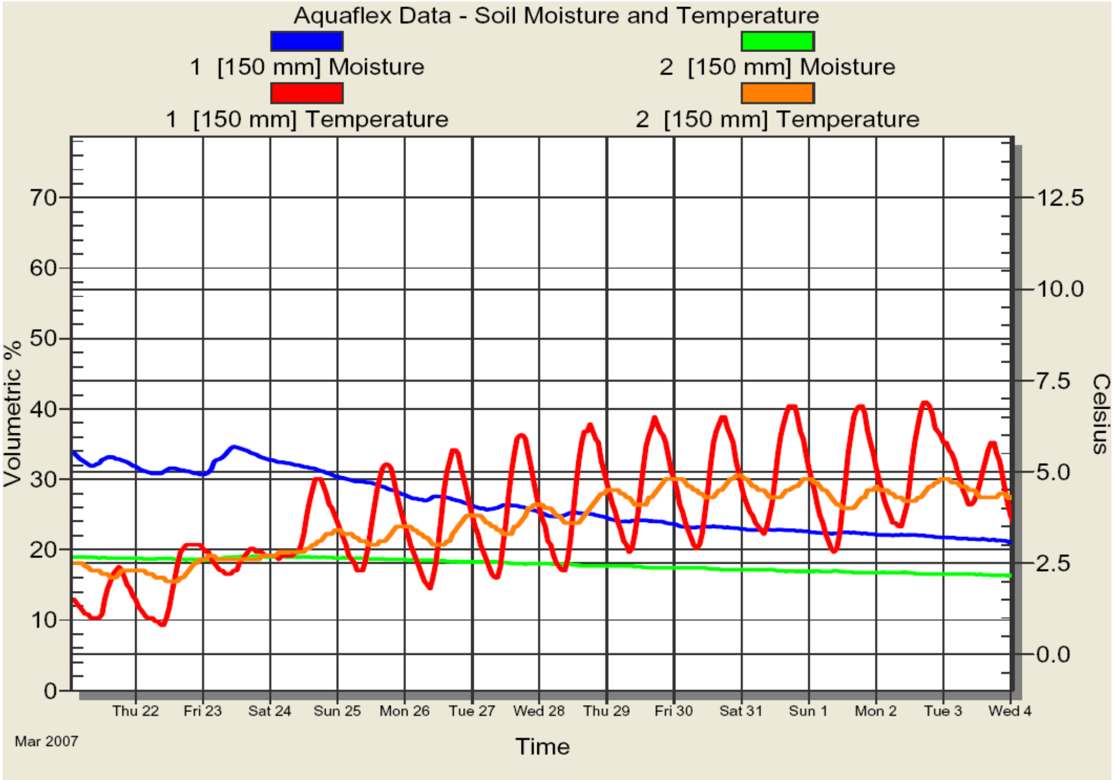

Figure 6.22: Soil moisture and soil temperature from 2007-03-21 to 2007-04-04.

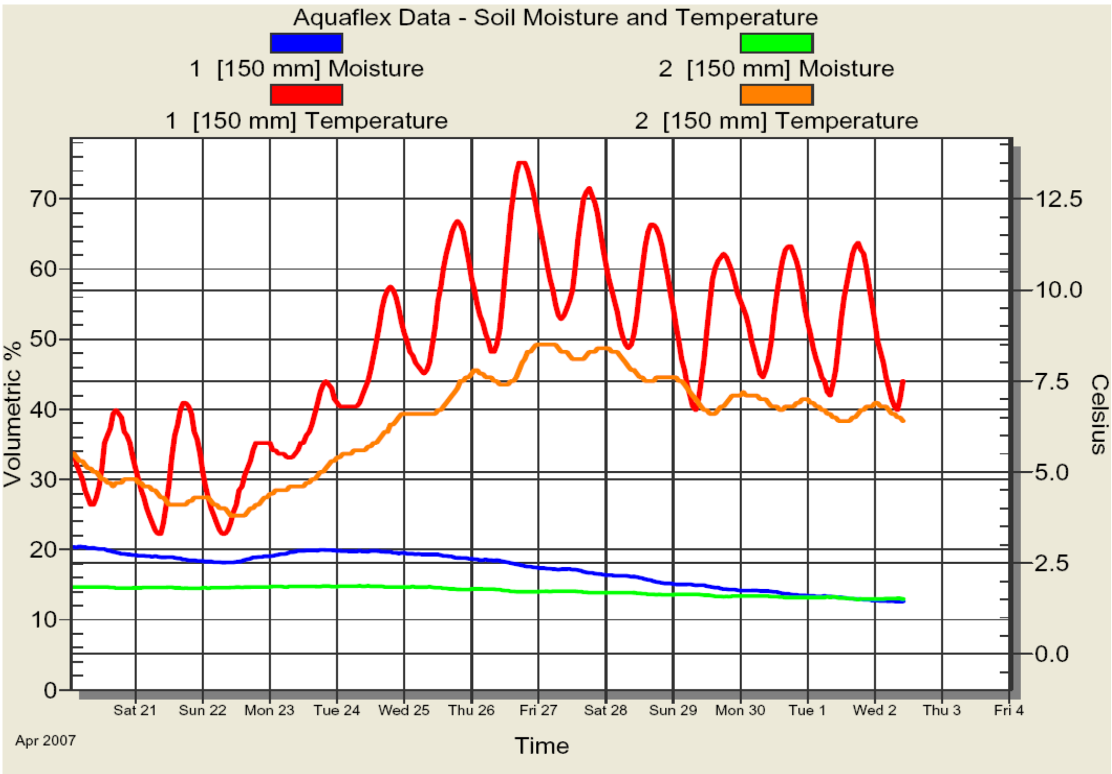

Figure 6.23: Soil moisture and soil temperature from 2007-04-20 to 2007-05-04.

5.19.1 References

[1] Lidköping airport, http://www.lidkopingairport.com.

[2] SWEPOS – A national network of reference stations for GPS, http://swepos.lmv.lm.se.

[3] M. Elmqvist, “Ground surface estimation from airborne laser scanner data using active shape models,” *Proc. ISPRS Photogrammetric Computer Vision*, held in Graz, Austria, 9-13 September 2002, pp. A 114 -118, 2002.

[4] Å. Persson, J. Holmgren, and U. Söderman, “Detecting and measuring individual trees using an airborne laser scanner,” *Photogrammetric Engineering & Remote Sensing*, 68(9):925-932, 2002.

[5] J. Holmgren and Å. Persson, “Identifying species of individual trees using airborne laser scanner,” *Remote Sensing of Environment*, 90:415-423, 2004.

[6] M. Magnusson, “Evaluation of remote sensing techniques for estimation of forest variables at stand level,” *Acta Universitatis Agriculturae Sueciae*, vol. 2006:85, Department of Forest Resource Management and Geomatics, SLU, Doctor´s dissertation, ISSN 1652-6880, 2006.

[7] M. Näslund, “Funktioner och tabeller för kubering av stående träd. Tall, gran och björk i södra Sverige samt hela landet,” *Meddelande från Statens skogsforskningsinstitut,* 36:3, 1947. (in Swedish).

[8] L.G. Marklund, “Biomassafunktioner för tall, gran och björk i Sverige,” *Institutionen för skogstaxering, Rapport 45*, Sveriges lantbruksuniversitet, Umeå, 1988. (in Swedish).

[9] SMHI - Swedish Meteorological and Hydrological Institute, http://www.smhi.se.

[10] Aquaflex soil sensors, http://www.streatsahead.com/Pages/Aquaflex%20Menu.html.

5.20 Ground Data Quality Check

5.20.1 Validation of tree height measurements

The data collected for the BioSAR campaign include two sets of height measurements which can be used to derive tree heights for individual trees. The first data set consists of *in situ* measurements of tree heights which made as part of the field data collection in 2007 to characterise 2082 individual trees. This resulted in a total of 2077 measured tree heights since five were removed for quality control reasons. The second data set consists of lidar measurements which have been transformed into an image of maximum height above ground within each 0.25 m x 0.25 m pixel. Estimates of tree height may thus also be extracted from the second data set, either by manual methods or by an automatic feature-extraction algorithm. Neither method has been applied to the full data set but manual measurements in the lidar data have been performed on a small sub-set of the data. The objective of the latter exercise was to do a cross-validation of the two tree height measurement in order to better understand the errors involved in the respective data set.

The procedure to select the test trees was a follows. Fifty random integer numbers were selected between 1 and 2082, which defined the test tree numbers. Two of the numbers were duplicates and therefore excluded. The total number of test trees was therefore forty-eight. For each of these trees, a manual measurement of the tree height was made in the lidar data. The procedure started by locating the tree pixel using the Easting and Northing position. A manual measurement was then made by locating the largest height value within the same tree crown as indicated by the the tree position pixel. A plot of comparing this measurement with the *in situ* height measurement is shown in Figure 6.24.

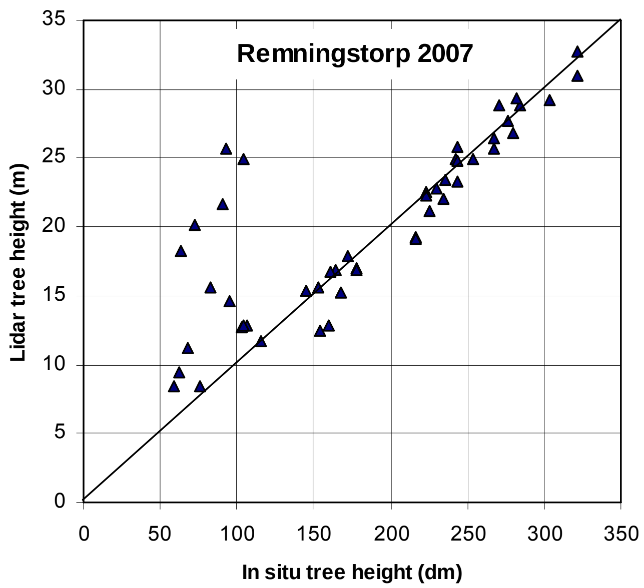

Figure 6.24: Comparison of lidar and in situ measurement of tree height based on a small random subset of the data. The results indicate that the two measurements agree quite well, except for some trees which are located close to taller trees.

The results show that the lidar and *in situ* data in many cases agree quite well, in particular in the subset corresponding to the high end of the *in situ* tree height measurements. However, in the lower end of the latter they do not agree at all. It was found, in all these cases, that a higher tree was located nearby such that the lidar measurement corresponds to height of this tree instead. The explanation is therefore most likely that the lidar is not able to resolve a tree located next to a higher tree. This conclusion is also supported by a visual inspection in the lidar data. The plot in Figure 6.25 shows the comparison after removal of the outliers.

We have computed the regression statistics between the two data sets. The R^2 and standard error for the lidar tree height are given in Table 6.16. The values for both cases, i.e. including and excluding outliers, are shown.

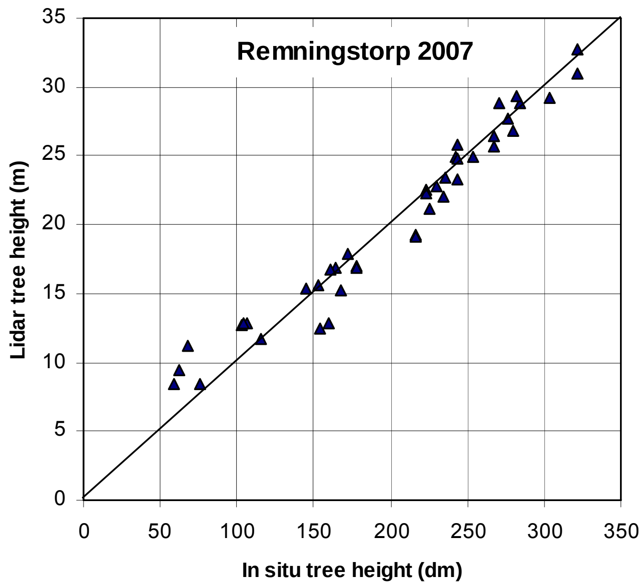

Figure 6.25: Comparison of lidar and in situ tree heights after outliers have been removed.

Regression parameter	Including outliers	Excluding outliers
Slope	0.103	0.098
R^2	0.948	0.994
Standard error [m]	4.9	1.6

Table 6.16: Regression parameters of lidar and in situ tree height measurements.

6 BIOSAR DATA BASE

The radar data have been made available over the DLR EOWEB, where a login and a password have been distributed to a responsible person of each participating institution (Figure 7.1).

All BIOSAR data are available via EOWEB http://taurus.caf.dlr.de:8080/index.html. Additionally, the following products have been delivered via USD hard discs.

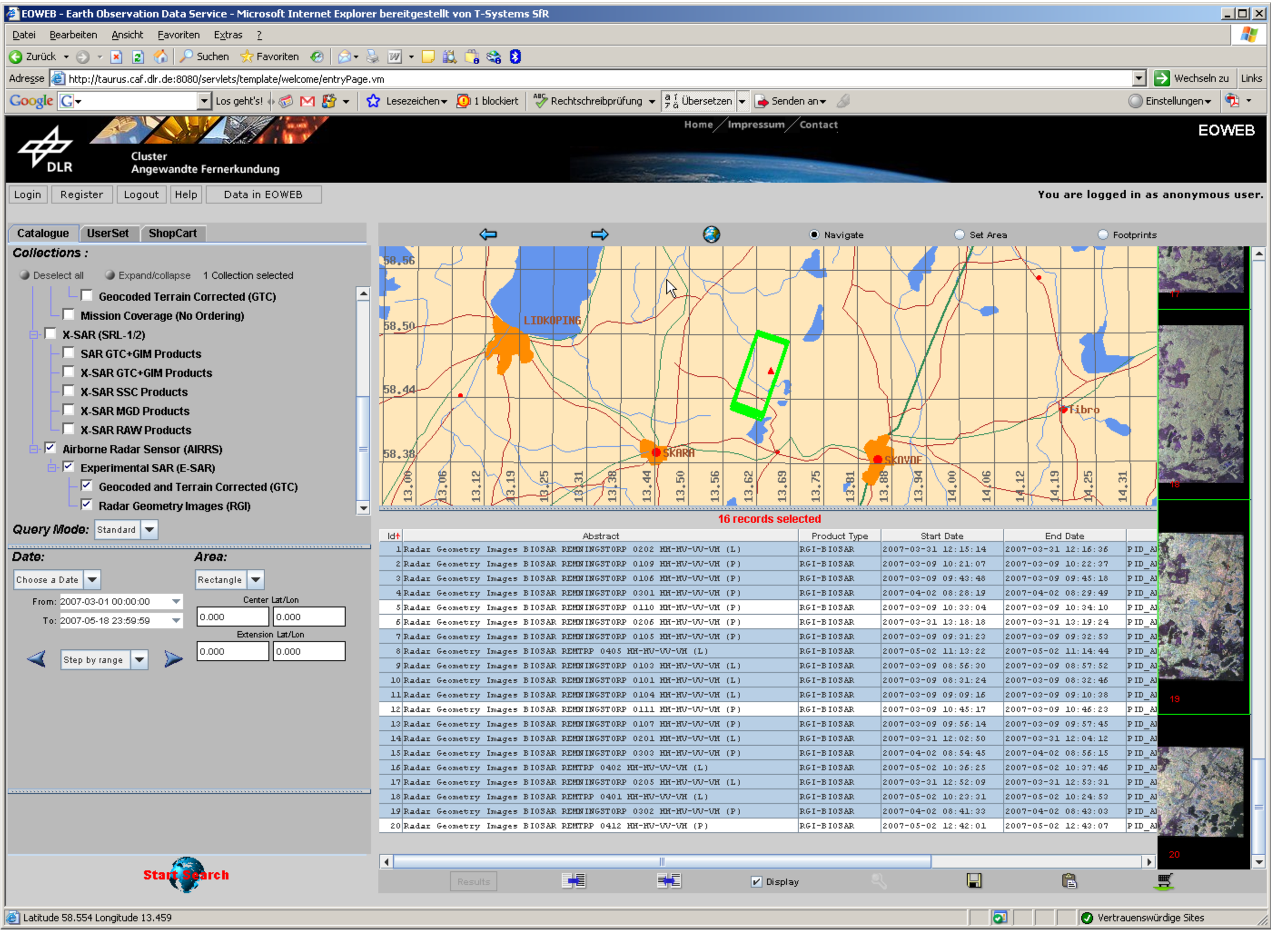

Figure 7.1: The DLR's EOWEB portal for BIOSAR radar data downloads

6.1 Stored RGI products

No.	Product ID	Remark	Freq	Pol	Product	Date
	P-BAND Pol-InSAR					
1	I07BIOSAR0105X1_T01	Master	P	PM	RGI	09/03/2007
2	I07BIOSAR0106X1_T01	Slave 10m	P	PM	RGI	09/03/2007
3	I07BIOSAR0107X1_T01	Slave 80m	P	PM	RGI	09/03/2007
4	I07BIOSAR0109X1_T01	Slave 0m	P	PM	RGI	09/03/2007
5	I07BIOSAR0301X1_T01	Master	P	PM	RGI	02/04/2007
6	I07BIOSAR0302X1_T01	Slave 30m	P	PM	RGI	02/04/2007
7	I07BIOSAR0303X1_T01	Slave 40m	P	PM	RGI	02/04/2007
8	I07BIOSAR0304X1_T01	Slave 50m	P	PM	RGI	02/04/2007
9	I07BIOSAR0306X1_T01	Slave 0m	P	PM	RGI	02/04/2007
10	I07BIOSAR0406X1_T01	Master	P	PM	RGI	02/05/2007
11	I07BIOSAR0407X1_T01	Slave 20m	P	PM	RGI	02/05/2007
12	I07BIOSAR0408X1_T01	Slave 60m	P	PM	RGI	02/05/2007
13	I07BIOSAR0409X1_T01	Slave 70m	P	PM	RGI	02/05/2007
14	I07BIOSAR0411X1_T01	Slave 0m (RP-Master)	P	PM	RGI	02/05/2007
	L-BAND Pol-InSAR					
15	I07BIOSAR0101X1_T01	Master	L	PM	RGI	09/03/2007
16	I07BIOSAR0103X1_T01	Slave 8m	L	PM	RGI	09/03/2007
17	I07BIOSAR0104X1_T01	Slave 0m	L	PM	RGI	09/03/2007
18	I07BIOSAR0201X1_T01	Master	L	PM	RGI	31/03/2007
19	I07BIOSAR0202X1_T01	Slave 8m	L	PM	RGI	31/03/2007
20	I07BIOSAR0205X1_T01	Slave 0m	L	PM	RGI	31/03/2007
21	I07BIOSAR0401X1_T01	Master (RP-Master)	L	PM	RGI	02/05/2007
22	I07BIOSAR0402X1_T01	Slave 8m	L	PM	RGI	02/05/2007
23	I07BIOSAR0405X1_T01	Slave 0m	L	PM	RGI	02/05/2007
	P-Band PolSAR					
24	I07BIOSAR0110X1_T02	PolSAR	P	PM	RGI	09/03/2007
25	I07BIOSAR0111X1_T02	PolSAR (6MHz)	P	PM	RGI	09/03/2007
26	I07BIOSAR0206X1_T02	PolSAR	P	PM	RGI	31/03/2007
27	I07BIOSAR0412X1_T02	PolSAR (RP-Master)	P	PM	RGI	02/05/2007

6.2 Stored GTC products

No.	Product ID	Remark	Freq	Pol	Product	Date
	P-BAND PolInSAR					
1	I07BIOSAR0105X1_T01	Master	P	PM	GTC	09/03/2007
2	I07BIOSAR0109X1_T01	Slave 0m	P	PM	GTC	09/03/2007
3	I07BIOSAR0301X1_T01	Master	P	PM	GTC	02/04/2007
4	I07BIOSAR0306X1_T01	Slave 0m	P	PM	GTC	02/04/2007
5	I07BIOSAR0406X1_T01	Master	P	PM	GTC	02/05/2007
6	I07BIOSAR0411X1_T01	Slave 0m (RP-Master)	P	PM	GTC	02/05/2007
	L-BAND PolInSAR					
7	I07BIOSAR0101X1_T01	Master	L	PM	GTC	09/03/2007
8	I07BIOSAR0104X1_T01	Slave 0m	L	PM	GTC	09/03/2007
9	I07BIOSAR0201X1_T01	Master	L	PM	GTC	31/03/2007
10	I07BIOSAR0205X1_T01	Slave 0m	L	PM	GTC	31/03/2007
11	I07BIOSAR0401X1_T01	Master (RP-Master)	L	PM	GTC	02/05/2007
12	I07BIOSAR0405X1_T01	Slave 0m	L	PM	GTC	02/05/2007
	P-Band PolSAR					
13	I07BIOSAR0110X1_T02	PolSAR	P	PM	GTC	09/03/2007
14	I07BIOSAR0111X1_T02	PolSAR (6MHz)	P	PM	GTC	09/03/2007
15	I07BIOSAR0206X1_T02	PolSAR	P	PM	GTC	31/03/2007
16	I07BIOSAR0412X1_T02	PolSAR (RP-Master)	P	PM	GTC	02/05/2007

7 BIOSAR DATA ANALYSIS – FIRST RESULTS

7.1 Assessement of Radarbackscattering at P-band for Biomass Estimation by FOI

7.1.1 Computation of relevant forest parameters

On each of the 11 test areas a number basic forest parameters were measured, including tree species, diameter at breast height (dbh), height, height to crown, and position of stem. From these measurements a set of area parameters summarizing the measurements were calculated. The relevant parameters for each area were selected to be:

- A polygon defining the area
- Area of polygon
- Stem volume in m^3/ha
- Total biomass in tons/ha
- Mean tree height
- Number density
- Species composition

In order to calculate forest parameters and extract SAR data on area level it was necessary to define the boundaries of each test area. This was done based on the measured positions of individual trees. First the convex hull of the tree positions were formed, i.e. the smallest convex polygon including all trees in an area was found. Then half of the mean distance between adjacent trees was calculated as:

$$r = \frac{1}{2N}\sum_{k=1}^{N}\min(|\mathbf{x}_k - \mathbf{x}_l|), \qquad l = 1,2,...k-1,k+1,...,N,$$

where $\mathbf{x}_k$ is the position of tree number k and N is the number of trees. The mass-center of the convex hull was also calculated. For each point defining the convex hull a new point was placed a distance r from the old point, in the direction away from the mass center of the convex hull, see Figure 8.1.

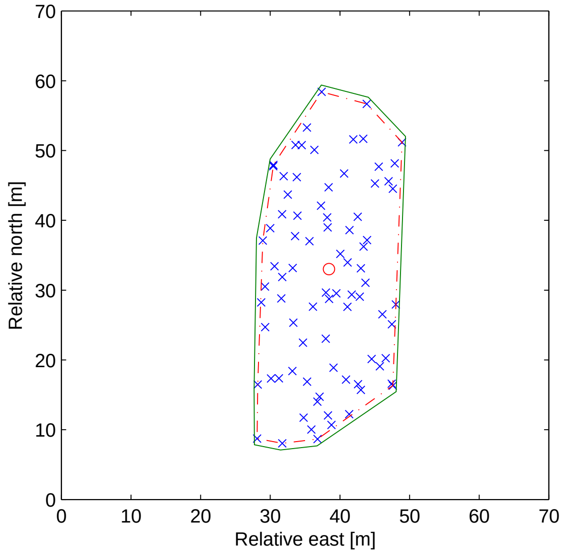

Figure 8.1: Illustration of polygon defining area 2. Blue crosses indicate tree positions, dash-dotted red line show the convex hull, red circle is the mass center and the solid green line show the final area polygon.

Once the polygon defining each area was defined, the stem volume and biomass measured in m^3/ha and tons/ha could be calculated. As explained in a previous section, allometric equations were used to calculate stem biomass, branch biomass and needle biomass for every tree, based on the measured diameter and height. The total above-ground dry biomass for each tree was then found as the sum of the stem and branch biomasses. Similarly the stem volume was calculated using allometric equations. Since all trees were measured in each area, the total biomass could be found by summing the individual tree biomasses. The area biomass was then found by dividing the total biomass by the area of the polygon defining the area. Analogous the area stem volume was found. In addition the number density was extracted, defined as number of trees/ area. An important note of caution is that the area parameters are dependent of how the area polygons are chosen. If the original convex hull is used instead of the polygons described here, the area biomass will on average increase by 22 tons/ha, with a maximum increase of 57 tons/ha.

In addition to stem volume and biomass the species composition was found. For the species categories pine, spruce, birch and other species, the relative species count and biomass was noted. Both these parameters were deemed useful, since the size of trees is strongly dependent on species. All area parameters are summarized in Table 8.1.

Area parameter	#1	#2	#3	#5	#6	#7	#8	#11	#13	#14	#15
Area [ha]	0,641	0,093	0,084	0,647	0,097	0,112	0,092	0,102	0,090	0,663	0,636
Biomass [tons/ha]	212,7	253,2	155,0	167,1	75,3	171,1	290,1	272,6	170,1	54,3	117,0
Stem vol [m^3/ha]	462,9	558,2	327,1	342,5	136,5	343,6	574,4	543,0	338,3	73,6	170,6
Mean height [m]	21,84	16,20	18,75	16,48	10,32	25,33	25,03	25,54	13,62	13,82	15,40
Forest density [trees/ha]	433,7	878,0	501,1	852,8	1450,0	258,8	499,8	402,8	1185,5	521,9	658,4
Fraction of pine [%]	49,64	37,80	64,29	48,19	82,86	0,00	0,00	0,00	36,45	0,00	0,00
Biomass pine [%]	76,00	89,04	97,97	95,39	95,24	0,00	0,00	0,00	88,41	0,00	0,00
Fraction of spruce [%]	42,81	31,71	28,57	0,36	0,00	89,66	86,96	95,12	0,00	4,34	11,93
Biomass, spruce [%]	23,76	7,67	1,82	0,03	0,00	100,00	97,88	100,00	0,00	2,02	4,37
Fraction of birch [%]	3,24	25,61	4,76	9,60	7,86	3,45	4,35	0,00	4,67	93,35	47,73
Biomass birch [%]	0,23	2,69	0,13	1,25	4,76	0,00	2,12	0,00	6,92	97,98	81,43
Fraction of other [%]	4,32	4,88	2,38	41,85	9,29	6,90	8,70	4,88	58,88	2,31	40,33
Biomass other [%]	0,01	0,60	0,08	3,32	0,00	0,00	0,00	0,00	4,67	0,00	14,21

Table 8.1: Summary of area parameters.

7.1.2 Extraction of backscattering coefficients from SAR data

SAR data have been extracted over each test area in order to investigate the dependence of backscattering coefficient on forest parameters. The extraction is based on the set of polygons defining the test areas described in the previous section. Only geocoded images were considered, since it was necessary to locate the test areas in the images. There were sixteen geocoded images available, all fully polarimetric. Six of these were L-band images with 94 MHz bandwidth, all from track 10 (heading 161 degrees, measured counter-clockwise from north). Nine images were P-band with 94 MHz bandwidth, six from track 10 and three from track 20 (178 degrees, measured clockwise from north). The final image was a P-band image with only 6 MHz bandwidth from track 20. There was also an incidence angle map available for every image. In the present analysis only five of the six full-resolution P-band images from track 10 were analyzed, since the remaining image was not found on EOWEB at the start of the analysis.

The first step in the data extraction was to transform the image files to be suitable for opening in ENVI. This required a rotation and flipping of the images, as well as the creation of a header file. All of this was done using an IDL script. The following data analysis was performed in Matlab. For every image and polarization, a rectangular area covering all test areas was defined and extracted from the image data. The corresponding area was also extracted from the incidence angle map. Each pixel was then associated with a coordinate corresponding to the center of the pixel. For each test area all pixel values and incidence angle values whose coordinates were within the polygon were extracted. From these values σ^0 and γ^0 were calculated as:

$$\sigma^0 = (\text{Pixel value} + 32768)^2 \cdot 10^{-6} \sin(\theta)$$

$$\gamma^0 = \frac{\sigma^0}{\cos(\theta)}$$

The pixel values were taken from the multi-look detected geocoded image files, and θ denotes the incidence angle. The quantities σ^0 and γ^0 were then averaged over each test area.

The regression analysis focused on the high-resolution P-band data. The temporal variations of σ^0 and γ^0 over the test areas were investigated, as well as differences between the tracks. In Figure 8.2 the variation in backscatter for HV is shown for the two tracks. The variation between tracks is much reduced when using γ^0 instead of σ^0 since the former partially corrects for the incidence angle dependency. Track 20 has steeper incidence angles to the test areas than track 20, so the difference between σ^0 and γ^0 was larger for track 20 than for track 10. Figure 8.3 shows the variation in time on area level. It is observed that the general trend is a decrease in backscatter for track 10, but that some areas, especially area 3, deviate from this trend. For track 20 no clear trend can be seen, but most areas change less than 1 dB. The most notable exceptions are area 2 and 3. Area 2 show a 2 dB decrease in backscatter between 9 March and 31 March, while area 3 increases 1-1.5 dB over the same time period.

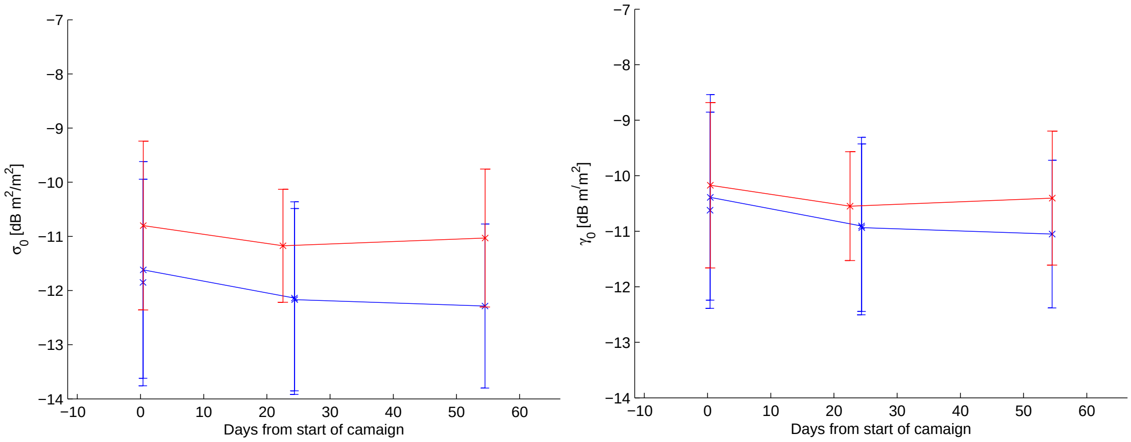

Figure 8.2: To the left σ^0, HV, averaged over all test areas is shown as a function of time. Blue is track 10, red is track 20 (north-south track) and the bars indicate the variation between areas (one standard deviation). To the right is the same but using γ^0.

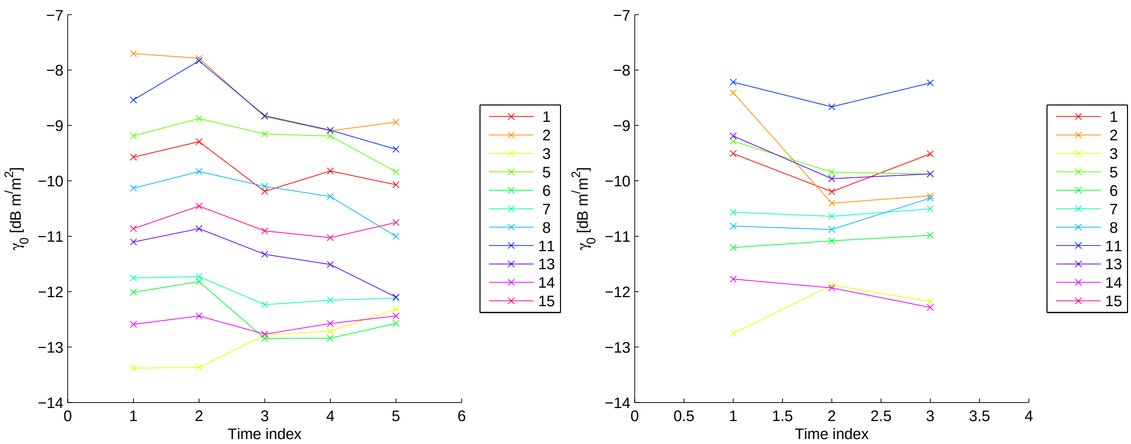

Figure 8.3: To To the left is the time variation of γ^0, HV, for track 10 for each area. On the x-axis is a time index, where 1-2 is from 9 March, 3-4 from 2 April and 5 from 5 May. To the right is the same but for track 20 (north-south track). Here the time index corresponds to 9 March, 31 March and 2 May, respectively.

In Tables 8.2 to 8.5 the extracted σ^0 values are listed for each area, polarization, campaign day and track. Note that Table 8.2 shows the results from the available L-band image data for comparison. When data with the same track, frequency and campaign day are available, the average value is shown. All values are in dB. In Table 8.6 the incidence angle for each area and track is shown. Some small variations in incidence angle between images were found, caused by small variations in flight track between flights, but these variations were found to be negligible in this context.

Area id	HH			HV			VV			VH		
	9 Mar	31 Mar	2 May	9 Mar	31 Mar	2 May	9 Mar	31 Mar	2 May	9 Mar	31 Mar	2 May
1	-6,0	-6,8	-6,1	-11,2	-12,0	-11,9	-7,3	-8,5	-8,1	-10,8	-12,0	-11,9
2	-5,5	-6,4	-5,7	-11,0	-11,6	-11,8	-7,1	-7,5	-7,1	-10,6	-11,6	-11,8
3	-8,7	-8,9	-8,2	-12,9	-13,5	-13,2	-10,3	-10,9	-10,3	-12,5	-13,5	-13,3
5	-6,7	-6,2	-5,8	-11,4	-12,1	-11,8	-7,9	-8,4	-7,6	-11,0	-12,0	-11,8
6	-6,9	-7,3	-6,9	-12,1	-13,2	-13,1	-9,1	-9,5	-9,4	-11,8	-13,1	-13,1
7	-6,9	-6,9	-6,2	-11,9	-11,9	-12,3	-9,0	-9,4	-8,9	-11,6	-11,9	-12,3
8	-5,4	-5,9	-5,6	-10,3	-11,0	-11,5	-7,6	-8,3	-8,1	-10,0	-11,0	-11,5
11	-5,2	-5,2	-4,6	-11,4	-11,0	-11,1	-7,9	-8,7	-7,5	-11,0	-11,0	-11,1
13	-7,3	-7,4	-6,6	-11,3	-12,4	-12,1	-8,1	-8,6	-8,0	-10,9	-12,3	-12,1
14	-8,3	-7,7	-6,4	-13,8	-13,4	-12,9	-9,5	-9,4	-8,2	-13,4	-13,4	-12,9
15	-6,0	-6,2	-5,1	-11,1	-11,2	-11,2	-6,5	-7,2	-6,6	-10,6	-11,1	-11,2

Table 8.2: The table shows measured σ^0 in dB. The frequency is L-band, full bandwidth. The data are from track 10.

Area id	HH			HV			VV			VH		
	9 Mar	31 Mar	2 May	9 Mar	31 Mar	2 May	9 Mar	31 Mar	2 May	9 Mar	31 Mar	2 May
1	-2,8	-3,0	-3,3	-10,7	-11,2	-11,3	-6,0	-6,5	-7,0	-10,7	-11,2	-11,3
2	-0,9	-1,8	-2,1	-9,0	-10,2	-10,1	-2,9	-4,7	-5,7	-9,0	-10,2	-10,0
3	-6,1	-4,9	-4,3	-14,4	-13,8	-13,4	-9,9	-9,8	-10,0	-14,4	-13,8	-13,4
5	-2,3	-1,9	-2,5	-10,1	-10,3	-11,0	-6,1	-6,0	-7,0	-10,1	-10,3	-11,0
6	-6,2	-6,1	-5,7	-13,5	-14,4	-14,2	-7,3	-6,5	-5,9	-13,6	-14,5	-14,1
7	-4,1	-4,3	-4,4	-13,3	-13,7	-13,7	-7,9	-8,5	-8,7	-13,3	-13,7	-13,7
8	-4,5	-4,1	-4,2	-11,4	-11,6	-12,4	-7,3	-7,8	-7,8	-11,4	-11,6	-12,3
11	0,8	0,8	0,2	-9,1	-9,8	-10,3	-4,4	-4,7	-5,0	-9,1	-9,9	-10,3
13	-6,1	-6,0	-5,9	-12,1	-12,5	-13,2	-8,7	-8,0	-8,1	-12,1	-12,5	-13,2
14	-5,4	-5,4	-5,4	-14,0	-14,2	-13,9	-5,2	-5,1	-5,0	-14,0	-14,2	-13,9
15	-3,0	-3,4	-3,0	-11,2	-11,5	-11,3	-6,1	-6,2	-6,0	-11,2	-11,6	-11,3

Table 8.3: The table shows measured σ^0 in dB. The frequency is P-band, full bandwidth. The data are from track 10.

Area id	HH			HV			VV			VH		
	9 Mar	31 Mar	2 May	9 Mar	31 Mar	2 May	9 Mar	31 Mar	2 May	9 Mar	31 Mar	2 May
1	-2,7	-3,3	-2,2	-10,0	-10,7	-10,0	-5,6	-6,2	-6,2	-10,0	-10,4	-10,0
2	-0,9	-2,9	-3,3	-9,0	-10,9	-10,8	-2,9	-4,9	-6,0	-9,0	-10,6	-10,8
3	-6,1	-5,0	-4,7	-13,3	-12,4	-12,7	-9,7	-9,2	-10,0	-13,3	-12,4	-12,7
5	-2,6	-2,7	-2,7	-9,8	-10,4	-10,4	-6,3	-6,2	-6,6	-9,8	-10,1	-10,4
6	-5,7	-5,6	-5,4	-12,2	-12,1	-12,0	-5,3	-4,0	-4,0	-12,2	-12,0	-12,0
7	-3,8	-3,7	-3,6	-11,4	-11,5	-11,4	-7,8	-7,9	-8,5	-11,4	-11,3	-11,3
8	-3,9	-3,8	-2,6	-11,4	-11,4	-10,9	-7,9	-8,2	-7,9	-11,4	-11,1	-10,8
11	0,6	-0,1	1,1	-8,8	-9,2	-8,8	-5,4	-5,7	-6,2	-8,7	-8,8	-8,8
13	-3,9	-4,0	-3,6	-9,9	-10,7	-10,6	-6,5	-6,8	-7,1	-9,9	-10,6	-10,6
14	-5,0	-5,3	-5,0	-12,4	-12,5	-12,8	-4,8	-5,2	-5,3	-12,4	-12,3	-12,8
15	-	-	-	-	-	-	-	-	-	-	-	-

Table 8.4: The table shows measured σ0 in dB. The frequency is P-band, full bandwidth. The data are from track 20. Area number 15 was not covered.

Area id	HH	HV	VV	VH
1	1,0	0,2	0,6	0,2
2	1,2	0,3	1,0	0,3
3	0,5	0,1	0,4	0,1
5	1,2	0,2	0,6	0,2
6	0,6	0,2	0,5	0,2
7	0,8	0,2	0,5	0,2
8	1,0	0,1	0,7	0,1
11	1,4	0,2	0,5	0,2
13	1,3	0,2	0,7	0,2
14	0,8	0,1	1,0	0,1
15	-	-	-	-

Table 8.5: The table shows σ0 in dB from the P-band image with 6 MHz bandwidth, from track 20. The image was acquired on 9 March. Area number 15 was not covered.

Area id	Track 10	Track 20
1	40,8°	27,3°
2	40,9°	28,9°
3	41,4°	32,5°
5	39,3°	27,8°
6	47,6°	35,7°
7	44,2°	30,9°
8	41,6°	27,1°
11	37,2°	27,5°
13	40,5°	31,5°
14	45,4°	29,4°
15	28,5°	-

Table 8.6: The table shows the incidence angle for the two tracks. Area 15 was not covered by track 20.

Area id	# pixels	# pixels, extended areas
1	1623	1763
2	242	1396
3	211	1565
5	1617	1541
6	243	607
7	279	336
8	235	636
11	255	1257
13	223	1088
14	1651	1561
15	1586	1551

Table 8.6a: The table shows the number of pixels included in the different areas for the normal and extended areas. Note that area 15 was not covered by track 20.

7.1.3 Regression analysis between forest parameters and backscattering coefficients

The main objective with the BioSAR campaign was to investigate the possibility to relate measured SAR parameters with forest parameters. PolInSAR measurements provide a tool for measuring e.g. forest height, while the intensity of the backscattered signal has shown good correlation with forest biomass in numerous studies. Especially the HV-polarized backscatter from P-band has been shown to be a good indicator of biomass [1], [2]. In this section a first analysis of the dependence between backscattered intensity and forest biomass is presented. The analysis is focused on the P-band measurements with full (94 MHz) bandwidth. Eight such images from 2 tracks (5 from track 10, 3 from track 20 (north-south track)) were analyzed. Ground measurements were available from eleven forest areas, as described in previous sections. Throughout the analysis γ^0 is used to reduce the dependence of incidence angle.

In Figure 8.4 (a) P-HV polarized γ^0 is plotted against biomass. The general trend is an increase in backscatter with increasing biomass, but there are large deviations from this trend. There are also large variations between images acquisitions and between tracks. It was noted that 7 of the 11 test areas were only about 20 m x 50 m in size, and it was hypothesized that some of the variation is caused by such a small area size. The claim was supported by the fact that the four areas of larger size (80 m x 80 m, area nr 1, 5, 14 and 15) show less variation than the other areas. In an attempt to decrease the variations between tracks and images, the areas were extended based on their appearance in available high resolution TopEye lidar data and aerial photographs. Two examples of this extension are shown in Figure 8.5.

The mean size of the extended areas was 0.51 ha, with a variation depending of the homogeneity of the surrounding area. The largest area was 0.71 ha (area 1). Area number 7 was surrounded by storm damages and could not be extended much. The process of increasing the area size decreased the accuracy of the ground measurements, but since homogeneous areas were selected the ground data should still be relevant. In Figure 8.4 (b-d) γ^0 for the extended areas is plotted against biomass for HV, HH and VV. For HV it is seen that the variation both within and between track is reduced, especially for track 13 and 2. The backscatter now increases with biomass, with the exception of areas number 3, 7 and 8. As previously mentioned area 7 could not be extended much, since it is surrounded by storm damages. Possible reasons for the reduced backscatter for area 3 and 8 are discussed in the next section. The HH polarized backscatter has some dependence on biomass, but the variations are large. The VV polarized backscatter shows little dependence on biomass. It should be noted however that the backscatter for areas number 3, 7 and 8 is significantly lower than for the rest of the areas even for VV.

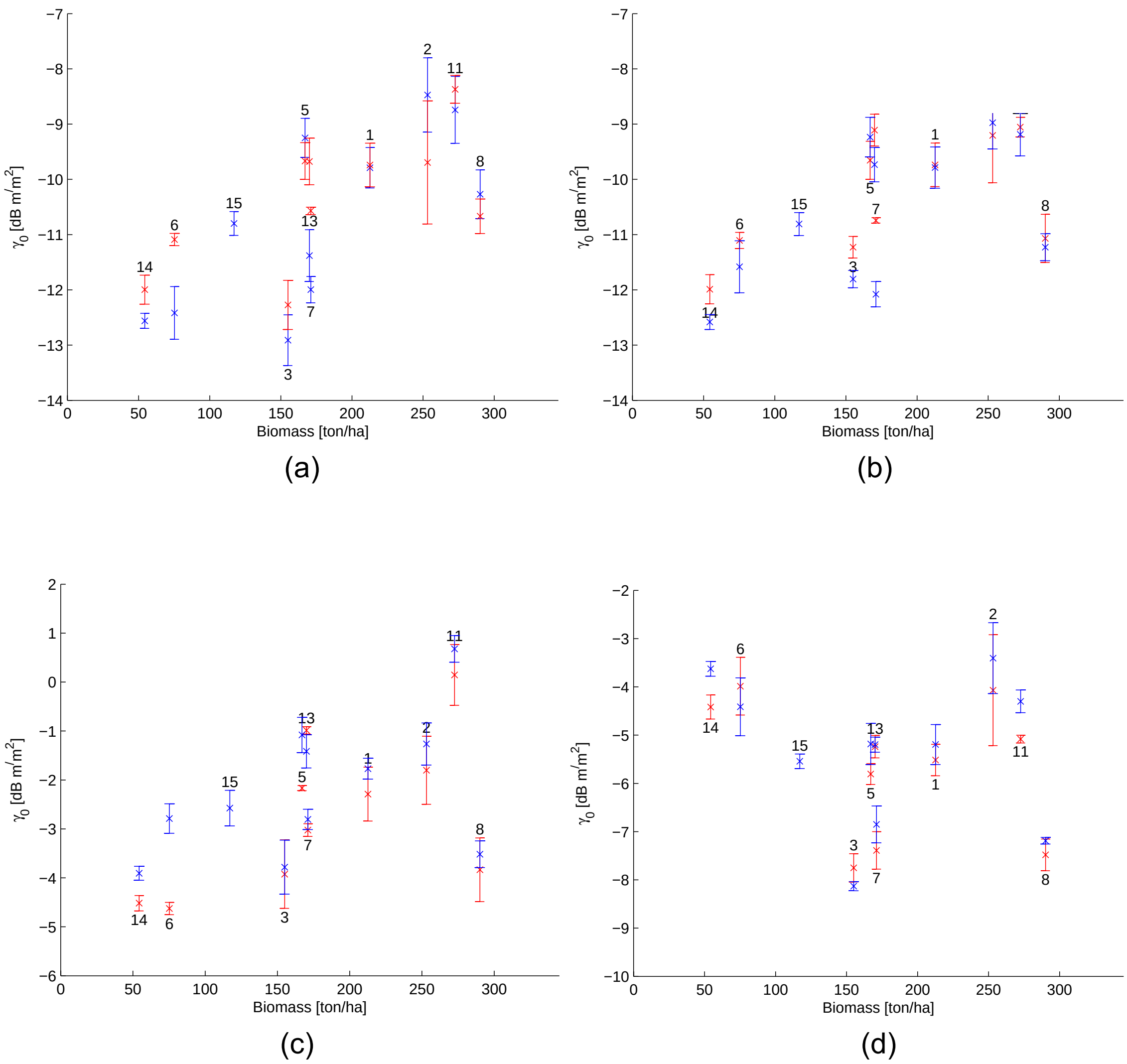

Figure 8.4: γ^0 is plotted against biomass for (a) P-HV, (b) P-HV, extended areas, (c) P-HH, extended areas and (d) P-VV, extended areas. Blue is track 10, red is track 20 (north-south track) and the bars indicate the variation between images (one standard deviation). The indicated number is the area identification number.

A simple linear regression analysis was made between biomass and the measured HV polarized backscatter (γ^0) for the extended areas. The result is shown in Figure 8.6 (a). The root mean square error is 58.4 tons/ha or 33.1 % of the mean biomass, and the coefficient of determination (R^2) is 0.36. The most deviating area is the one with the largest biomass (area 8), with an error of 139.5 tons/ha. This area is responsible for a large part of the error.

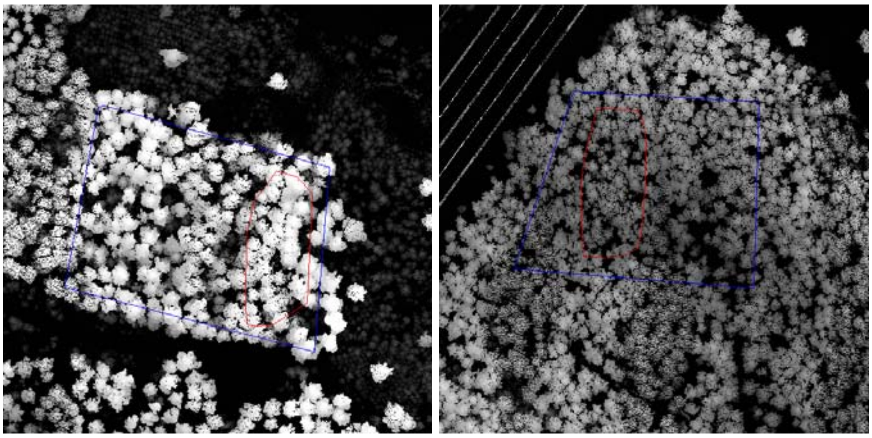

Figure 8.5: The images show vegetation height images derived from TopEye lidar data form area 2 (left) and area 6 (right). Overlaid is the area boundaries (red) the boundaries of the extended area (red).

One way to improve the biomass estimation would be to include a height estimation based on PolInSAR techniques. In order to assess the possibilities of such a method the mean tree height, obtained from ground measurements, was included in the linear regression. A regression using only the height as parameter was also made. The results are shown to the Figure 8.6 (b-c). Using both height and backscatter the root mean square error is 32.2 tons/ha or 18.3 % of the mean biomass, and the coefficient of determination (R^2) is 0.81. Using only the height to estimate biomass the relative mean rms error was found to be 28.4 %, i.e. in the same order as when using only backscatter. The biomass estimation is thus improved significantly, and the information in height and backscatter complement each other. If PolInSAR techniques can provide a good height estimate a good estimate of biomass can be obtained from the SAR data.

The three models with estimated constants are as follows:

(a) Biomass = $587.4 \pm 414.3 + 39.1 \pm 39.2 \cdot \gamma^0_{HV}$ [dB]

(b) Biomass = $-16.8 \pm 142.6 + 10.5 \pm 7.5 \cdot$ tree height

(c) Biomass = $360.2 \pm 276.4 + 34.4 \pm 23.6 \cdot \gamma^0_{HV}$ [dB] + $9.7 \pm 5.2 \cdot$ tree height

The error intervals indicated by the ± symbol are 95% confidence intervals for the estimated constants.

Quantity	Model (a)	Model (b)	Model (c)
RMS error [tons/ha]	58.4	50.2	32.2
RMS error [% of mean biomass]	33.1	28.5	18.3
R^2	0.36	0.53	0.81

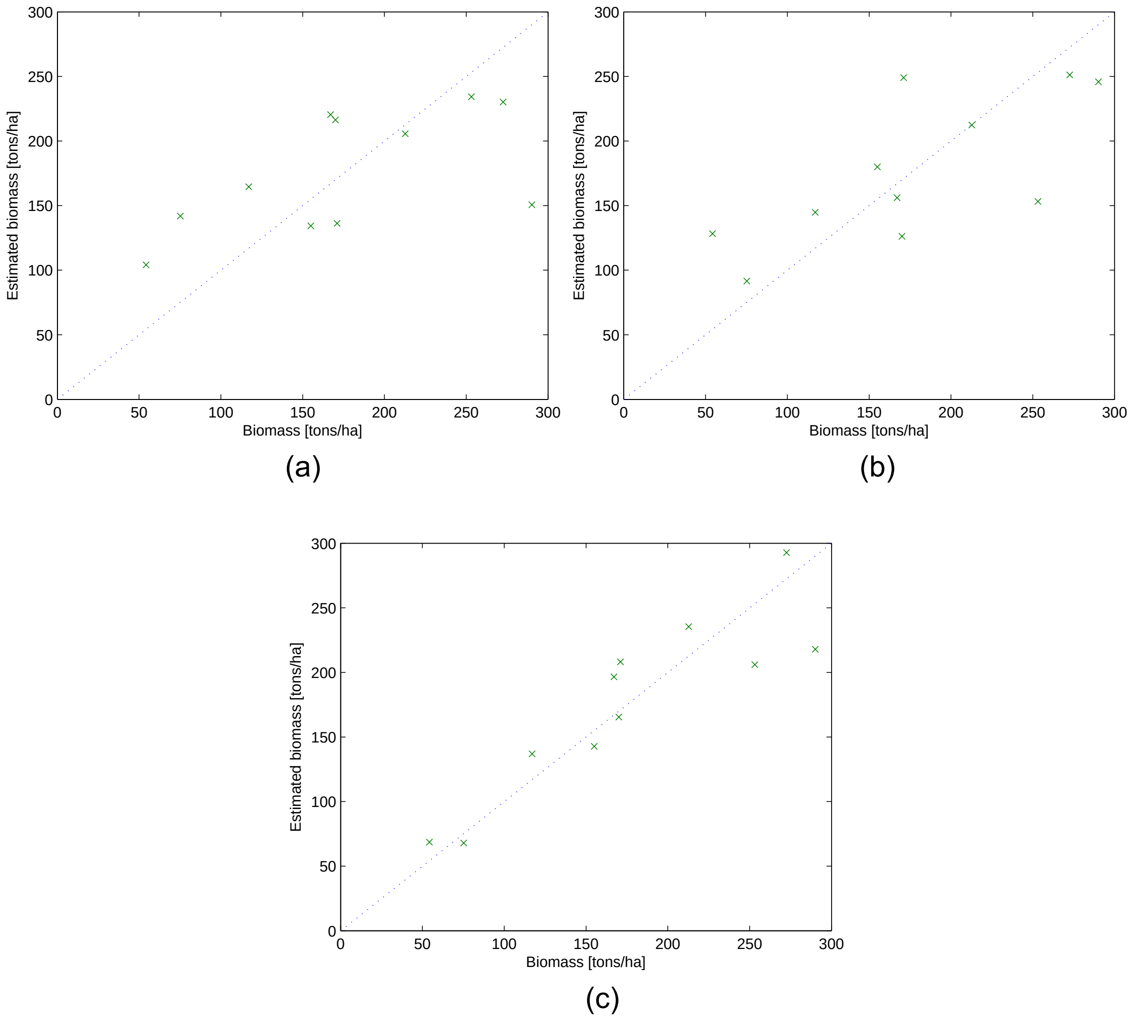

Figure 8.6: Measured biomass plotted against biomass estimation using linear regression. In (a) the biomass is modeled as a function of γ^0 (P-HV), in (b) as a function of (field-measured) mean tree height and in (c) both γ^0 (P-HV) and mean tree height are used.

7.1.4 Evaluation of the impact of additional parameters

This section is devoted to a study of how parameters other than biomass affect the backscatter. The focus will be on HV polarized backscatter, since this is the main indicator of biomass. Some of the parameters worthy of attention are soil moisture, topography, species and incidence angle.

In most airborne campaigns the incidence angles to the test sites are in the order of 40-50°. For a satellite system the incidence angles would be steeper than this, in the order of 20-30°. One of the objectives of the BioSAR campaign was to obtain airborne data using incidence angles resembling a space borne scenario. A seen in Table 8.6 track 20 has steep incidence angles to the test areas, whereas track 10 has more shallow angles. In Figure 8.4 it is seen that when using γ^0 there are no major differences between the tracks, and it can thus be concluded that the backscatter-biomass relation do not strongly depend on the incidence angle.

The ground topography has been shown to have significant impact on the HH polarized backscatter. Both models and simulations indicate that the effect on HV of topography is smaller, but it may still be worth examination. The BioSAR data set is not very well suited for topographic studies, since only two track separated with quite similar headings were flown. If tracks with multiple heading were available, topographic effects can be studied since the same areas will be viewed from different directions (for the LORA system operated by FOI there are such data available). However, it should be noted that area number 3, which has a lower backscatter level than the overall trend in all polarizations, is the area with most significant topographic variation. In Figure 8.7 a digital elevation model (DEM) obtained from lidar measurements is shown. Black corresponds to 125 m and white to 140 m above mean sea level. The maximum slope angle in the area is about 4 degrees. Topography could explain the behaviour of area 3, but without further data the uncertainties remains large. Topographic effects will be the subject for future work using this and other data sets as well as simulations.

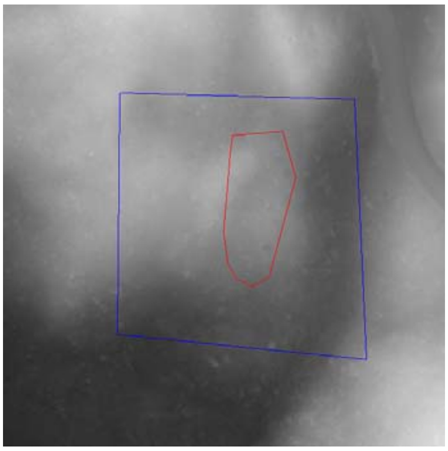

Figure 8.7: Ground DEM from area 3, derived from lidar measurements. Black corresponds to 125 m and white to 140 m above mean sea level. Overlaid are the area boundary (red) and the boundary of the extended area (blue).

The soil moisture conditions in the forest were in most cases similar on the different acquisition dates in the BioSAR campaign. No in-depth analysis has been made, but an examination of the SAR data over the forest areas indicates that no great changes due to soil moisture can be found. Further analysis should be made, but other data sets, e.g. the RAMSES data from LORAM 2004 campaign [3], are more suitable for soil moisture studies.

The final parameter of interest is the species composition. It has been found in simulations that branch size and orientation can have a strong effect on the backscatter level for HV. Branch parameters are in turn strongly dependent on species, so a dependence of species on the backscatter level would be expected. In the Remningstorp test site the dominating tree species are pine, spruce and some birch. In the current data set there are two areas highly dominated by birch (14, 15), three spruce stands (7, 8 and 11), one stand where both pine and spruce are present (1) and five pine stands. The birch stands have a low biomass level, which is typical for birch, and the corresponding backscatter level is also low. Of the three spruce stands, two have a lower then average backscatter (7, 8), while the third has a very high backscatter level, so no simple species dependence can be found.

For the future there are several interesting ways forward. There are ground measurements available from 2006, which were not included in this analysis due to a storm in early 2007 which made the measurements unreliable. The ground measurements have now been updated and will be included in a further analysis. There is also a possibility to extend the "ground" data using the high resolution lidar data available. Of interest would also be a further analysis on how ground area parameters (biomass, number density etc.) are affected by the choice of area boundaries.

7.1.5 References

[1] T. Le Toan, A. Beaudoin, J. Riom, and D. Guyon, "Relating forest biomass to SAR data," *IEEE Trans. Geosci. Remote Sensing*, vol. 30, no. 2, pp. 403-411, 1992.

[2] M.C. Dobson, T. Ulaby, T. Le Toan, A. Beaudoin, E. Kasischeke, and N.L. Christenses, "Dependence of radar backscatter on coniferous biomass," *IEEE Trans. Geosci. Remote Sensing*, vol. 30, no. 2, pp. 412-415, 1992.

[3] L.M.H. Ulander, M. Blom, B. Flood, P. Follo, P.-O. Frölind, A. Gustavsson, G. Haapalahti, T. Jonsson, M. Lundberg, D. Murdin, and G. Stenström, "The LORAM airborne radar experiment: Final report," Technical Report, FOI-R--2077--SE, Swedish Defence Research Agency (FOI), 2006.

7.2 Assessment of Pol-InSAR for Forest Height and Biomass Estimation by DLR

7.2.1 Data Selection

The E-SAR system flew over the Remninstrop forest in Sweden at three different times. During these three data acquisitions, L-band and P-band airborne radar and complementary data acquisitions were performed. The flown configurations and the available data sets are summarized in Table 8.7. In general, two spatial baselines of about 0m and 8m have been acquired with a maximum temporal baseline of about 50 min for three acquisition dates with L-band and P-band frequency with a time difference of of 1 hour. For second campaign the time gap between L- and P-band is two days. The spatial baselines at P-band vary from 0 m to 80 m and the spatial baseline spacing is 10 m. The spatial baselines have been acquired with approximately the temporal baseline of maximum 60 min at P-band.

Flight Date		L-Band Quad Pol		P-Band Quad Pol	
		Temporal [min]	Spatial [m]	Temporal [min]	Spatial [m]
Campaign 1	**09 March 2007**	40, 25	0, 8	50, 15, 25	0, 10, 80
Campaign 2	**31 March 2007**	50, 15	0, 8	-	
	02 April 2007	-		60, 15, 25, 40	0, 30, 40, 50
Campaign 3	**02 May 2007**	50, 15	0, 8	60, 50, 40, 30	0, 20, 60, 70

Table 8.7: Selected E-SAR modes for the BIOSAR campaign.

7.2.2 Pol-InSAR Data

In this section a qualitative and quantitative analysis of the L- and P-band SAR data is performed in terms of frequency, baseline, polarization and volume decorrelation.

P-band

Figure 8.8 shows the data corresponding to 20m spatial baseline. The HH amplitude image of scene is shown on the upper left image of Figure 8.8, where the data were acquired on 2 May 2007. The amplitude (HH), interferometric phase and vertical wave-number (k_z) images are shown on the top from left to right. A power cable and road appear as the line from upper middle to bottom right in the amplitude image. Some surfaces and lakes appear darker in the amplitude image. The rest part of the image is covered with forest. On the upper middle image the interferometric phase is shown. The small and smooth phase variations indicate the flatness of terrain. The vertical wave-number (k_z) image reflects the 2-D baseline variation typical for the airborne case; from near to far range due to the wide incidence angle variation and along azimuth the deviation of the platform from the nominal track. All images have the negative vertical wave-number. The range of k_z is from -0.16 to -0.03. The interferometric coherence in the HH, VV, and HV polarizations – scaled from 0 to 1 – are shown in the bottom. The lakes of both sides in the image decorrelate completely (coherence close to 0) in all polarizations as a result of temporal decorrelation. The forest is characterized by the volume decorrelation from near to far range as indicated by the vertical wave-number image. The forest structures become visible in the coherence images due to the sensitivity of the coherence to vertical structure variation.

In Figure 8.9 the corresponding images for 30 m spatial baseline are shown. As expected, with increasing baseline the volume decorrelation over the forest areas increases. The vertical wave-number changes from -0.24 to -0.05.

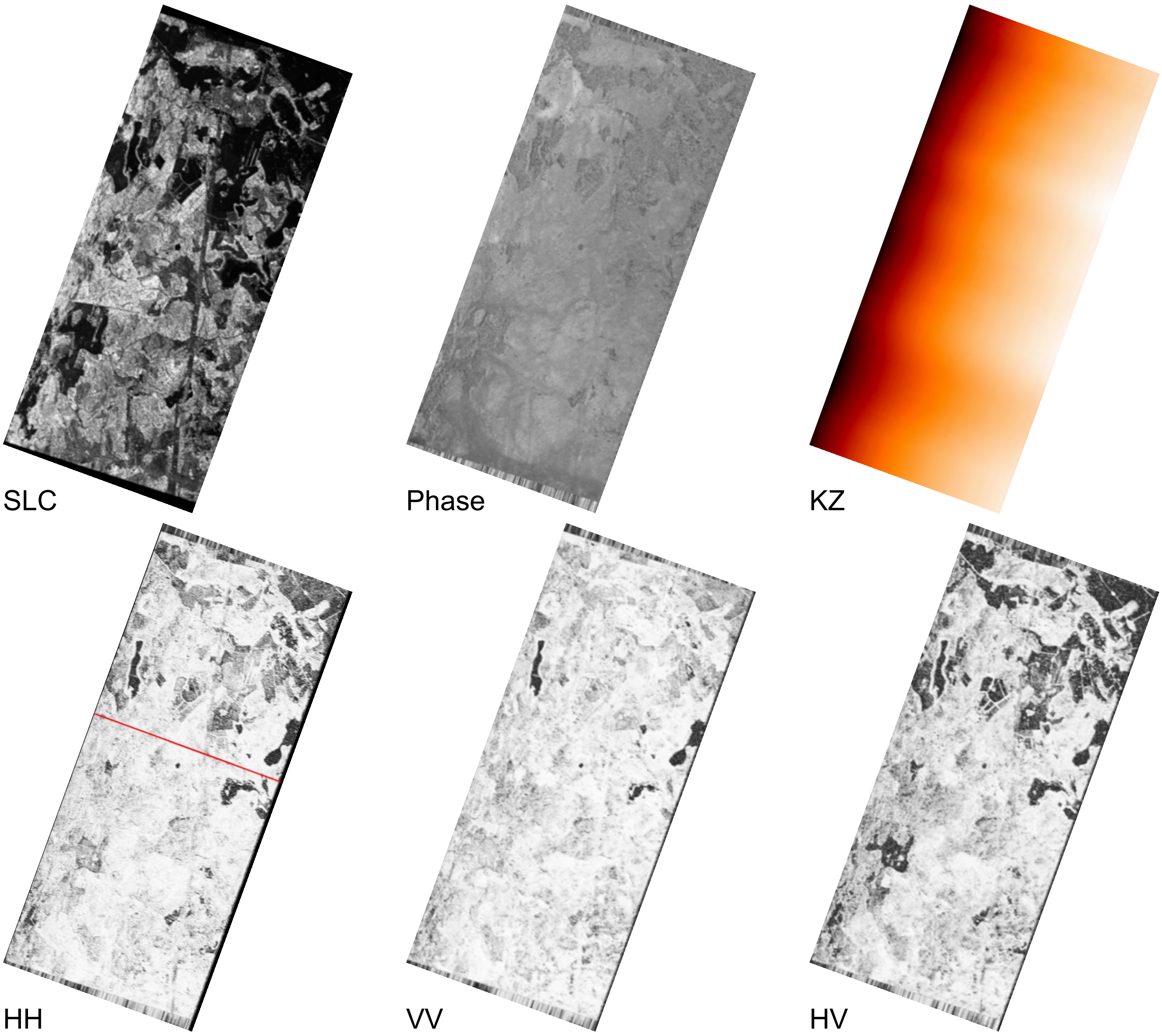

Figure 8.8: Interferometric coherences for a 20m spatial baseline in P Band on 2 May 2007; from left to right upper part: amplitude image (HH polarisation), interferometric phase (HH polarisation), vertical wave-number (kz:-0.16 ~ -0.03); from left to right middle part: coherence in HH, VV, and HV polarisation; from left to right lower.

Going to the large baseline, 60m, in Figure 8.10 the coherence decreases especially in near range, in consequence to high volume decorrelation. The coherence over surfaces stays still at high levels in spite of large baseline. The range of k_z is from -0.46 to -0.09.

In Figure 8.10 the corresponding images for the 0 m spatial baseline are shown. The 0 m spatial baselines were acquired during every acquisition campaign and both frequencies. The vertical wave-number has a distinguish features and a very small range between -0.04 and 0.02 at 0 m spatial baseline. The k_z becomes 0 where the two tracks cross each other. A larger relative variation of the vertical wave-number within the scene (especially along azimuth) can be observed. Comparing other baselines, 0 m spatial baseline has high coherence levels of every polarization due to a similar look angle.

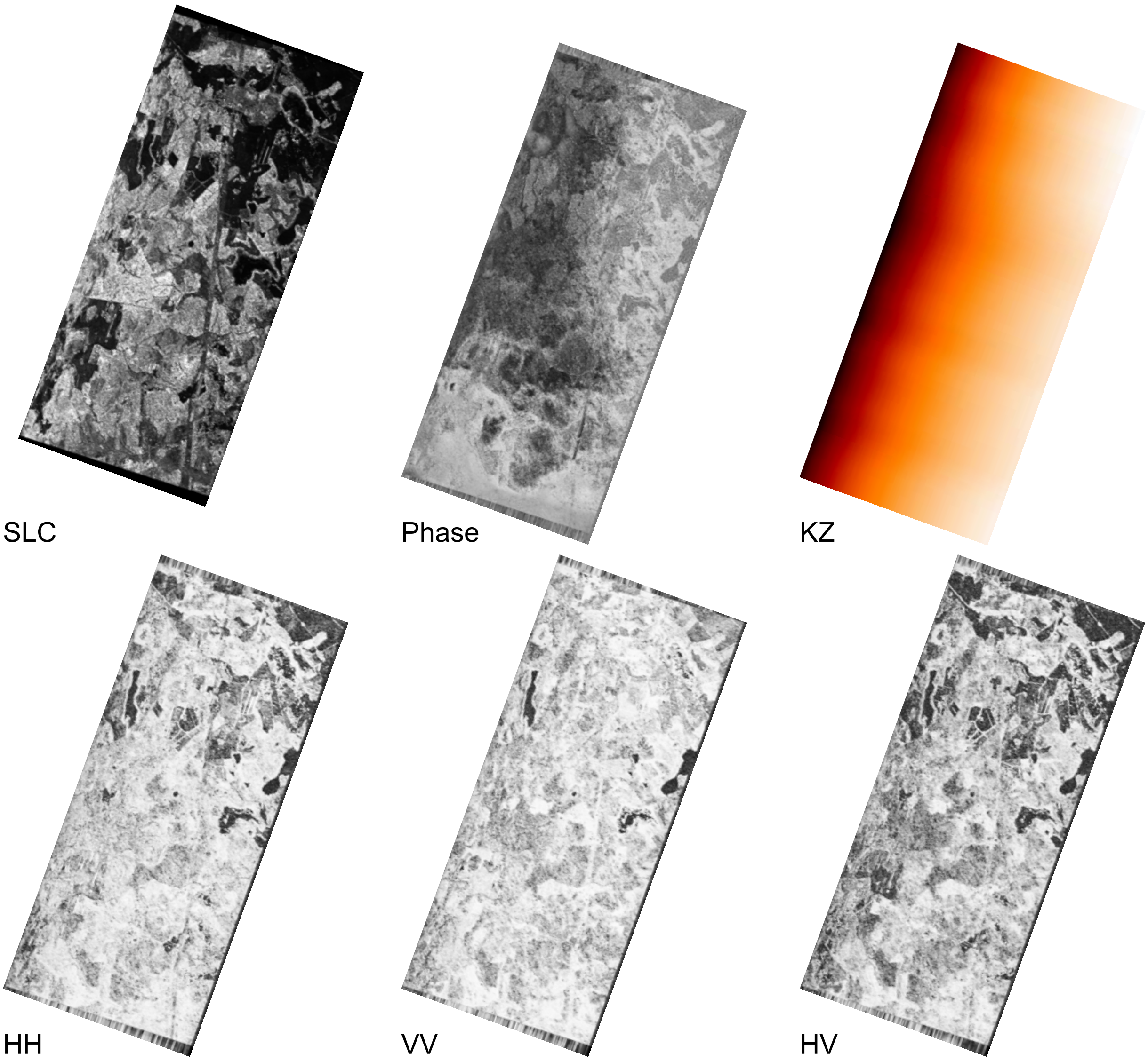

Figure 8.9: Interferometric coherences for a 30m spatial baseline in P Band on 2 April 2007; from left to right upper part: amplitude image (HH polarisation), interferometric phase (HH polarisation), vertical wave-number (kz:-0.24 ~ -0.05); from left to right middle part: coherence in HH, VV, and HV polarisation; from left to right lower.

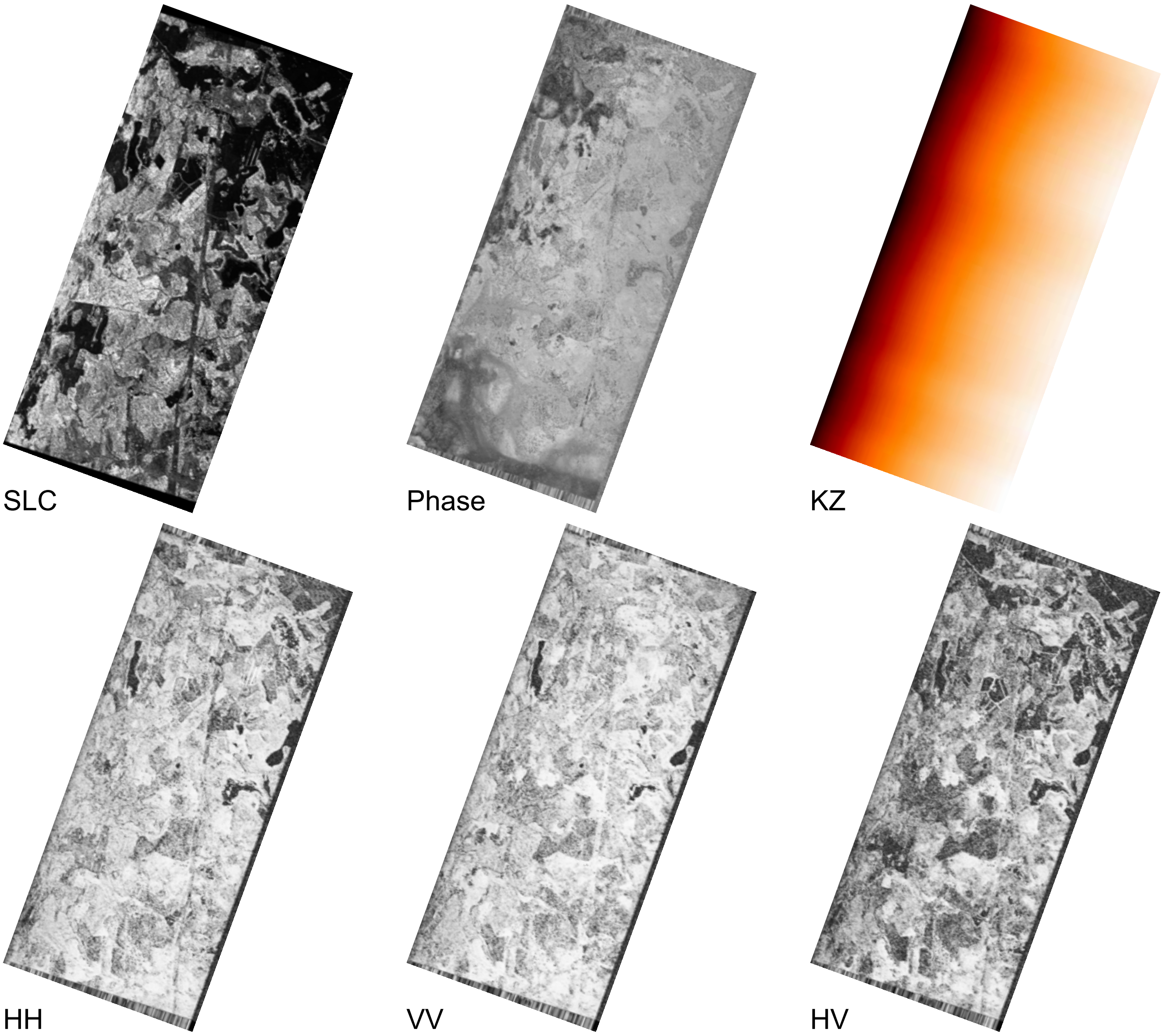

Figure 8.10: Interferometric coherences for a 60m spatial baseline in P Band on 2 May 2007; from left to right upper part: amplitude image (HH polarisation), interferometric phase (HH polarisation), vertical wave-number (kz:-0.49 ~ -0.09); from left to right middle part: coherence in HH, VV, and HV polarisation; from left to right lower.

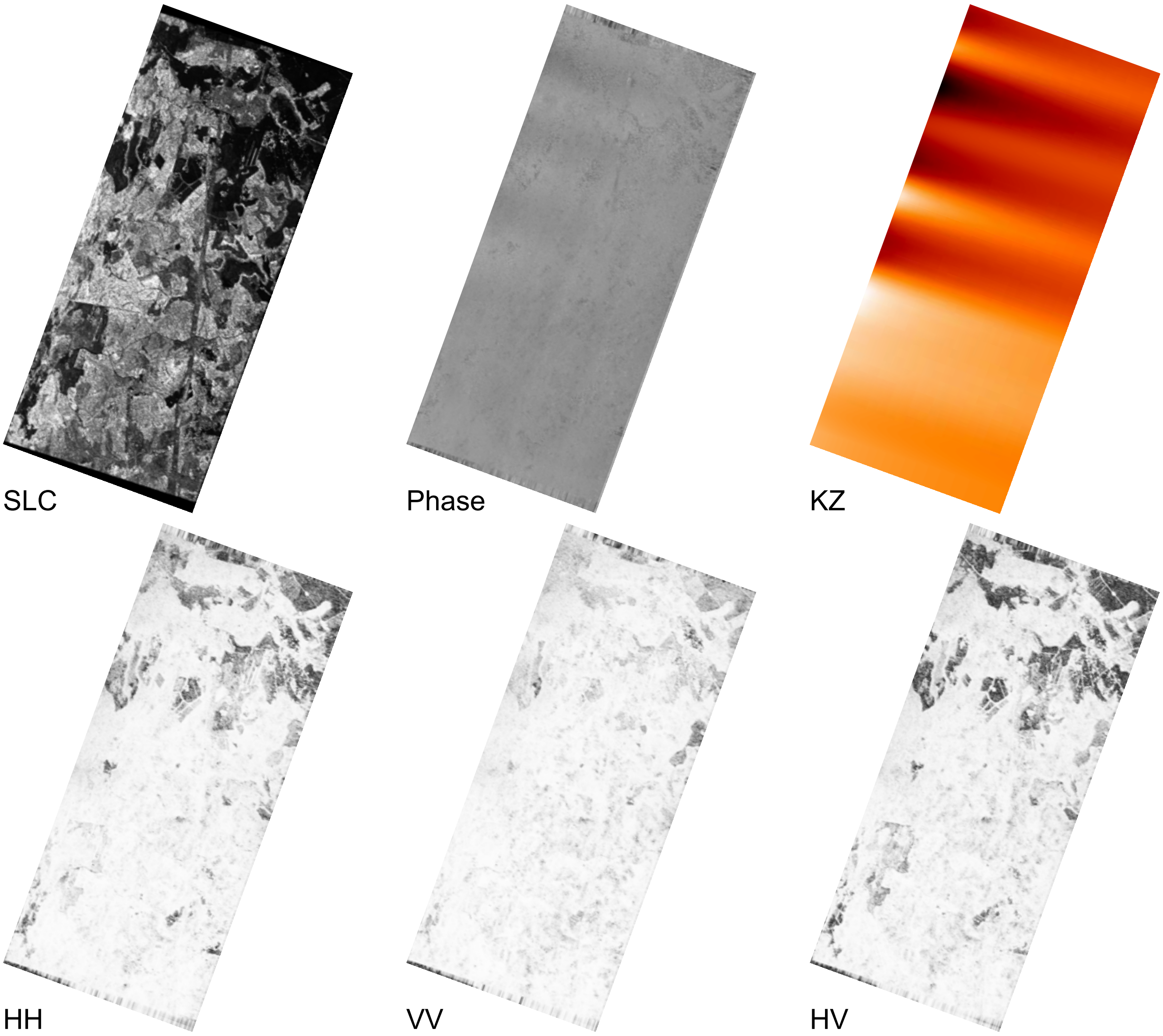

Figure 8.11: Interferometric coherences for a 0m spatial baseline in P Band on 9 March 2007; from left to right upper part: amplitude image (HH polarisation), interferometric phase (HH polarisation), vertical wave-number (kz:-0.04 ~ 0.02); from left to right middle part: coherence in HH, VV, and HV polarisation; from left to right lower.

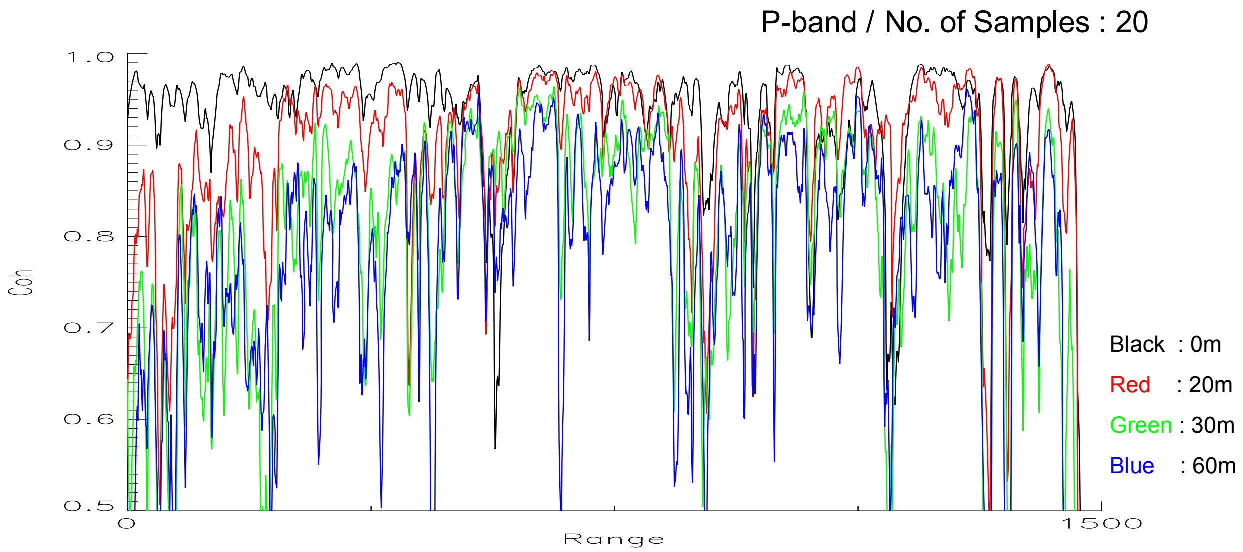

Figure 8.11a: Range plot (averaged over 20 azimuth samples) for different spatial coherences in HH polarisation. The range line estimated is marked in the Figure 8.8 on the HH coherence image.

In Figure 8.11a coherences with different spatial baselines are ploted against the local incidence angle that is varying in range from 25 to 55 degree corresponding to a range line length to 1500. It can be observed that the the lowest spatial baseline has in average the highest coherence and the coherence level decreases with increasing spatial baseline. This has been already observed in Figure 8.8 to 8.11 in the images and is now shown in a quantitative way. A more quantitatively way is to present the average coherence value of the whole scene for the different spatial baselines as shown in Table 8.7.a.

Baseline	0m	10m	20m	30m	40m	50m	60m	70m	80m
Coherence	0.92	0.90	0.85	0.77	0.74	0.72	0.73	0.72	0.71

Table 8.7a: Average interferometric coherences over the whole scene in HH polarisation for different spatial baselines in P-band.

L-Band

In Figure 8.12 shows 0 m spatial baseline at L-band from the 31 March 2007. In L band the 0 m baselines were also obtained during the three campaigns. The HH amplitude, interferometric phase and vertical wave-number images are shown on the top from left to right. Especially, this image has a positive vertical number (k_z: 0.01 ~ 0.09) and has no intersection point of two tracks (k_z=0). The vertical wave-number image shows stronger variation along the azimuth directions caused by the flight track deviations. The coherences at the lexicographic polarizations are shown on the bottom. Compared with P-band the level of coherences is generally lower.

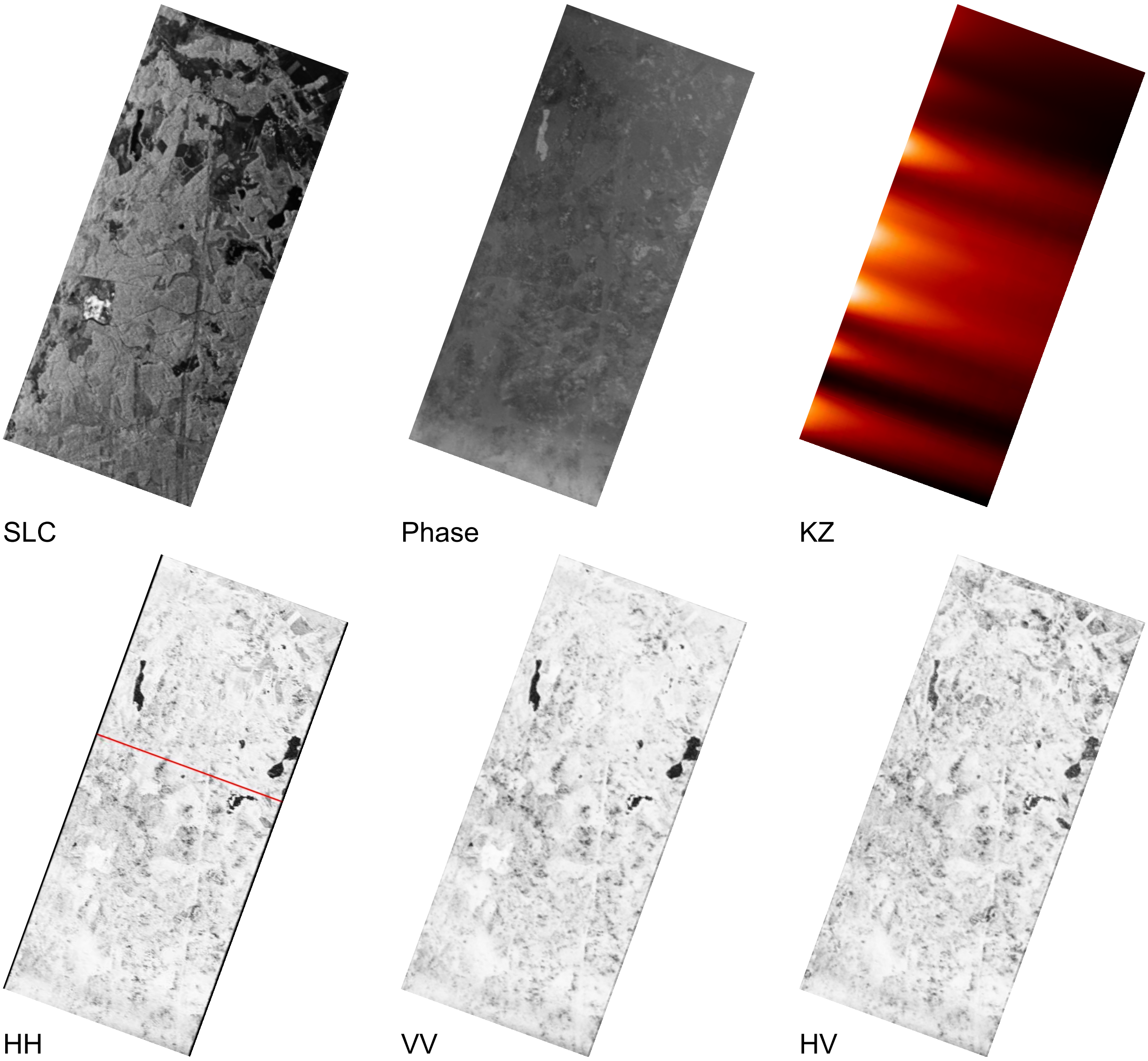

Figure 8.12: Interferometric coherences for a 0m spatial baseline in L Band; from left to right upper part: amplitude image (HH polarisation), interferometric phase (HH polarisation), vertical wave-number (kz: 0.01 ~ 0.09); from left to right middle part: coherence in HH, VV, and HV polarisation; from left to right lower.

The Figure 8.13 shows images of 8 m spatial baseline (corresponding to about 30 m baseline at P-band). This image is similar in the vertical wave-number to 30 m P-band (k_z: -0.24 ~ -0.02). Along azimuth, this image has also the larger variation of the vertical wave-number. The coherence level over the forest decreases dramatically (especially in near range) due to the increased volume decorrelation contribution (that is stronger in near range than in far range). The forest is also characterized by volume decorrelation that varies with spatial baseline (i.e. from near to far range – as seen on the vertical wave-number image). In contrast to the forest, coherence level over surface scatterer remains constant with baseline. Specially, the coherence levels of road and power cable do not change as much as the one of forest.

The high coherence levels obtained over all spatial baselines and both frequencies on acquisition days indicate a high system acquisition and data processing quality of data set.

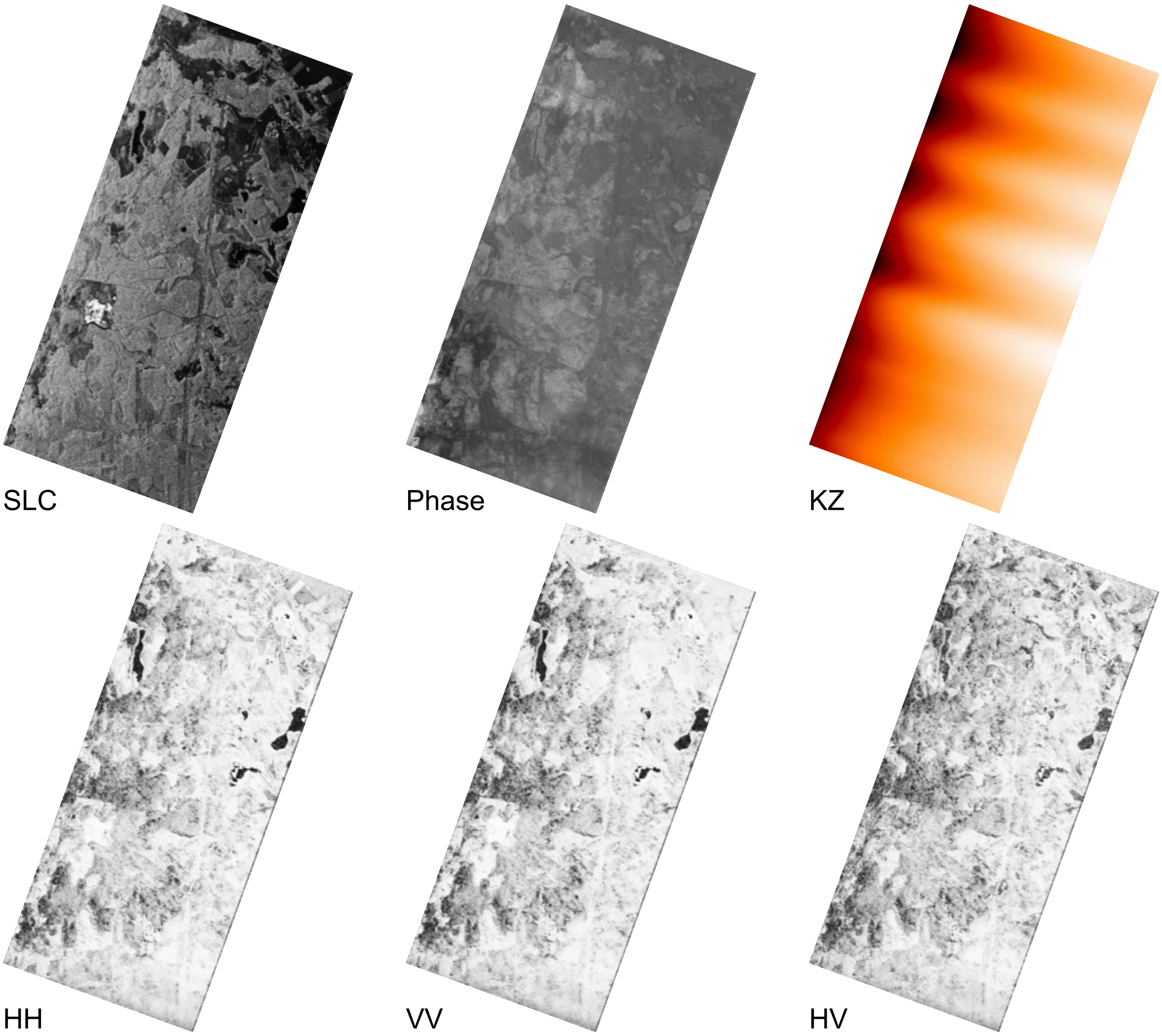

Figure 8.13: Interferometric coherences for a 8m spatial baseline in L Band on 31 March 2007; from left to right upper part: amplitude image (HH polarisation), interferometric phase (HH polarisation), vertical wave-number (kz:-0.24 ~ -0.02); from left to right middle part: coherence in HH, VV, and HV polarisation; from left to right lower.

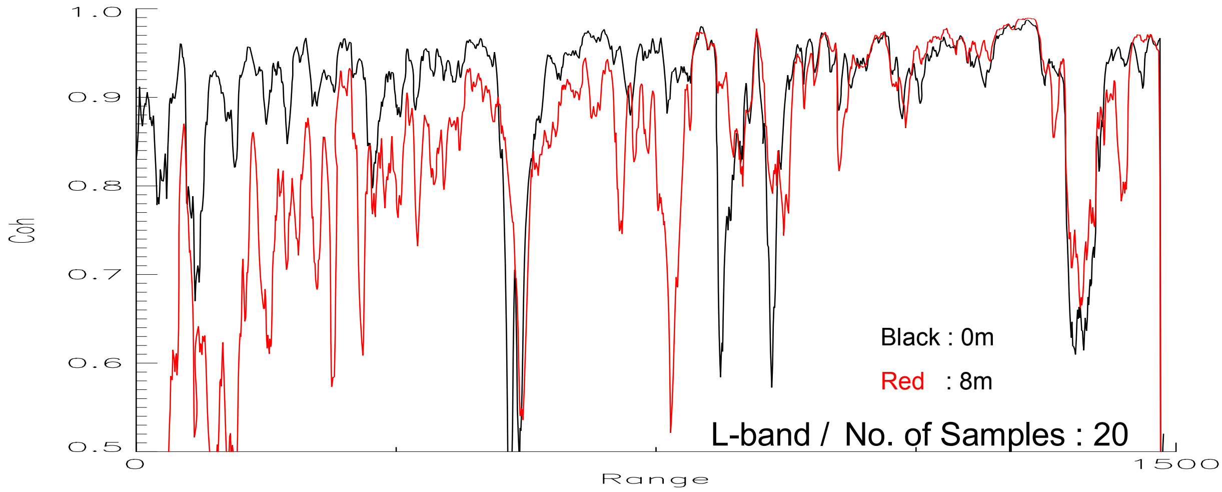

Figure 8.13a: Range plot (averaged over 20 azimuth samples) for different spatial coherences in HH polarisation. The range line estimated is marked in the Figure 8.12 on the HH coherence image.

Also in L-band a quntitiative view of the two spatial baselines are presented in Figure 8.13a against the local indicence angle ranging from 25 to 55 degree. As expected the smallest spatial baseline shows also in L-band in average the highest interferometric coherence. This can be also confirmed by the average values displayed in Table 8.7b

Baseline	0m	8m
Coherence	0.90	0.84

Table 8.7b: Average interferometric coherences over the whole scene in HH polarisation for different spatial baselines in L-band.

7.2.3 Pol-InSAR Data Analysis

In this section the volume model that is used for forest height inversion is presented and a performance analysis of the BIOSAR data is shown. The main focus is given to the appearing interferometric decorrelation term.

7.2.3.1 Pol-InSAR forest height inversion model

The complex interferometric coherence observed for random vertical distribution of scatterers can be formulated as a ratio of integrals [1], [2].

$$\tilde{\gamma}_V = \exp(i\,k_z z_0)\frac{\int_0^{h_v} f(z')\exp(i\,k_z\,z')dz'}{\int_0^{h_v} f(z')dz'} \qquad 1)$$

where $f(z)$ is the vertical structure function , z_0 the position of the bottom of the scattering layer and k_z the effective vertical wave number that depends on the imaging geometry and the radar wavelength

$$k_z = \frac{k\,\Delta\theta}{\sin(\theta_0)} \quad \text{and} \quad k = \frac{4\pi}{\lambda} \qquad 2)$$

and $\Delta\theta$ is the incidence angle between the two interferometric images by baselines.

The RVoG model gives the (complex) volume decorrelation contribution of the interferometric coherence:

$$\tilde{\gamma}_V = \exp(i\,k_z\,z_0)\frac{\tilde{\gamma}_{V_0} + m}{1+m} \qquad 3)$$

where m is the (real) ratio of surface-to-volume scattering amplitudes.

$$m = \frac{m_{Ground}}{m_{Volume}\,I_0} \qquad 4)$$

$\tilde{\gamma}_{V_0}$ is the volume-only coherence and is dominated by volume scattering so m_{Ground} = 0.

$$\tilde{\gamma}_{V_0} = \exp(i\,\phi_0)\frac{\int_0^{h_v} \exp(i\,k_z\,z')\exp\left(\frac{2\sigma z'}{\cos\theta_0}\right)dz'}{\int_0^{h_v} \exp\left(\frac{2\sigma z'}{\cos\theta_0}\right)dz'} \qquad 5)$$

where $\phi_0 = k_z\,z_0$ is the topographic or ground phase and σ is the mean wave extinction.

The main idea is to invert a model relating structural parameters to observed coherences in multiple polarization channels, after a sufficient calibration/compensation of system (e.g. SNR) and geometry (range/azimuth spectral shift) induced decorrelation contributions. We can write the estimation problem formally as shown in Eq. 3 There are five unknown parameters ($h_V, \sigma, \phi_0, m_1, m_2$) in equation.

$$\begin{bmatrix} Forest\ Height\,(h_V) \\ Canopy\ Extinction\,(\sigma) \\ Unlying\ Topography\,(\phi_0) \\ Ground\,/\,Volume Amplitude\ Ratio\,(m_1, m_2) \end{bmatrix} = [M]^{-1} \begin{bmatrix} Interferometric\ Phase\ and \\ Coherence\ in\ three\ Polarizations \end{bmatrix}$$

Consequently, the inversion of the RVoG model using a single baseline requires as least three independent polarizations, and therefore, fully polarimetirc interferometric data [3].

7.2.3.2 Coherence Calibration

As discussed in the previous section, the inversion of forest height is based on the evaluation of the volume decorrelation contribution of three interferometric coherences. Non-volumetric decorrelation contributions cause the height error on the Pol-InSAR inverted heights.

The plots in Figure 8.14 quantify the estimation error due to un-compensated non-volumetric decorrelation contributions: The left graph shows the relation between the vertical baseline and height error. The height error for a 20 m volume is plotted as a function of the baseline (expressed in form of the vertical wave-number, k_z) for different decorrelation contribution. Accordingly, already a small decorrelation contribution 0.95 causes at k_z of 0.1 a height error about 2.5 m. The height error is larger than 10%. That means small baselines (i.e. small wave-number) are affected more by decorrelation than large baselines.

On the right hand side, the height error is plotted as a function height for a constant baseline (k_z = 0.1) for different decorrelation contribution. Note that the smaller volume height has a higher height error. The 30 m volume height has just 1.5 m height error and a small decorrelation contribution of 0.95. As the volume height decreases to 10 m the height error increases to 3 m. This plot indicates that lower forest heights are stronger affected by uncompensated decorrelation effects. The estimated interferometric coherences are affected by additional system and/or processing induced decorrelation effects that have to be compensated / calibrated before the Pol-InSAR inversion. Figure 8.15 shows several kinds of decorrelation effects. These individual contributions and correlations are discussed in the following.

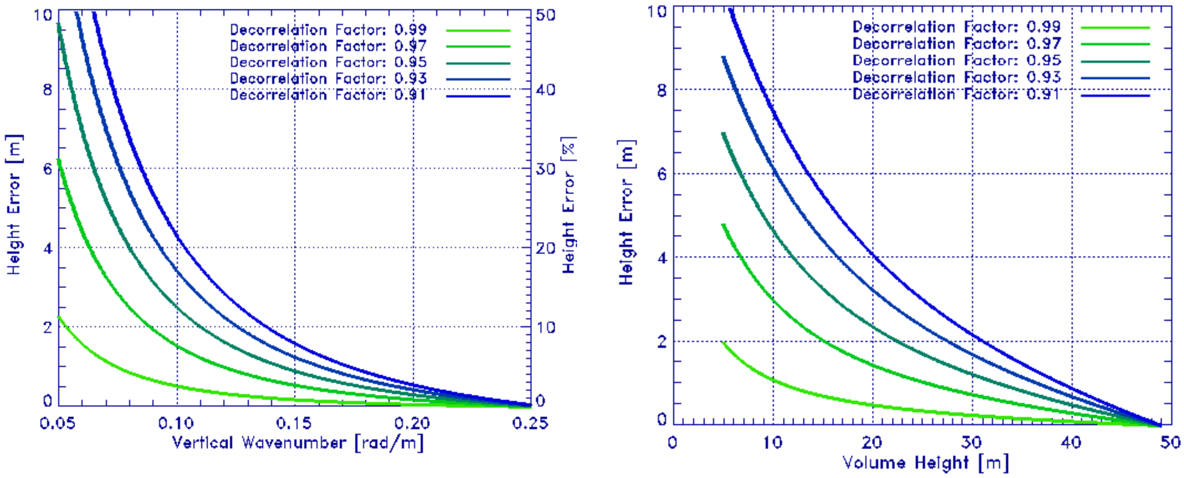

Figure 8.14: Impact of uncompensated decorrelation effects. Left: Height error against vertica wave-number for different decorrelation factors assuming a constant volume height of 20m. Right: Height error against volume height for different decorrelation factors for a constant vertical wave-number of 0.1.

$$\tilde{\gamma}_{OBS} = \tilde{\gamma}_{TRANS}\,\tilde{\gamma}_{SCAT}$$

$$\tilde{\gamma}_{SCAT} = \tilde{\gamma}_{TEMP}\,\tilde{\gamma}_{BAS}$$

$$\tilde{\gamma}_{BAS} = \gamma_{AZ}\,\gamma_{RG}\,\tilde{\gamma}_{VOL}$$

$$\tilde{\gamma}_{TRANS} = \gamma_{SYS}\,\tilde{\gamma}_{PRO}\,\gamma_{EST}$$

$$\gamma_{SYS} = \gamma_{QUAN}\,\gamma_{AMB}\,\gamma_{SNR}$$

$$\tilde{\gamma}_{PRO} = \gamma_{CAL}\,\tilde{\gamma}_{FR}\,\gamma_{COR}$$

$$\gamma_{EST} = \gamma_{BIAS}\,\gamma_{TOPO}$$

Figure 8.15: Decorrelation Effects: γ SCAT=Scatterer Induced Decorrelation: γ TEMP=Temporal Decorrelation, γ BAS=Baseline Decorrelation, γ AZ=Doppler Spectral Decorrelation, γ RG=Range Spectral Decorrelation, γ VOL=Volume Decorrelation. γ SYS=System Induced Decorrelation: γ QUAN =Quantisation Decorrelation, γ AMB=Ambiguities Decorrelation, γ SNR =SNR Decorrelation. γ PRO=Processing Decorrelation: γ CAL=Calibration, Decorrelation, γ FR=Faraday Rotation Compensation, (not relevant for airborne systems), γ EST=Coherence Estimation Bias, γ COR=Coregistratison Decorrelation. γ EST=Estimation Bias: γ BIAS=Cohernece Estimation Bias, γ TOPO=Topography Induced Cohrence Bias.

SNR Decorrelation: γ_{SNR} is defined as [4]

$$\gamma_{SNR} = \frac{1}{1 + (SNR)^{-1}} \qquad \text{with} \qquad 0 \le \gamma_{SNR} \le 1 \tag{6}$$

where

$$SNR = \frac{Signal\,Power}{Noise\,Power} \tag{7}$$

SNR can't be estimated - within the required accuracy - in a direct way therefore the approach proposed in [5] is used. The proposed estimation of noise power has been applied. For monostatic SAR systems and reciprocal scatterers, the cross-pol channels HV and VH are completely correlated in the absence of noise. As the two cross-channels are measured independently by SAR system they represent different realizations of noise process. The correlation between HV and VH decreases allowing an assessment of the noise level. The HV – VH coherence obtained for the Remningstrop forest at P band is shown in Figure 8.16. The low backscattering regions are more affected by the noise.

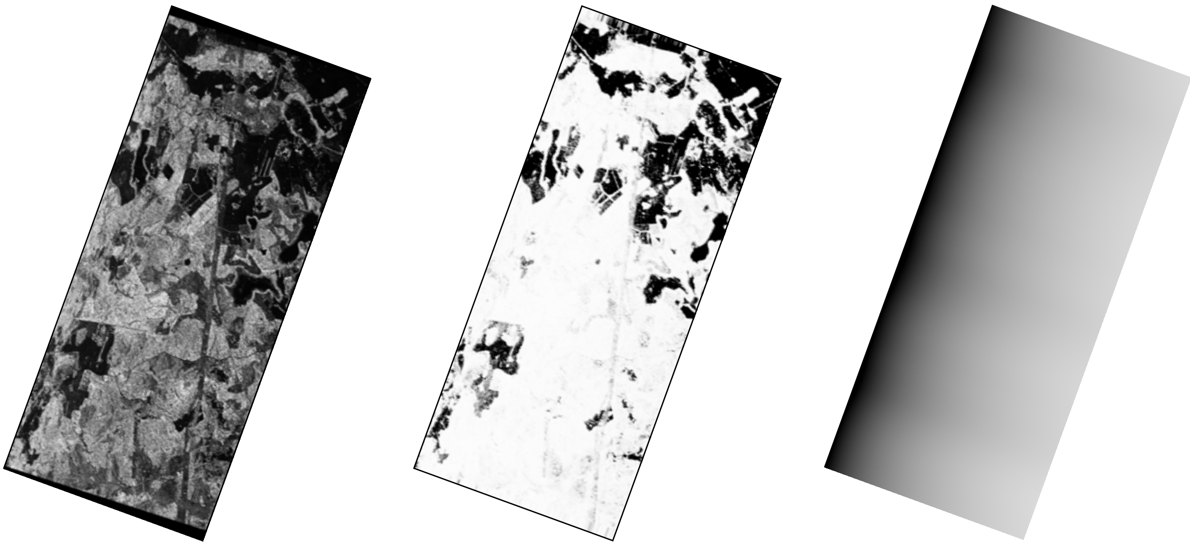

Figure 8.16: SNR Decorrelation; left: Amplitude image of Remningstrop forest scene; middle: SNR Decorrelation of Remningstrop scene scaled from 0.9=black to 1=white; right: Range decorrelation for 30m baseline scaled from 0.95=black to 1=white.

Range Spectral Decorrelation: The slightly different look angles of two images cause the range spectral decorrelation [6]. Assuming a rectangular transfer function in range the correlation decreases linearly with increasing angular baseline $\Delta\theta$ that generates a shift:

$$\gamma_{RG} = 1 - \frac{|\Delta f|}{W_{RG}} \text{ and } \qquad \Delta f = -\frac{f_0\,\Delta\theta}{\tan(\theta_0 - \alpha)} \tag{8}$$

where Δf denotes the range spectral shift, W_{RG} the (range) system bandwidth, f_0 the central frequency, θ_0 the incidence angle and α terrain slope. The terrain slope, α, is negligible in the Remningstrop forest. The range spectral decorrelation is shown in Fig. 8.16.

Coregistration Decorrelation: The misregistration of the interferometric images causes a decorrelation according to:

$$\gamma_{COR} = \frac{\sin(\pi\delta_{AZ})}{\pi\delta_{AZ}} \frac{\sin(\pi\delta_{RG})}{\pi\delta_{RG}} \tag{9}$$

where δ_{AZ} and δ_{RG} are the relative shift between the images in azimuth and range, respectively [7]. It is obvious that a shift of a full resolution cell leads to a total decorrelation. Assuming a coregistration accuracy of about 1/10 of an image pixel leads to γ_{COR} = 0.97. Note that the coregistration accuracy depends on locally on the coherence level. In low coherence areas the coregistration performance decreases increasing (locally) the decorrelation.

7.2.3.3 Mask Generation

Even after coherence calibration, coherence constrains still may limit the Pol-InSAR inversion performance. To avoid this, ill-conditioned regions have to be masked out. In addition to ill-condition regions, non-forest areas exist in the test site (i.e. surface area, power cable and lake). These areas are also covered by a mask. The mask types applied are described in the following.

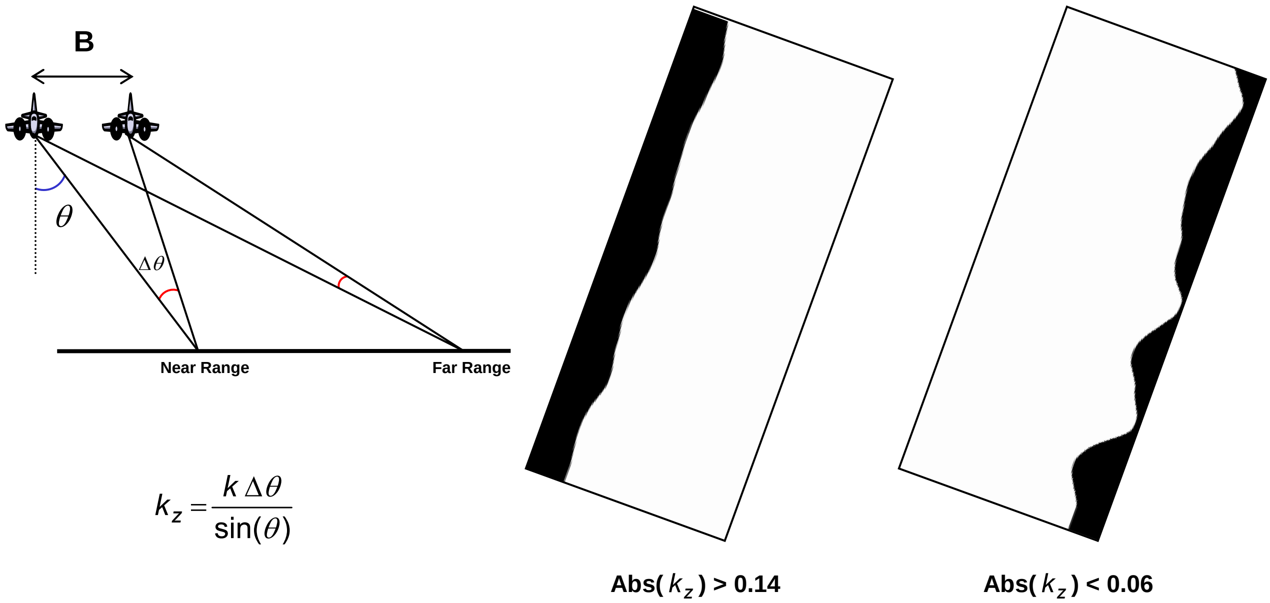

The Vertical Wave-Number Mask Generation: In general, the airborne SAR system has strong

Figure 8.17: Left: example of vertical wave-number effect by the variation of the incidence angle from near to far range, Middle: Kz mask for height values, Right: Kz mask for low values.

variation of the incidence angle (and thus effective baseline) from near to far range. Therefore, the inversion performance is also variying with range. For a good inversion performance a variation in range need to be excluded.

At large effective baselines (i.e. large absolute k_z values) the sensitivity of the coherence to forest height can saturate at heights lower than the forest heights in the scene. The overall coherence level is too low for valuable inversion. Such areas are mask out. The corresponding mask (threshold: the absolute value of k_z > 0.14) is shown in Figure 8.17. The large k_z mask acts primarily in near range. On the other hand, at small effective baselines (i.e. small absolute k_z values) the unfavorable coherence to height scaling leads to high height errors for small residual non-volumetric decorrelations (i.e. the small decorrelation contributions introduce large height errors). Such areas are also covered by a mask. The corresponding mask (threshold: the absolute value of k_z < 0.06) is shown in Figure 8.17. The small k_z mask acts primarily in far range.

The Coherence Mask Generation: Low coherences make accurate inversion at a reasonable spatial resolution inpossible. Therefore, areas with coherences lower than 0.3 have been excluded. The lowest coherence threshold of 0.3 was derived from experiences and forest height inversion model validations. Forest height inversion under this threshold is not reasonable, as the variance of height becomes to high. The corresponding mask is shown in Figure 8.18, and acts across the whole image.

The Non Forest Mask Generation: The test site is mainly covered by forests. But, there are also some surface areas, road, power cable and lakes. These kinds of non-forest areas make the inversion results unreasonable and are also excluded. The corresponding mask is shown in Fig 8.18 and acts across the whole image.

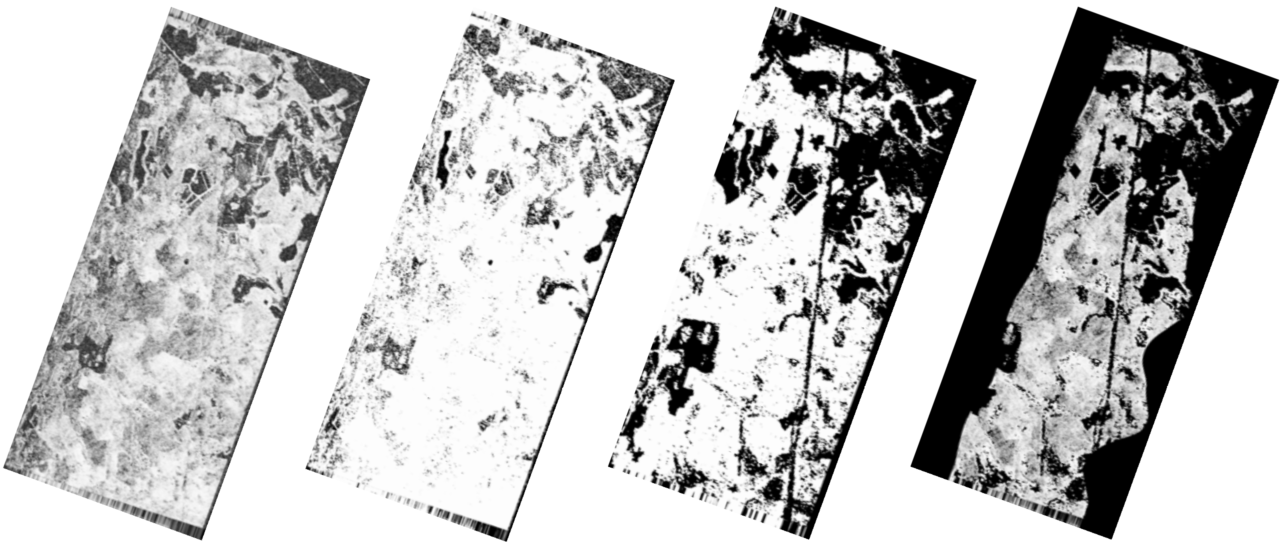

Coherence HV   Coherence Mask   Non forest Mask   Masked Coherence

Figure 8.18: Coherence image of polarization HV, Coherence mask (Coh > 0.3), Non forest area mask and Combination of all mask, valid points are white.

7.2.4 Forest height inversion results

After masking out of non-valid coherence areas and applying the forest height inversion model, forest maps in each spatial baseline are obtained. Depending on the spatial baselines different coherence part in the image can be obtained. In case of large baselines, it is too large for valuable inversion in near range. Otherwise, the wave-number is too small (<0.06) so that small decorrelation contributions introduce large height errors.

Considering the polarimetirc condition, we can combine height inversion results of multi spatial baseline. Figure 8.19 shows the good inversion performances for the whole image in P band. The inversion height maps are scaled from 0 to 40m. The images show few underestimated and overestimated forest areas in near and far range as the results of the coherence compensations and some masks. On the left image of Figure 8.19 the forest height is estimated by the data set acquired in May. With the same wave-number threshold, the height inversion is also applied to the data set acquired in April. The result is shown in the middle of Figure 8.19. Although the April data sets have a different spatial baselines to May's, the results of height inversion are quite similar. That means Pol-InSAR forest height inversion provides consistent results at any date. On March, E-SAR obtained very small and large spatial baselines on P band (i.e. 10 and 80m). For this reason the height map for March is not covered completely over the whole image range. But, the obtained height map is also similar to the others. In Figure 8.19a the variation of the height in range for the three acquisition dates are ploted. In average the estimated height have only a low devisation. For the area where in March are no data only the May and April data were displayed. The low variance betweent the different acquisition dates can be also seen right in Figure 8.19a were a histogram is displayed. Temporal decorrelation is present at each spatial baseline for repeat-pass time intervals on the order of minutes (see Table 8.7). The Pol-InSAR inversion was performed using coherence with little temporal decorrelation.

Figure 8.20 shows the height result of L band on April. This image is also scaled from 0 to 40m. L band data have not enough spatial baselines, compared with P band. Thus, some parts for height inversion are could not be considered. The comparison of different height maps (P- and L-band) shows no significant differences. Both images cover a quite similar height range and reflect a similar forest structure. Height variance is higher in L band than at P band because of the lower coherence, but the height inversion is stable and effective on both frequencies.

7.2.5 Forest height validation

The obtained forest heights need to be validated. For comparison and validation of the inverted forest height, we used two approaches. At first, a comparison of forest height estimates with LIDAR measurements is done; second a validation of inverted forest heights using ground measurement has been performed.

7.2.5.1 Validation by LIDAR measurements

Figure 8.21 shows the height estimates form LIDAR measurements. On the left side of Figure 8.21 the LIDAR height map is overlaid on the P-band SLC image. In order to preserve most of the information for the inversion all validation data were transformed to the slant range geometry. The LIDAR heights covering only a small part of the E-SAR scene.

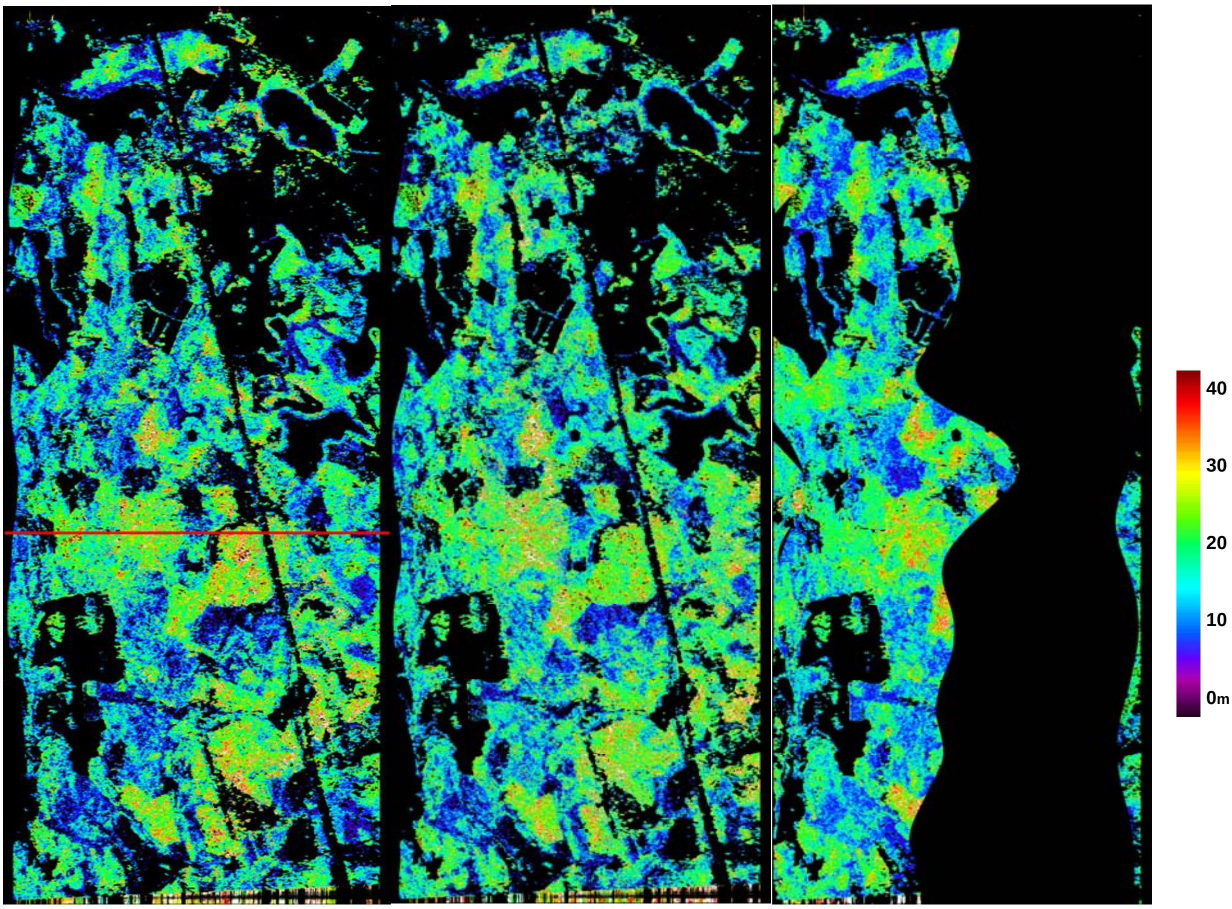

May **April** **March**

Figure 8.19: P-band forest height maps for Remningstrp forest, scaled from 0 to 40m. Masked areas are black. Left: May, Middle: April and Right: March. The red line in the May forest height image dispays the range line taken for height representation.

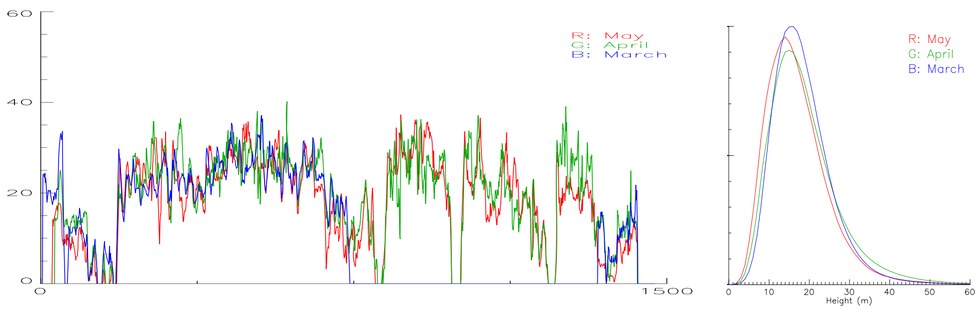

Figure 8.19a: Forest height at P-band for the different acquisition dates plotted against the local incidence angle - ranging from 25 to 55 degree (left). Forest height distribution represented in a histogram for the three acquisition dates.

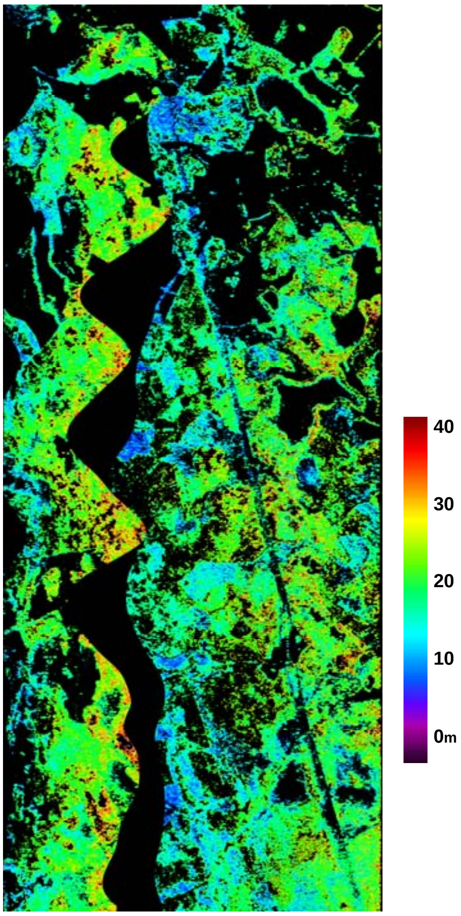

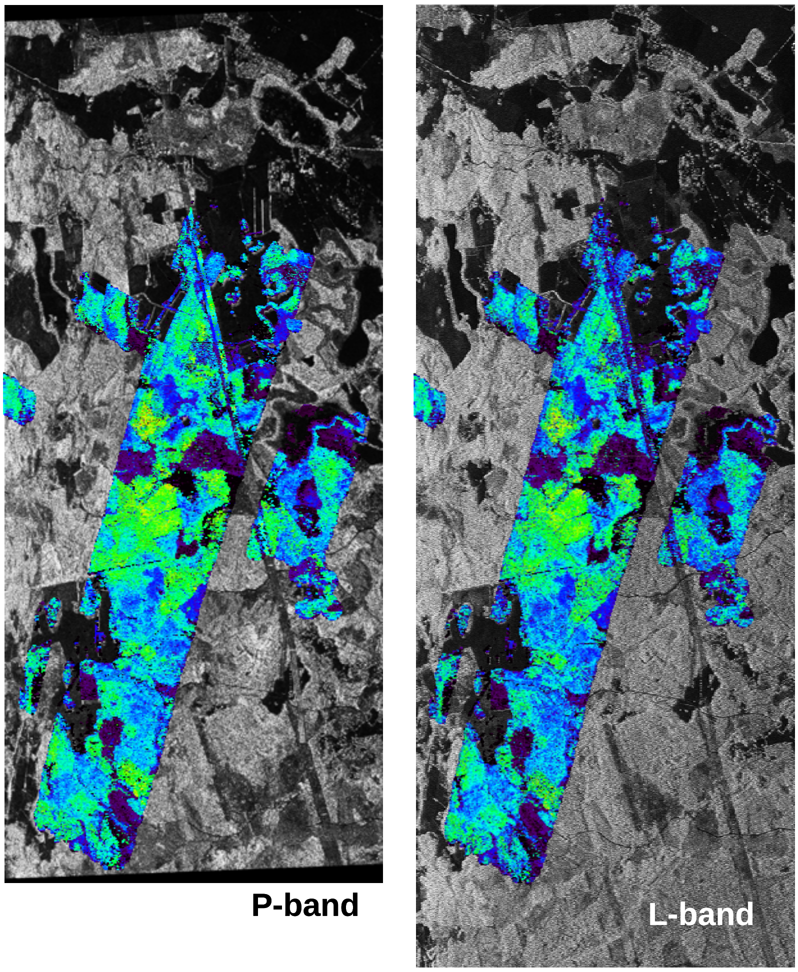

Figure 8.20: L-band forest height maps for Remningstrp forest, scaled from 0 to 40m. Masked areas are black

Figure 8.21: L-band forest height maps for Remningstrp forest, scaled from 0 to 40 m. Masked areas are black.

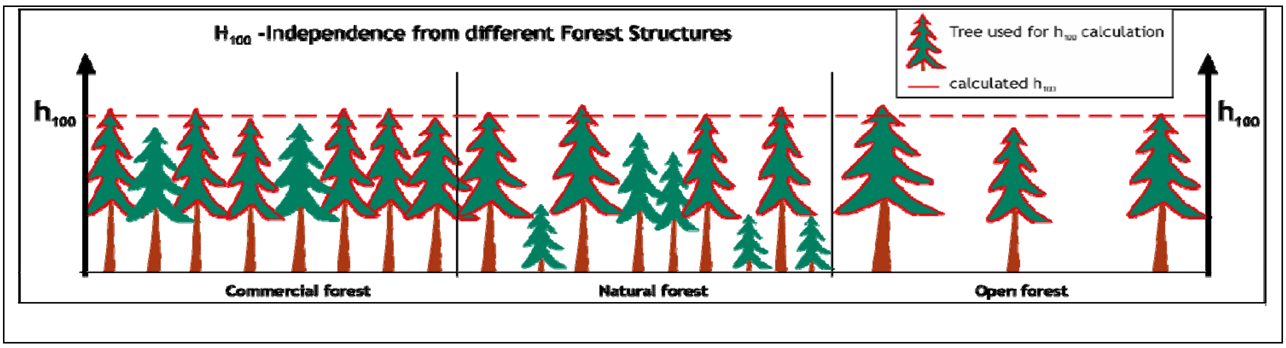

Figure 8.22: H_{100} : The top height H_{100} refers to the 100 trees per hectare.

Before a validation of the E-SAR inversion height has been done the H_{100} as a reference forest height was estimated from the LIDAR forest height. The H_{100} is a forestry standard parameter that describes the 100 tallest trees per hectare. H_{100} was estimated from LIDAR data by taking the highest heights within a 10 by 10 m window (see Figure 8.23). In Figure 8.22 a schematic plot is presented showing the same H_{100} values for variying forests. The H_{100} is independence of forest structures [8].

The comparison of both heights was done in slant range on a polygon basis. For the polygon based comparison, the individually homogenous polygons were selected from the original LIDAR height map. Figure 8.23 shows H_{100} and Pol-InSAR inversion height maps in slant geometry overlaid with 78 polygons. These images are also scaled from 0 to 40 m as before. For the March derived forest height some part were masked out and cannot be compared with the LIDAR heights.

For validation of both heights a correlation plot was made. The mean values of each polygon were estimated from the LIDAR H_{100} and the Pol-InSAR esitmated height and plotted in Figure 8.24 against each other. In the first column of Figure 8.24 a comparison of mean height values is presented. In the second and third columns the standard deviations of the Pol-InSAR inverted heights and LIDAR heights are presented.

For the different campaigns the inversion results are presented. For May the P-band derived Pol-InSAR heights correlate strongly and significant with the LIDAR H_{100} with a correlation of 0.76 (first row Figure 8.24). The forest height varies mainly between 10 and 35 m. The height estimates in P band are little lower than the one in H_{100}. Especially for forest with lower that 10m several inversion results are overestimated. The reason is that lower forest has higher height error (already presented in Figure 8.14). There is a steady increase in the standard deviation of the P-band inverted height, but not of the derived H_{100} from LIDAR. The window size used to estimate the highest tree in H_{100} seems to be appropriate as the standard deviation is stable. The next two rows show the comparison of April and May data. Specially, the results of April data are also well correlated with H_{100}. In general it can be stated that the Pearson correlation is very high with 0.9 and the root mean square deviation is low in the order of 4 m.

The relationship between inversion of L band and H_{100} is shown in the bottom of Figure 8.24. Both heights are significantly less correlated. In this case, the inverted heights are from the L band frequencies and are little lower than H_{100}. That means the inversion heights from P band are lower than the ones of L band. There are two possible reasons for this behavior. The first is the reduced sensitivity of P band to height variations caused by low extinction values. This can lead to an underestimation of forest height at P band in less dense forest environments. The other reason could be the impact of temporal (or other) decorrelation sources at L band that can lead to an overestimation of forest height. The validation results for L-band show a Pearson correlation of 0.8 and a root mean square deviation of 6 m. The values are a little bit worther than the one obtained from P-band. The main reason for it is that L-band is stronger effected by temporal decorrelation than P-band.

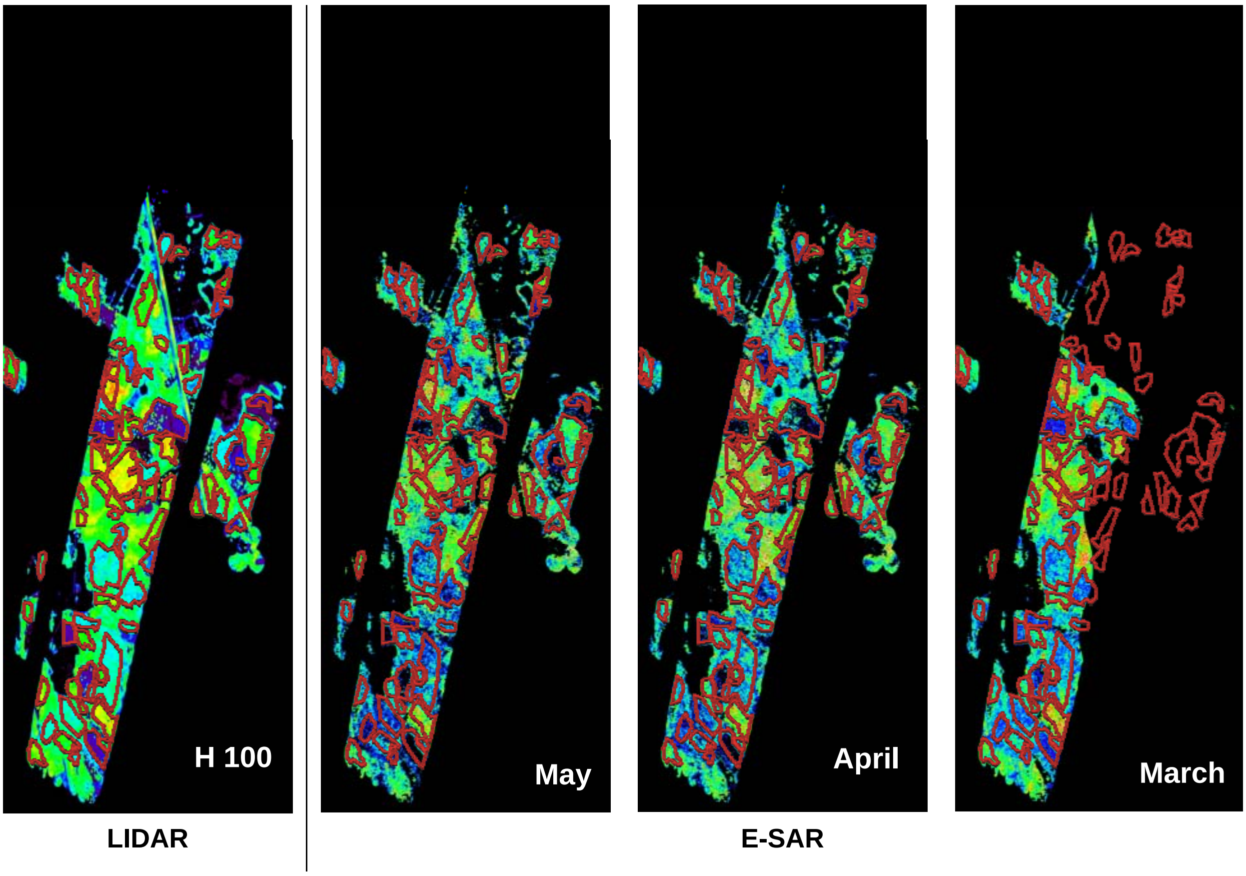

Figure 8.23: Polygons on each image. Every inversion height maps and H_{100} from LIDAR data are overlaid with polygons (red).

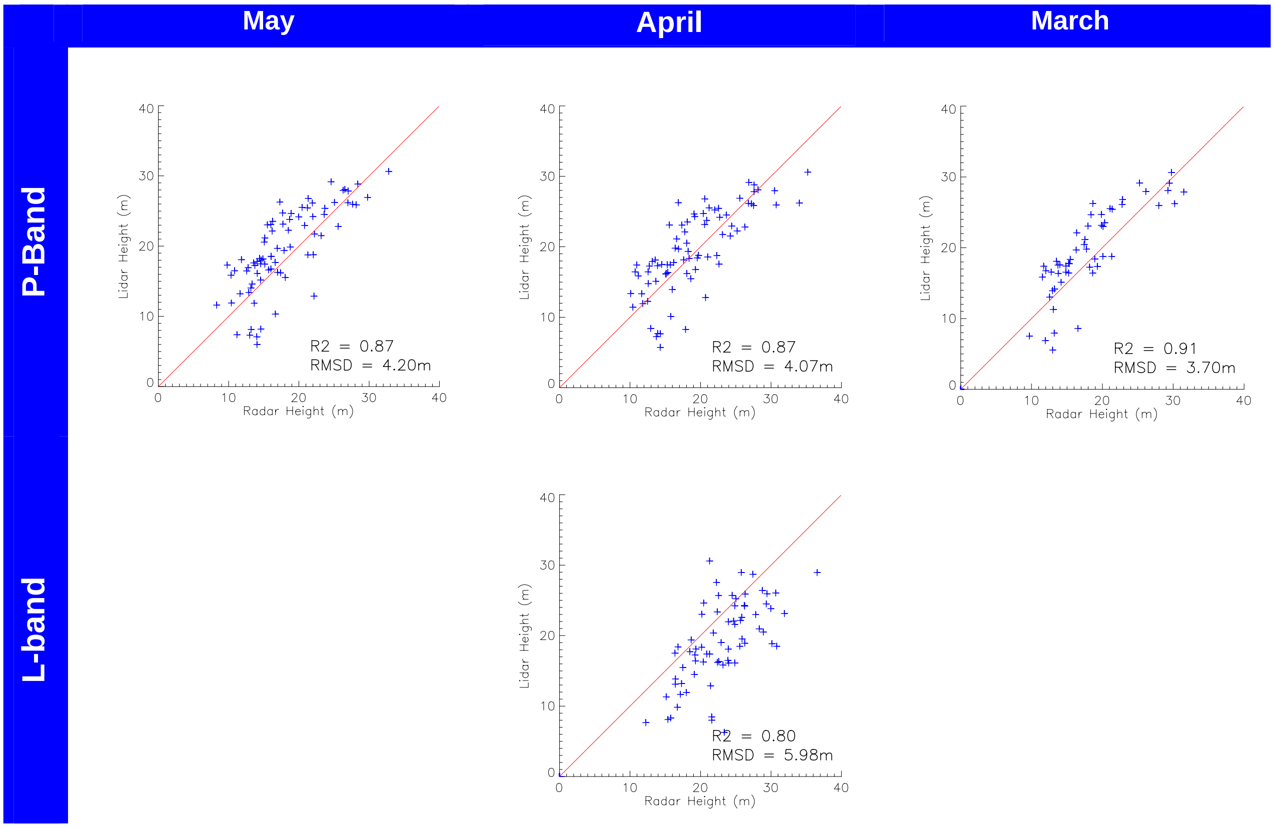

Figure 8.24: The comparison between inversion height from E-SAR and H_{100} from LIDAR.

	P-band			L-band
Date	**May**	**April**	**March**	**April**
R^2	0.87	0.87	0.91	0.80
RMSD (m)	4.20	4.07	3.70	5.98

Table 8.7c: Statistical average values for forest height validation at different acquisition dates. Two statistical parameters are displayed; the Pearson correlation (R^2) and the root mean aquare deviation (RMSD).

7.2.5.2 Validation by ground measurements

In the addition to LIDAR data, the ground measurements on individual trees on 11 stands were measured during spring 2007. This section investigates the relation between forest inversion heights and ground measured heights. There are 4 areas with an extention of 80 by 80 m and 7 areas with an extention of 20 by 50 m were different forest specific paramters were measured.

The comparison of inversion height and using a simple mean value of ground measurement heights was found to be difficult. The main problems were caused especially due to the similar populations, but with different forest heights within one stand. There is a high variation of smaller and higher trees. Although the shorter trees are less affected by radar signal than higher trees, they reduce considerably the mean forest height of the ground measurements (see Figure 8.24).

Thus, also for the ground measurements the H_{100} has been estimated and used for the validation with ground measurement instead of using a simple average height. The H_{100} values of ground measurements were estimated in 11 stands and compared with inversion heights corresponding to same areas. The results are illustrated in Figure 8.25. The horizontal axis presents the inversion height, and the vertical axis the H_{100} of the ground measured heights. Red and blue points show the values of 20 by 50 and 80 by 80 m sample plots, respectively. On the left side of Figure 8.25 the comparison between H_{100} and the inverted height from May is shown. Strong correlation is observed betweent the inverted and the inventory heights. Right plot shows the comparison of inversion height with April data and H_{100} derived from ground measurements. The inverted forest height for the April campaign is slightly overestimated than the one for the May campaign. The 20 by 50 m sample plot has a lower correlation than the 80 by 80 m sample plot. The Pearson correlation of the 20 by 50 m sample plot is ranging from 0.7 to 0.9 and for the 80 by 80 sample plot it is ranging between 0.94 and 0.96. Also the root mean square deviation is the bigger sample plot show the lower deviation with 2-3 m, whereas the smaller sample plot is variying up to 4 m.

The main reason for it is that the sample plot is statistically too small to have a significant meaning. The H_{100} is in general defined as the estimate of the 100 tallest trees per hectare, but the 20 by 50 m samle plot corresponds just to 0.1 hectare. Thus, for the smaller sample plot the average of only 10 highest trees are accounted for H_{100}. This can lead to an overestimation or underestimation of H_{100}. A small area affects also the mean value of the inverted height. In addition due to the exclusion of non-valid coherences the amoun of valid estimated point withn the smaller sample plot region are reduced and only few values for a validation correlation can be used. Owing to fewer available pixels, the comparisons between ground measurements and inversion height for P-band in March and L-band were found to be difficult.

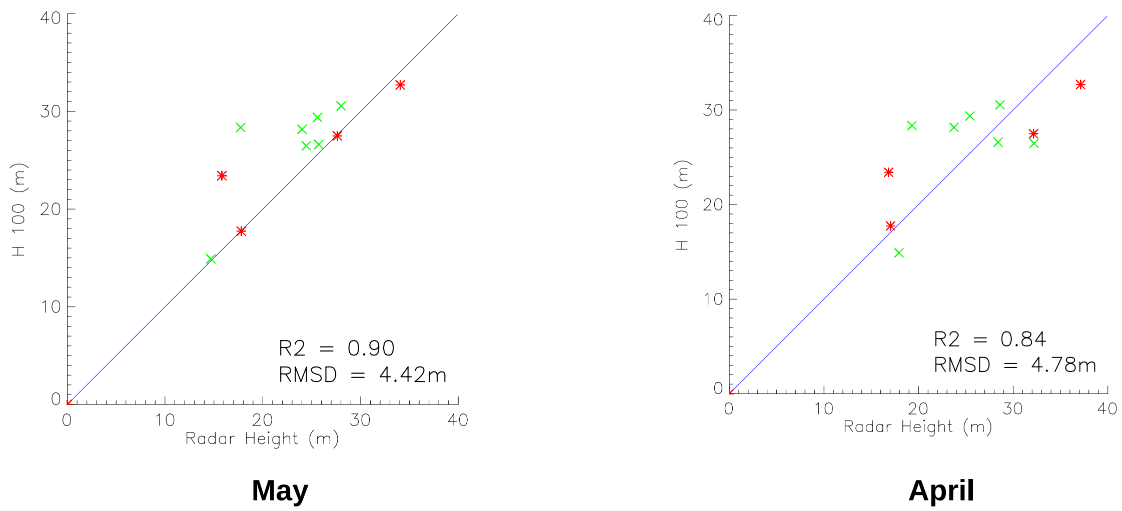

Figure 8.25: The comparison between inversion height from E-SAR and H_{100} from ground measurements on 20 by 50m (red) and 80 by 80m (blue). Left: Inversion height on May and ground measurements. Right: Inversion height on April and ground measurements.

Stands	All		20 by 50 m		80 by 80 m	
Date	May	April	May	April	May	April
R2	0.90	0.84	0.88	0.72	0.94	0.96
RMSD (m)	4.42	4.78	3.76	3.89	2.33	2.78

Table 8.7d: Statistical average values for forest height validation at different acquisition dates. Two statistical parameters are displayed; the Pearson correlation (R^2) and the root mean aquare deviation (RMSD).

7.2.5.3 Biomass estimation and comparison

In the previous section it could be demonstrated that a validation with Pol-InSAR permits accurate forest height estimation using the Random Volume over Ground (RVoG) model and validate it with LIDAR data and ground measurements. In this section the relation of forest height to forest biomass is presented. In this case forest heights are converted to forest volume through an allometric relation between forest height *h* and stem volume *V*. The relation has been provided by FOI for Swedish dominated coniferous forest and is expressed as $h(V)=(2.44V)^{0.46}$ [9]. The volume is expressed in terms of m3/ha and h shows the height of forest per hectare. The inversion height was closely related to the H_{100} (i.e. average height of the 100 highest trees per hectare). For converting from the inverted heights to usable forest biomass, the relation between the simple mean height and H_{100} for the sample plots was investigated. H_{100} and the mean values in 80 by 80 m areas were estimated and plotted in Figure. 8.26. A linear relation is assuemed between H_{100} and the mean forest height. Due to the linear relation (factor: 0.71) the inverted height is set to be the effective height, that need to be defined for the biomass estimation when reversing the height-biomass allometric equation. The results of the biomass-allometric transformation are presented as a stem volume map in Figure 8.27. The values of the stem volume are scaled from 0 to 600 m3/ha.

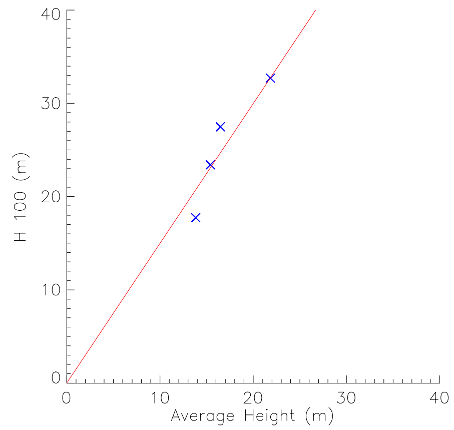

Figure 8.26: The relation between H_{100} and the mean height for the ground measurements.

The stem volume converted with the SAR inverted heights were compared with the stem volume derived from the ground measurements. For the individual trees measured on ground the stem volume is derived from height and diameter parameter for the 4 selected areas. Whereas, the total stem volume was adapted from 1 ha to 0.64 ha as the areas were smaller then 1ha and the unit for the stem volume is m3/ha in the regression formula. Figure 8.28 shows the relation between the stem volume of the ground measurement versus the derived from the SAR data. The results of area 14 and area15 are quite stable, but the ones of area 01 and area 05 has about 100 m3/ha difference between the two acquisition dates. The reason could be that the regression curve is more sensitive to higher forest.

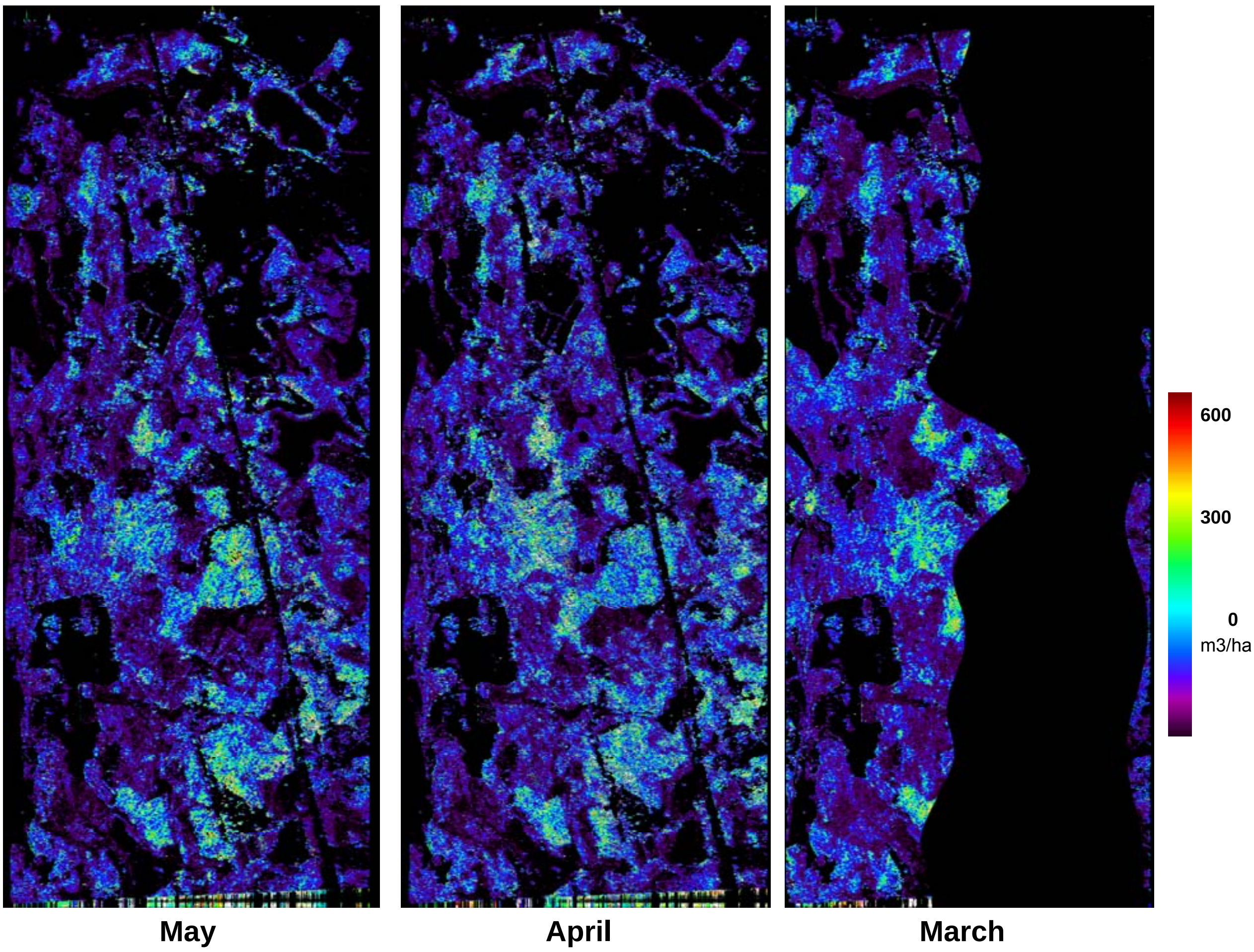

Figure 8.27: The estimated stem volume height maps for whole of images at three different acquisition times. Images are scaled 0 to 600 m3/ha.

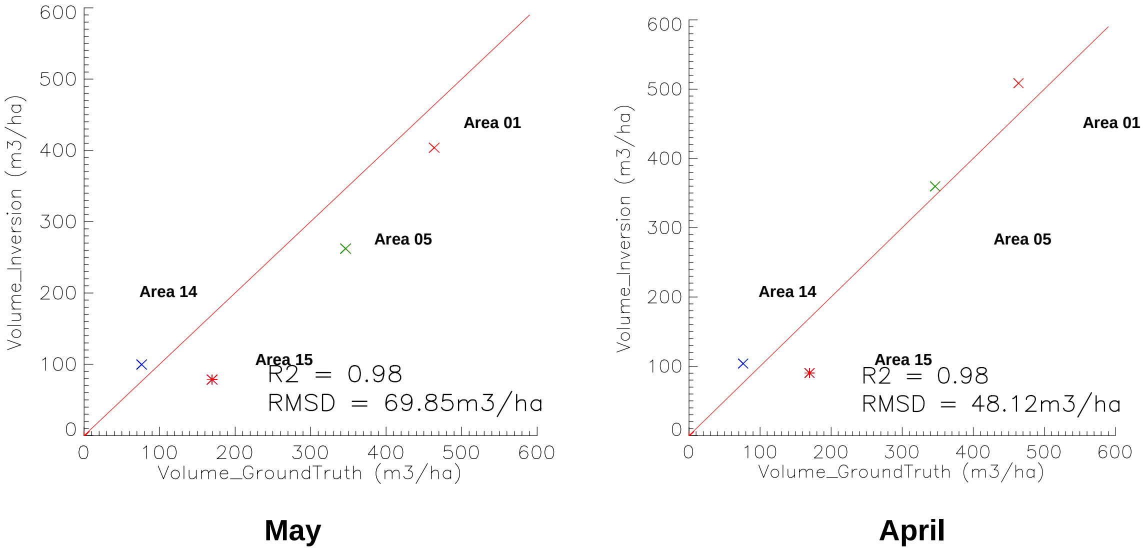

Figure 8.28: The validation of stem volume estimated by ground measurement and inversion height.

Date	May	April
R2	0.98	0.98
RMSD (m3/ha)	69.85	48.12

Table 8.7e: Statistical average values for forest height validation at different acquisition dates. Two statistical parameters are displayed; the Pearson correlation (R^2) and the root mean aquare deviation (RMSD).

7.2.6 Effect of temporal decorrelation

A critical decorrelation source in repeat-pass interferometry is temporal decorrelation. Temporal effects are difficult to quantify and can appear in a more or less stochastic way within one scene. Temporal decorrelation decreases the interferometric coherence and increases the variation of interferometric phase and biases forest height estimates. A seperation of temporal and volume decorrelation is – due to the stochastic nature of temporal disturbance effects – difficult if not impossible [9]. Figure 8.29 is a good example for temporal decorrelation effects in the HH coherence maps with 0m spatial baseline. The repeat-pass acquisitions are affected by wind induced temporal decorrelation. As the result of the temporal decorrelation the coherence level decreases. Histograms of average coherences over the whole scene with temporal decorrelation are plotted in Figure 8.30. The level of temporal decorrelation within the 30 days repeat-pass cycle still keeps a high coherence level (i.e. 0.85 at P-band / 0.65 at L-band). The L-band frequency is more affected by temporal decorrelation as the sensitivity at smaller wavelength is heigher. In case of L-band data with 56 days temporal baseline, the coherence level is very low that almost the whole image might be covered by the non-validity coherence mask.

The inversion for tree heights was done for P-band for 30 days temporal baseline and is shown in Figure 8.31. Comparing to the 0 day temporal baseline the inverted height of 30 days temporal baseline is overestimated and this can be observed mainly in the middle part in Figure 8.31. An inversion by means of Eq. 3 without accounting for temporal decorrelation leads to an overestimation of forest height. The differential height between non temporal decorrelation and temporal decorrelation was estimated (Figure 8.31). It has been observed, that the differential height has about 5 m higher forests heights in near range caused by temporal decorrelation. From near to far range, the differential height gradually increases to about 20 m. This is probably caused by the effective baseline adding temporal decorrelation in the image.

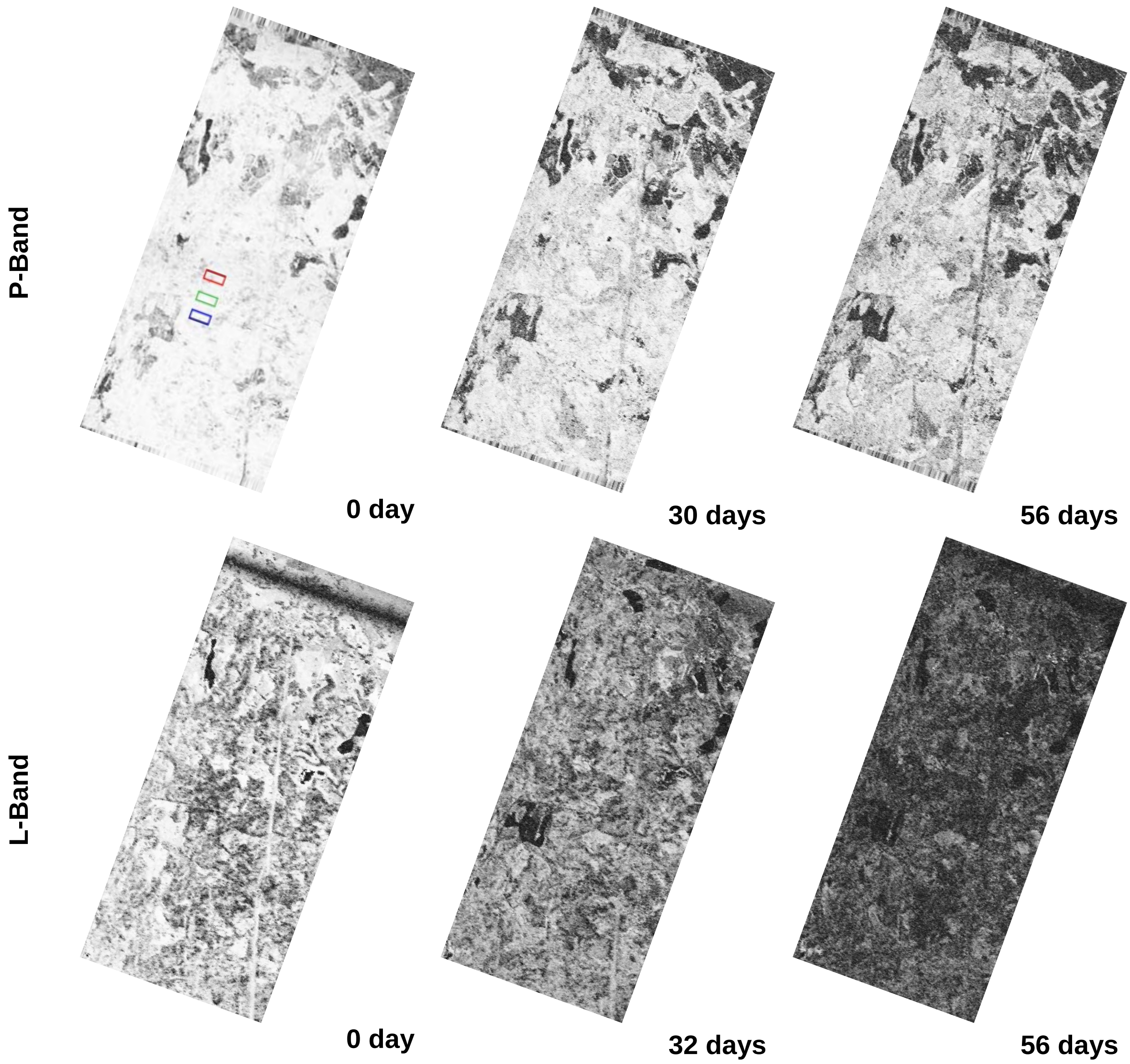

Figure 8.29: Interferometric coherence of HH polarization for three temporal baselines, spatial baselines 0m; from left to right upper part: the coherence maps of 0 day, 30 days and 56 days temporal baselines; the coherence maps of L-band show in lower part.

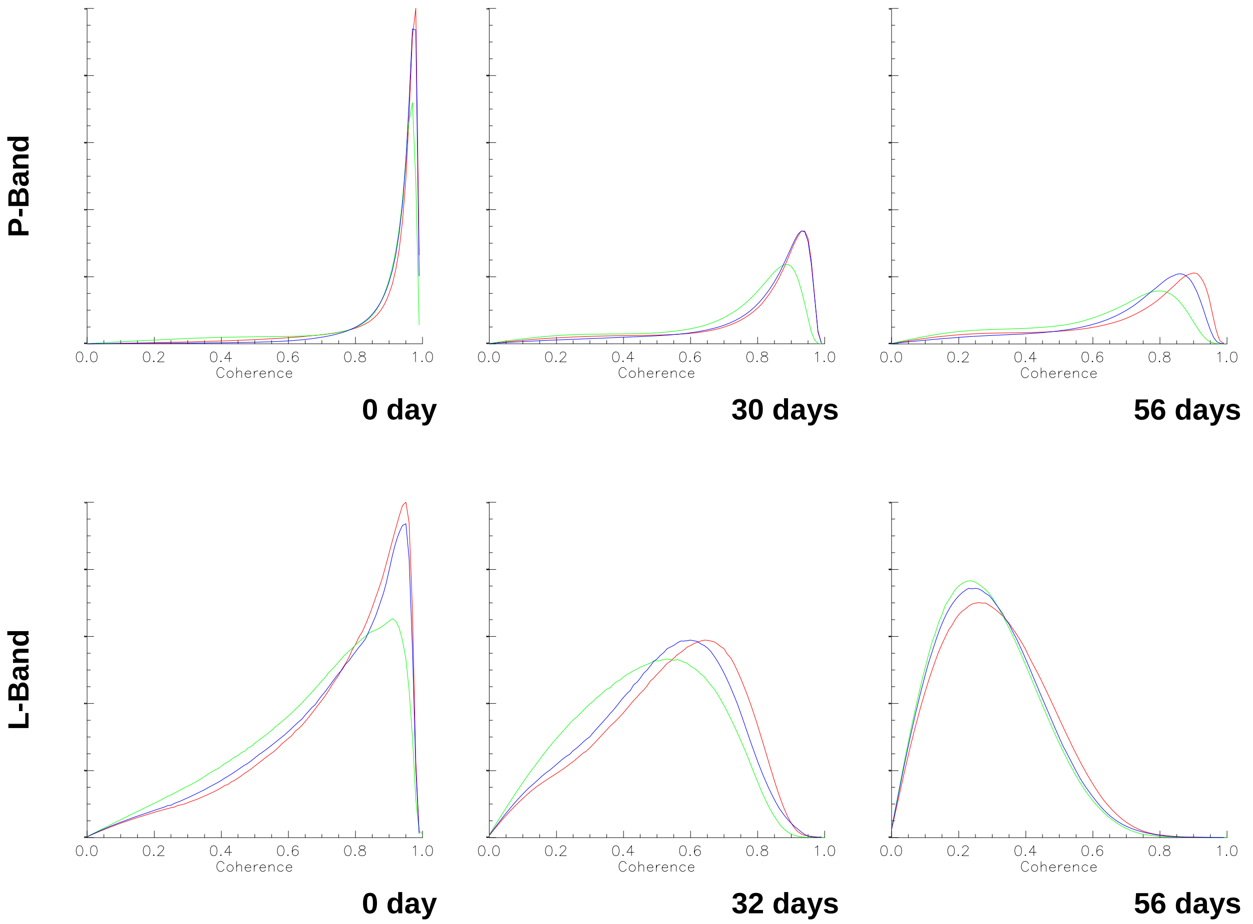

Figure 8.30: Coherence histograms of Figure 8.29 HH coherence is red, HV coherence is green and VV coherence is blue; from left to right upper part; the coherence histograms of 0 day, 30 days and 56 days temporal baselines; the coherence histograms of L-band show in lower part.

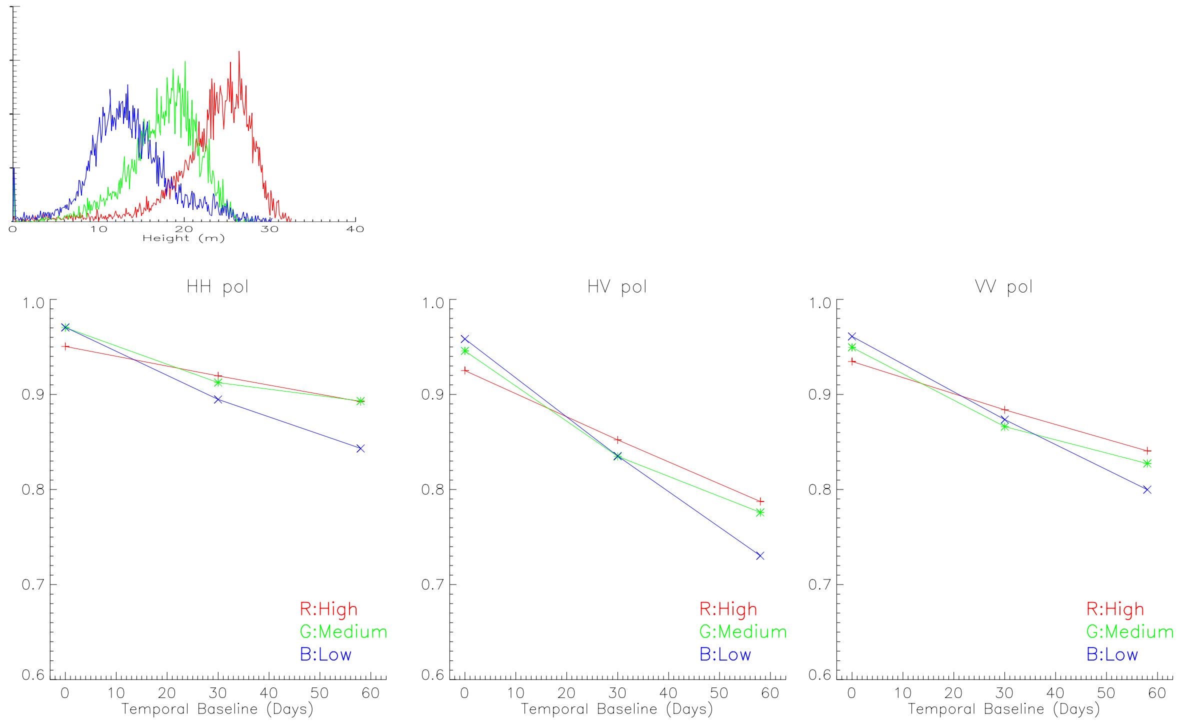

Figure 8.30-1: Upper plot: Histogram of height selected to be even distributed from Lidar (red: high forest heights, green: medium forest heights, blue: low forest heights), Lower plot: Evolution of three forest height categories plotted as interferometric coherences at different polarisations in P-band versus spatial baseline.

In order to estimate the effect of different forest height categoeries on the variation of the interferometric coherence three classes of forest heights were defined and selected using the Lidar data. In the lidar data three areas were selected with the same amount of samples to keep the balance in the statistics. The area selected were then estimated on the interferometric coherence and plotted versus the temporal baselines for different polarisations. The mean height of the three forest height categories is for the low forest around 11m for the medium height forest around 19m and for the high forest around 28m. In summary it can be stated, that the three forest height categories are not differing significantly in the interferometric coherence in the beginning of the time span. The main difference is around 0.2. The highest difference in time is observed for the lowest forest height category at P-band for all polarizations, were the strongest effect is observed at HV polarization. One explanation of this effect can be that for the lowest forest height the change on the soil surface has an important influence. The change in time on the soil surface was strong from a very wet soil surface to a dry soil surface. But the open question is still why in HV polarization the strongest temporal effect on the interferometric coherence can be observed. On this point a deeper analysis of the interferometric coherence is required.

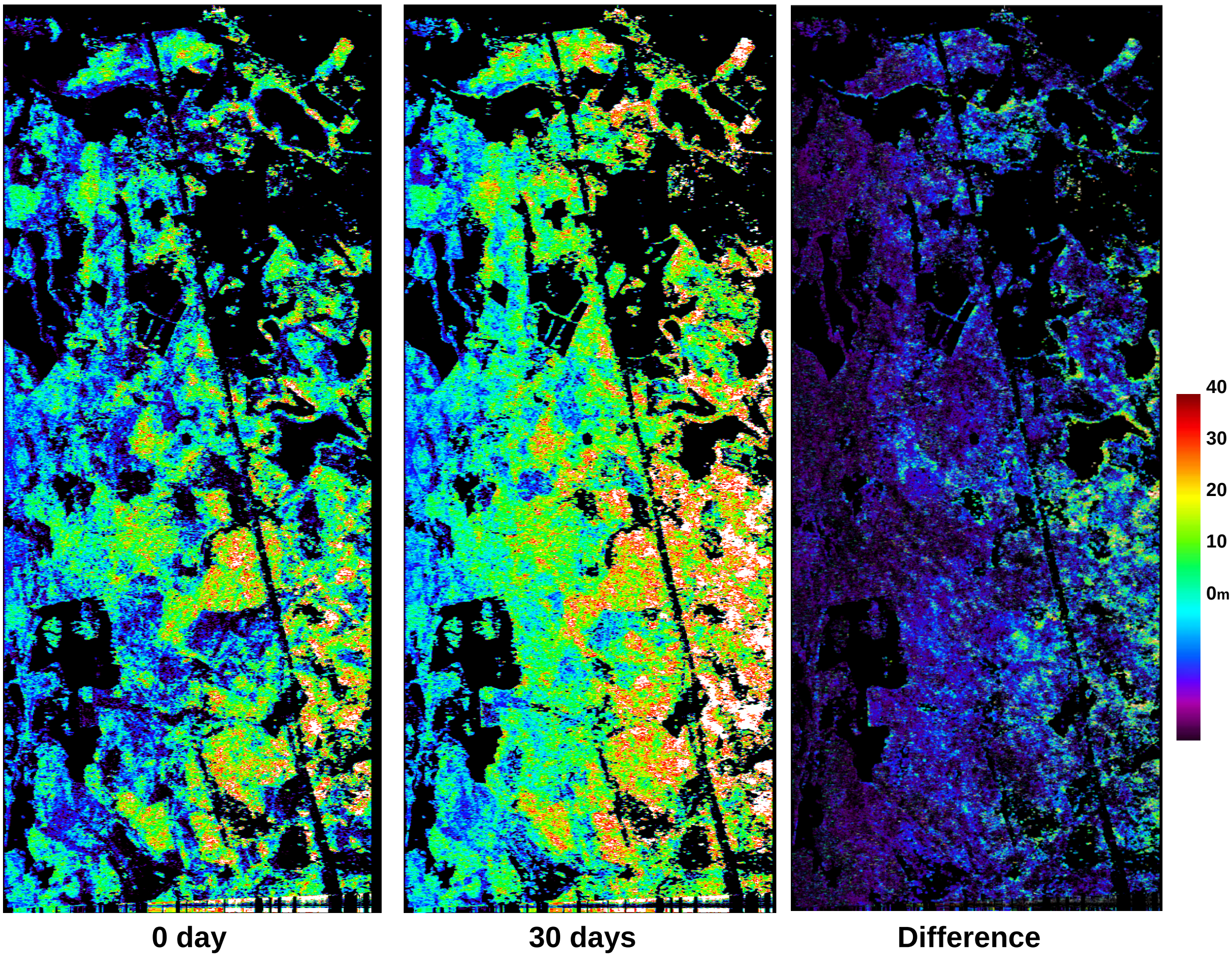

Figure 8.31: Inversion height maps; Left: Height map without temporal decorrelation; Middle: Height map with 1 month temporal decorrelation; Right: Differential image between left image and middle image.

In Figure 8.31-1 a histogram of the derived forest heights from the 0 day versus the 30 days temporal baseline is plotted. In average the 0 day temporal baseline provides of 18 m were the 30 day temporal baseline provides heights of 23 m. The main difference appear in far range and represents around 78 % of the whole pixels.

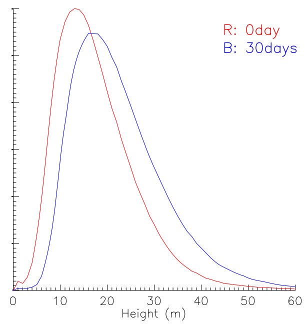

Figure 8.31-1: Histogram of the height distribution for no temporal baseline and for a 30 days baseline

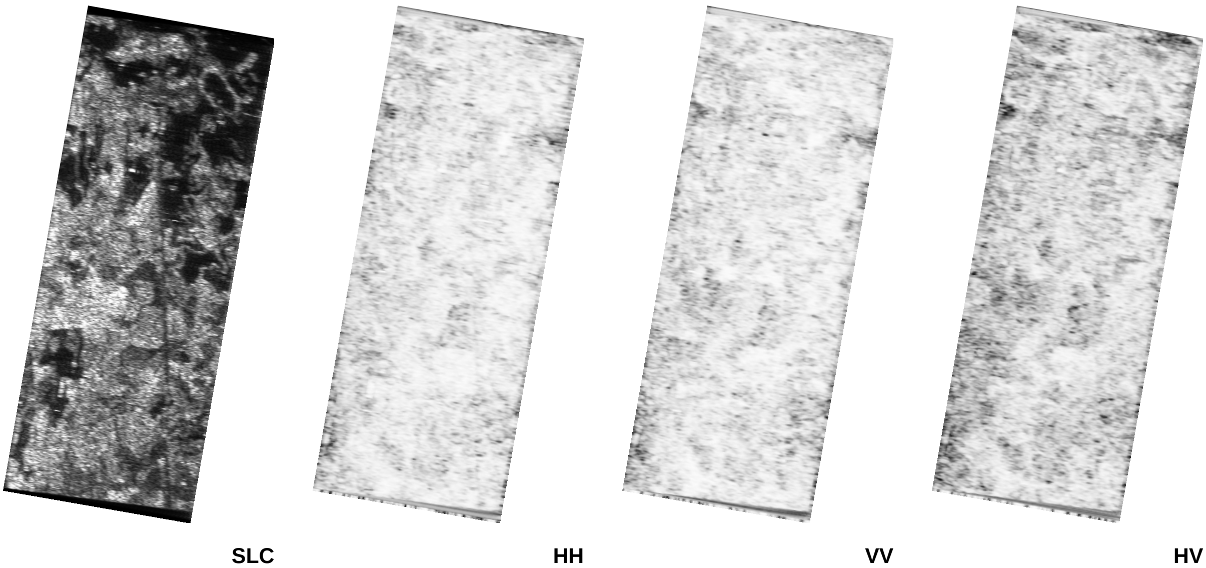

Figure 8.32: 6MHz P-band; Spatial baseline 20m; Left: the amplitude (HH polarization), Next images show HH, VV and HV coherence maps, scaled from 0 to 1.

7.2.7 6 MHz bandwith at P-Band

In this section a comparison of the inversion results from 70 MHz to the 6 MHz bandwith in P-band data are presented. In a first step the 70 MHz P-band data needed to be reduced in bandwidth. In order to reduce it a selection in the spectrum is performed. For this an un-Hamming process is applied to recover the original imge spectrum. From this the 6 MHz bandwidth was selected from the center frequency and then a Hamming is again performed on the selected spectrum.

Figure 8.32 the amplitude (HH) and coherences at different polarisation HH, VV and HV are presented. Comparing with 70 MHz amplitude image in Figure 8.8 (with the same spatial baseline 20 m) the 6 MHz amplitude image has a lower range resolution because the range resolution is proportional to the bandwidth. The effective bandwidth reduction is leading to higher range spectral decorrelation and critical baseline decrease. After a range filtering [11], the high coherence was obtained as high as 70 MHz coherence. The 6 MHz inversion results show similar level of forest height. The 6 MHz forest height was in detail investigated by polygons as used for the LIDAR validation (Figure 8.23). High correlation between the both inversion heights could be obtained as shown in Figure 8.34. There is only a small oversteimation of the height observed that can result from the low range resolution.

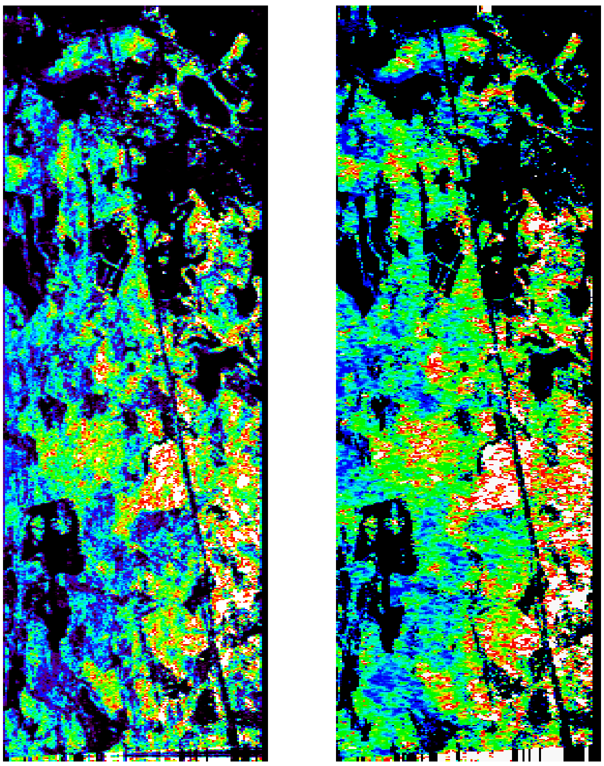

Figure 8.33: 70 MHz and 6 MHz P-band forest height maps for Remningstrop forest, scaled from 0 to 40m; Left: 70MHz inversion height; Right: 6MHz inversion height.

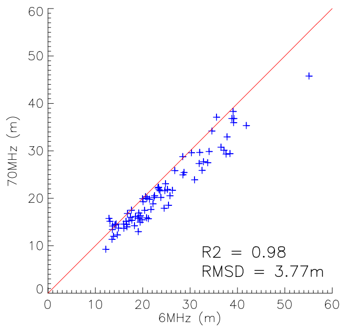

70MHz vs 6MHz

Figure 8.34: The comparison between 6MHz inversion height 70MHz inversion height. Left: the mean value of 6 and 70MHz in stands; Middle: the standard deviation of 6MHz height; Right: the standard deviation of 6MHz height

7.2.8 Summary and discussion

During the campaign, the data have been abundantly acquired by L- and P-band on various spatial and temporal baselines, and besides, LIDAR data and ground measurements have been obtained. In addition 6 MHz P-band data could be generated from the original P-band data. The following statements can be made based on the obtained results:

- **Pol-InSAR inversion:** Temporal decorrelation was present at both frequencies even for repeat-pass time interval on the order of minutes (BioSAR's smallest temporal baseline: 15 min); Uncompensated temporal decorrelation introduces a height bias. The decorrelation can be minimized by increasing baseline on the cost of lower coherence level (due to an increased volume decorrelation). Generally, the P-band estimates are a few meters lower than the inversion height at L -band. This is probably caused by the sensitivity of frequency. P-band is less sensitive to the top vegetation layer than L-band and L-band is more affected by several decorrelation effects (e.g. temporal decorrelation) which introduce a bias resulting in overestimated heights.
- **Validation:** The detail validation against the LIDAR data was investigated. H_{100} was estimated from LIDAR height. The results have very high correlation level. However, there are two biases; overestimation in higher forest and underestimation in lower forest. The overestimation can be interpreted by the H_{100} . The H_{100} represents the 100 highest trees per ha and therefore the highest vegetation layer. On the other hand, P-band has a higher penetration capability through vegetation layers than L-band. This leads to underestimation in higher forest area. The reason of overestimation can be different from the one of underestimation. In RVoG model, the lower forest estimates have more height errors. This can probably make inversion height in lower forest overestimated.The other validation was investigated by ground measurements in 11 stands. Also, H_{100} of each stand was used and

correlated to inversion height. Comparing simple mean height, H_{100} improved fairly the correlation level in forest area where two species have a same population and completely different height level. The results of th comparison of the heights in 20 by 50 m sample plots are less stable than the one in 80 by 80m depending on the acquisition date. The 20m by 50m sample plots are less roubst in a statistical sense as the amount of valid coherence regions were too small. This is the reason that 20 by 50m sample plot were excluded for stem volume estimates.

- **Biomass**: With the regression formula of the Remningstrop forest, the inversion height was converted to stem volume. The stem volume for the whole image was estimated and validated with ground measurement. Higher forest areas had larger variation of the biomass depending on the acquisition date. It can be explained that the regression curve is more sensitive to higher forest. Because a small variation of height in higher forest causes larger variation of the stem volume.
- **Temporal decorrelation**: The level of temporal decorrelation with the 30 days repeat-pass cycle of BioSAR makes a height inversion still feasible. Especially, the coherence included 30 days kept high coherence level (0.85 at P-band / 0.65 at L-band). As expected, L-band was more affect by temporal decorrelation. The temporal decorrelation makes inversion height about 5m higher in near range. Overestimated height steadly increases to about 20m in far range. This can be interpreted by the effective baseline. Small baseline adding 30 days temporal decorrelation introduced higher height bias in far range.
- **6MHz P-band**: We showed the possibility to estimate forest height with 6 MHz data on P-band over boreal forest site. In spite of reduced bandwidth, 6 MHz data still kept the high coherence level in forest and successfully estimated forest height as 70 MHz data. The comparison between 6 MHz and 70 MHz inversion hight shows Pol-InSAR forest inversion at 6 MHz data is also robust and matured enough to provide consistent results.

7.2.9 Reference

[1] Shane, R. C. Papathanassiou, K. P. “Polarimetric SAR Interferometry”, IEEE Transactions on Geoscience and Remote Sensing, VOL. 36, NO. 5, September 1998, pp. 1551 – 1565

[2] Papathanassiou, K.,& Cloude, S.; ”Single Baseline Polarimetric SAR Interferometry”; IEEE Transactions on Geosccience and Remote Sensing, 2001, vol. 39, no. 11, pp. 2352-2363

[3] Cloude, S.R. Papathanassiou, K.P. “A 3-Stage Inverion Process for Polarimetric SAR Interferometry” IEE Proceedings Radar Sonar & Navigation, vol 150, issue 3, 2003

[4] Bamler, R. & Hartl, P. “Synthetic Aperture Radar Interferometry“, Inverse Problems, vol. 14, pp. R1-R54, 1998.; IEEE Transactions on Geosccience and Remote Sensing, 1994, vol. 32, no. 4, pp.855-865

[5] Hajnsek, I. Papathanassiou, K.P. Cloude, S.R. “Removal of Additive Noise in Polarimetric Eigenvalue Processing”, Proceedings IGARSS’01, Sydney Australia, 2001

[6] Gatelli, F. Guarnierni, A.M. Parizzi, F. Pasquali, P. Prati, C. Rocca, F. “The Wavenumber Shift in SAR Interferometry”,

[7] Just D. Bamler, R. “Phase Statistics of Interferograms with Applications to Synthetic Aperture Radar”, Applied Optics, Vol.33, Nr.20, S. 4361-4368, Juli 1994.

[8] Mette, T., Papathanassiou, K & Hajnsek, I., 'Biomass estimation from polarimetric SAR interferometry over heterogenous forest terrain', Proc. IGARSS04, 20.-24. Sept. 2004, Anchorage, vol. I ,pp. 511-514

[9] Technical note by Jan Askne "An allometric relation between forest height and stem volume for area in Sweden and remote sensing applications" July 2007.

[10] Kugler, F. Papathanssiou, K.. Hajnsek, I. Hoekman, D. "Forest Height Estimation in Tropical Rain Forest using Pol-InSAR Techniques", Proc. IGARSS06, Denver, 31.7-4.8.2006

[11] Reigber, A "Range Dependent Spectral Filtering to Minimize the Baseline Decorrelation in Airborne SAR interferometry" Proc. IGARSS99, 28.6-2.7.1999, Hamburg, vol 3, pp. 1721-1723

7.3 Assessment of Multi-InSAR and Tomographic Observation by POLIMI

7.3.1 Work objectives

The work addresses the preliminary development of techniques able to efficiently exploit the multibaseline information content of SAR data that will be produced by incoming new P-band satellites or satellite formations, to provide 3D imaging capabilities and range resolution enhancement. The work has been carried out with reference to airborne P-band data from DLR, constituting an emulation of the spaceborne case. In particular, the following points have been addressed:

1. 3D tomography of the scene basing on a two layered model constituted by the ground and the canopy layers and evaluation of the backscattered powers from each layer.
2. Range resolution enhancement on the corner reflectors through band synthesis.
3. Range resolution enhancement on selected areas through statistical layer cancellation and band synthesis.
4. Separation between ground and ground-trunk contributions through analysis of the co-polar information.
5. 3D tomography through adaptive spectral estimation techniques, see Appendix.
6. Coherent layer cancellation, see Appendix.

Points 5 and 6 have been covered by Fabrizio Lombardini and Matteo Pardini from the University of Pisa.

7.3.2 Description of the data

The data available for WP-43 is represented by a set of single look complex (SLC) SAR images from 9 tracks for each polarimetric channel. The images have been motion compensated, co-registered, and phase-locked to a reference point by DLR, according to the standard processing used for Pol-InSAR too. Along with the SLC data, also the coefficients for height to phase conversion and the reference phases corresponding to flat terrain have been provided. The acquisition campaign has been carried out during the spring time (March until May). The parameters of the acquisition system are briefly summarized in Table 8.8:

Carrier Frequency	f_0	350 [MHz]
Carrier Wavelength	λ	0.86 [m]
Sampling Frequency	f_S	100 [MHz]
Slant Range Pixel Spacing	*dr*	1.5 [m]
Azimuth Pixel Spacing	*da*	0.74 [m]
Horizontal Baseline Span	*A*	80 [m]
Look Angle	θ	25° (Near Range) – 55° (Far Range)
Flight Height	*H*	3900 [m]

Table 8.8: Parameters of the E-SAR acquisition system.

The data has been delivered to Polimi on September 17th, 2007. Figure (8.35) shows an optical image of the scene extracted from Google Earth and projected onto SAR slant range, azimuth coordinates.

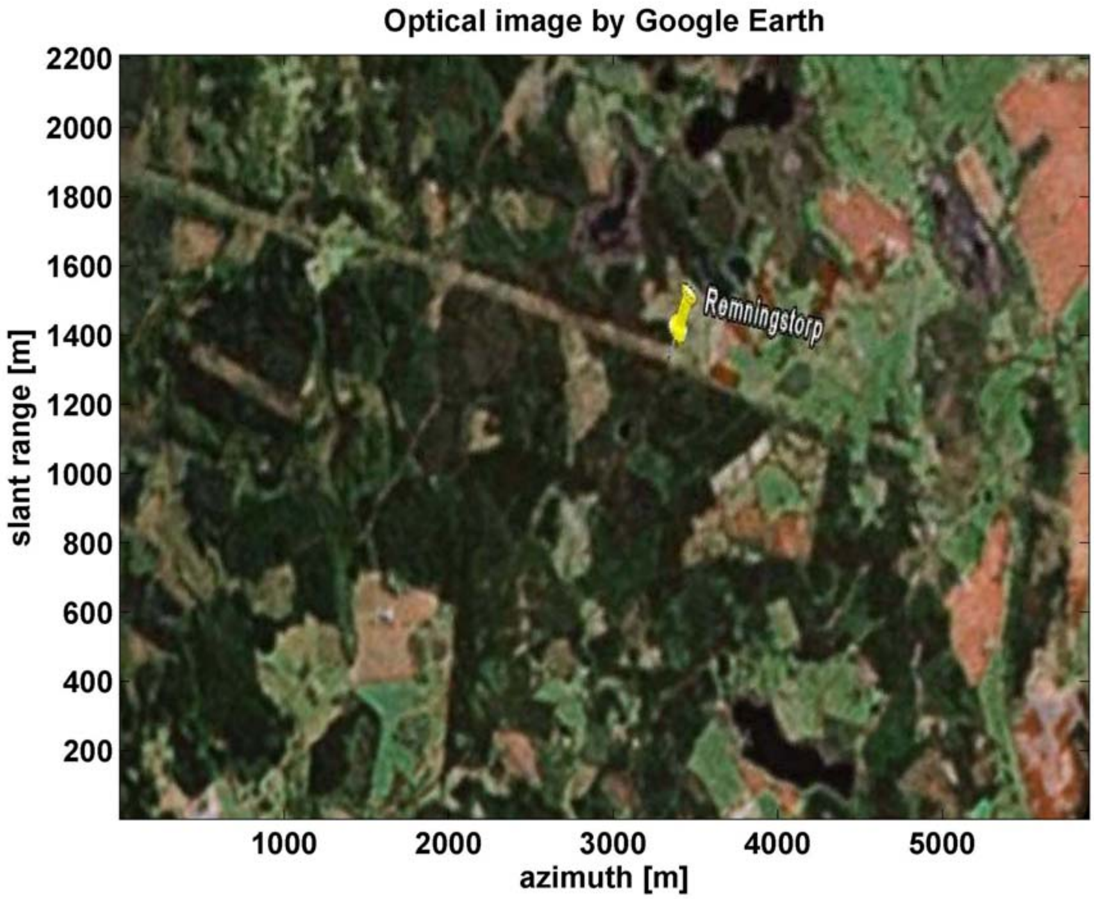

Figure 8.35: Optical image by Google Earth, projected onto the SAR slant range, azimuth coordinates

7.3.3 Pulse bandwidth reduction

In order to emulate the features of the future BIOSAR system, the data has been filtered in the slant range direction in such a way as to reduce the pulse bandwidth to 6 MHz, keeping a central frequency of 350 MHz. The filter design was performed through Least-Squares techniques, resulting in an attenuation of 50 dB at ± 10 MHz from the central frequency and no phase distortion in the 6 MHz bandwidth. The filter impulse response and transfer function are shown in Fig. (8.36). The power spectra of the data before and after filtering are shown in Fig. (8.37).

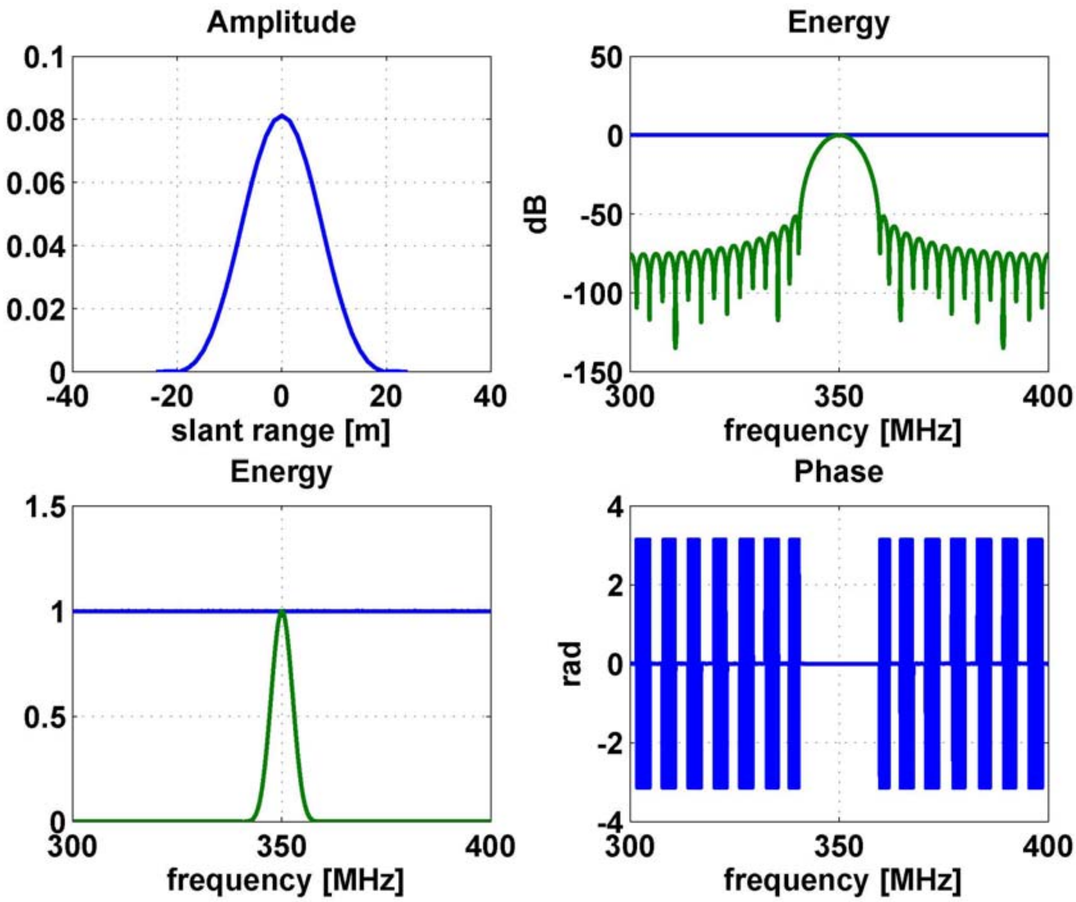

Figure 8.36: Filter design. Top left: impulse response. Top right: power spectrum in dB. Bottom left: power spectrum. Bottom right: phase

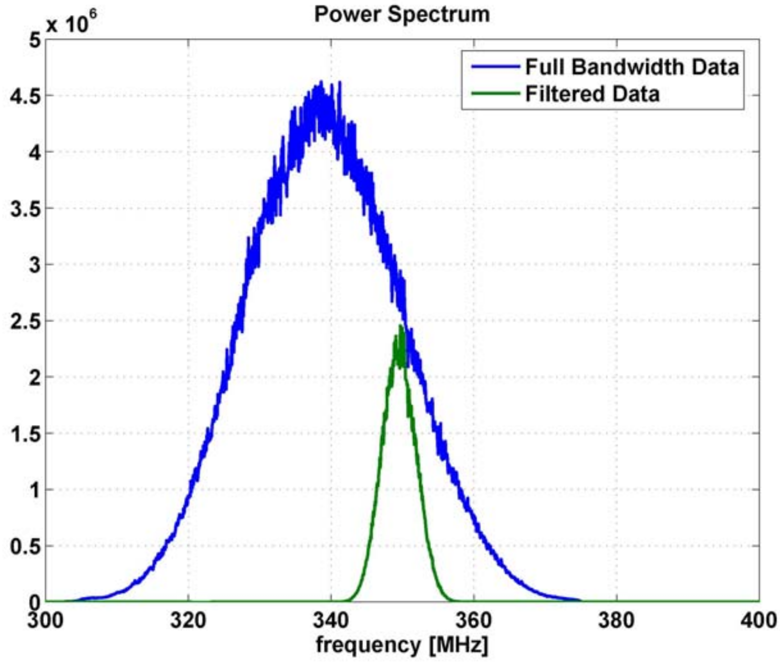

Figure 8.37: Slant range Power Spectra of the original full bandwidth data and of the filtered data

7.3.4 Scene Analysis and Calibration

This section is devoted to providing an analysis of the imaged scene as for amplitude and phase stability features.

7.3.4.1 Corner Reflectors

Two of the three trihedral reflectors used by DLR for validation were included in the portion of the scene imaged by the data available to Polimi. These reflectors may be identified in both the full bandwidth and the 6 MHz data basing on their shape and backscattered power, see Fig. (8.38, 8.39).

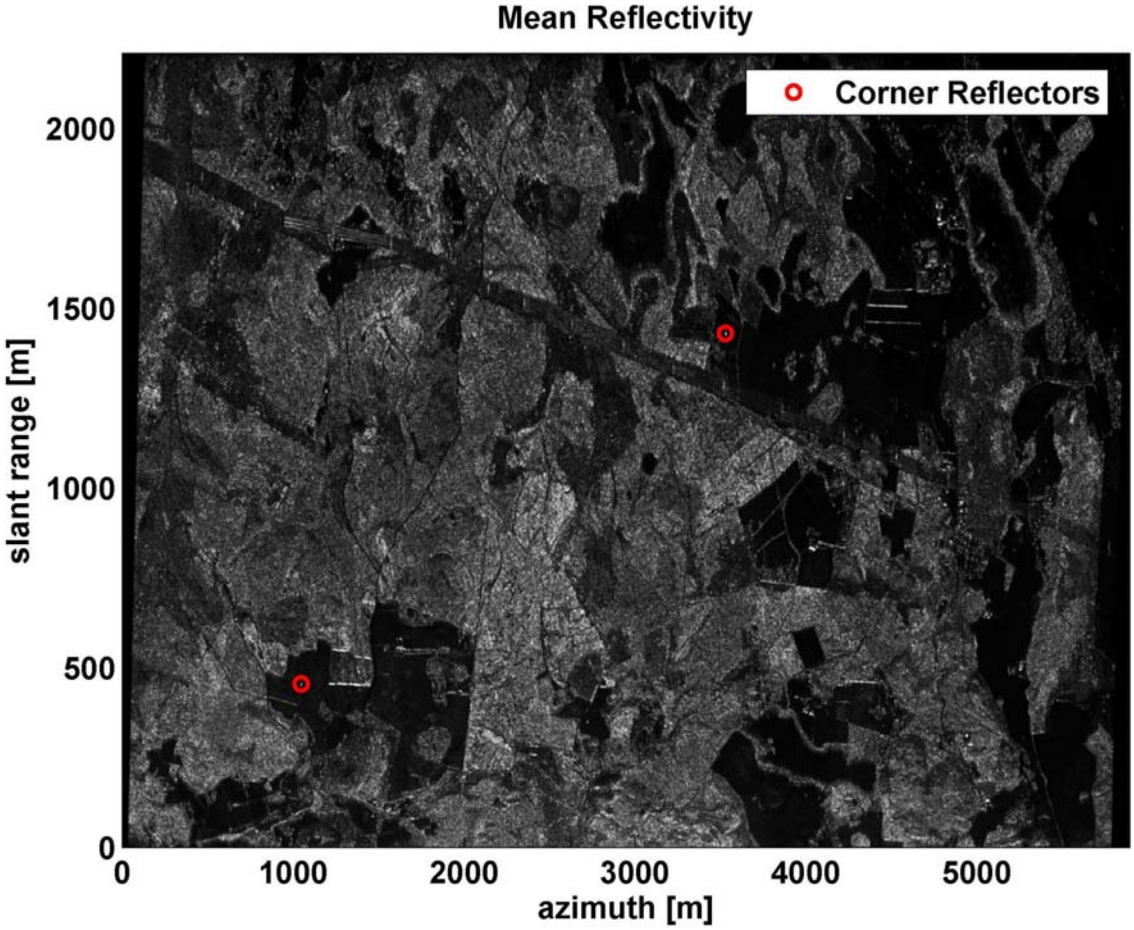

Figure 8.38 : Incoherent mean of the full bandwidth acquisitions and position of the corner reflectors, channel HH.

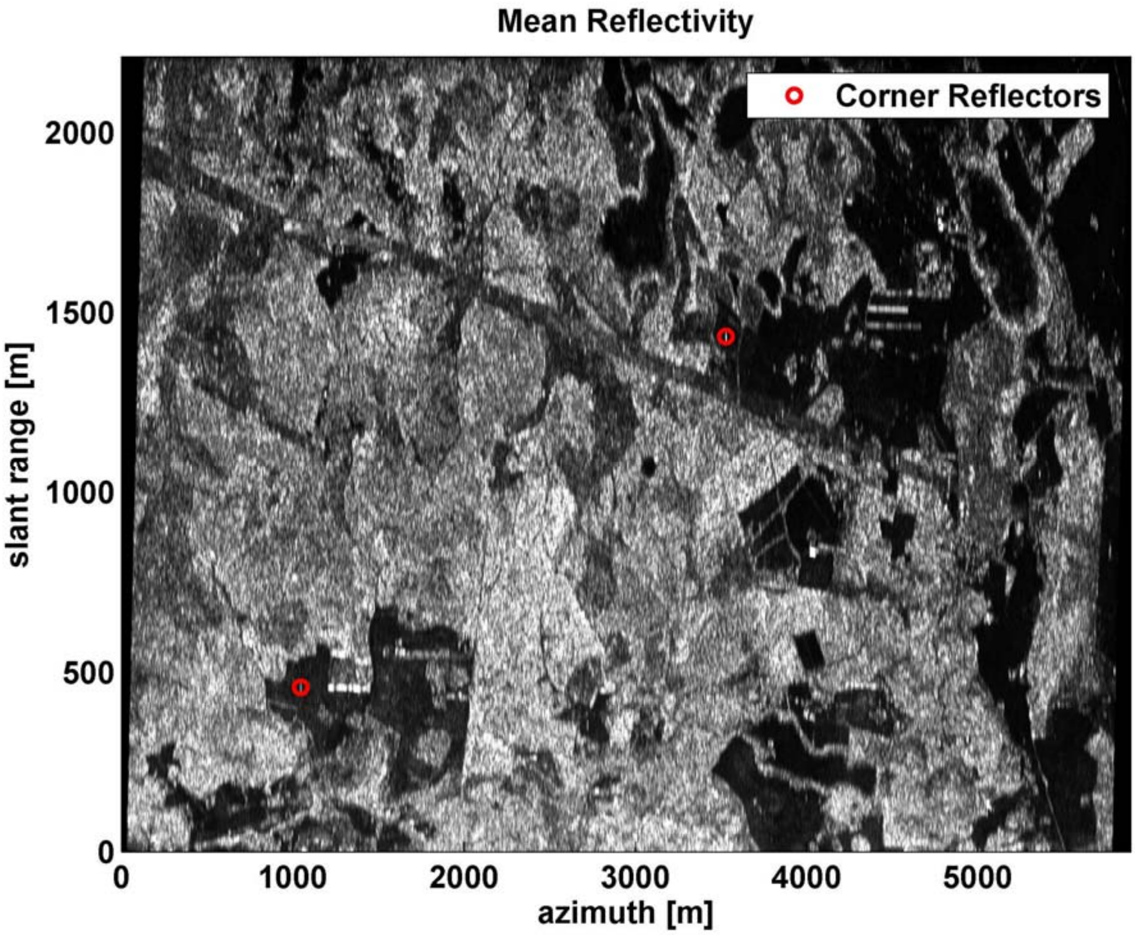

Figure 8.39: Incoherent mean of the 6 MHz acquisitions and position of the corner reflectors, channel HH.

7.3.4.2 Phase Stability

Phase stability is a crucial issue for performing tomographic analysis through radar measurements. Uncompensated phase terms other than those due target position impact on the data as a multiplicative noise. Techniques to estimate a target's position basing on its phase history, such as SAR interferometry, are very sensitive to multiplicative noise [1], [2], [3], and thus require a proper phase calibration step, as usually done in spaceborne applications [4], [5]. SAR tomography, which attempts to identify more than one target within the system resolution cell, is even more sensitive to this kind of disturbances.

An analysis of the phase histories of the corner reflectors shows a significant discrepancy with respect to the expected linear trend, see Fig. (8.39). To evaluate the amount of the phase disturbance, we estimated the corner elevation basing on its phase history, and measured the phase disturbance as:

$$\sigma = \frac{1}{8}\sqrt{\sum_n \left(k_z(n)\hat{h} - \varphi_n\right)^2}$$

Eq. 1

where φ_n is the phase of the corner in the n-th image, after compensating for the flat terrain, $k_z(n)$ is the coefficient for the height to phase conversion in the n-th image, and $\hat{h}$ is the estimated corner elevation. As a result, we obtained σ = 0.84 rad for the far range corner and σ = 0.98 rad for the near range corner. The phase disturbances in the phase histories of the two corners appear to be highly correlated but not identical. The standard deviation of their difference may be assessed in σ = 0.22 rad. These measurements are relative to the HH channel. Analogous results may be obtained from the VV channel.

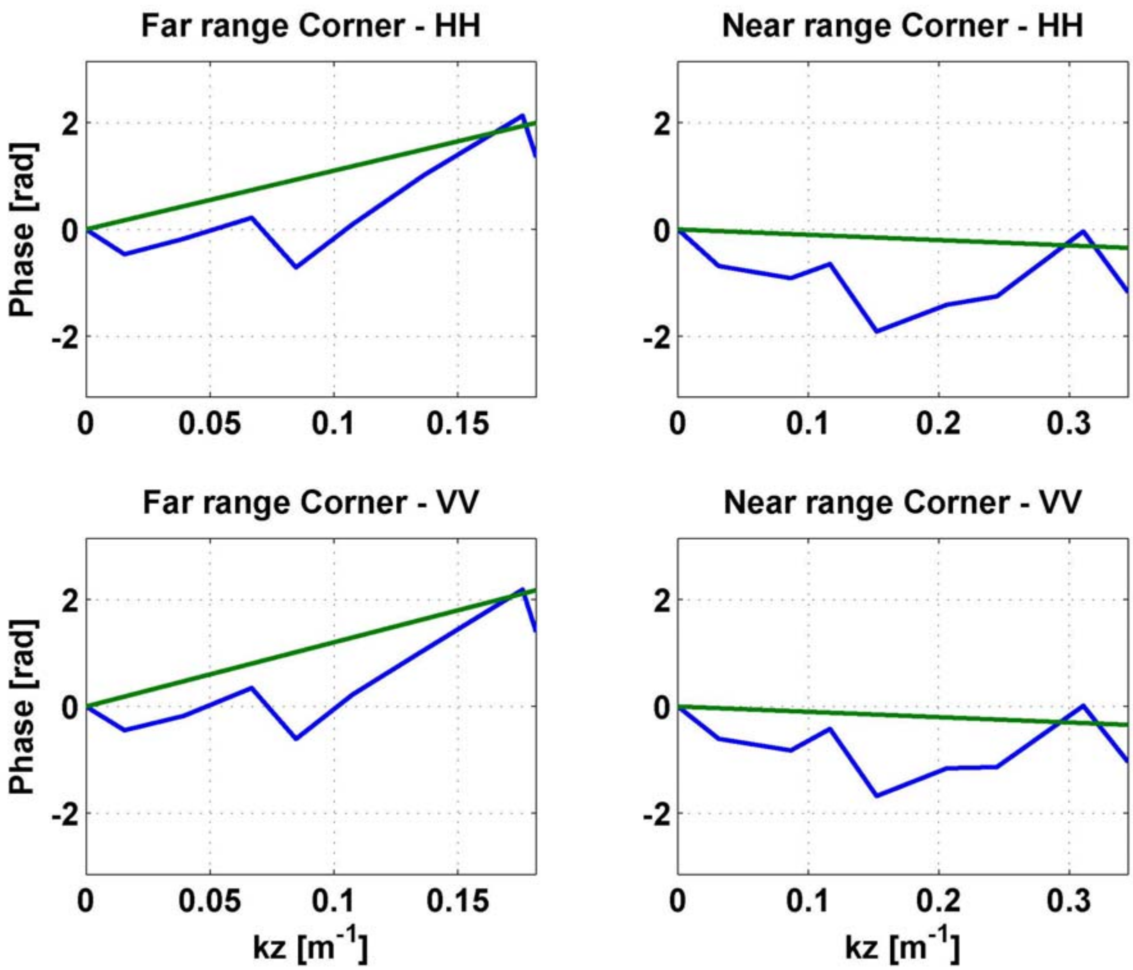

Figure 8.39: Phase histories of the corner reflectors in the HH and VV channels (blue lines) and estimated linear trends (green line).

The effect of phase disturbances is also visible in the power spectra of the data with respect to target elevation, obtained by Fourier transforming the multibaseline SLC data with respect to the normal baselines. Figure (8.40) reports the power spectra of the HH channel obtained by computing the power spectra along four slant range lines within an estimation windows as wide as 50×50 square meters (ground-range, azimuth). In three of the four panels a periodic pattern is clearly visible in correspondence of the road cutting the whole image, see Fig. (8.41). This phenomenon is likely to be due to the presence of a power line passing all over the road. The main issue with these power spectra, however, is the presence of significant sidelobes, visible in all the four panels. The impact of the phase disturbances appears to be very similar in the four panels, confirming the idea that it is highly spatial correlated. Furthermore, similar results may be found analyzing the power spectra of the VV channel.

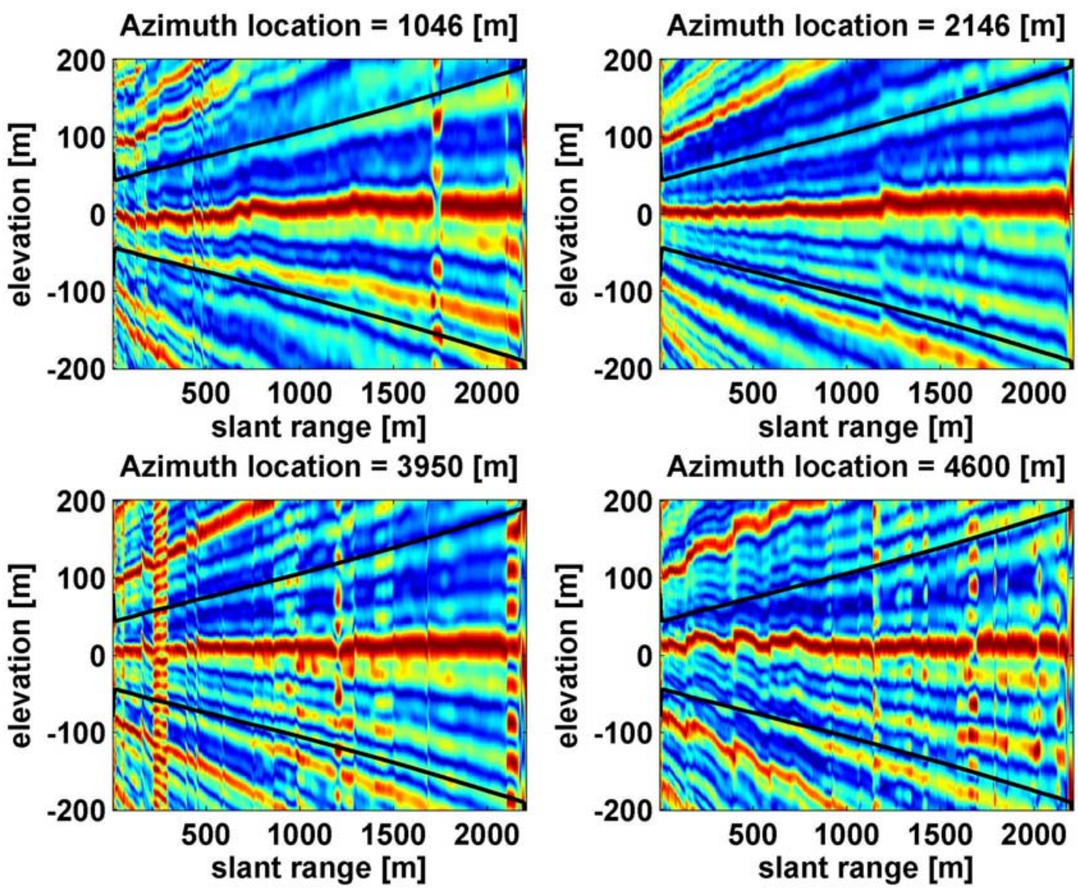

Figure 8.40: Power spectra with respect to normal baselines corresponding to four slant range lines. The black lines denote the elevation corresponding to the Nyquist frequency. For each range bin, the power spectrum maximum has been normalized to one

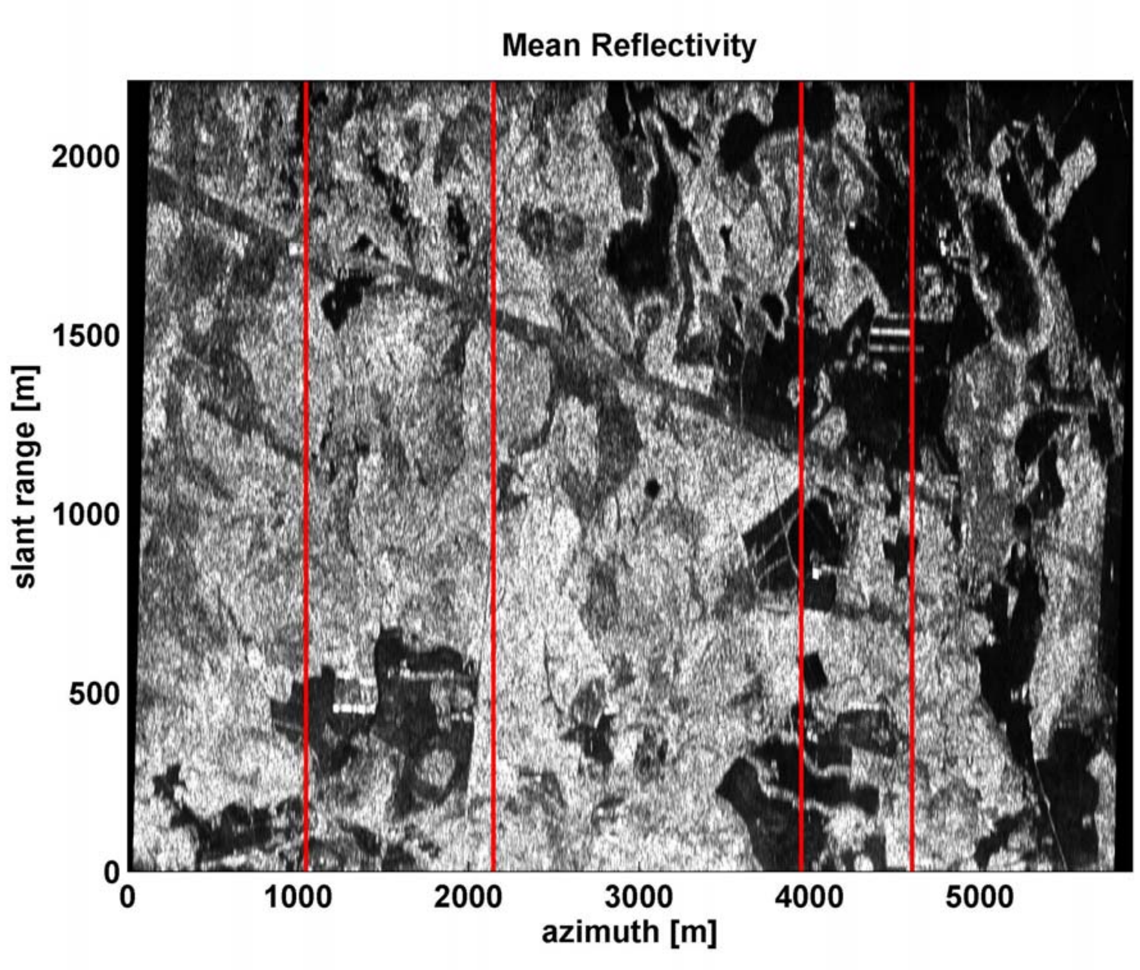

Figure 8.41: Incoherent mean of the 6 MHz acquisitions, channel HH. The slant range lines analyzed in Fig. (7) are shown in red

7.3.4.3 Amplitude Stability

An analysis of the amplitude stability of the data has been performed by computing the ratio μ/σ, where μ and σ are the mean and the standard deviation of the SLC data amplitudes [5]. Figure (8.42) shows the histogram of the ratios μ/σ obtained for the HH channel. The presence of very high values of this index - in spaceborne applications, a point may be regarded as a Permanent Scatterers (PS) for μ/σ >4 [5] - indicates that backscattered signal in the HH channel is mainly determined by highly stable scatterers. The selection of a suitable set of points may proceed on the basis of the index value and the spatial distribution of the points. Figure (8.43) shows the result of the point selection obtained by looking for points for which μ/σ >10 and imposing an average distance of 100 meters from a selected point to another.

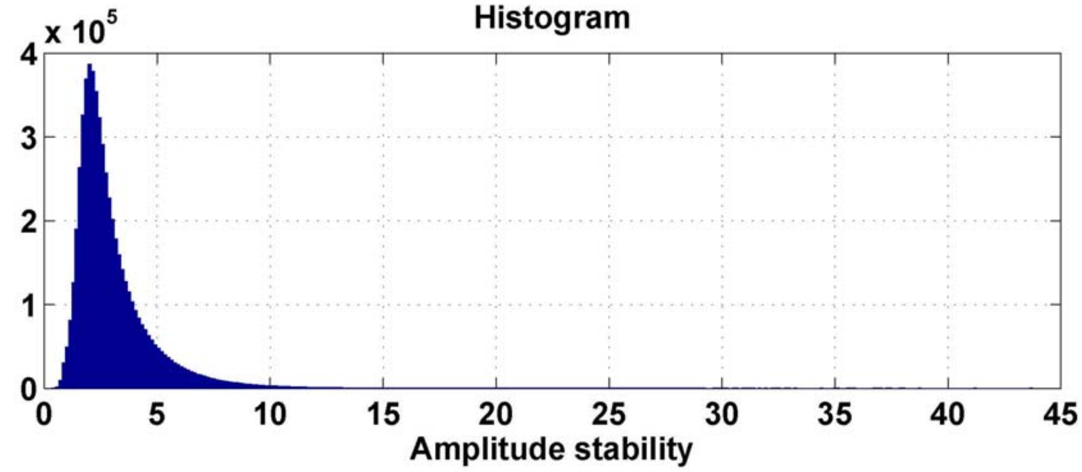

Figure 8.42: Histogram of the ratios μ/σ computed for the HH channel.

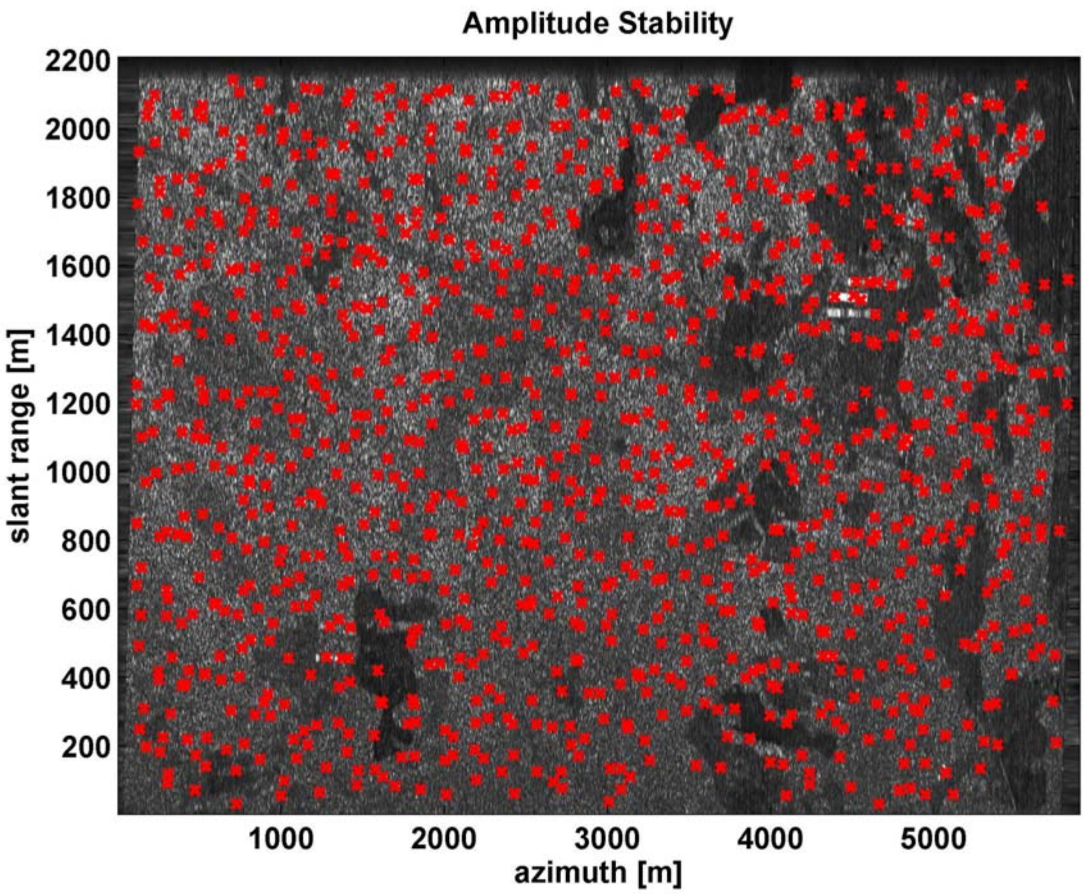

Figure 8.43 Amplitude stability map of the HH channel. The red crossed indicate points for which μ/σ >10

Comparing Fig. (8.43) to Fig. (8.35, 8.38, 8.39) it is easy to see that the selected points correspond to forested areas or to isolated peaks in bald areas, indicating that they are likely to be regarded as double bounce contributions resulting from the ground - trunk interaction. Similar results may be found analyzing the VV channel.

7.3.4.4 Phase Calibration

Basing on the analysis in section 8.3.4.3, the phase disturbance is to be regarded as a stochastic process, highly correlated in space and almost identical in the HH and VV channels. These features seem to confirm the idea that it is the result of uncompensated propagation terms. The results from the analysis of amplitude stability suggest that an effective phase calibration may be obtained by exploiting the phase histories of the selected points. To this aim, we estimated the elevation of each point and then proceeded to a further point selection basing on phase stability [5], see Figure 8.44 .

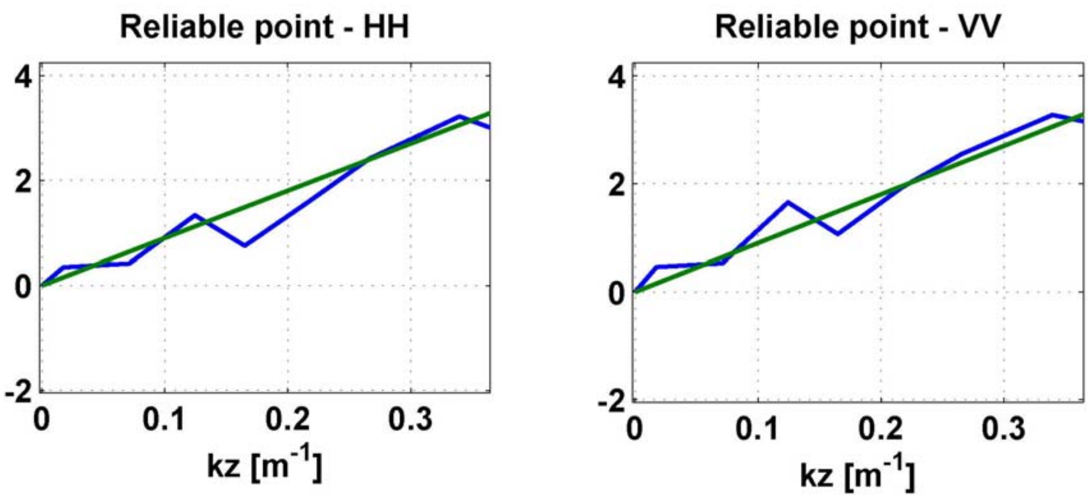

Figure 8.44: Phase histories of a selected reliable point (blue line) and estimated linear trend (green line). The variance of the phase disturbance, computed according to Eq. 1, is =0.32 rad.

As a result, almost one half of the points previously selected has been discarded. It is interesting to note that the near range corner, which also showed a significant amplitude variation throughout the 9 acquisitions, has been discarded. At this point, the phase differences between the phase of the selected points and the estimated linear trend is to be interpreted as an estimate of the phase disturbance. Hence, after an interpolation step, it is possible to remove the phase disturbance from the whole stack of acquisitions. The benefit deriving from this operation is visible in Fig. (8.45).

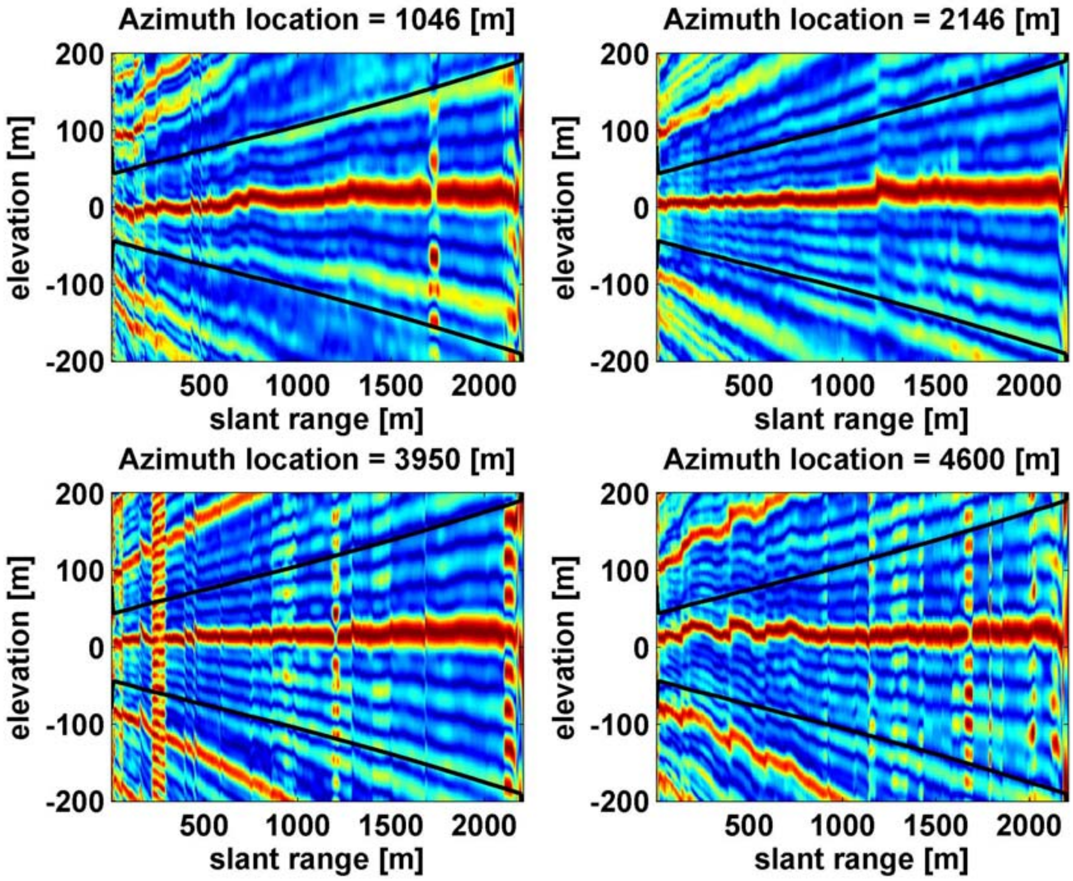

Figure 8.45: Power spectra of the HH channel with respect to normal baselines corresponding to four slant range lines. Phase calibration is performed according to section 8.3.4.4. The black lines denote the elevation corresponding to the Nyquist frequency

7.3.4.5 Co-polar analysis

The hypothesis that ground - trunk interactions are dominant in the co-polar channels is enforced by an analysis of the co-polar interferograms (HH-VV). According to [6], odd bounces metallic reflectors, such as mirrors and trihedrals, determine a null phase value in the co-polar interferogram, whereas even bounce metallic reflectors, such as dihedrals, determine a phase of 180°. Considering the double bounce contributions from ground - trunk interactions, one must account for a reduction in the phase of the co-polar interferogram from the theoretical value, due to the electromagnetic features of the ground - trunk ensemble [7]. The average co-polar interferogram, obtained by averaging the 9 co-polar interferograms corresponding to each track, is shown in Fig. (8.46).

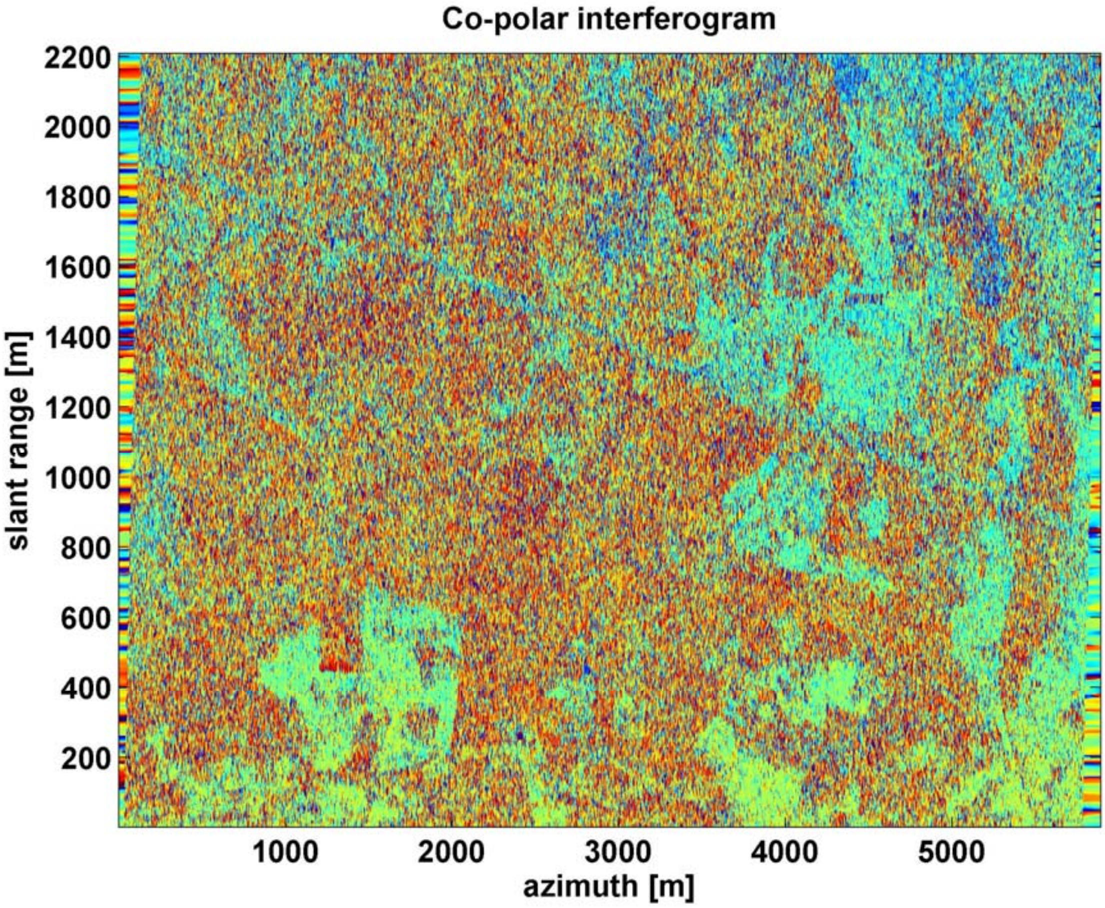

Figure 8.46: Co-polar interferogram phase. The color axis corresponds to the phase interval (-π, π).

Comparing Fig. (8.46) to Fig. (8.35, 8.38, 8.39) it is easy to see the strong correlation between the spatial distribution of high co-polar phase values and forested areas. We interpret this result as a further confirmation that the forested areas contribution to co-polar channels is essentially given by ground - trunk interactions [8].

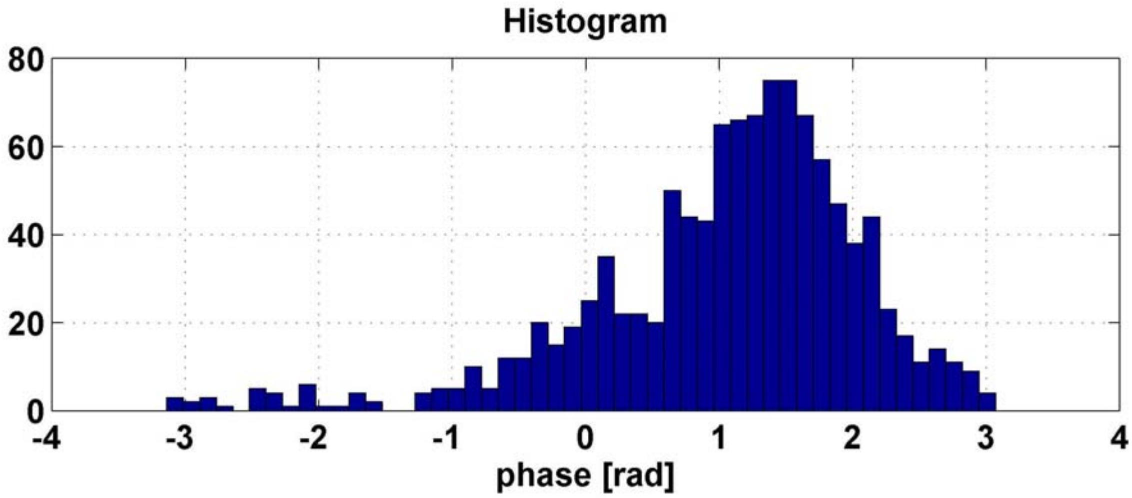

Figure 8.47: Histogram of the co-polar phases of the selected points.

Figure 8.47 shows the histogram of the co-polar phases read in correspondence to the points selected according to section 8.3.4.3. The peak of the histogram corresponds to about 80°.

7.3.5 Band synthesis

This section presents the algorithms for performing band synthesis and statistical layer cancellation. Firstly, we face the problem of band synthesis under the hypothesis of a single layered scene, providing a solution suitable for obtaining a super-resolution estimate of the reflectivity of the co-polar channels, including the case of corner reflectors. Then, we extend the algorithm to a two layered scene, and propose a solution suitable for performing band synthesis on the HV channel.

7.3.5.1 Band Synthesis as an Inverse Problem

The concept of slant range resolution enhancement is directly related to that of spectral shift. Under the assumption that the reflectors lie on a surface (i.e.: the scene is to be modelled as a single thin layer), it is possible to show that each acquisition senses a different portion of the slant range spectrum of the complex reflectivity of the scene, depending on the surface slope and the normal baselines. Therefore, it is possible to combine the available acquisition in order to produce a wide band version of the reflectivity spectrum [9], [10], [11]. Basing on this concept, this operation may be referred to as band synthesis.

The effectiveness of band synthesis depends mainly on the maximum spectral shift among the acquisitions, and hence on the normal baseline span. With reference to the parameters in table (1) and under the hypothesis of flat terrain, the maximum spectral shift may be assessed in 2 MHz to12 MHz, depending on the slant range location, see Fig. 8.48. The maximum theoretical synthesizable bandwidth is obtained as the sum of the pulse bandwidth and the maximum spectral shift.

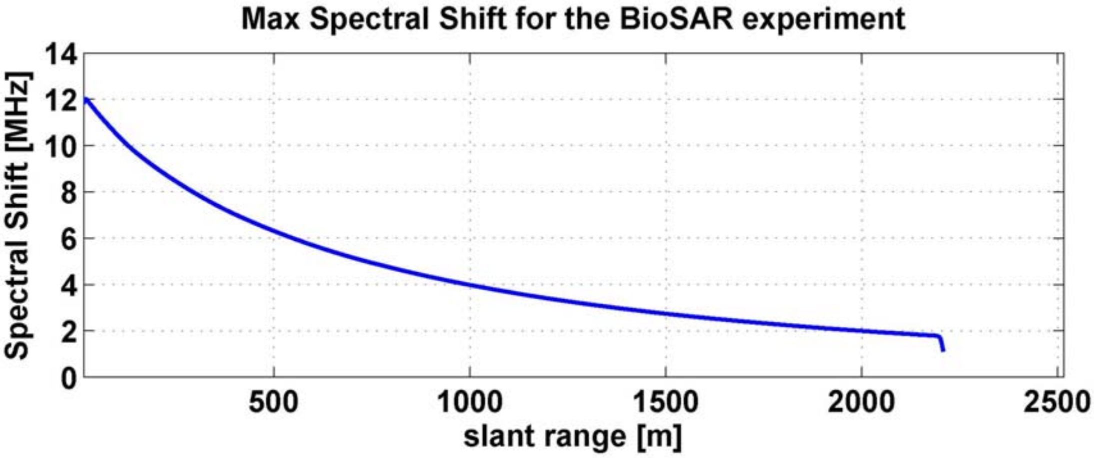

Figure 8.48: Spectral shift for the BioSAR experiment, computed for 80 m horizontal baseline and under the hypothesis of flat terrain.

It is worthwhile noticing that, in principle, spectral shift should be computed accounting for local variations of the terrain slope. This can be done basing on a Digital Elevation Model, if available, or by direct estimation of the terrain slope, as depicted in [12]. In the case of the Remningstorp test site, however, the topography may be regarded as being sufficiently smooth not to cause significant variations with respect to the flat terrain case.

To depict how the band synthesis algorithm works, consider the forward model relating the complex reflectivity to the n-th acquisition:

$$y_n(r_0) = \int f(r - r_0) g(r) \exp(j\varphi_n(r)) dr \qquad \text{Eq. 2}$$

where:

- $y_n(r_0)$ is the n-th acquisition at slant range location r_0;
- r is the slant range;
- f( ) is the 6 MHz filter shaping the slant range spectrum of the SLC data;
- $\varphi_n(r)$ is the topography induced phase at slant range location r, flat terrain contributions included;
- g(r) is the complex reflectivity.

Discretizing the integral in Eq. 2 the forward model may be cast in the following matricial form:

$$\mathbf{y}(r_0) = \mathbf{Hg} \qquad \text{Eq. 3}$$

where $\mathbf{y}(r_0)$ is the stack of N=9 acquisitions at slant range location r, $\mathbf{g}$ is a sampled version of g(r) in Eq. 2 and $\mathbf{H}$ is a matrix corresponding to the integral in Eq. 2. Depending on the sampling rate used for discretizing the integral the problem in Eq. 3 may be either overdetermined or underdetermined. In order to obtain the highest resolution, it makes sense to choose a high sampling rate for representing the complex reflectivity. Therefore the problem is to be regarded as being underdetermined, and the solution is to be computed through the right pseudoinverse operator:

$$\hat{\mathbf{g}}(r_0) = \mathbf{H}^*\left(\mathbf{HH}^*\right)^{-1}\mathbf{y}(r_0) \qquad \text{Eq. 4}$$

where * stands for Hermitian transposition. After some matrix manipulations, it is possible to show that Eq. 4 may be cast in the following form:

$$\hat{g}(r_0) = \underbrace{[1 \quad 1 \quad \ldots \quad 1]}_{N}\left(\Gamma_{flat}(r_0)\right)^{-1}\Phi^*(r_0)\mathbf{y}(r_0) \qquad \text{Eq. 5}$$

where:

- $\hat{g}(r_0)$ is the estimated wide band reflectivity at slant range location r_0;
- $\Phi(r_0)$ is the diagonal matrix

$$\Phi(r_0) = diag\{\exp(j\varphi_1(r_0)) \quad \exp(j\varphi_2(r_0)) \quad \ldots \quad \exp(j\varphi_N(r_0))\} \qquad \text{Eq. 6}$$

$\Gamma_{flat}(r_0)$ is the N×N matrix of the coherence of each interferometric pair induced by flat terrain decorrelation at slant range location r_0.

It is easy to see that $\Phi^*(r_0)\mathbf{y}(r_0)$ corresponds to the stack of the N acquisitions after being compensated for topography induced phase. The term $\left(\Gamma_{flat}(r_0)\right)^{-1}$ may be regarded as a whitening filter for the synthesized wide band reflectivity. Its role is to equalize the synthesized spectrum in such a way as to distribute the energy of the estimated reflectivity over all the synthesized frequencies.

7.3.5.1.1 Phase estimates

The most critical part in applying Eq. 5 is to estimate the topography induced phase terms in Eq. 6 at every location of the grid used for representing the wide band complex reflectivity. This is due to the unbalance between the nominal slant range resolution cell, determined by pulse bandwidth, and the sampling interval of the high sampling grid, resulting in a strong spatial correlation among nearby samples in every single acquisition. This prevents from performing independent phase estimation for every sample of the high resolution grid. To solve this problem, we estimate the phase of the most stable sample (according to the concepts exposed in section 8.3.4.3) within each nominal resolution cell, and interpolate to find the phases at every location of the high resolution grid. The interpolation step is justified by the assumption of local smoothness of the scene topography.

7.3.5.2 Results

In this section we present some results obtained by applying the concepts exposed above. Accordingly to the analysis in section 8.3.4, we assume that the HH and VV channels may be reasonably characterized as being constituted by a single layer even in forested areas, due to the dominant contributions of the ground-trunk interactions. All the results to follow in this section have been obtained by processing the HH channel. However, similar results may be obtained with the VV channel. Figure 8.49 shows the amplitudes of a small patch of the scene containing the near range corner reflector computed from the 6 Mhz acquisitions and through
Eq. 5, for which the solutions hereinafter referred to as Equalized Band Synthesis (EBS) or Band Synthesis (BS) denote whether the equalization kernel is used or not.

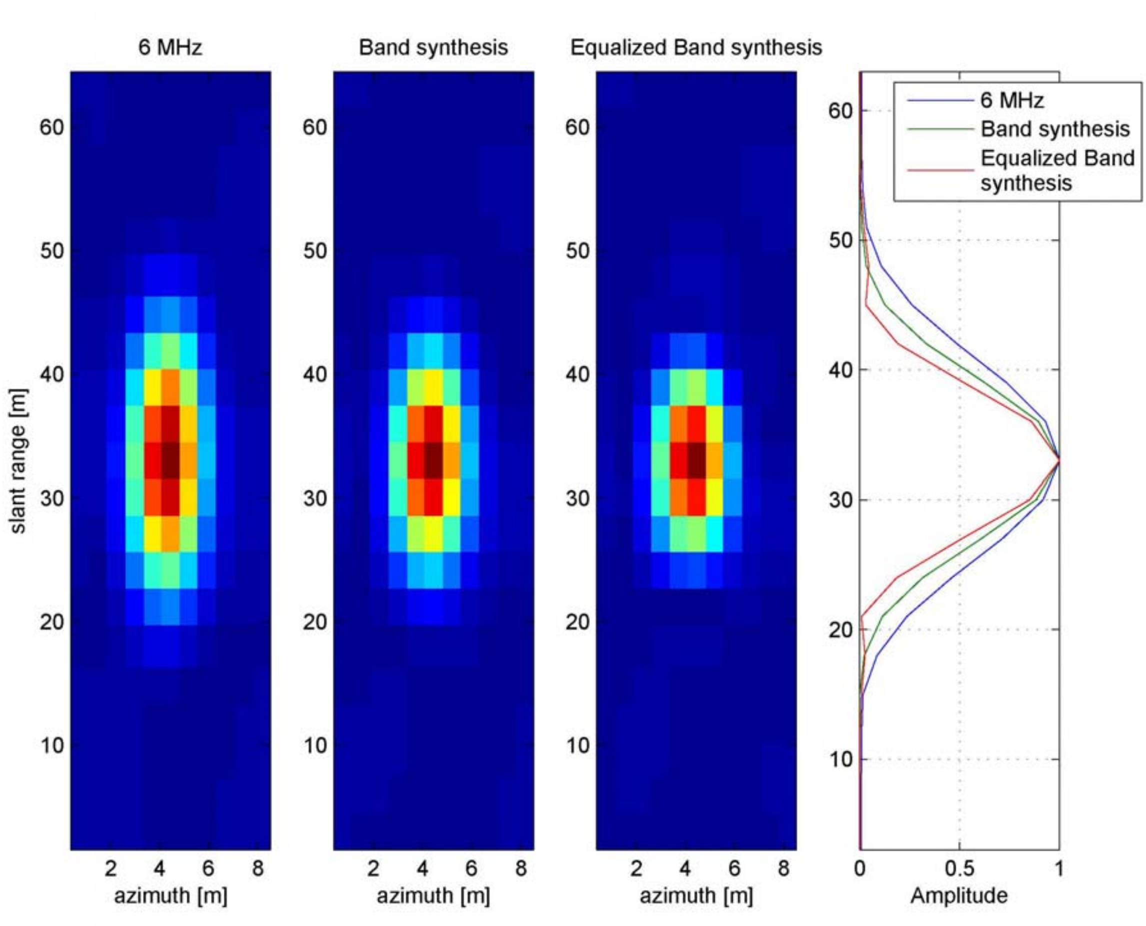

Figure 8.49: Amplitude of the near range corner reflector. From left to right: incoherent mean of the 9 acquisitions; absolute value of the wide band reflectivity estimated without the equalization kernel; absolute value of the wide band reflectivity estimated exploiting the equalization kernel; comparison of the three amplitude profiles

The slant resolution enhancement of the far range corner, not reported here, did not produce significant results, due to the small normal baseline span at far ranges. The application of the BS and EBS algorithm to a larger area is reported in Fig. 8.50. It is interesting to note that the slant resolution improves moving from far to near ranges, accordingly to the graph in Fig. 8.48. To better appreciate this phenomenon, we evaluated the slant range power spectrum of the estimated wide band complex reflectivity in three areas, corresponding to near, middle and far ranges, according to table 8.9. The slant range power spectra obtained by the BS and the EBS algorithms are shown in the first two columns of Fig. 8.51. The third column of the same figure shows the average cross-correlations, evaluated at near, middle, and far ranges, between the original full bandwidth data and the wide band complex reflectivity estimated by the EBS algorithm. Finally, Fig. 8.52 shows the results of the application of the EBS algorithm on the near range part of the whole scene. These results show that the usage of the equalization kernel is actually able to provide a benefit, yielding in all cases a larger spectrum with respect to the BS algorithm. In all cases, the bandwidth of the reconstructed reflectivity is only 2 MHz to 3 MHz below the theoretical values. This discrepancy is to be imputed to a non perfect matching between the equalization kernel and the pulse waveform, resulting in a slight damping of the highest frequency components of the reconstructed reflectivity. We also tested a more rigorous implementation of the equalization kernel, which, however, resulted in the arising of undesired side lobes.

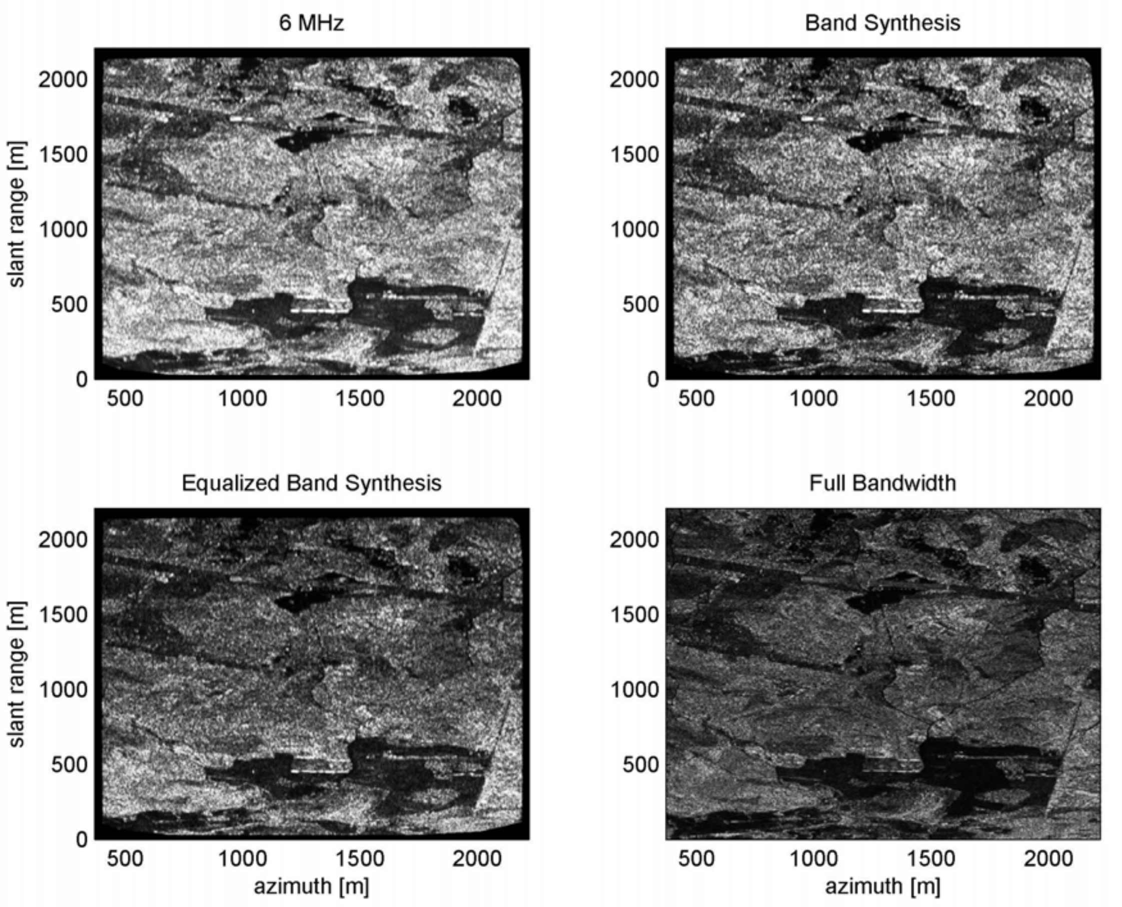

Figure 8.50: Left column: near, middle, and far range power spectrum of the wide band reflectivity estimated without the equalization kernel. Middle column: near, middle, and far range power spectrum of the wide band reflectivity estimated exploiting the equalization kernel. Right column: near, middle, and far range average cross-correlation between the original full bandwidth data and the wide band complex reflectivity estimated by the EBS algorithm.

Near range	(0,150) [m]
Middle range	(900,1050) [m]
Far range	(1950,2100) [m]

Table 8.9: near, middle, and far range locations used for spectral analysis

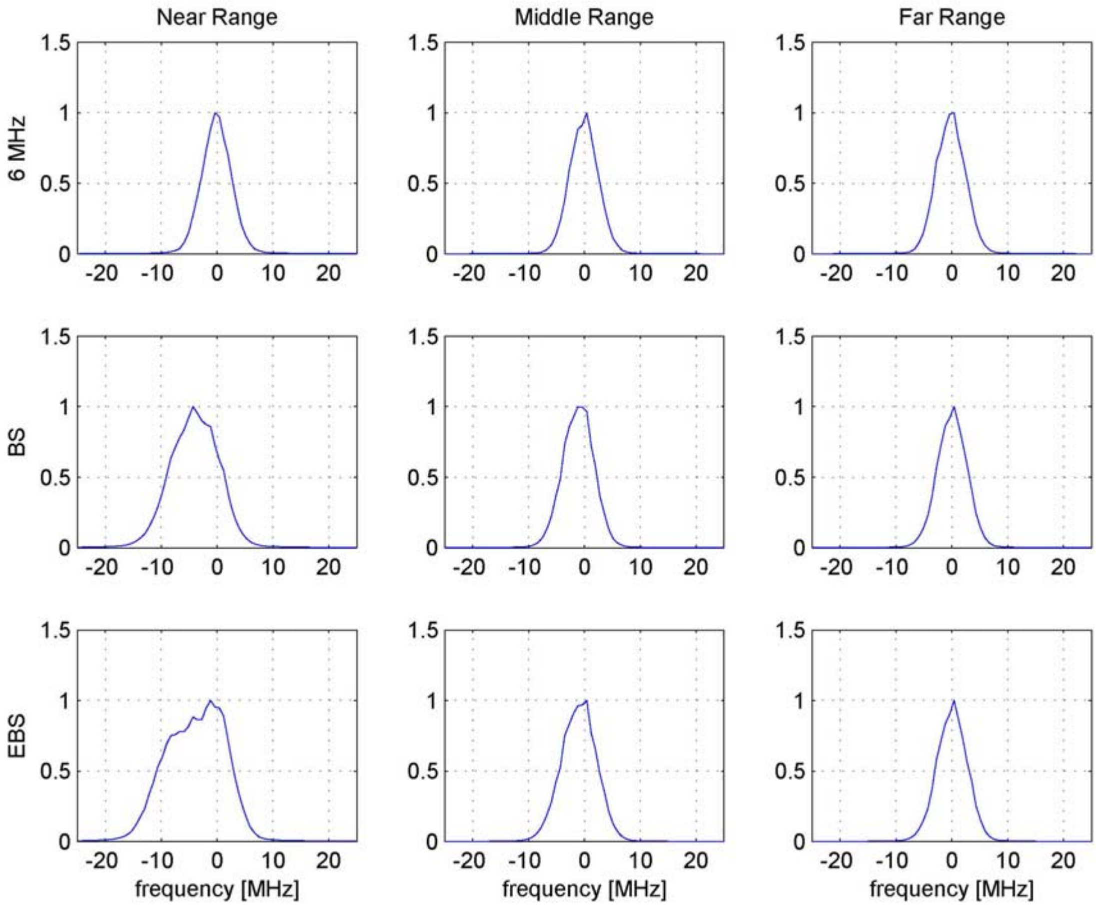

Figure 8.51: Top row: near, middle, and far range power spectrum of the 6 MHz. Middle row: near, middle, and far range power spectrum of the wide band reflectivity estimated without the equalization kernel. Bottom row: near, middle, and far range power spectrum of the wide band reflectivity estimated exploiting the equalization kernel.

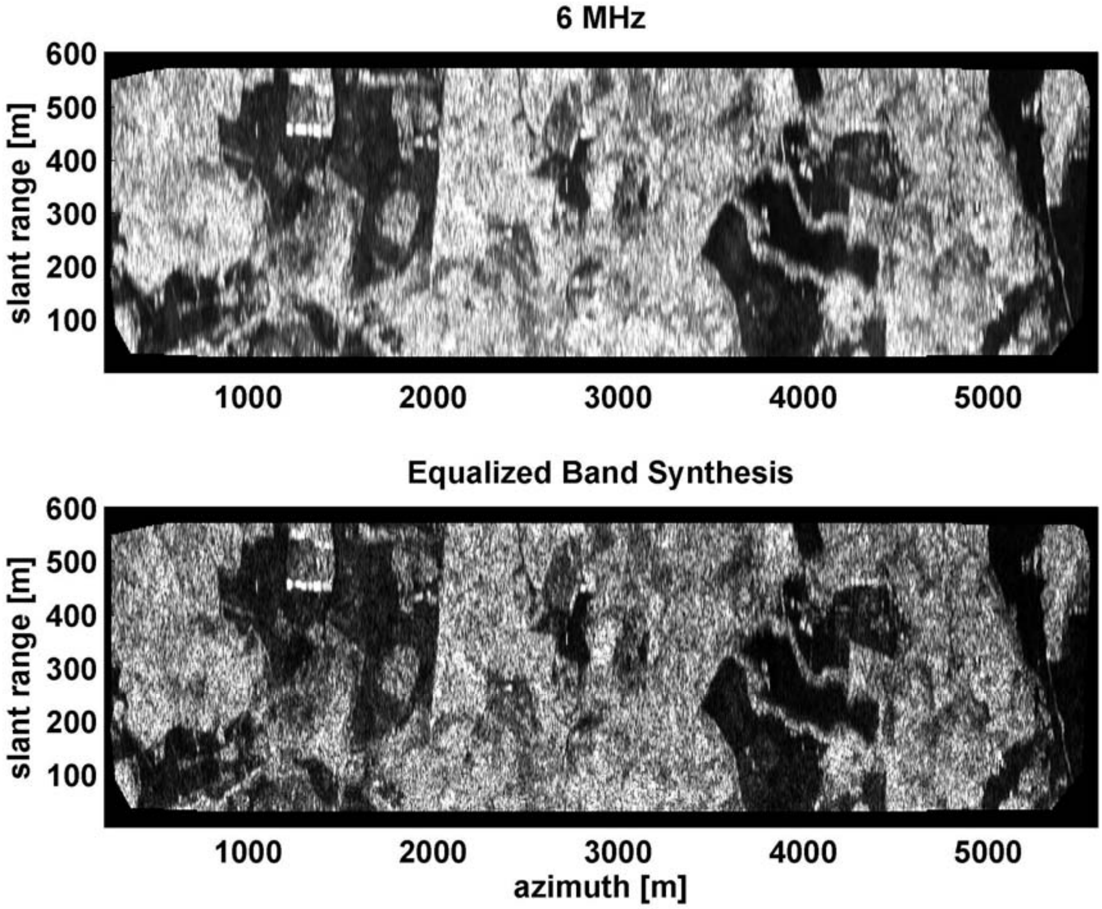

Figure 8.52: Top row: incoherent mean of the 9 acquisitions. Bottom row: absolute value of the wide band reflectivity estimated by the EBS algorithm.

7.3.5.3 Extension to a two Layered Model

In the case of the HV channel the assumption that the ground contributions are dominant is, at least in principle, no longer valid. Therefore, a further processing step is required prior to performing band synthesis, in order to remove the contributions from the canopy layer. In principle, the problem may be faced either from the statistical or the deterministic point of view. In the following, a statistical solution is pursued, derived from considering the contributions of the canopy layer as a realization of a stochastic process. A deterministic solution is reported in Appendix. To account from the contribution of the canopy layer, we modify

Eq. 3 as follows:

$$\mathbf{y}(r_0) = \mathbf{Hg} + \mathbf{c} \qquad \text{Eq. 7}$$

where c is the N×1 vector accounting for the contributions of the canopy layer in the N acquisitions at slant range location r_0. At this point, it is immediate to write down a Minimum Mean Square Error (MMSE) estimate of the ground reflectivity as:

$$\hat{\mathbf{g}} = E\left[\mathbf{g}\mathbf{y}^*\right]\left(E\left[\mathbf{y}\mathbf{y}^*\right]\right)^{-1}\mathbf{y} \qquad \text{Eq. 8}$$

Assuming statistical independence between g and c, and after some matrix manipulation, the solution may be cast into the form:

$$\hat{g}(r_0) = \underbrace{[1 \quad 1 \quad \ldots \quad 1]}_{N}(\Xi(r_0))^{-1}\Phi^*(r_0)\mathbf{y}(r_0) \qquad \text{Eq. 9}$$

The kernel Ξ is given by:

$$\Xi(r_0) = \Gamma_{flat}(r_0) + \frac{\sigma_c^2}{\sigma_g^2}\Delta\Phi^*(r_0)\Gamma_{canopy}(r_0)\Delta\Phi(r_0) \qquad \text{Eq. 10}$$

where $\Delta\Phi(r_0)$ is the diagonal matrix

- $\Delta\Phi(r_0) = diag\{\exp(j\Delta\varphi_1(r_0)) \quad \exp(j\Delta\varphi_2(r_0)) \quad \ldots \quad \exp(j\Delta\varphi_N(r_0))\}$
- $\Delta\varphi_n(r_0)$ being the phase difference between the ground layer and the phase center of the canopy layer in the n-th image at slant range location r_0;
- σ_g^2, σ_c^2 are the backscattered powers from the ground and the canopy layer, respectively;
- $\Gamma_{canopy}(r_0)$ is the N×N matrix of the coherence of each interferometric pair induced by flat terrain and volume decorrelation at slant range location r_0.

It is easy to see that Eq. 9 defaults to Eq. 5 when σ_g^2,>> σ_c^2.
The role of the new kernel in Eq. 10 is to account for both spectral equalization of the estimated ground reflectivity and statistical cancellation of the volumetric terms. The difficulty in applying Eq. 9 lies in the assessment of the backscattered powers σ_g^2, $\sigma_c^2$² and of the phase differences $\Delta\varphi_n(r_0)$, for which a tomographic analysis is required. Figure 3.53 shows the results obtained by applying Eq. 5 and Eq. 9 to the stack of the HV channel data. In the latter case, the kernel in Eq. 10 has been implemented by setting σ_c^2=0.35□ σ_g^2 and assuming an average height difference of 10 meters between the ground and the canopy layers, accordingly to the results to be presented in section 8.3.6.

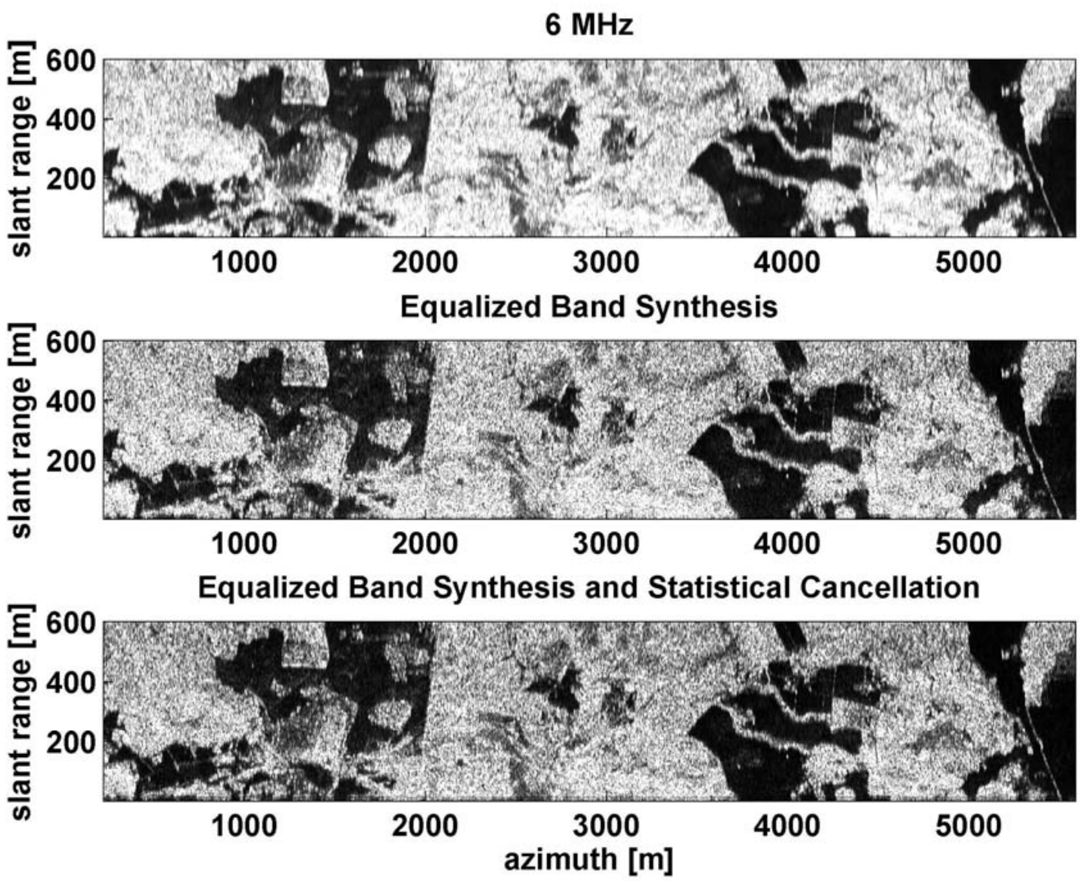

Figure 8.53 : Top row: incoherent mean of the 9 acquisitions. Middle row: absolute value of the wide band reflectivity estimated by the EBS algorithm. Bottom row: absolute value of the wide band reflectivity estimated by the EBS algorithm with statistical layer cancellation.

In this case, the difference between applying or not the cancellation term in Eq. 10 is actually minimal. We interpret this result as follows. First of all, the EBS algorithm has been implemented in such a way as to focus the reflectivity at ground level, and thus it already performs a rough filtering of the contributions other than those from the ground. Another point to be remarked is that even in the HV channel the backscattered power from the ground appears to be stronger than the one from the canopy layer, making in difficult to appreciate whether the canopy has been removed.

7.3.6 Tomographic Analysis

The first part of this section depicts the concepts and the solutions which have been exploited to perform a tomographic analysis of the imaged scene. SAR tomography is posed in terms of a parametric estimation problem, basing on a two layered model of the scene. Results are presented at the end of this section.

7.3.6.1 Signal Models for SAR Tomography of Forested Areas

The vertical resolution of a SAR system designed for performing tomographic analysis over forested area is mainly determined by two factors:

- total baseline aperture
- pulse bandwidth.

The limit to vertical resolution due to baseline aperture corresponds to the Rayleigh limit: larger baseline aperture allow the system to sense a larger interval of the angles forming the object spectrum, resulting in a better spatial resolution. With reference to the parameters in table 8.8, the vertical resolution due to baseline aperture may be assessed as:

$$\Delta h_a = \frac{\lambda H}{2A\cos^2\theta}\sin\theta \qquad \text{Eq. 11}$$

If the scene is constituted by point-like scatterer, as it may be the case of an urban environment, this is the only limit to vertical resolution. To overcome this limit several techniques have been proposed in the Direction of Arrival (DOA) literature, such as MUSIC, APES, ESPRIT, or more sophisticated Maximum Likelihood (ML) solutions. All these techniques assume the received signal to be constituted by a number of sinusoids plus noise. Basing on this assumption, the signal parameters are estimated exploiting the concepts of array manifold and spaces of signal and noise [13], [14], [15], [16].

In remote sensing of forested areas, however, this assumption is likely not to be verified, due to the angular spreading of the received signal resulting from the spatial distribution of the target within the system resolution cell. This phenomenon is directly related to pulse bandwidth, since this parameter determines the slant range extension of the system resolution cell. For a single layered scene, angular spreading may be described in terms of spectral shift [9]. If we model the forest as a two layered scene, then the main limit to vertical resolution arises from the angular overlapping of the two layers. As a rule of the thumb, the vertical resolution due to pulse bandwidth is given by:

$$\Delta h_{pb} = \frac{c}{2B}\cos\theta \qquad \text{Eq. 12}$$

where c is the speed of light and B is the pulse bandwidth.

An effective way to deal with angular spreading is to consider the received signal as a realization of a stochastic process, the parameters of interest, such as elevation and backscattered power, being embedded in the second order statistic of the process. This assumption leads to formulating the problem of finding the DOA of a source affected by angular spreading as a parametric estimation problem, exploiting concepts from parametric spectral identification techniques and theory of estimation [17], [18], [19], [20], [21], [22].

Figure 8.54 shows the expected vertical resolution due to baseline aperture and pulse bandwidth, computed with reference to the parameters in table 8.8.

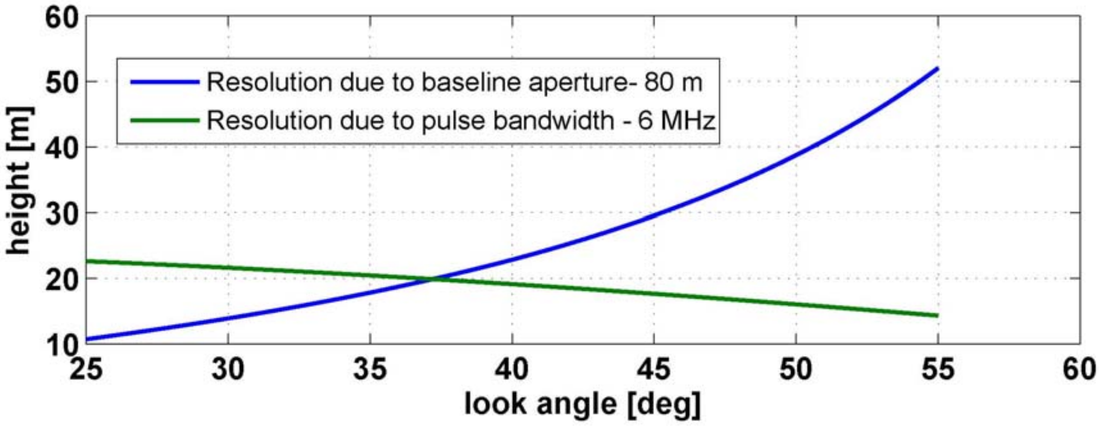

Figure 3.54: Vertical resolution due to baseline aperture (blue line) and to pulse bandwidth (green line) for the BioSAR experiment.

This graph shows that the vertical resolution is dominated by Eq. 11 at far ranges and by Eq. 12 at near ranges. Therefore, the best characterization to be given to the received signal may be either stochastic or deterministic, depending on the look angle.

7.3.6.1.1 A Note on System Design

If the number of tracks is fixed, as it happens in practical cases, baseline aperture must be constrained in order to avoid the raising of aliasing phenomena on the received signal. Letting N the number of tracks, and assuming homogeneous baseline spacing, the elevation of ambiguity (corresponding to the Nyquist frequency of the multi-baseline SAR system) is given by:

$$h_{amb} = N\Delta h_a$$

Therefore, if the scene to be analyzed is constituted by targets affected by angular spreading, the following constraint must be respected

$$\Delta h_{pb} \ll h_{amb}$$

According to this analysis, the choice of an 80 m horizontal baseline aperture is to be considered suitable to performing a tomographic analysis on the whole imaged scene. Choosing a larger baseline aperture would improve the system performance at far ranges, but it would result in the impossibility to extract information from near range areas, due to signal aliasing.

7.3.6.2 Covariance Matching Approach

The analysis depicted in the previous section shows that the problem of SAR tomography is to be considered range variant. This phenomenon, however, is going to be strongly mitigated as for future spaceborne applications, for which an average look angle of 25° may be assumed. For this reason we model the received signal as a realization of a stochastic process, and pose the problem in terms of a parametric estimation. With reference to a two layered scene, constituted by the ground and the canopy layer, a suitable model for the covariance matrix of the SLC data is given as follows:

$$\mathbf{R}_{AB} = \sigma^2_{g,AB}\mathbf{R}_g + \sigma^2_{c,AB}\mathbf{R}_c \qquad \text{Eq. 13}$$

where:

- AB={HH,HV,VV}
- $\mathbf{R}_{AB}$ is the covariance matrix of the SLC data in the AB channel (N×N)
- $\sigma^2_{g,AB}$ is the backscattered power from the ground layer in the AB channel
- $\sigma^2_{c,AB}$ is the backscattered power from the canopy layer in the AB channel
- $\mathbf{R}_g$ is the structure matrix for the ground layer (N×N)
- $\mathbf{R}_c$ is the structure matrix for the canopy layer (N×N)

The structure matrices account for the spatial distribution of the scatterers within the system resolution cell. In order not to raise excessively the number of the unknowns, we let each structure matrix depend upon two parameters:

Mean elevation, $h_{g,c}$ This parameter affects the phase of the off-diagonal terms of the structure matrices according to the law:

$$\angle\{\mathbf{R}_{g,c}\}_{nm} = (k_z(n) - k_z(m))h_{g,c} \qquad \text{Eq. 14}$$

Decorrelation constant, $\rho_{g,c}$. This parameter affects the absolute value of the off-diagonal terms of the structure matrices according to the law:

$$\left|\{\mathbf{R}_{g,c}\}_{nm}\right| = (\rho_{g,c})^{-|k_z(n)-k_z(m)|\zeta} \qquad \text{Eq. 15}$$

where ζ is a normalizing constant such that the exponent in (15) is dimensionless. The role of the decorrelation constant is to describe in a simple fashion the degree of correlation among the acquisitions, avoiding the dependence upon a particular target model. Given the definition above, the decorrelation constant ranges from 0 to 1 corresponding to the cases of pure noise and of a perfectly coherent received signal, respectively. It is worthwhile noticing that this definition accounts only for spatial decorrelation phenomena. Temporal decorrelation could be handled by adding a further pair of unknowns.

To sum up, the tomographic problem is framed as the problem of estimating 10 unknowns from 27 SLC images (9 tracks times 3 polarimetric channels). Therefore, the problem is not, in principle, ill-posed, even though it is highly non linear.

Assuming, for the moment, that the data distribution is Gaussian and zero mean [23], the data covariance matrix represents a sufficient statistics for estimating the unknowns. In principle, the availability of a model for the covariance matrix suffices for solving for the unknowns through Maximum Likelihood Estimation (MLE). This solution, however, would not be efficient, since it requires an exhaustive search in a 10 parameter space. A significant complexity reduction may be achieved by applying the Extended Invariance Principle (EXIP) [20], [22], which allows solving the problem by minimizing a weighted Frobenius norm of the difference between the sample covariance matrix and the model in Eq. 13 [21], [24]. This approach, known in literature as covariance matching, has three major advantages:

- it may be applied even in the case of non-Gaussian distributions;
- it is asymptotically equivalent to MLE in the case of a Gaussian distribution;
- the estimates of the backscattered powers for each layer and for each channel are obtained in closed form.

In this way, we managed to reduce the dimension of the search space from 10 to 4. To further speed up the algorithm, we also employ adaptive spectral estimation techniques; see [25], to provide a first estimate of the mean elevations and decorrelation constants of the two layers.

7.3.6.3 Results

This section reports the results obtained by applying the covariance matching approach to the multi-baseline, fully polarimetric data acquired by DLR's E-SAR over the site of Remningstorp. All the figures presented in this section have been obtained by using 50×50 square meters (ground range, azimuth) estimation window.

As stated in the previous section, the estimation of the parameters of interest has been initialized by exploiting adaptive spectral estimation techniques. In particular, the estimation of the mean elevation and the decorrelation constant of the ground layer have been performed by analyzing the HH and VV channels, while the estimation of the mean elevation and the decorrelation constant of the canopy layer has been performed by analyzing the HV channels. This choice is due to the analysis in section 8.3.6, from which it resulted that the co-polar channels are mainly affected by ground and ground-trunk contributions. It is important to point out that the estimates produced by the covariance matching algorithm did not show any significant deviation from the initial values. This result led us to separate the estimation of the mean elevations and decorrelation constants from the estimation of the backscattered powers. This simplification allowed us to add a test for selecting the number of layers, in such a way as to univoquely mark an area as being bald or vegetated. Figure 8.55 shows the results from a tomographic analysis of a single slant range line. As expected, in the co-polar channels the backscattered power from the ground layer is significantly larger than that from the canopy layer, confirming the hypothesis that the ground layer is dominant in the co-polar channels. The power loss corresponding to the bald area in the bottom left part of the image shows that the contributions from ground-trunk interactions dominate those from bald ground by an order of magnitude. In the HV channel the backscattered powers from the ground and the canopy layers are closer to each other, even though the ground layer contributions still appear to be dominant. Bald areas are correctly identified. Table 8.10 summarizes the results of the estimation of the backscattered powers from the ground and the canopy layers for three different stands, corresponding to an average canopy elevation of 20 meters, 10 meters, and to an open area. Each stand measures approximately 150 x 150 square meters (ground range, azimuth). The location of each stand is indicated in Figure 8.56. Canopy elevation has been extracted from the LIDAR measurements provided by FOI, according to the following processing. First, an adaptive spatial smoothing has been performed, such that every sample of the processed map represented the average canopy layer elevation within a 50 x 50 square meter window, having care to include in the computation only those samples where a return from the canopy was actually present. Then, a re-sampling operation has been performed to code the processed map onto SAR coordinates.

The results obtained for the whole scene are reported hereinafter, from Figure 8.57 to Figure 8.63

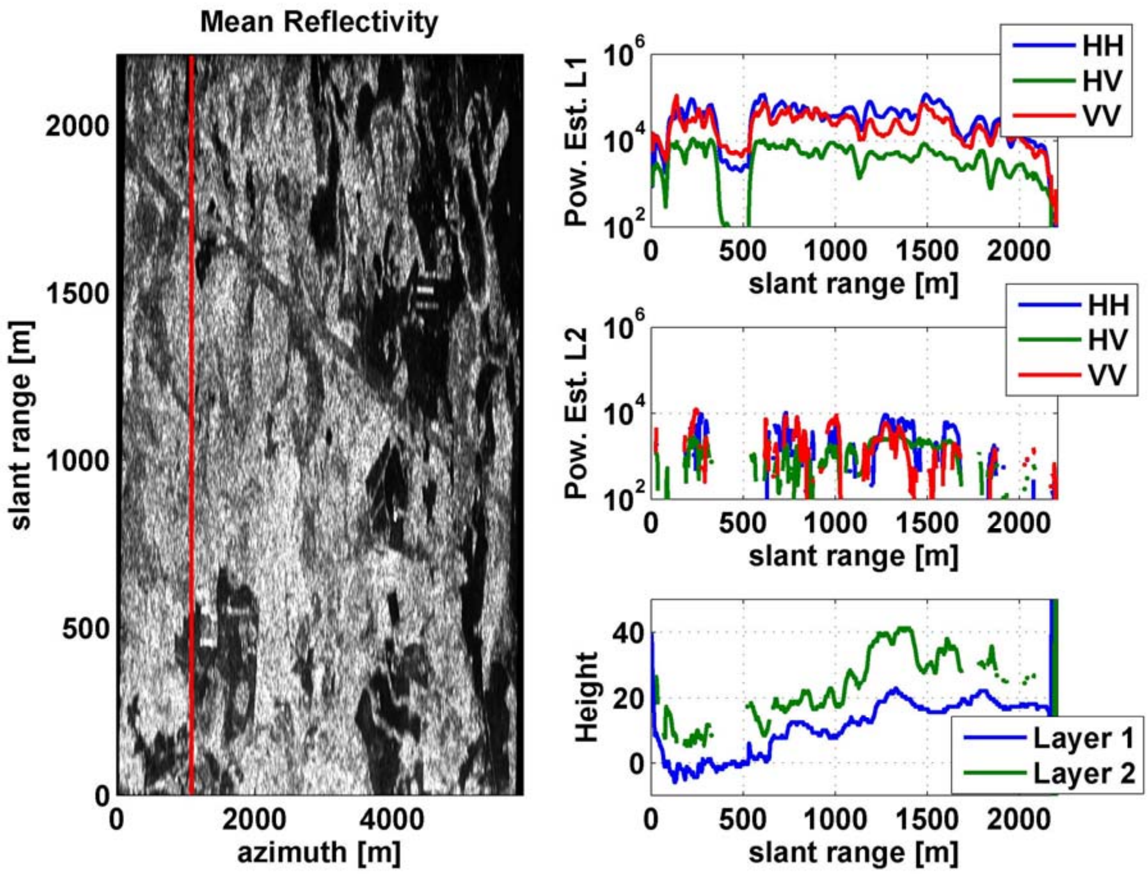

Figure 8.55: Left: the red line indicates the inspected slant range line. Top right estimated backscattered power from the ground layer. Middle right: estimated backscattered power from the canopy layer. Bottom right: estimated elevation of the ground and canopy layers.

Area	Color	Location (slant range, azimuth) [m]	Average canopy elevation [m]	$\sigma^2_{g,HH}$ [dB]	$\sigma^2_{c,HH}$ [dB]	$\sigma^2_{g,HV}$ [dB]	$\sigma^2_{c,HV}$ [dB]	$\sigma^2_{g,VV}$ [dB]	$\sigma^2_{c,VV}$ [dB]
High Canopy	blue	840, 2335	20.8	51.7	34.3	39.3	36.0	46.8	32.9
Low Canopy	red	1044, 2398	11	48.7	30.6	37.2	30.1	45.9	32.5
Open Area	yellow	381, 1569	0.1	32.9	absent	19.4	absent	34.6	absent

Table 8.10: Backscattered power from the ground and the canopy layers for three different stands. The location of each stand is to be referred to the slant range, azimuth coordinates of the Range Geometry Image (RGI) data files delivered by DLR. The reported backscattered power values are to be intended as the average values for each stand.

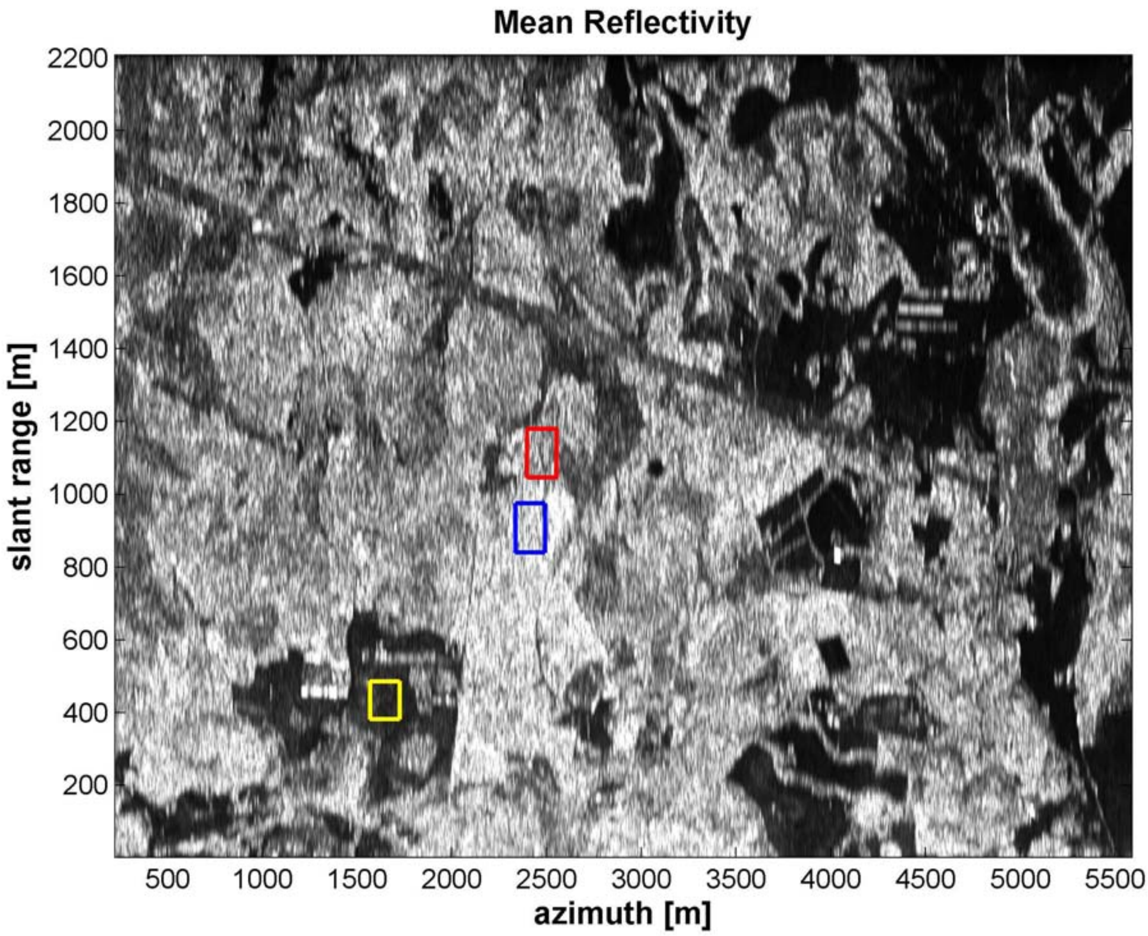

Figure 8.56:Location of the three stands inspected in Table 8.10 . Each stand measures approximetely 150 x 150 square meters (ground range, azimuth).

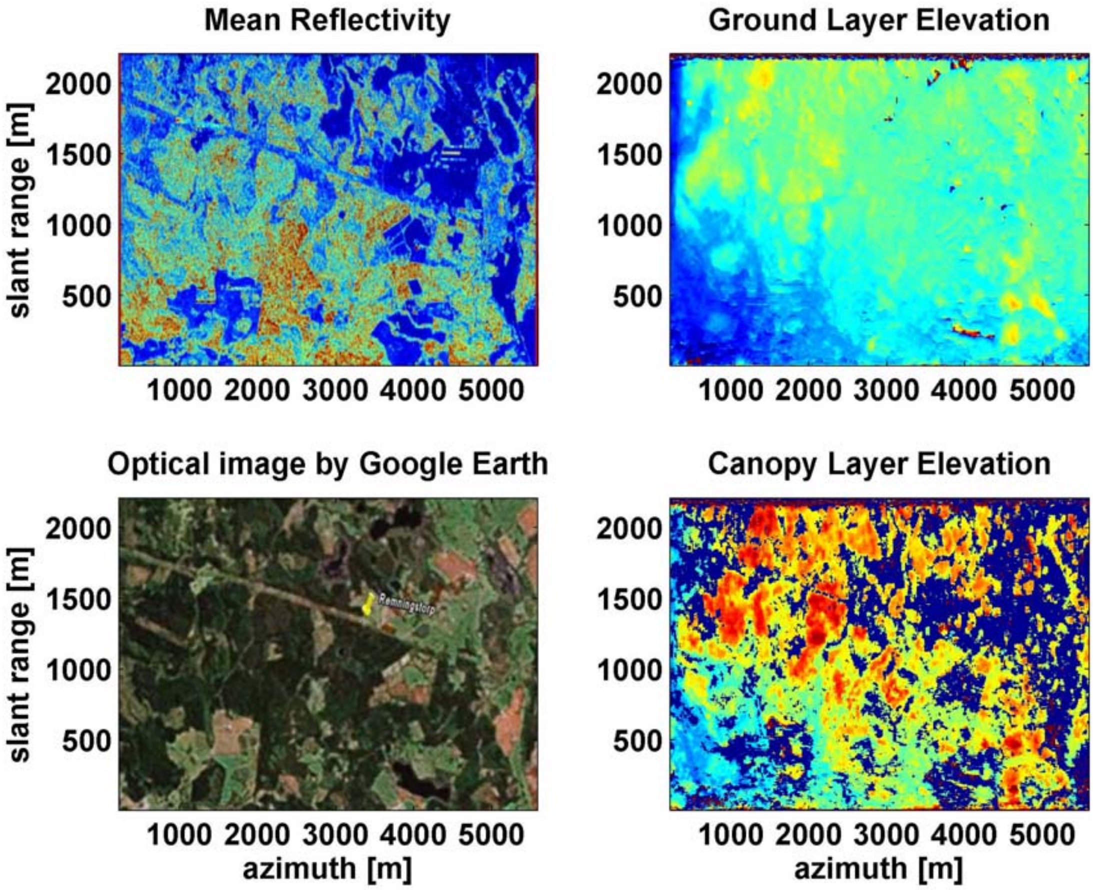

Figure 8.57: Top left: mean reflectivity of the HH channel. Bottom left: optical image by Google Earth. Top right: estimated elevations for the ground layer. Bottom right: estimated elevations for the canopy layer. The color scale of the panels relative to elevations ranges from -10 m to 50 m. The dark blue areas in the bottom right panel are identified as being bald areas.

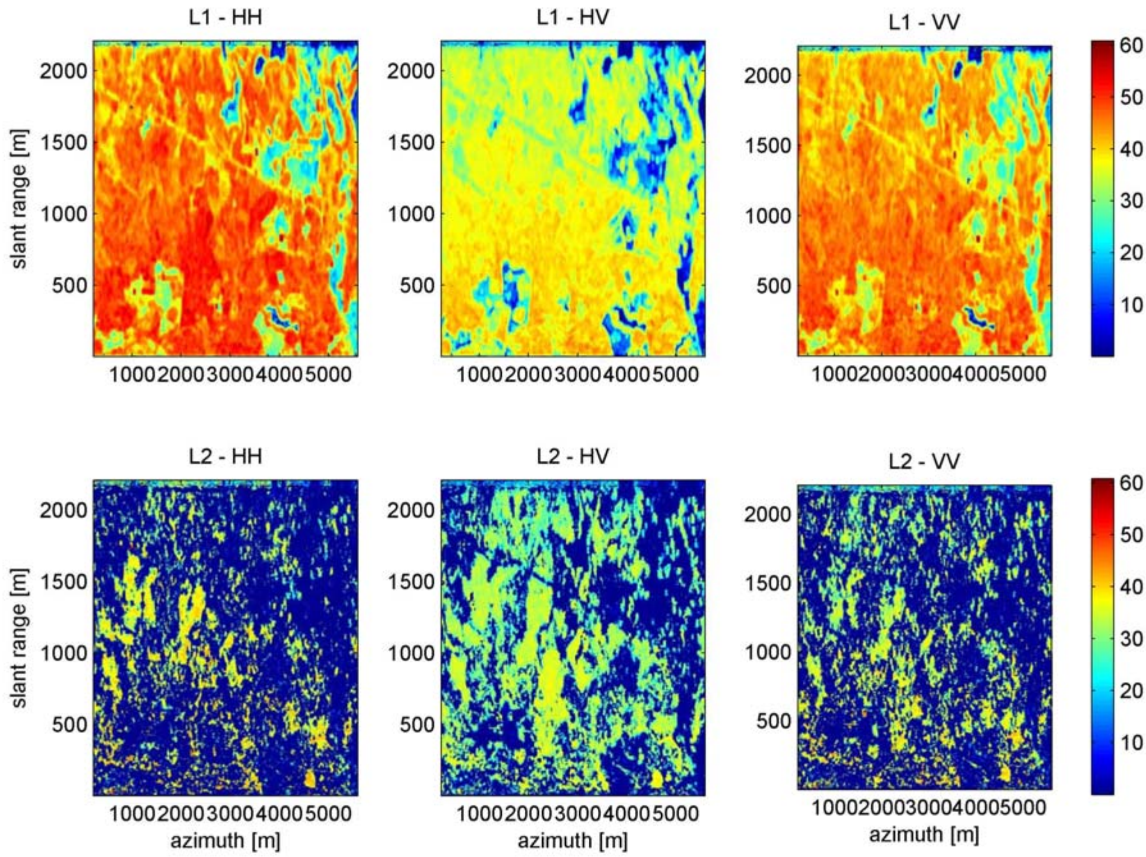

Figure 8.58: Top: estimated backscattered power (dB) from the ground layer for each polarimetric channel. Bottom: estimated backscattered power (dB) from the canopy layer for each polarimetric channel.

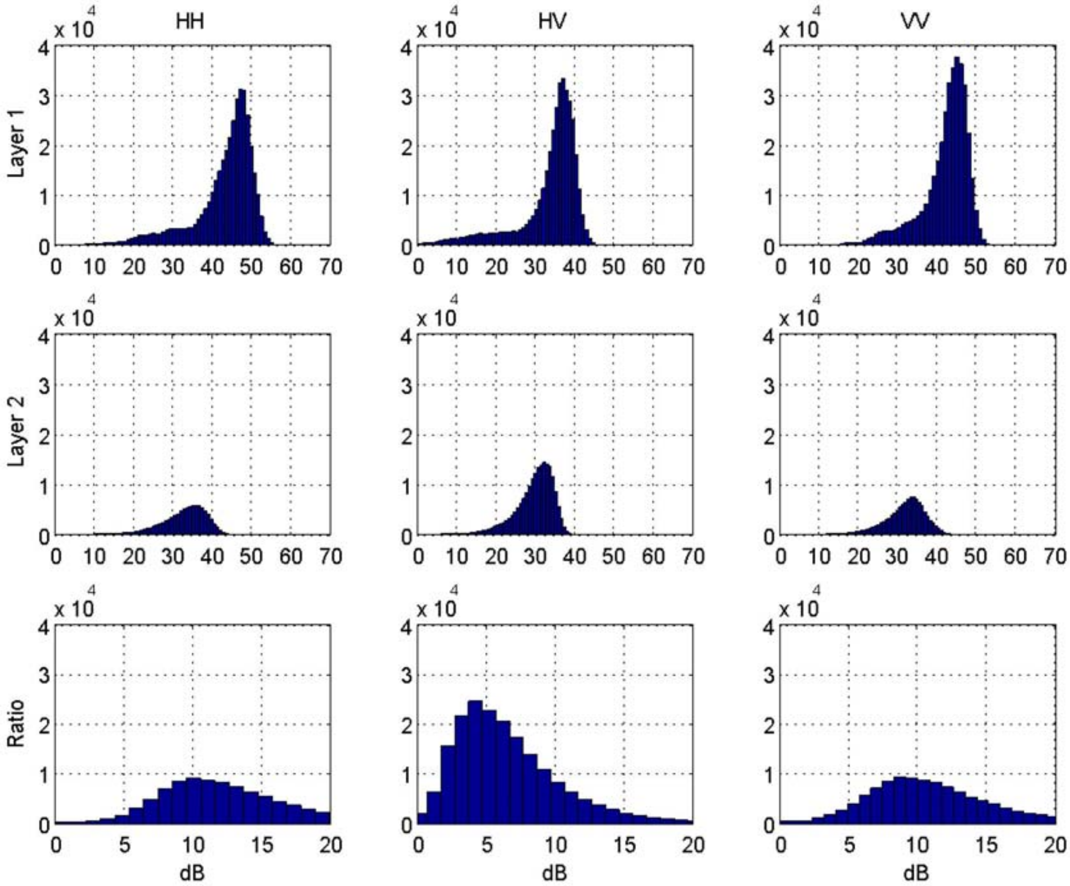

Figure 8.59: Histograms of the estimated backscattered power from each layer and for each polarimetric channel. Top row: backscattered power from the ground layer. Middle row: backscattered power from the canopy layer. Bottom row: ratio between the backscattered powers from the two layers.

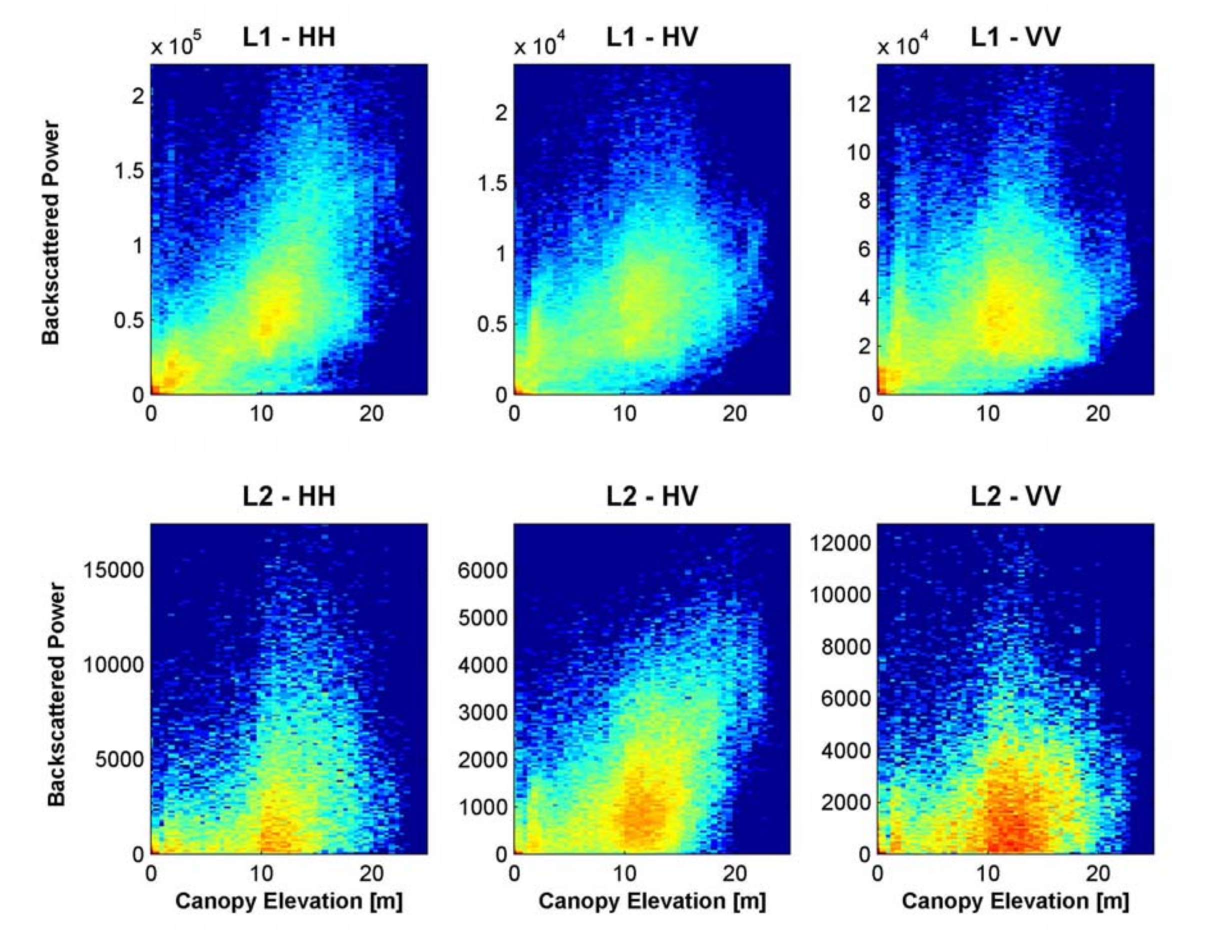

Figure8.60: 2D histograms of the canopy elevation, extracted from LIDAR measurements, and the estimated backscattered power from the ground (top row) and the canopy (bottom row) layers for each polarimetric channel. The color scale is proportional to the number of counts within each bin in the backscattered power – canopy elevation plane.

The main result emerging from the analysis of the estimated backscattered powers, reported in Figure 8.58, Figure 8.59, and Figure 8.60, is that the signal received by the SAR sensor is dominated by ground layer contributions for every polarimetric channel. Furthermore, the 2D histograms in Figure 8.60, top row, show that contributions from the ground layer are correlated with canopy elevation. As for the co-polar channels, this result is not surprising, having shown in Section 7.3.4 that the co-polar channels are mainly determined by contributions from ground-trunk interactions, which are clearly related to canopy elevation. Unexpectedly, also in the HV channel there seems to be a significant correlation between the backscattered power from the ground layer and canopy elevation. This phenomenon seems to indicate that ground-trunk contributions affect also the HV channel, probably due to ground and trunk roughness. The histograms relative to canopy layer reported in Figure 8.60, bottom row, show that the co-polar channels are barely influenced by contributions from the canopy, whereas a rising trend with respect to canopy elevation is visible in the HV channel

The top row of Figure 8.61 shows a comparison between the ground elevation estimates obtained by SAR tomography and LIDAR, re-sampled on the SAR slant range, azimuth grid. The estimated ground elevation maps look very similar. Only at far ranges the estimates provided by SAR tomography appear to be slightly biased toward higher elevations than those provided by LIDAR, presumably due to the reduction of spatial diversity among the acquisitions. The histogram of the differences between SAR and LIDAR measurements relative to ground elevation is shown in the left panel of Figure 8.62. The dispersion of the ground elevation estimate yielded by SAR tomography may be assessed in about 1.5 m.

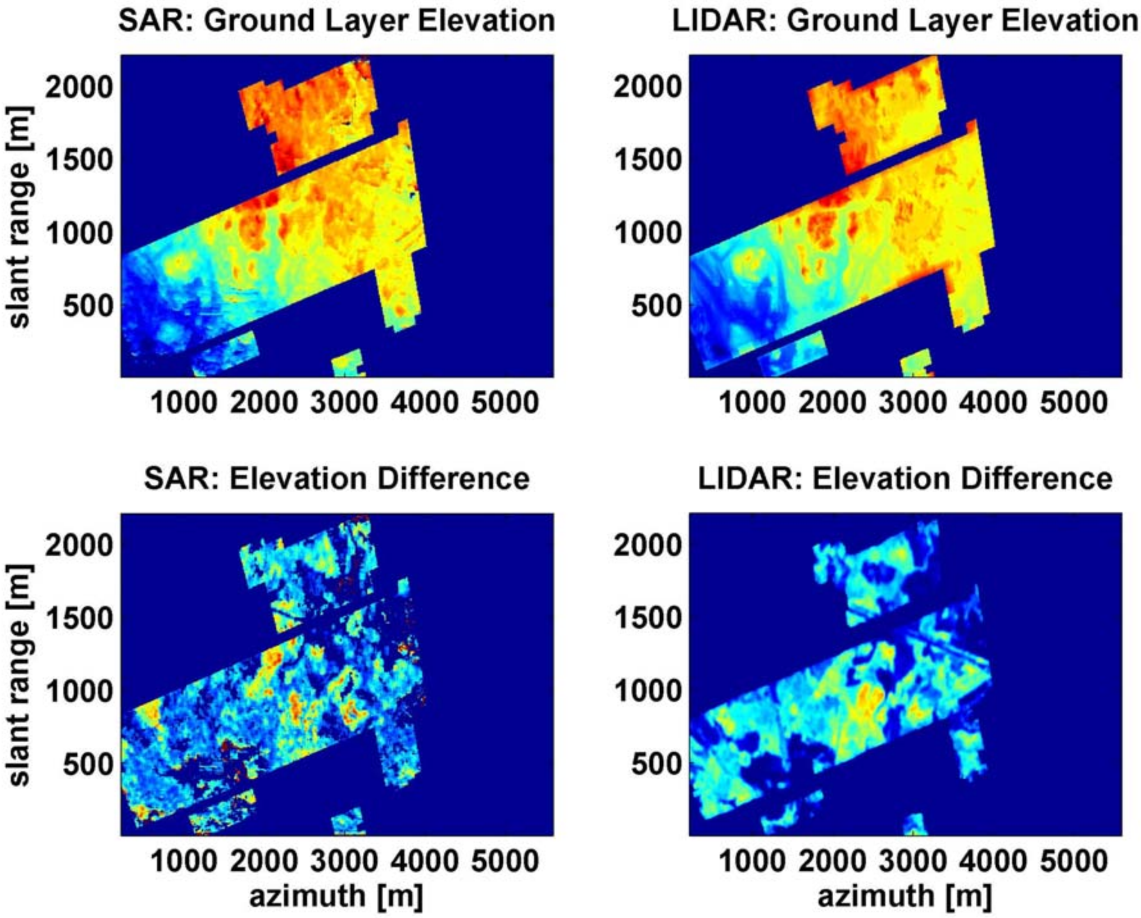

Figure 8.61: Top left: ground layer elevations estimated by SAR tomography. Bottom left: elevation differences between the ground and the canopy layer estimated by SAR tomography. Top right: ground layer elevations estimated by LIDAR. Bottom right: elevation differences between the ground and the canopy layer estimated by LIDAR. The color scale of the four panels ranges from 0 m to 33 m.

The maps relative to the elevation difference between the two layers, which may be thought of as the estimated canopy elevation above ground, are shown in the bottom row of Figure 8.61. The estimated canopy elevation maps show a satisfactory agreement, event though the result is not that brilliant as the one relative to ground elevation. The reason for this discrepancy is to be imputable to the huge diversity between SAR and LIDAR systems as for wavelength, look angle, and processing methods, resulting in an intrinsic difficulty in relating the two measurements, so that there is not actually a physical reason why the “electromagnetic” spatial average performed by SAR should be equivalent to performing a numeric spatial average of the LIDAR measurements. The histogram of the differences between SAR and LIDAR measurements relative to canopy elevation is shown in the right panel of Figure 8.62.

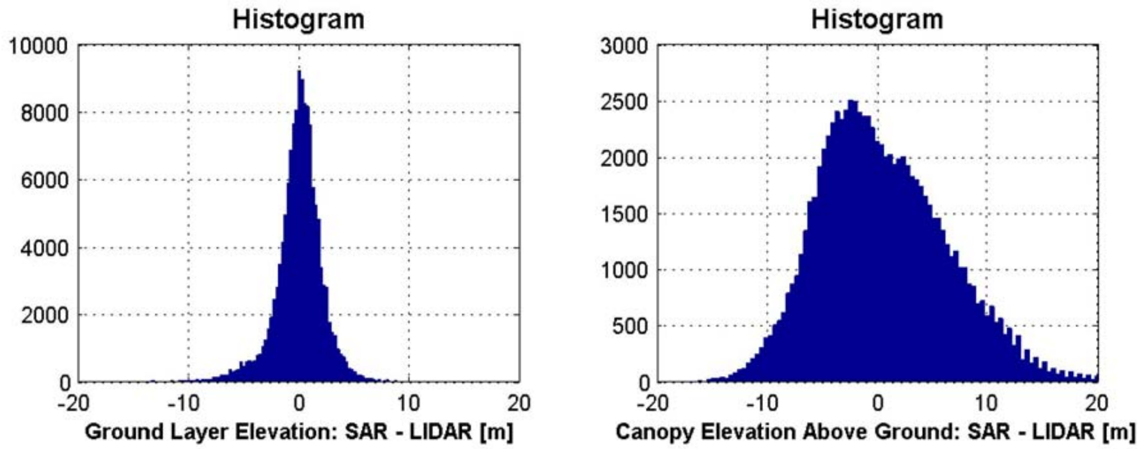

Figure 8.62: Histograms of the differences of the elevation estimates relative to the ground and the canopy layers yielded by SAR tomography and LIDAR measurementes.

Finally, Fig. 8.63 shows the estimates of the decorrelation constants for the ground and the canopy layers. As expected, the decorrelation constants increase as the slant range increases, due to a reduction of spatial decorrelation phenomena. Notice that in the brighter area in the bottom part of the image phase calibration was not performed, resulting in large estimate errors. What is interesting in these panels is that bald areas are characterized by lower values than forested areas, confirming our ideas that the scattering mechanism in forested areas is to be regarded as being determined by clusters of point-like scatterers, rather than a decorrelating layer.

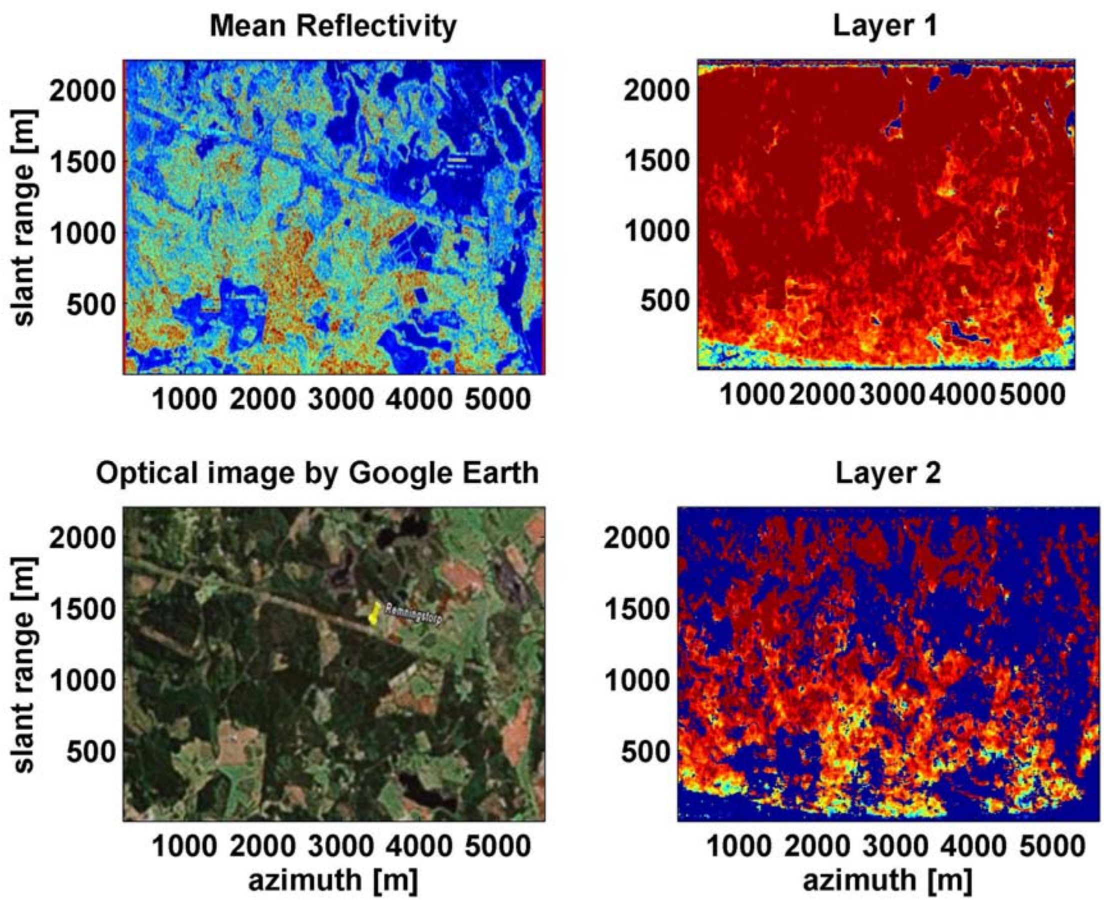

Figure 8.63: Top left: mean reflectivity of the HH channel. Bottom left: optical image by Google Earth. Top right: estimated decorrelation constants for the ground layer. Bottom right: estimated decorrelation constants for the canopy layer. The color scale of the panels relative to the decorrelation constants ranges from 0 to 1.

7.3.6.4 Effects of a Reduced Azimuth Resolution

In order to better emulate the features of a SAR equipment to be mounted aboard a satellite, we performed a further tomographic analysis of the scene after filtering the SLC data in the azimuth direction, in such a way as to reduce the azimuth resolution up to about 7.5 meters, see Fig. 8.64, 8.65. Compared to the results obtained in the previous section, the estimated elevations and backscattered powers appear to be more dispersed. In the average, however, these results demonstrate the feasibility of SAR tomography through spaceborne sensors.

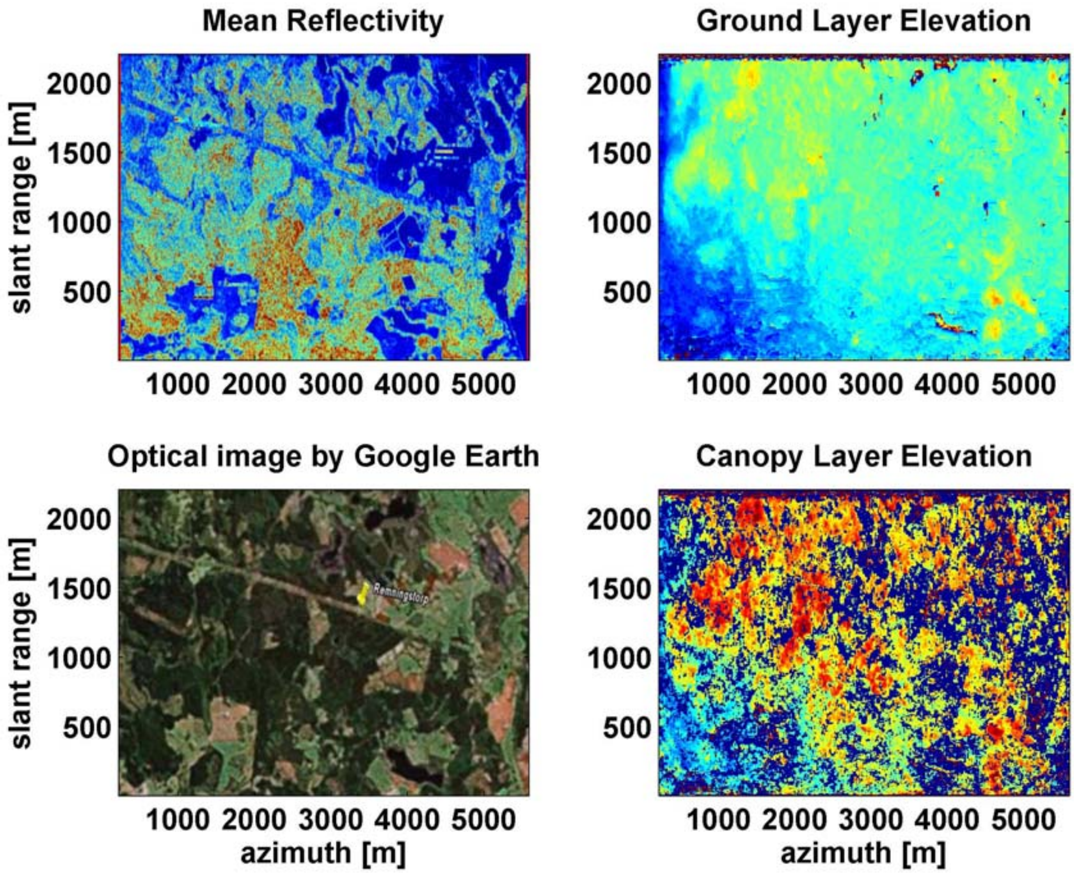

Figure 8.64: Top left: mean reflectivity of the HH channel. Bottom left: optical image by Google Earth. Top right: estimated elevations for the ground layer. Bottom right: estimated elevations for the canopy layer. The color scale of the panels relative to elevations ranges from -10 m to 50 m. The dark blue areas in the bottom right panel are identified as being bald areas.

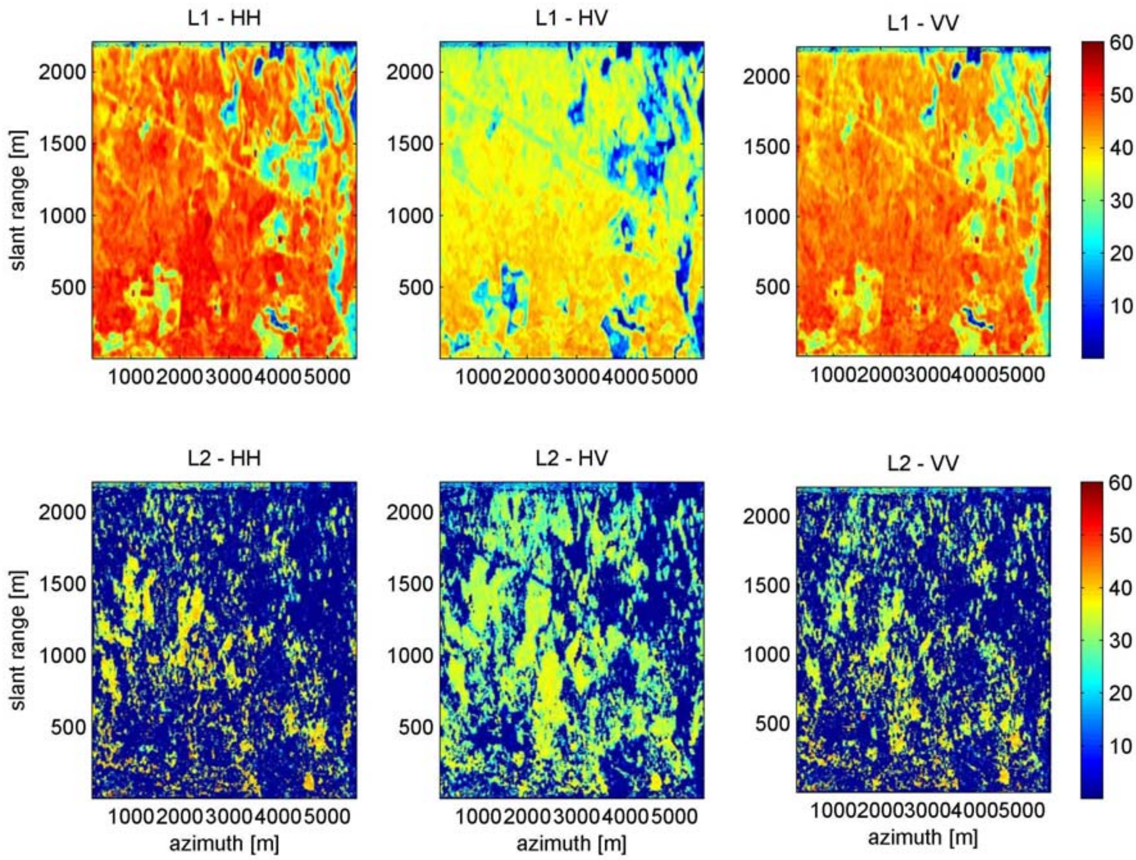

Figure 3.65: Top: estimated backscattered power (dB) from the ground layer for each polarimetric channel. Bottom: estimated backscattered power (dB) from the canopy layer for each polarimetric channel.

7.3.7 Trunks and Ground Separation through Co-Polar Analysis

The last section of this report is focused on performing a further characterization of the scene by attempting to separate the backscattered power from the ground layer into the contributions of ground and ground-trunk interactions. Similarly to section 8.3.4.5, the starting point of our analysis is the information provided by the co-polar channels. The average co-polar interferogram, obtained by averaging the 9 co-polar interferograms corresponding to each track, is shown in Fig. 8.46. Figure 3.63 reports the histogram of the co-polar phases, obtained after a spatial smoothing along the azimuth direction. Shaping the contributions from the ground layer as the result of a single bounce due to ground reflection plus a double bounce due to ground-trunk interactions, it makes sense to identify co-polar phase values around zero with ground and co-polar phase values beyond, say, 0.5 rad with trunks, accordingly to [6], [7].

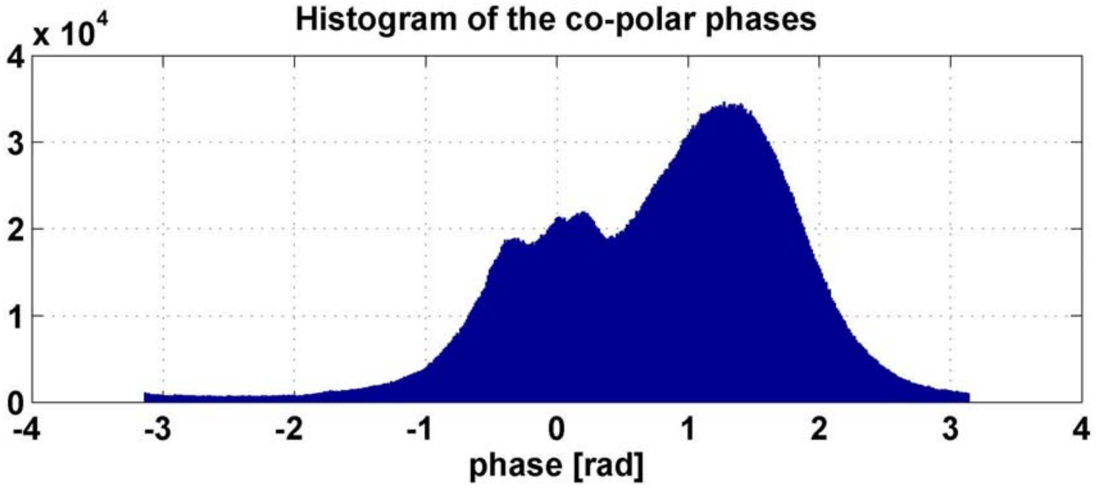

Figure 3.66: Histogram of the co-polar phases.

On this basis, we try to separate the two contributions by exploiting the following model:

$$\begin{aligned} I_{HV} &= \left(\sigma_d^2 \cdot r_{HH} r_{VV}^* + \sigma_s^2\right) \cdot \eta \\ E_{HH} &= \sigma_d^2 \cdot \left|r_{HH}\right|^2 + \sigma_s^2 \\ E_{VV} &= \left(\sigma_d^2 \cdot \left|r_{VV}\right|^2 + \sigma_s^2\right) \cdot \eta^2 \end{aligned} \qquad \text{Eq. 16}$$

where:

- E_{HH} and E_{VV} are the expected values of the energies of the HH and VV channels.
- I_{HV} is the expected value of the co-polar interferogram
- σ_d^2, σ_s^2 are the backscattered powers of double and single bounces
- r_{HH}, r_{VV} are the reflection coefficients of the double bounce contributions in the HH and VV channels;
- η is an unknown real positive number

Notice that model in
$$\begin{aligned} I_{HV} &= \left(\sigma_d^2 \cdot r_{HH} r_{VV}^* + \sigma_s^2\right) \cdot \eta \\ E_{HH} &= \sigma_d^2 \cdot \left|r_{HH}\right|^2 + \sigma_s^2 \\ E_{VV} &= \left(\sigma_d^2 \cdot \left|r_{VV}\right|^2 + \sigma_s^2\right) \cdot \eta^2 \end{aligned}$$
Eq. 16 implies that we assume statistical independence between the contributions of ground and ground-trunk interactions Solving
$$\begin{aligned} I_{HV} &= \left(\sigma_d^2 \cdot r_{HH} r_{VV}^* + \sigma_s^2\right) \cdot \eta \\ E_{HH} &= \sigma_d^2 \cdot \left|r_{HH}\right|^2 + \sigma_s^2 \\ E_{VV} &= \left(\sigma_d^2 \cdot \left|r_{VV}\right|^2 + \sigma_s^2\right) \cdot \eta^2 \end{aligned}$$
Eq. 16 with

respect to σ_d^2, σ_s^2 we obtain the desired separation between single and double bounces, see Fig. (31).To further simplify this model we pose $|r_{HH}| = |r_{VV}| = 1$, in such a way as to solve

$$I_{HV} = \left(\sigma_d^2 \cdot r_{HH} r_{VV}^* + \sigma_s^2\right) \cdot \eta$$
$$E_{HH} = \sigma_d^2 \cdot |r_{HH}|^2 + \sigma_s^2$$
$$E_{VV} = \left(\sigma_d^2 \cdot |r_{VV}|^2 + \sigma_s^2\right) \cdot \eta^2$$

Eq. 16 with respect to σ_d^2, σ_s^2 in a closed form. The results are shown in Figure 8.67.

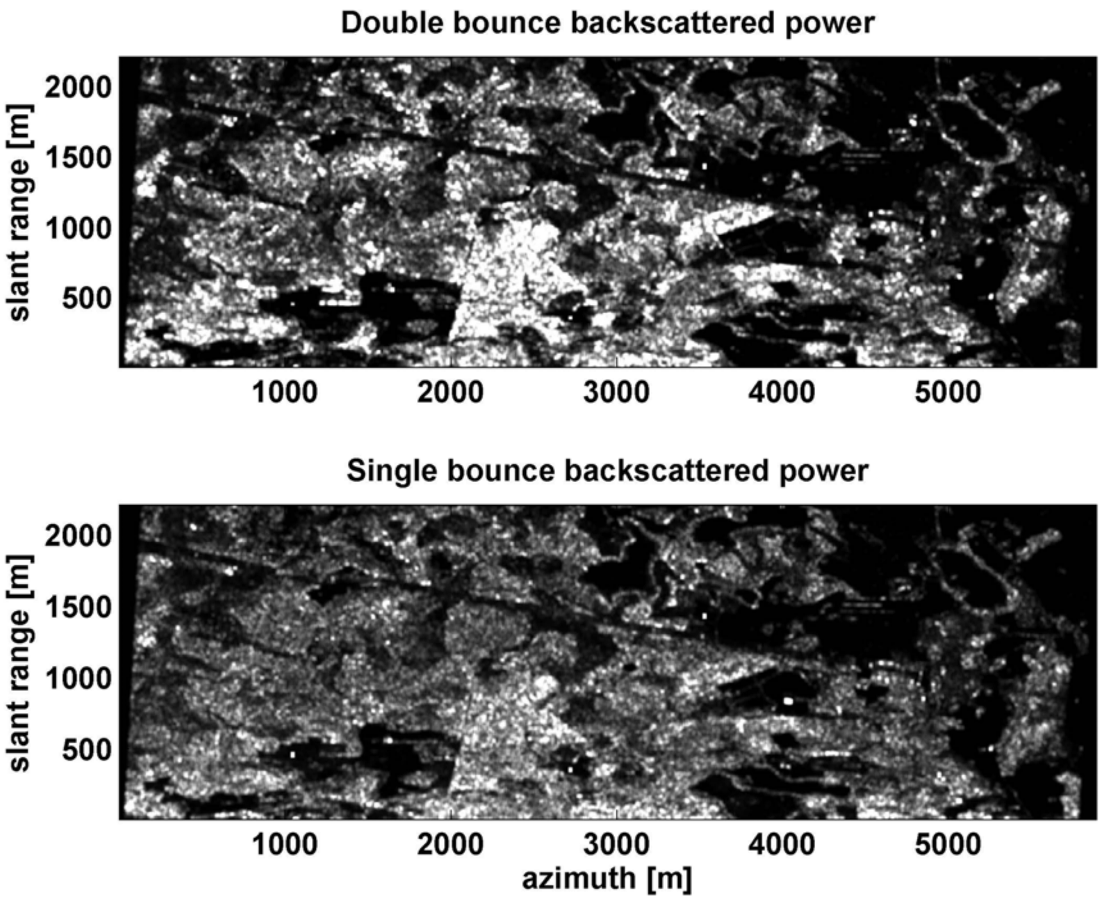

Figure 3.67: Top raw: estimated double bounce backscattered power. Bottom raw: estimated single bounce backscattered power.

It is interesting to note that, as expected, double bounce contribution are dominant in forested areas, whereas single bounce contributions are dominant in bald areas. With regard to this point, we computed the difference between the estimated backscattered powers from double and single bounces, normalized by E_{HH}, see Fig. 3.68.

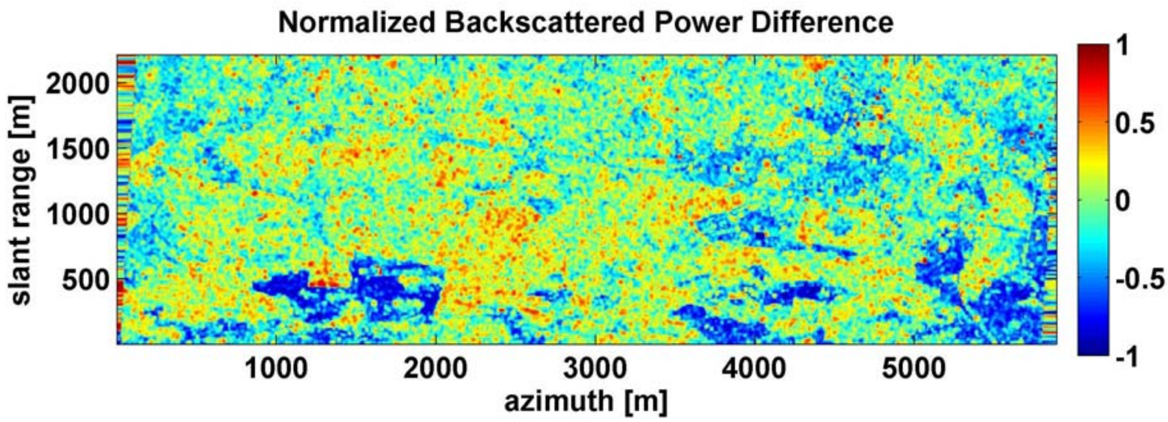

Figure 3.68: Difference between the estimated backscattered powers from double and single bounces, normalized by E_{HH}.

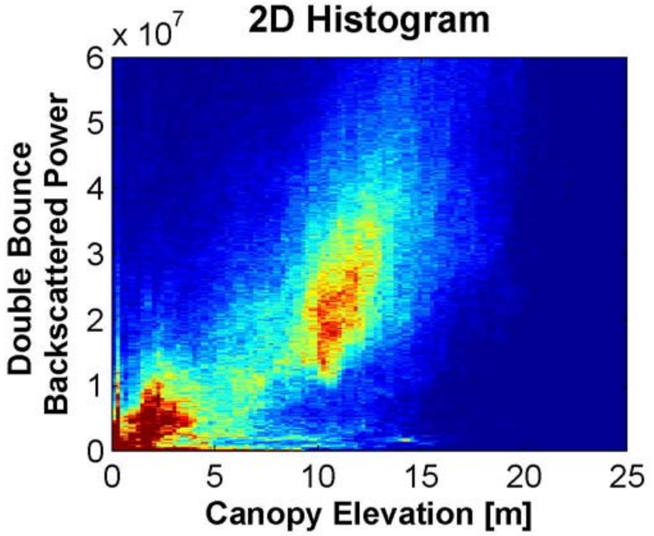

Figure 8.69: 2D histogram of the estimated double bounce backscattered power and canopy elevation measured by LIDAR. The color scale is proportional to the number of counts within each bin in the backscattered power – canopy elevation plane.

Despite the simplistic assumptions within the model in

$$I_{HV} = \left(\sigma_d^2 \cdot r_{HH} r_{VV}^* + \sigma_s^2\right) \cdot \eta$$
$$E_{HH} = \sigma_d^2 \cdot |r_{HH}|^2 + \sigma_s^2$$
$$E_{VV} = \left(\sigma_d^2 \cdot |r_{VV}|^2 + \sigma_s^2\right) \cdot \eta^2$$

Eq. 16, the results show that a significant separation between double and single bounces may be achieved exploiting the co-polar information. Some errors may be noticed. In particular, while the near range corner reflector is correctly identified as a ground component (that trihedral reflectors determine an odd number of bounces, and thus must be associated to ground [6]), the backscattered power of the far range corner is shared between the two panels in Fig. 3.67. Nevertheless, the results are encouraging. Nevertheless, the results are encouraging. Finally, Figure 8.69 reports the 2D histogram of the estimated double bounce backscattered power and canopy elevation measurements yielded by LIDAR and processed as depicted in the previous section. This figure shows that a clear correlation exists between canopy elevation and double bounce backscattered power, further confirming the importance of ground-trunk interactions in the tomographic characterization of forested areas.

7.3.8 Summary and conclusions

This work reported the results of the SAR tomographic analysis carried out on the basis of P-band airborne acquisitions over the site of Remningstorp, Sweden, finalized to testing the feasibility of P-band tomography through spaceborne SAR sensors.

The first achievement of this work is the experimental demonstration that in P-band the co-polar channels are mainly determined, as for forested areas, by ground-trunk interactions. Furthermore, it is sensible to retain that the ground-trunk phase centers are located at ground level, as witnessed by the comparison with the LIDAR data provided by FOI. On this basis, we showed that it is possible to perform a reliable phase calibration basing on natural scatterers, which is an important achievement with regard to future spaceborne applications.

An algorithm for slant range resolution enhancement has been developed and successfully applied to co-polar channels, producing a synthesized bandwidth close to the theoretical limit and avoiding the arising of side lobes. This result shows that band synthesis is practically feasible and limited only by the normal baseline span. Obtaining a significant layer cancellation results a more difficult task, due to the small baseline span and the low backscattered power from the canopy.

On the basis of a two layered model, the tomographic analysis provided a sensible identification of bald and forested areas and a separation of the backscattered powers from the ground and canopy layers for each polarimetric channel. Furthermore, these results have been replicated in the case of an azimuth resolution comparable to that of spaceborne SAR sensor, which is another important achievement to the aim of spaceborne applications.

Finally, a model has been developed to separate ground contributions from ground-trunk interactions. Despite the simplistic assumptions within this model, we obtained encouraging results. It is important to remark, however, that some of the results presented in this report could not be achieved in the case of a tilted terrain, which would result in the contributions from ground-trunk interactions to be strongly mitigated, or even zeroed, therefore loosing important information to characterize a forested area. Nevertheless, performing a tomographic analysis would still be a viable solution, due to its capability to separate the contributions from the ground and the canopy layers in presence of both point-like and distributed scattereres.

7.3.9 Future works

Carrying out this work provided us with many ideas for future researches. First of all, we intend to extend the covariance matching algorithm in such a way as to account for the information provided by the co-polar interferograms. This will allow to directly model the scene as the ensemble of ground, ground-trunk interactions, and canopy, hopefully resulting in more accurate results. Another important lead of research is the estimation of the thickness of the canopy layer. The feasibility of this task seems to be confirmed by the results obtained as for the estimation of the decorrelation constants, showing that the information about the thickness is somehow accessible. Finally, the co-polar analysis could be improved by exploiting the super-resolution reflectivity estimates obtained from the HH and VV channels.

7.3.10 References

[12] Ramon F Hanssen, Radar Interferometry: Data Interpretation and Error Analysis, Springer Verlag, Heidelberg, 2 edition, 2005.

[13] Joaquìın Munoz Sabater, Ramon Hanssen, Bert M Kampes, Adele Fusco, and Nico Adam, “Physical analysis of atmospheric delay signal observed in stacked radar interferometric data,” in International Geoscience and Remote Sensing Symposium, Toulouse, France, 21–25 July 2003, 2003

[14] S. Tebaldini and A. Monti Guarnieri, “Hybrid Cramér-Rao bounds for crustal displacement field estimators in SAR Interferometry,” IEEE Letters on Signal Processing, to be published.

[15] Alessandro Ferretti, Claudio Prati, and Fabio Rocca, “Nonlinear subsidence rate estimation using permanent scatterers in differential SAR interferometry,” IEEE Transactions on Geoscience and Remote Sensing, vol. 38, no. 5, pp. 2202–2212, Sept. 2000.

[16] Alessandro Ferretti, Claudio Prati, and Fabio Rocca, “Permanent scatterers in SAR interferometry,” IEEE Transactions on Geoscience and Remote Sensing, vol. 39, no. 1, pp. 8–20, Jan. 2001.

[17] D. Giuli, “Polarization diversity in radars,” Proceedings of the IEEE, vol. 74, no. 2, pp. 245–269, Feb. 1986.

[18] N.L.; Shackman S.J.; Wiseman D.L.; Elenbogen L.P.; Rowson R.F. Sheen, D.R.; VandenBerg, “P-3 ultra-wideband sar: description and examples,” Aerospace and Electronic Systems Magazine, IEEE, vol. 11, no. 11, pp. 25–30, Nov 1996.

[19] H.; Zink M. Seifert, F.M.; Kietzmann, “Multifrequency and polarimetric analysis of forests with sir-c/x-sar data,” Geoscience and Remote Sensing Symposium, 1996. IGARSS ’96. ’Remote Sensing for a Sustainable Future.’, International, vol. 2, pp. 1086–1088 vol.2, 27-31 May 1996.

[20] Fabio Gatelli, Andrea Monti Guarnieri, Francesco Parizzi, Paolo Pasquali, Claudio Prati, and Fabio Rocca, “The wavenumber shift in SAR interferometry,” IEEE Transactions on Geoscience and Remote Sensing, vol. 32, no. 4, pp. 855–865, July 1994.

[21] C Prati and F Rocca, “Range resolution enhancement with multiple SAR surveys combination,” in International Geoscience and Remote Sensing Symposium, Houston, Texas, USA, May 26–29 1992, 1992, pp. 1576–1578.

[22] V.; Schirinzi G. Fornaro, G.; Pascazio, “Range resolution limits in multi-pass sar data processing,” Geoscience and Remote Sensing Symposium, 2002. IGARSS ’02. 2002 IEEE International, vol. 1, pp. 182–184 vol.1, 2002.

[23] A. M. Guarnieri and S. Tebaldini, “Channel phase estimate in time variant simo systems,” in Proc. IEEE International Conference on Acoustics, Speech, and Signal Processing (ICASSP’06), Tolouse, France, May 2006, pp. 817–820.

[24] I. Ziskind and M. Wax, “Maximum likelihood localization of multiple sources by alternating projection,” IEEE Trans. Acoustics, Speech and Signal Processing, vol. ASSP-36, no. 10, pp. 1553, 1988.

[25] Richard Roy and Thomas Kailath, “ESPRIT-estimation of signal parameters via rotational invariance techniques,” Acoustics, Speech, and Signal Processing, IEEE Transactions on, vol. 37, 1989.

[26] P. Stoica, H. Li, and J. Li, “A new derivation of the apes filter,” Signal Processing Letters, , no. 6, pp. 205–206, 1999.

[27] M. Montanari F. Gini, F. Lombardini, “Layover solution in multibaseline sar interferometry,” IEEE Trans. on Aerospace and Electronic Systems, Apr. 2002.

[28] J Cadzow, “Arma spectral estimation: A model equation error procedure,” Acoustics, Speech, and Signal Processing, IEEE Transactions on, vol. 5, 1980.

[29] J. A. Cadzow, “High performance spectral estimation–A new ARMA method,” IEEE Trans. Acoustics, Speech and Signal Processing, vol. ASSP-28, no. 5, pp. 524, 1980.

[30] P. Larsson, E.; Stoica, “Direction-of-arrival estimation from incomplete data,” Acoustics, Speech, and Signal Processing, 2000. ICASSP ’00. Proceedings. 2000 IEEE International Conference on, vol. 5, pp. 3081–3084 vol.5, 2000.

[31] P. Stoica and T. Soderstrom, “on reparametrization of loss functions used in estimation and the invariance principle,” Signal Processing, , no. 17, pp. 383–387, 1989.

[32] P. Stoica B. Ottersten and R. Roy, “Covariance matching estimation techniques for array signal processing applications,” Signal Processing, , no. 8(3), pp. 185–210, 1998.

[33] A. Swindlehurst and P. Stoica, “Maximum likelihood methods in radar array signal processing,” 1998.

[34] Richard Bamler and Philipp Hartl, “Synthetic aperture radar interferometry,” Inverse Problems, vol. 14, pp. R1–R54, 1998.

[35] B. Jansson, M.; Ottersten, “Structured covariance matrix estimation: a parametric approach,” Acoustics, Speech, and Signal Processing, 2000. ICASSP ’00. Proceedings. 2000 IEEE International Conference on, vol. 5, pp. 3172–3175 vol.5, 2000.

[36] T. Bronez and J. Cadzow, “An algebraic approach to superresolution array processing,” IEEE Trans. Aerospace and Electronic Systems, vol. 19, pp. 123–133, Jan. 1983.

8 SUMMARY

The BIOSAR camapaign was conducted in spring 2007 were multi-temporal SAR acquisitions were made with a time interval of 30 and 56 days. The L- and P-band data were acquired over a consolidated test site that is located in southern Sweden Remmingstorp.

NEED TO BE DELIVERED!

9 RECOMMENDATION

NEED TO BE DELIVERED!

10 APPENDIX TOMOGRAPHY BY UNIVERSITY OF PISA

10.1 Spatial Adaptive Spectral Estimation

10.1.1 Theoretical background

The problem of the height image reconstruction for a given range-azimuth cell can be cast in the spatial spectral estimation problem of the backscattered power distribution $P(h)$ along the height dimension from the multibaseline (MB) data $\mathbf{y}$, possibly using multiple looks.

We assume to process the data from a MB cross-track array of N phase centers [1]. This is synthesized from the N repeated flight tracks of the SAR sensor over the area of interest after image coregistration and deramping (phase locking). As usual in SAR imaging and interferometry, in each SAR image we can consider M looks to reduce statistical variations, e.g. multiple homogeneous adjacent pixels. For each m-th look, $m = 1,\ldots,M$, the complex amplitudes of the pixels observed in the N SAR images at a given range-azimuth cell are arranged in the $N \times 1$ vector $\mathbf{y}(m)$. Once one of the images has been selected as master image, the phase variations of each image with respect to the master one can be expressed by means of the $N \times 1$ array steering vector $\mathbf{a}(h)$, coding the MB cross-track array response to a backscattered signal component coming from the vertical height h [1], which is a spatial harmonic:

$$a(h) = \left[e^{jk_{z,1}h} \quad e^{jk_{z,2}h} \quad \cdots \quad e^{jk_{z,N}h} \right]^T \tag{0.1}$$

Here, $k_{z,n}$ is the vertical wavenumber for the nth array phase center relative to the selected range-azimuth cell, $n = 1,\ldots,N$, which multiplied for the height h furnishes the n-th interferometric phase φ_n with respect to the master image, for which $k_{z,n} = 0$. $h = 0$ corresponds to the reference height of the deramping procedure.

Given the formulation above, several spatial spectral estimation methods can be employed to derive the height power distribution $P(h)$; in this work we considered both non-parametric and parametric techniques. The classical beamforming (multilook periodogram) and the adaptive beamforming (i.e. the Capon spectral estimator) belong to the first category, and they need only the array data covariance matrix to work. Among the parametric methods, we considered the MUSIC (multiple signal classification) spectral estimator, which is matched to elevation point-like sources. It has been shown that MUSIC can also operate under model mismatch with extended sources [2]. As it will be showed in the following, the superresolution properties of MUSIC, that are higher than those of Capon, have been exploited in the tomographic processing to distinguish in critical conditions between the ground and the canopy heights in the analysis of the P-band real data, which are characterized by a low resolution in height. As a drawback, MUSIC does not provide power information, while Capon does.

The beamforming spatial spectral estimator coincides with the classical Fourier height imaging (i.e. the periodogram), after multilook averaging. It can also be seen as belonging to the class of filterbank approaches for spectral estimation, i.e. its expression can be derived by designing a finite impulse response filter of order N that passes the spatial harmonic corresponding to the height h of interest without distortions, uniformly rejecting possible other components from noise and other heights. At the end of the algebraic manipulations, the beamforming estimate of the spectrum $P(h)$ is [2]:

$$\hat{P}_B(h) = \frac{\mathbf{a}^H(h)\hat{\mathbf{R}}\mathbf{a}(h)}{N^2}, \tag{0.2}$$

where $(\cdot)^H$ is the hermitian operator, and $\hat{\mathbf{R}}$ is the multilook estimate of the MB array data covariance matrix:

$$\hat{\mathbf{R}} = \frac{1}{M}\sum_{m=1}^{M}\mathbf{y}(m)\mathbf{y}^H(m) \tag{0.3}$$

In the Capon method [2] a set of complex array re-phasing coefficients $\mathbf{g}_c(h)$ is designed that passes the signal component coming from height h in $\mathbf{y}$ without distortion and, at the same time, attenuates the interfering total power from all the other actual signal components from noise and different heights as much as possible. The resulting spatial filter changes both with h and, notably, with the power height spectrum - thus it is data-adaptive. The produced beam shape changes during the height scan depending on the input data, strongly rejecting interference coming from scattering from other heights than the selected. This allows gains in terms of both resolution and leakage (sidelobe) level [2]. The design criterion described before [2] leads to the following expression for the filter coefficient vector:

$$\mathbf{g}_C(h) = \frac{\hat{\mathbf{R}}^{-1}\mathbf{a}(h)}{\mathbf{a}^H(h)\hat{\mathbf{R}}^{-1}\mathbf{a}(h)}. \tag{0.4}$$

The Capon estimate $\hat{P}_C(h)$ of the tomographic power profile is then given by:

$$\hat{P}_C(h) = \mathbf{g}_C^H\hat{\mathbf{R}}\mathbf{g}_C \tag{0.5}$$

Since the data vector can be affected by residual array calibration errors, to mitigate the Capon non linear radiometric effects (e.g. self cancellation phenomenon), and to ensure stability in the inversion of the sample covariance matrix (0.3) a diagonal loading of $\hat{\mathbf{R}}$ can be included in the filter calculation as follows:

$$\hat{\mathbf{R}}_L = \hat{\mathbf{R}} + \delta \hat{\sigma}_V^2 \mathbf{I} \tag{0.6}$$

where $\hat{\sigma}_V^2$ is an estimate of the thermal noise power. It is worth noting that there is not any simple rule for the choice of the loading factor δ; this parameter is usually determined empirically in the analysis of the data.

MUSIC is a parametric spectral estimation method which was originally conceived for the estimation of the frequency of sinusoidal signals embedded in additive white noise, and it relies on the eigen-decomposition of the covariance matrix (0.3). The set of eigenvalues of $\hat{\mathbf{R}}$ can be split into two subsets. Denote

with $\{\lambda_1 \quad \cdots \quad \lambda_N\}$ the eigenvalues of $\hat{\mathbf{R}}$ arranged in nonincreasing order. For elevation point-like sources, i.e. in absence of speckle (viz. multiplicative noise) baseline decorrelation, the following property holds:

$$\begin{cases} \lambda_k > \sigma_V^2 & \text{for } k = 1, \ldots, N_S \\ \lambda_k = \sigma_V^2 & \text{for } k = N_S + 1, \ldots, N \end{cases} \tag{0.7}$$

where N_S is the number of backscattering sources ($N_S < N$) and σ_V^2 is the noise power. Denote with $\{\mathbf{s}_1 \quad \cdots \quad \mathbf{s}_{N_S}\}$ the eigenvectors corresponding to the first N_S eigenvalues, and with $\{\mathbf{g}_1 \quad \cdots \quad \mathbf{g}_{N-N_S}\}$ the eigenvectors corresponding to the remaining $N - N_S$ eigenvalues. Then define $\mathbf{S} = [\mathbf{s}_1 \quad \cdots \quad \mathbf{s}_{N_S}]$ and $\mathbf{G} = [\mathbf{g}_1 \quad \cdots \quad \mathbf{g}_{N-N_S}]$ the matrices which collect the so-called ``signal'' and the ``noise'' eigenvectors, respectively. The MUSIC (pseudo) spectral estimator is then given by [2]:

$$\hat{P}_M(h) = \frac{1}{\mathbf{a}^H(h)\mathbf{G}\mathbf{G}^H\mathbf{a}(h)} \tag{0.8}$$

It is worth noting that to perform a spectral estimation with MUSIC, the number of backscattering sources (model order) in the same range-azimuth cell must be a priori known (or estimated from the available data). For our analysis, we have fixed the MUSIC order to $N_S = 2$ (ground and canopy contributions) for all the analyzed cells.

10.1.2 Spatial spectral analyis of simulated data.

We carried out an extensive simulated analysis to assess the performance obtainable with the adaptive tomographic processing in the estimation of the height power distribution and of the height of the centroids of the layers in the observed scenario. The data vector $\mathbf{y}$ has been generated with a set of system parameters which correspond to those adopted by DLR's E-SAR

BioSAR campaign in the P-band data acquisition (see Table 1.1), considering the bandwidth reduction that will be applied to the real data to emulate the BIOMASS satellite. The reference scenario is constituted by a layer compact in height to represent the ground component, and a distributed layer to represent the tree canopy above the ground.

Using the parameters of Table 1.1 it is possible to calculate the height resolution and the ground-range resolution, the extension of the height unambiguous range, the critical baseline, and the ratio between orthogonal baseline and critical baseline (b), which controls the baseline decorrelation. These quantities have been calculated for three different look angles, 30° (near range), 43.6° (mid range), and 45° (far range), and they have been reported in Table 1.2.

Carrier frequency	350 Mhz (P-band)
System bandwidth	6 MHz
Horizontal baselines (m)	0, 10, 20, 30, 40, 50, 60, 70, 80
Flight height	3900 m
Look angle	from 25° to 50° (near range - far range)

Table 1.1.: System parameters used for the statistical analysis.

Parameter	$\theta = 30°$ (near range)	$\theta = 43.6°$ (mid range)	$\theta = 45°$ (far range)
Height resolution (m)	19.3	27.5	29.6
Ground-range resolution (m)	50	36.3	35.4
Height unamb. range (m)	154.3	219.8	236.4
Critical orthogonal baseline (m)	44.6	87.9	94.6
b	1.6	0.7	0.6

Table 1.2: Parameters characterizing the acquisition; b is the orthogonal-to-critical baseline.

In this hypothesis, the signal model which has been used to generate statistically the data can be written as:

$$\mathbf{y}(m) = \sqrt{P_g}\,\mathbf{x}_g(m) \odot \mathbf{a}(h_g) + \sqrt{P_g}\,\mathbf{x}_g(m) \odot \mathbf{a}(h_g) + \mathbf{v}(m) \qquad (0.9)$$

where subscript g stands for “ground” and subscript c for “canopy”, for $m = 1,\dots,M$, being M the number of independent looks. More in detail:

- $P_{(g,c)}$ is the power of each backscattering layer;
- $x_{(g,c)}(m)$ is the $N \times 1$ speckle vector of the corresponding layer; it has been assumed as a spatially (baseline) correlated complex Gaussian process. Further details about the speckle correlation are given in the following;
- “$\odot$” is the Shur-Hadamard product between vectors, performing an element-by-element product;
- $\mathbf{a}(h_{(g,c)})$ is the steering vector defined by (0.1) corresponding to each layer centroid $h_{(g,c)}$.

The elements of the speckle array autocovariance matrix $\mathbf{R}_{x,(g,c)}$ are set according to the hypothesized spatial spectral density of the speckle (i.e. the height distribution of the layer) and the effect of the projection of the range resolution cell along the cross-range direction. Since the two layers are assumed homogeneous in height, the resulting height power profile is given by a convolution between a rectangular spectrum (the power spectrum of the layer), whose largeness is given by the layer extension in height, and a sinc2-shaped spectrum, which models the mentioned projection effect. As a consequence, for uniform baselines, the (i,j)-th element of $\mathbf{R}_{x,(g,c)}$ is given by:

$$
\left[\mathbf{R}_{x,(g,c)}\right]_{i,j} = \begin{cases} \dfrac{1}{N-1}\operatorname{sinc}\left[\dfrac{\Delta h_{(g,c)}}{N-1}(i-j)\right]\left[1-\dfrac{|i-j|W_{(g,c)}}{2(N-1)}\right] & \text{for } |i-j| \le 2(N-1)/W_{(g,c)} \\ 0 & \text{otherwise} \end{cases} \tag{0.10}
$$

where $\Delta h_{(g,c)}$ is the layer thickness expressed in vertical height resolution units, and $W_{(g,c)}$ is the extension of the projection of the ground-range resolution cell along the normal-to-slant range direction (or the height direction), normalized with respect to the normal-to-slant range resolution (or height resolution).

10.1.3 Results of the simulated analysis

In this Section, the results of the simulated analysis are reported of two different scenarios, related to two different heights of the canopy centroid. The tomographic profiles have been derived with the Capon method; the classical beamforming has been also reported for comparison. It is worth noting that in this framework, where no residual calibration error is present, the Capon beamformer has been used without loading, and it provided acceptable results. However, in the experiments with real data, the loading will be necessary.

The canopy layer has been assumed with an extension of 8 m in height. The layer centroid has been fixed to 23 m and 33 m over the ground. The ground layer has been assumed with a height extension of 0.6 m from local tilt and roughness, centered around 0 m. The backscattered power of the canopy layer has been assumed 2.5 times the backscattered power of the ground layer; the total signal-to-noise ratio is 20 dB. The tomographic processing has been carried out by processing 32 independent looks. It is worth noting that this power distribution may mimic a cross-polarized (e.g. HV) acquisition.

We also measured the statistical accuracy and the precision in the extraction of the heights of the canopy and the ground layers from the tomographic profile. To carry out this statistical analysis, the following procedure has been employed. First of all, a separation threshold is fixed at the mid distance between the centroids (i.e., 11.5 m or 16.5 m depending on the analyzed scenario). Then, the position of the two strongest peaks in the tomographic profile is calculated and depending on their position with respect to the threshold, they are classified as canopy or terrain. If the two candidate peaks are on the same side of the threshold, the weaker peak is discarded, and a third peak is searched in the other side. This procedure furnishes two labelled centroid estimates corresponding to the two physical layers which are present in the scene.

Figure 1.1 reports tomographic profiles (vertical height) obtained with beamforming and Capon for the conditions of near, mid and far range in presence of the ground layer only. It is apparent that Capon maintains its high resolution capabilities also in far range, whereas beamforming degrades. The measured accuracy and precision in the ground centroid height estimation in this case study are reported in Table 1.3; these values have been calculated by means of 1000 Monte Carlo runs. Some comments are in order. First of all, biases equal to 0.0 have been reported in the table, since the simulation furnishes a value of the order of the mm. Since these biases should be equal to 0 for reasons of symmetry, the simulation is in good agreement with the theory. Secondly, even if Capon peaks are sharper than beamforming peaks, it has been observed a reduced precision in the centroid estimation with respect to beamforming, especially in near range. This is due to the fact that the baseline decorrelation (b higher) is stronger in near range, and Capon is more sensitive than beamforming to this kind of effect for very high orthogonal-to-critical baseline ratios, as outlined also by the theoretical analysis in [2].

		BEAMFORMING		CAPON	
		Terrain	Canopy	Terrain	Canopy
NEAR RANGE					
	Bias (m)	0.0	-	0.0	-
	Std (m)	0.7	-	1.3	-
MID RANGE					
	Bias (m)	0.0	-	0.0	-
	Std (m)	0.6	-	0.8	-
FAR RANGE					
	Bias (m)	0.0	-	0.0	-
	Std (m)	0.7	-	0.7	-

Table 1.3: Estimation performance of the layer centroids heights obtained with the two analyzed tomographic processor in the ground layer only scenario.

Figure 1.2 shows the tomographic profiles obtained with the same two methods when the canopy centroid is placed at 30 m and again for the conditions of near, mid and far range. Estimation precision and accuracy are reported of the layer centroid heights in Table 1.4. Both tomographic techniques are able to distinguish between the two layers, however it is apparent the superiority of Capon in deriving the tomographic profile in terms of both resolution and sidelobe level. Concerning the centroids estimation performance, beamforming accuracy and precision worsen at the increase of the range coordinate, whereas Capon now tends to have stable efficiency. Moreover, Capon now tends to be better than beamforming in the centroid estimation in mid and far range. It is also worth noting that the precision of Capon tends to be quite similar for terrain and canopy. Conversely, beamforming furnishes much better estimates of the canopy centroid in mid and far range than the ground centroid estimates. In fact, the terrain is detected with more difficulties in mid and far range, because of the reduced resolution in height and its lower power with respect to the canopy layer.

		BEAMFORMING		CAPON	
		Terrain	Canopy	Terrain	Canopy
NEAR RANGE					
	Bias (m)	0.1	<0.1	<0.1	<0.1
	Std (m)	0.9	0.9	1.1	1.5
MID RANGE					
	Bias (m)	-0.2	<0.1	0.1	<0.1
	Std (m)	1.5	0.8	1.0	1.0
FAR RANGE					
	Bias (m)	-0.6	0.2	0.3	0.1
	Std (m)	2.0	1.0	1.1	0.9

Table 1.4: Estimation performance of the layer centroid heights obtained with the two analyzed tomographic processors; canopy centroid 33 m.

A more challenging scenario is that reported in Figure 1.3, where the canopy centroid has been moved down to 23 m. As showed in Figure 1.3, beamforming can detect correctly the terrain layer only in near range, whereas in mid and far range generally fails. Conversely, Capon is able to detect both layers also in far range. Without any labelling strategy for the peak extraction, beamforming detects the terrain layer with a probability of the 16% in mid range, and a probability of the 6% in far range; these probabilities have been evaluated again over 1000 Monte Carlo runs. By adopting the refined strategy for centroid estimation based on fixing a labelling threshold, the obtained performance is summarized in Table 1.5. From the table, it is apparent that also Capon still exhibits some non-negligible inaccuracies in terrain centroid estimation; however it is generally more efficent than beamforming in estimating the canopy centroid.

For the sake of completeness, Figures 1.4-1.6 report the tomographic profiles averaged over 100 realizations. In these figures, they have been superimposed to the graphs showing the power level and the extension of the true height profile which has been considered to generate the data in the case study under analysis.

To conclude with the simulated analysis, we considered also a case study with 17 uniform baselines and a total baseline of 160 m. Given the improved interferometric sensitivity due to the longer total baseline, it is expected an improvement in the estimation accuracy and precision of the centroid estimation for both layers, also in the more challenging case of canopy centroid at the height of 23 m. This improvement is confirmed in Table 1.6, and in the Figures 1.7-1.8.

		BEAMFORMING		CAPON	
		Terrain	Canopy	Terrain	Canopy
NEAR RANGE					
	Bias (m)	0.4	-0.1	0.1	-0.1
	Std (m)	1.1	1.0	1.1	1.5
MID RANGE					
	Bias (m)	-12.5	-0.7	-1.5	0.1
	Std (m)	20.7	1.7	8.6	1.0
FAR RANGE					
	Bias (m)	-24.5	-1.1	-2.3	0.1
	Std (m)	31.2	2.8	10.2	1.0

Table 1.5: Estimation performance of the layer centroid heights obtained with the two analyzed tomographic processors; canopy centroid 23 m.

		Beamforming		Capon	
		Terrain	Canopy	Terrain	Canopy
Near range					
	Bias (m)	<0.1	<0.1	0.2	<0.1
	Std (m)	1.4	1.5	1.8	1.9
Mid range					
	Bias (m)	0.4	-0.1	<0.1	<0.1
	Std (m)	0.9	0.8	1.0	1.5
Far range					
	Bias (m)	0.5	-0.2	0.1	-0.2
	Std (m)	1.0	0.8	1.0	1.4

Table 1.6: Estimation performance of the layer centroids heights obtained with the two analyzed tomographic processors; canopy centroid 23 m, total baseline length 160 m.

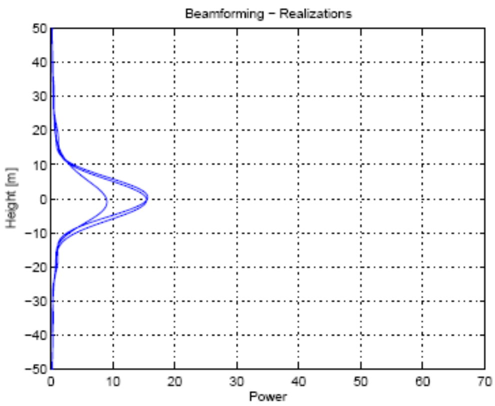

(a) Beamforming - Near range

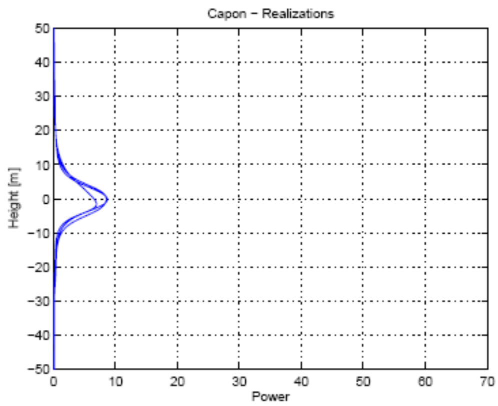

(b) Capon - Near range

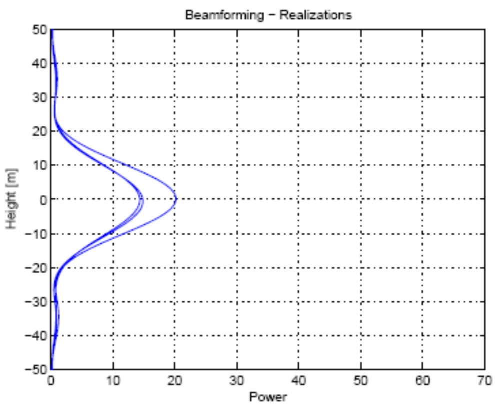

(c) Beamforming - Mid range

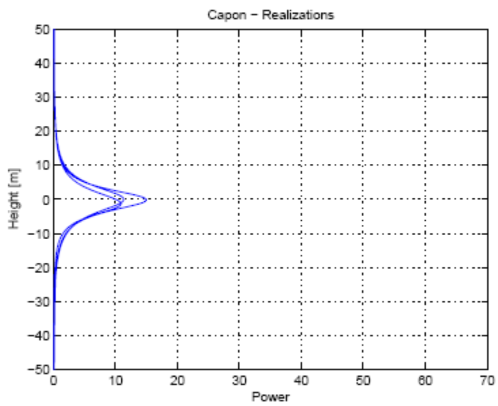

(d) Capon - Mid range

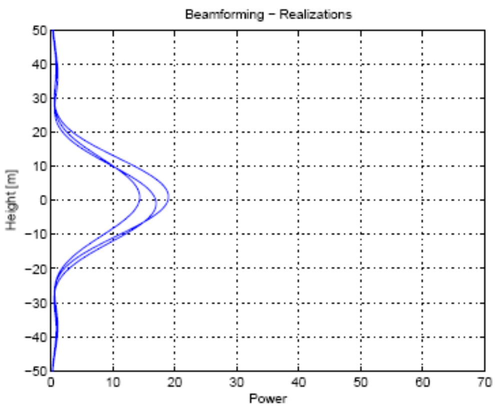

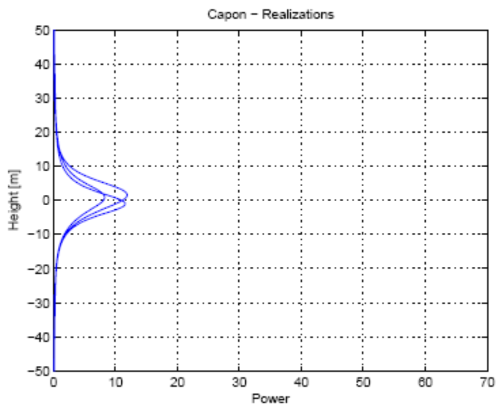

Figure 1.1: Realizations of tomographic profiles with the ground layer only.

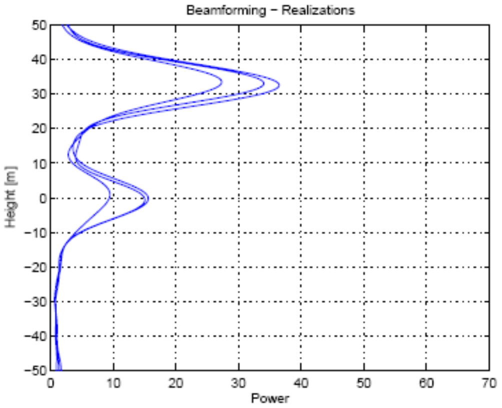

(a) Beamforming - Near range

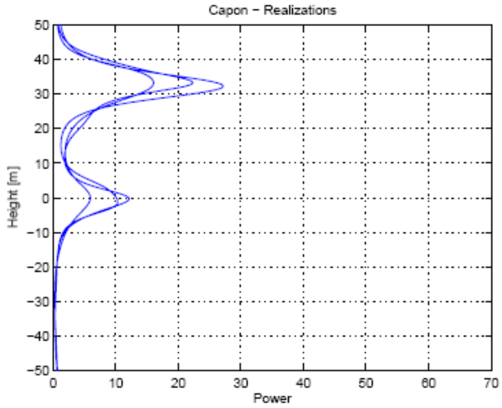

(b) Capon - Near range

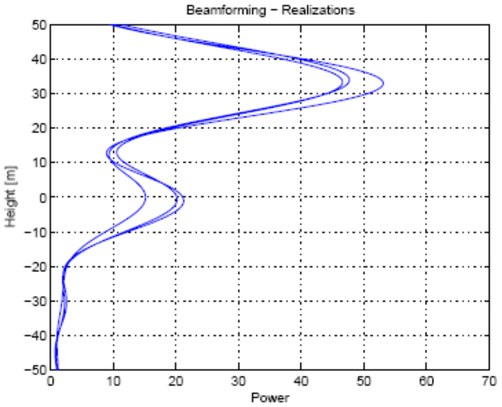

(c) Beamforming - Mid range

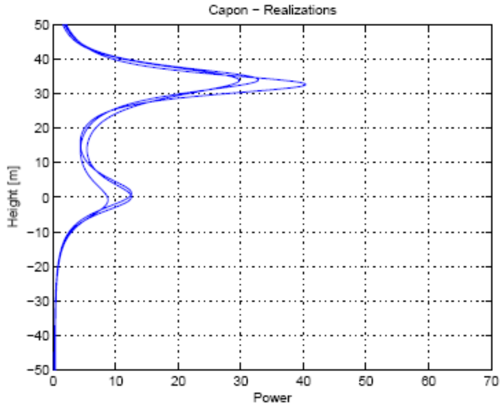

(d) Capon - Mid range

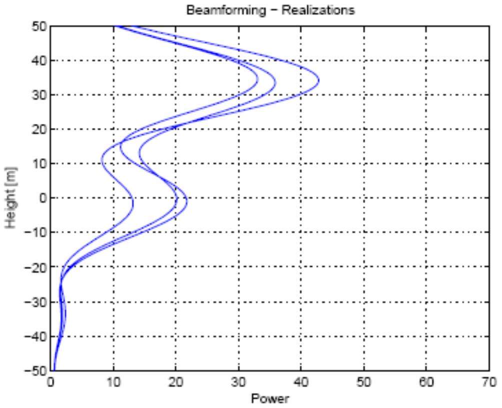

(e) Beamforming - Far range

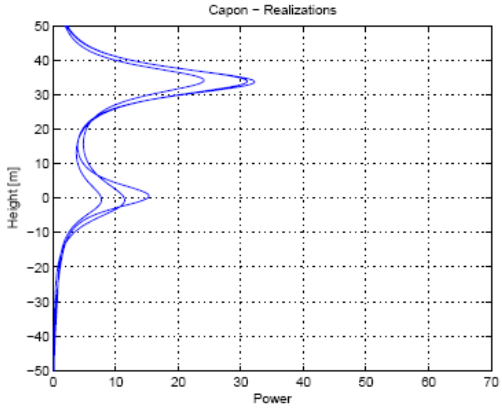

(f) Capon - Far range

Figure 1.2: Realizations of tomographic profiles; canopy centroid height: 33 m.

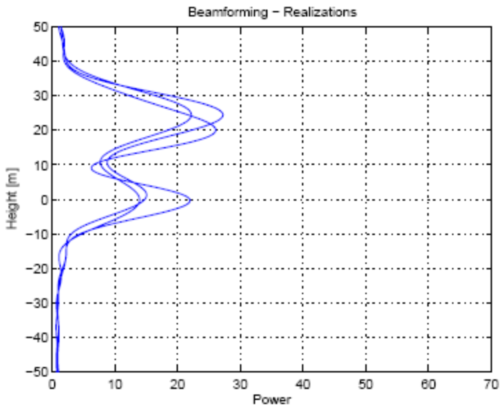

(a) Beamforming - Near range

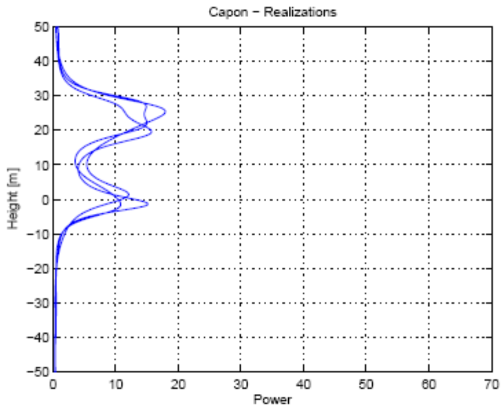

(b) Capon - Near range

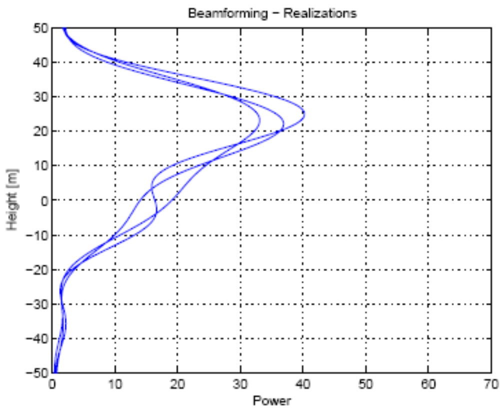

(c) Beamforming - Mid range

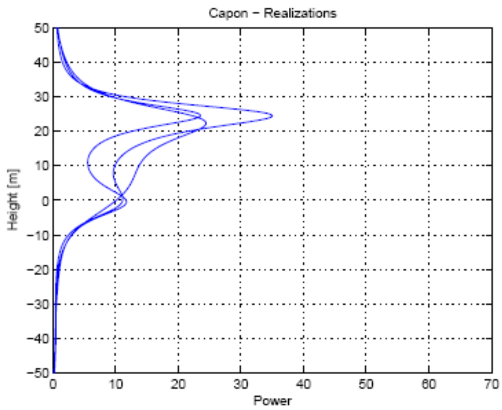

(d) Capon - Mid range

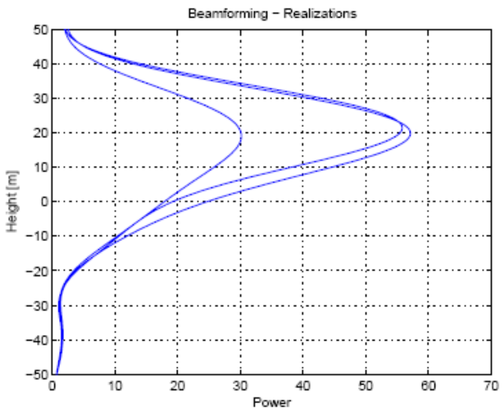

(e) Beamforming - Far range

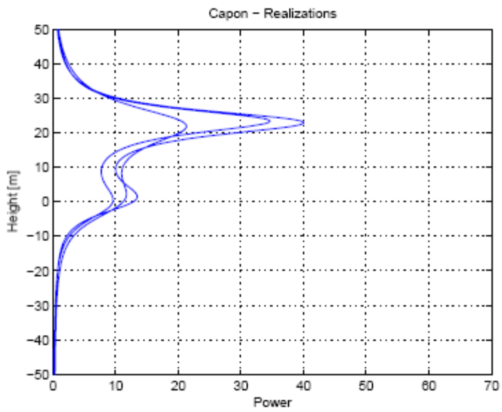

(f) Capon - Far range

Figure 1.3: Realizations of tomographic profiles; canopy centroid height: 23 m.

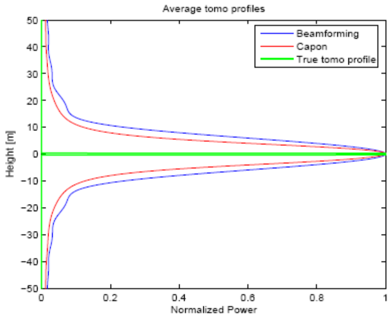

(a) Near range

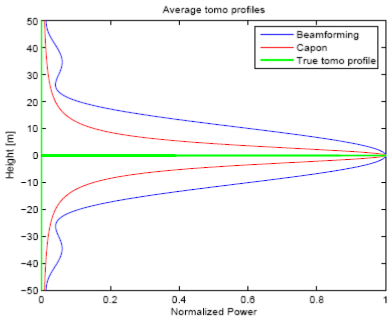

(b) Mid range

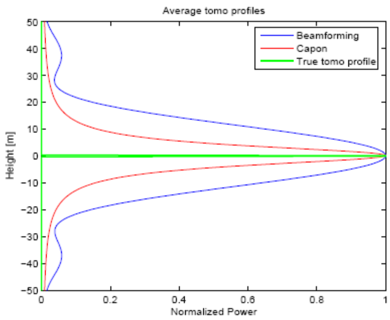

(c) Far range

1.4 Ground layer only

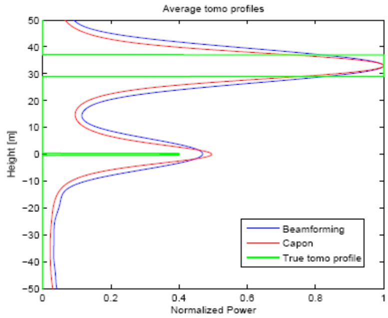

(a) Near range

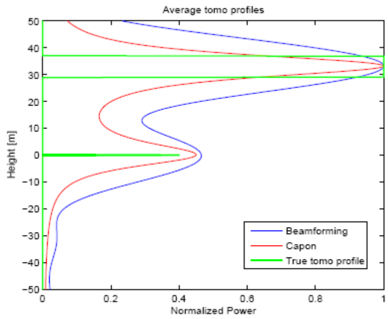

(b) Mid range

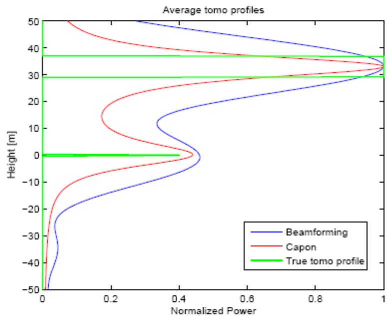

(c) Far range

1.5 Canopy height: 33 m

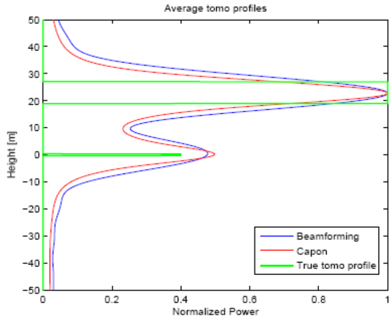

(a) Near range

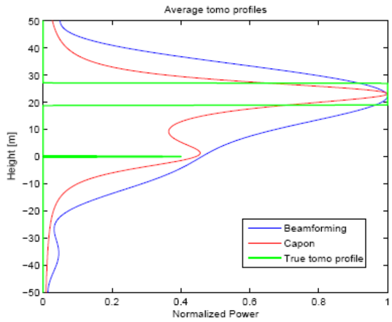

(b) Mid range

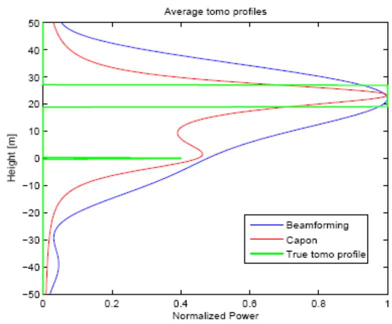

(c) Far range

1.6 Canopy height: 23 m

Figure 1.4-1.6: Average tomographic profiles

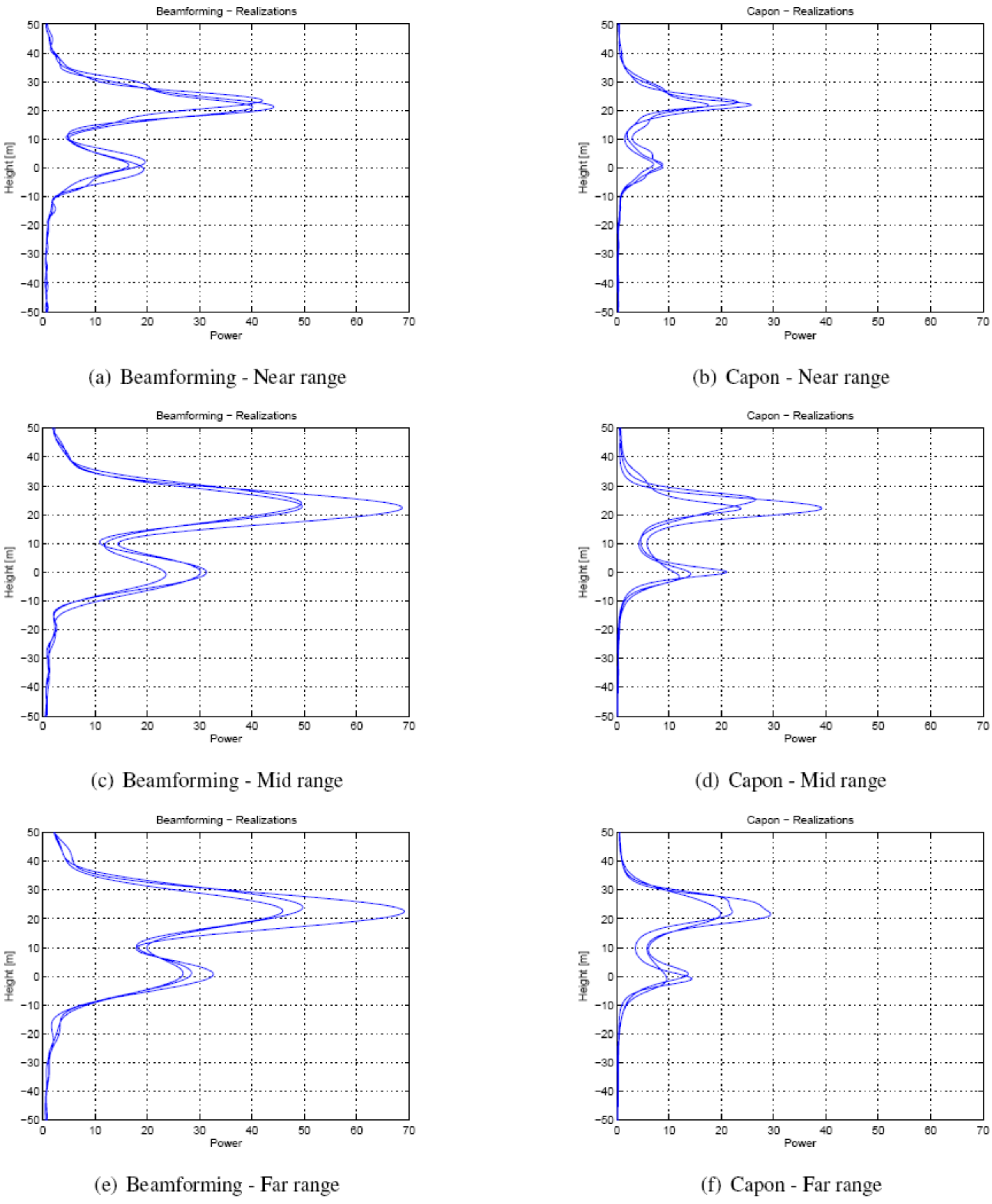

(a) Beamforming - Near range

(b) Capon - Near range

(c) Beamforming - Mid range

(d) Capon - Mid range

(e) Beamforming - Far range

(f) Capon - Far range

Figure 1.7: Realizations of tomographic profiles; canopy centroid height: 23 m, total baseline length 160 m.

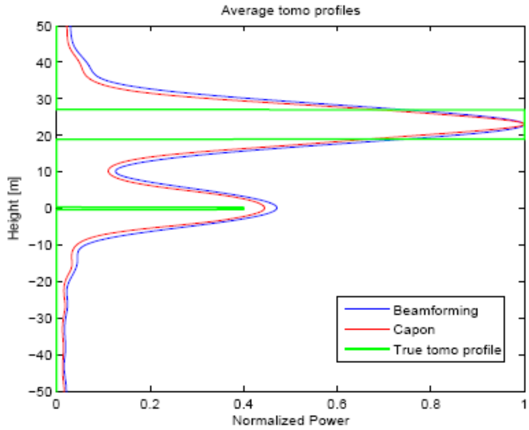

(a) Near range

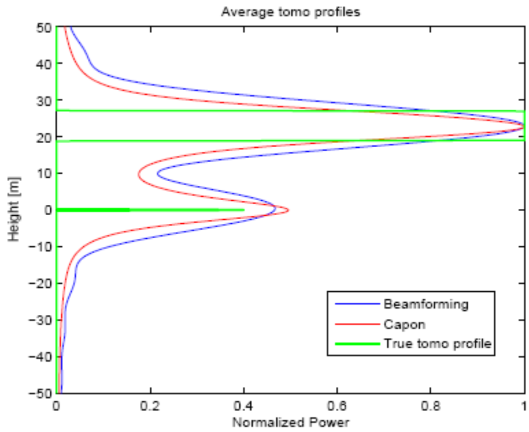

(b) Mid range

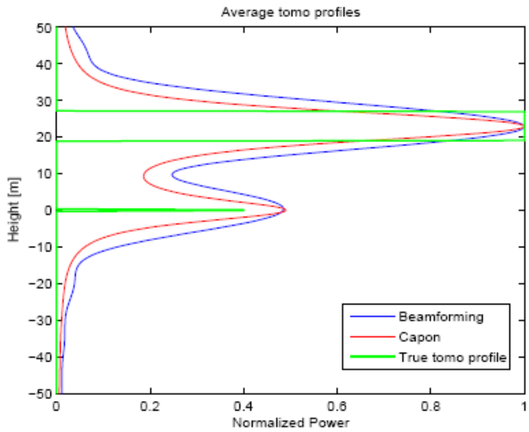

(c) Far range

Figure 1.8: Average tomographi profiles; canopy centroid height: 23 m, total baseline length 160 m.

10.2 Spatial spectral analysis of real data

In this section we present the results of the adaptive tomographic processing on the real P-band data acquired by DLR with the E-SAR airborne platform over the site of Remningstorp (Sweden). In particular, we focused on the three range lines corresponding to the lines containing the two corner reflectors and the point-like scatterer present in the scene; they are indicated in Figure 1.9. Beamforming is also considered as a reference, together with MUSIC tomography.

To emulate the range and azimuth resolutions of the BIOMASS satellite mission, we firstly applied a moving-window filtering along the two coordinates. In particular:

- the slant-range filtering has been carried out by means of a filter coefficient set according to a design criterion based on the Hamming window. We calculated 200 coefficient in order to include some sidelobes in the impulse response (see Figure 1.10);
- the azimuth filtering has been carried out with a set of 17 constant unitary coefficients.

After this filtering (conservative case), the resulting image has not been decimated, to maintain the same bin grid of the original. Moreover, the processing compensates for all the shifts coming from transient effects due to filtering.

The tomographic processing has been performed after a selection of 9 images (from the 14 available) corresponding to the nominal baselines reported in Table 1.1. The multilook coherent averaging has been implemented in order to achieve a final tomographic ground range-azimuth resolution cell of 50 m $\times$ 50 m (at near range). For this reason, we considered a number of range and azimuth bins $M_r = 17$ and M_a looks respectively. Accounting for the emulated satellite resolution, this corresponds to about $M = 4$ looks. We considered both a co-polar (HH) and a cross-polar (HV) polarization. For the forested areas, in HH polarization, it is expected that the dominant scattering mechanism is the double bounce between terrain and tree trunks, with a low canopy scattering. This can affect negatively the identification of the terrain and canopy contribution, unless the superresolution adaptive algorithm with leakage suppression capabilities, or the parametric MUSIC algorithm, is employed. Conversely, it is expected the HV polarization to be more sensitive to the scattering coming from the canopy, with terrain level scattering low.

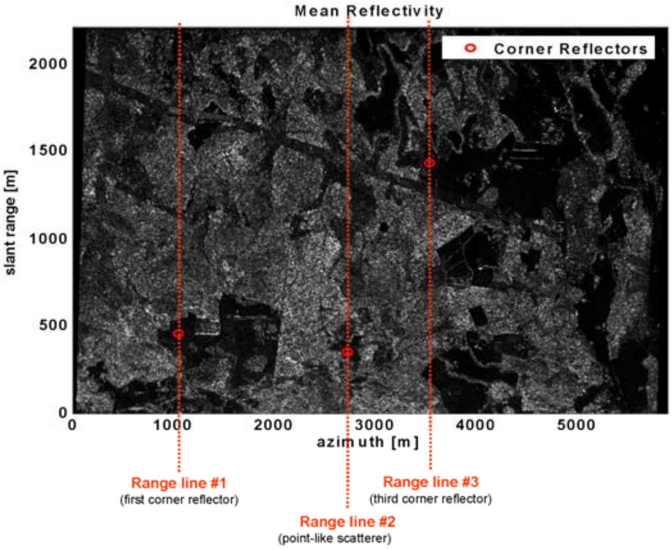

Figure 1.9: Range lines considered for tomographic image extraction.

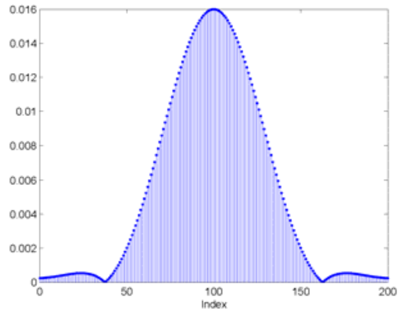

Figure 1.10: Impulse response of the FIR filter for range filtering.

10.2.1 HH polarization

10.2.1.1 Range line #1

Figure 1.11 shows a portion including the first corner reflector of the incoherent MB average of the selected 9 SAR images in HH polarization with full resolution as acquired by E-SAR, with azimuth bin spanning from 860 to 1460 and the range bin from 0 to 1200 (absolute coordinates). It is clearly visible the corner reflector. Figure 1.12 shows the same image after range and azimuth filtering for the resolution reduction. Some structures present in the upper part of the image are lost, whereas it is still visible the terrain area around the corner.

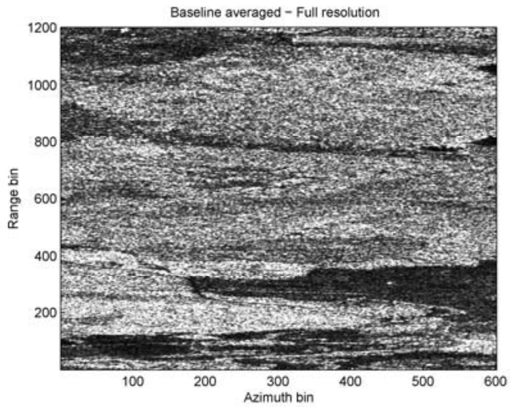

Figure 1.11: SAR image for the first analyzed range line, full resolution.

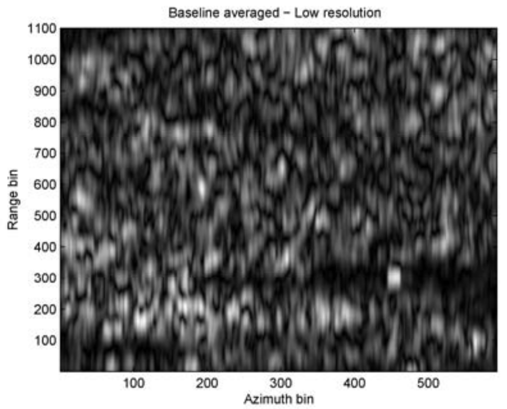

Figure 1.12: SAR image for the first analyzed range line, satellite resolution.

The first range line analyzed is at the absolute azimuth bin 1414 (454 relatively to the selected sub-image); the range coordinate span from bin 1 to bin 1100. First of all, we calculated the nominal point spread function (PSF) over that range line, which is shown in Figure 1.14 (reported in amplitude, with the vertical axis showing height in meters). Observing the enlargement of the PSF mainlobe at the increase of the range bin, it is apparent the reduction of height resolution which has been pointed out in the previous Section. Moreover, it has an ideal sinc shape around zero height, but an inflated sidelobe arises for positive heights. This is because the actual baselines are slightly non-uniform, differently from the nominal conditions.

In a second stage of the analysis, we extracted the tomo profile in correspondence of the corner reflector (rg. bin 303, relative az. bin 454) from the full resolution images. As shown in Figure 1.14, this profile is very different from the PSF in that range coordinates. As a consequence, a further re-calibration step is needed before proceeding with the tomographic processing. Two different re-calibration strategies can be followed:

- a recalibration based on interpolated sparse grid of point-like scatterers (marked 'boxcar average');
- a phase lock over the corner.

The second strategy is expected to be more efficient locally around the corner, whereas the first can be employed to re-calibrate larger areas; moreover, the second strategy fixes the corner height to zero, and can introduce a tilt effect along range. The tomo profiles in correspondence of the corner reflector obtained after recalibration with both strategies are reported in Figure 1.5. The result obtained with both strategies is quite similar, and now resembles the PSF in that point (Figure 1.13). Of course, the tomo profile obtained with the point phase lock is exactly the PSF.

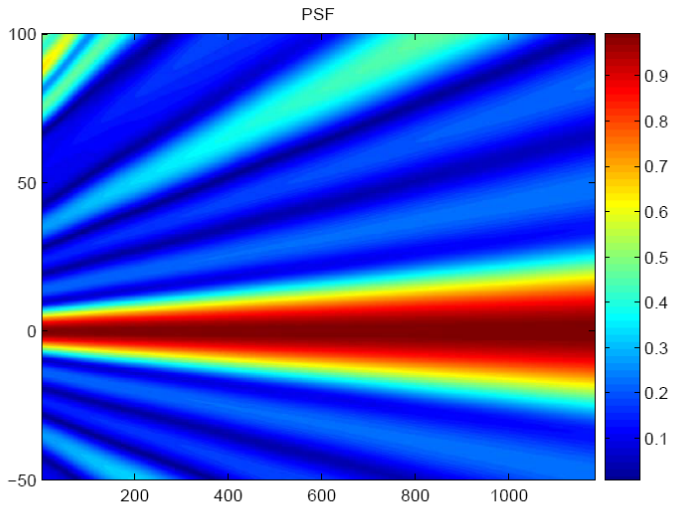

Figure 1.13: Nominal height PSF calculated for the range line #1.

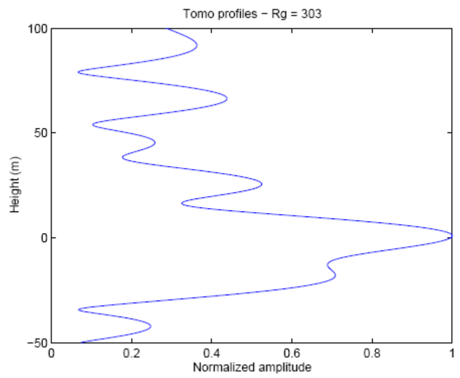

Figure 1.14: Beamforming tomo profile in correspondence of the corner reflector (rg. bin 303, relative az. bin 454), before re-calibration.

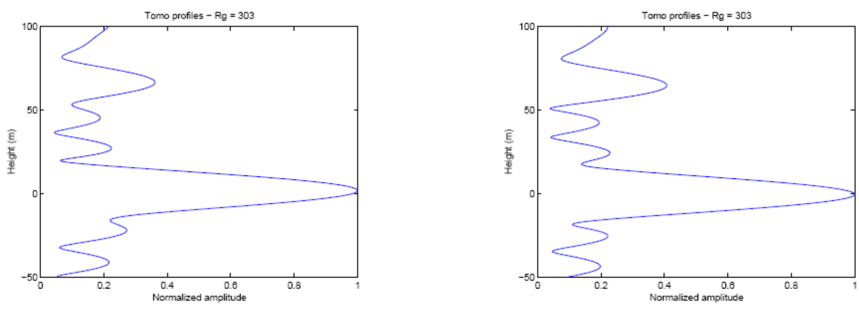

(a) Boxcar average phase lock (b) Phase lock on the corner

Figure 1.15: Beamforming tomo profiles in correspondence of the corner reflector (rg. bin 303, relative az. bin 454), after re-calibration.

After this re-calibration, the data can be processed to extract the tomo images (tomo sections) at the selected azimuth coordinate. This has been carried out on the satellite resolution level data. A common band filtering can produce some benefits. Concerning the Capon method, we applied the diagonal loading in the adaptive filtering with a factor $\delta = 5$. This has been chosen as a trade off between non-linearity mitigation and superresolution preservation. The tomographic images have been extracted again at the relative azimuth bin 454. In order to test the progressive resolution enhancement given by the three spectral estimation methods, the range segment containing the corner (i.e. from absolute rg. bin 1 to rg. bin 350) has been considered firstly. The tomo images obtained with beamforming, Capon and MUSIC (sparse grid recalibration) are shown in Figure 1.16; it is apparent that the highest height superresolution is achieved with MUSIC, with also a progressive sidelobe cleaning. However, the MUSIC amplitude is not a signal amplitude. Conversely, the Capon tomo section contains signal amplitude information with satisfactory superresolution and sidelobe cleaning.

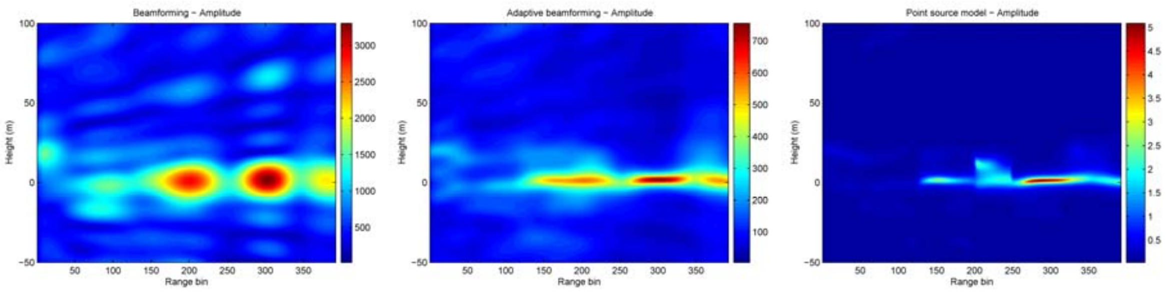

Figure 1.16: Tomo images in correspondence of the corner reflector (absolute rg. bin 1-350, relative az. bin 454), after sparse grid re-calibration.

Figure 1.17 shows the tomo images obtained with the two re-calibration strategies on the whole selected range line. Beamforming cannot resolve the two layers; also, by comparing these images with the PSF, the sidelobes are clearly visible. Thanks to its leakage suppression capabilities, Capon furnishes much better results (Figure 1.18). However, the forest scattering contribution is still not clearly visible for much part of the tomo image, except for the range interval between bin 700 and bin 800. In fact, here the estimated spatial spectrum is quite asymmetric along the height dimension, indicating the presence of a possible canopy between the ground level (clearly visible) and a height of about 30 m, which is reasonable for a forest in this area. However, it is worth noting that canopy centroid remains still unresolved. Finally, Figure 1.19 shows the tomo images on the same range line obtained with MUSIC; the ground profile is further superresolved, and the presence of a possible forest is confirmed between range bins 700 and 800, even if it is not clearly visible in the figure due to the high MUSIC amplitude of other scatterer.

Further indications are given by the tomographic profiles in height, for example those extracted at range bin 753 (Figure 1.20). In fact, observing the Capon and MUSIC spectral estimates it is apparent the presence of another scatterer different from the terrain, since the spectra exhibit a large inflection point over the dominant peak of the terrain. With the re-calibration based on the phase lock on the corner, MUSIC resolves the two peaks.

Finally, Figure 1.21 shows the terrain topography extracted from the tomographic slice in the range line under analysis. Since in HH polarization the dominant scattering mechanism is due to the double bounce tree trunks-ground, it is possible to estimate the ground topography simply by extracting the position of the dominant scatterer in each range bin. This procedure can be refined by limiting the height interval where to perform the peak search; in particular, we assume the interval -10 m to 50 m. Also, to obtain a robust method that may be applied also to HV data, we look for the two dominant peaks in that interval, and select that with lower height as the ground contribution. The results of procedure based on the dominant peak extraction are reported in Figure 1.21 for the three tomographic processors (with sparse grid recalibration). We observe that the terrain topographies are generally very similar between each others, confirming the hypothesis of the single scattering mechanism, while for the range bin interval between 700 and 800 (and around range bin 950) they differ noticeably. Remembering that in the first area the tomo images of Capon and MUSIC have indicated the presence of canopy, this difference is reasonable because of the different resolution capability of the methods and hence of the different influence on ground peak by canopy contribution. The result obtained with the refined procedure is reported in Figure 1.22; we observe that the terrain topography extracted with the double peaks method is generally very similar to the dominant peak method.

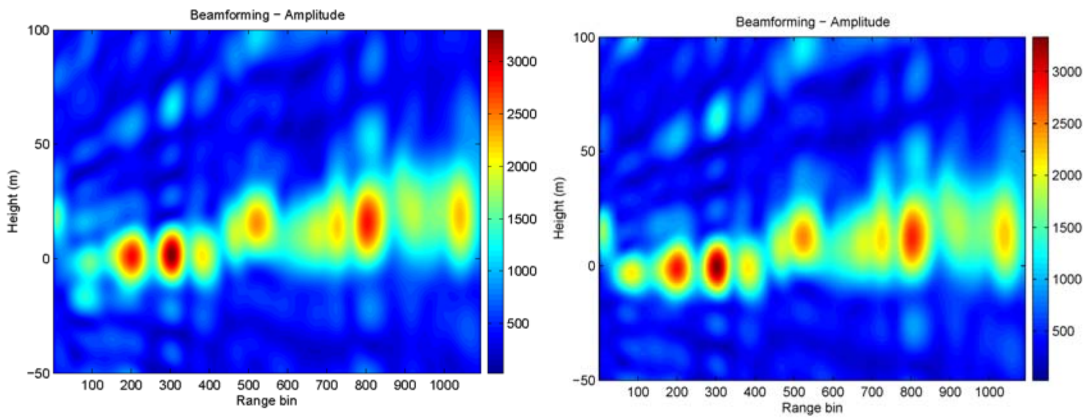

Figure 1.17: Tomo images with beamforming, relative az. bin 454.
(a) Sparse grid recalibration; (b) Phase lock on the corner.

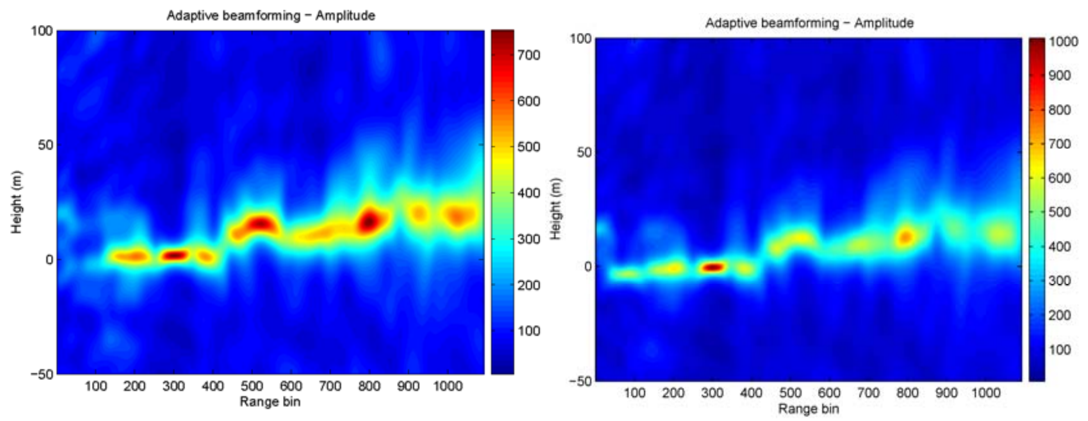

Figure 1.18: Tomo images with Capon, relative az. bin 454.
(a) Sparse grid recalibration; (b) Phase lock on the corner.

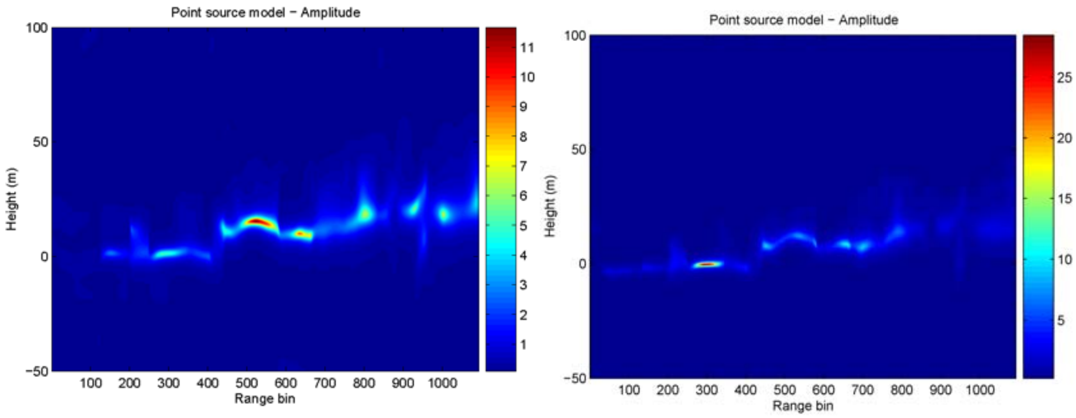

Figure 1.19: Tomo images with MUSIC, relative az. bin 454.
(a) Sparse grid recalibration; (b) Phase lock on the corner.

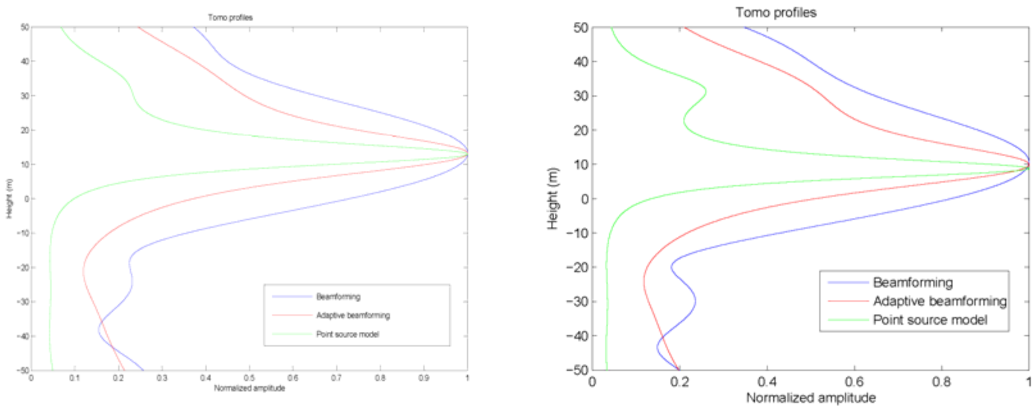

Figure 1.20: Tomo profiles, rg. bin 753, relative az. bin 454.
(a) Sparse grid recalibration; (b) Phase lock on the corner.

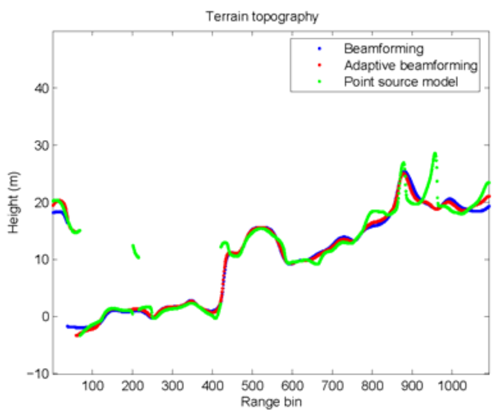

Figure 1.21: Terrain topography (relative az. bin 454), sparse grid recalibration.

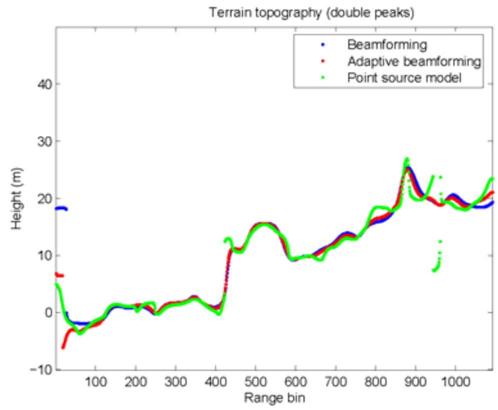

Figure 1.22: Terrain topography extracted with the double peaks method (relative az. bin 454), sparse grid recalibration.

10.2.1.2 Range line #2

In this subsection we report the results of the tomographic processing carried out on the second range line (absolute azimuth bin 3667). In this range line it is present a natural point-like scatterer, whose behavior is similar to that of a corner reflector. The full resolution image portion containing this line is shown in Figure 1.23 (rg. bin from 1 to 1100, az. bin 3550 to 3900, absolute coordinates), whereas the satellite resolution image after range and azimuth filtering is reported in Figure 1.24. The area where the point-like scatterer is located is not forested. After the resolution reduction, the point-like scatterer (rg. bin 234, relative az. bin 177) assume nearly the same intensity of the forested area.

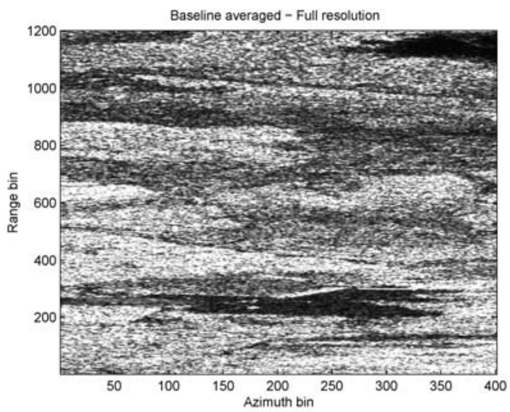

Figure 1.23: SAR image for the second analyzed range line, full resolution.

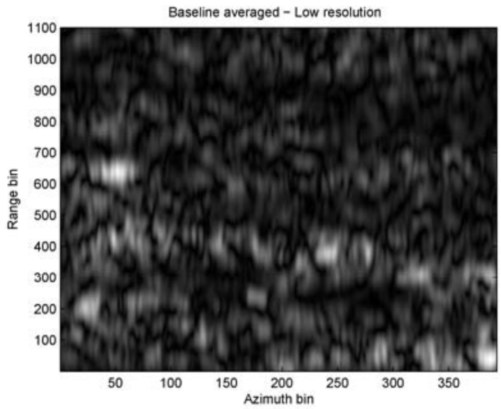

Figure 1.24: SAR image for the second analyzed range line, satellite resolution.

The nominal PSF as a function of the range bin is showed in Figure 1.25. Again, it is apparent the characteristic loss of resolution in height at the increase of the range coordinates. Moreover, the PSF now exhibits relatively high sidelobes of constant amplitude, which does not behave as the sidelobe amplitude of the PSF from an ideal uniform baseline distribution.

Figure 1.26 and 1.27 report the beamforming tomographic profile extracted in the image pixel corresponding to the point-like scatterer (rg. bin 234, relative az. bin 177), before and after calibration with the sparse grid recalibration. By comparing Figure 1.25 and Figure 1.27, it is apparent that after re-calibration the tomo profile on the point-like scatterer is very similar to the PSF at that coordinate.

In the sequel, if not otherwise specified, calibration is the sparse grid one. The tomographic images are reported in Figures 1.28-1.30. In this range line the ground contribution is again dominant, as it is expected in HH polarization. However, at some range bins it is possible to find clear power contributions above the terrain layer, see the Capon tomography in Figure 1.29. Most part of them are given by an almost flat spectral portion which extends for 10-20 m above the terrain centroid. By employing Capon or MUSIC it is also possible to find some points where the ground and the canopy centroids are well distinct; with reference to Figure 1.31, showing tomographic profiles for range bin 570, the two peaks are found at a reasonable distance (around 20 m) for a temperate forest.

Finally, Figure 1.32 shows the terrain topography extracted with the three methods by picking the dominant peak of the spectrum. The curves do not shows irregularities (apart from the MUSIC based one in the beginning of the range line), and exhibit an excursion in height between 10 m and 20 m.

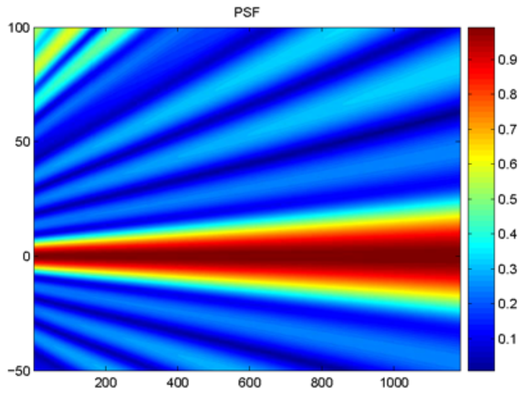

Figure 1.25: PSF calculated for the range line #2.

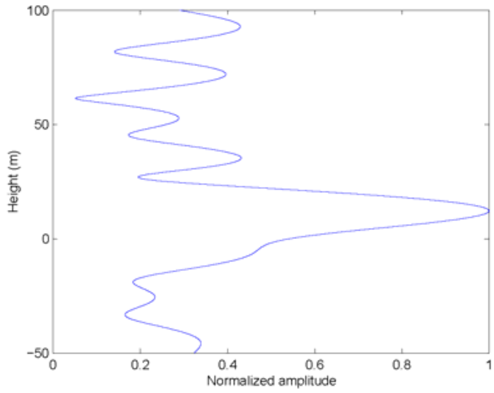

Figure 1.26: Beamforming tomo profile in correspondence of the point-like scatterer (rg. bin 303, relative az. bin 454), before re-calibration.

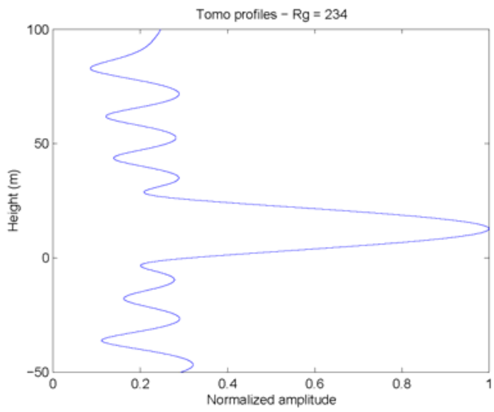

Figure 1.27: Beamforming tomo profile in correspondence of the point-like scatterer (rg. bin 303, relative az. bin 454), after sparse grid recalibration.

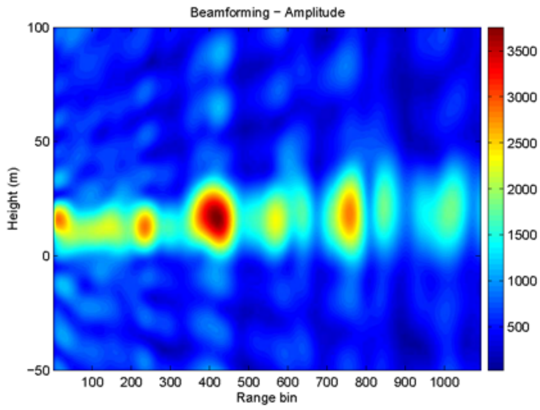

Figure 1.28: Tomo image with beamforming, relative az. bin 177.

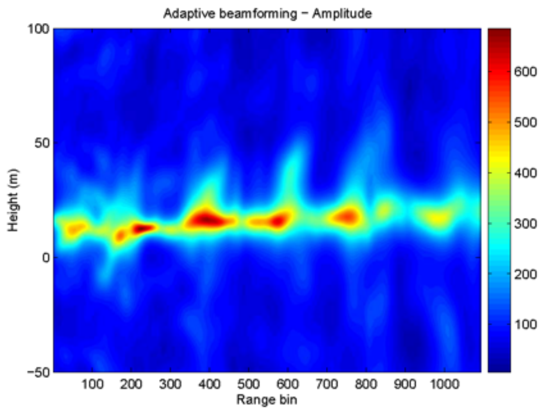

Figure 1.29: Tomo image with Capon, relative az. bin 177.

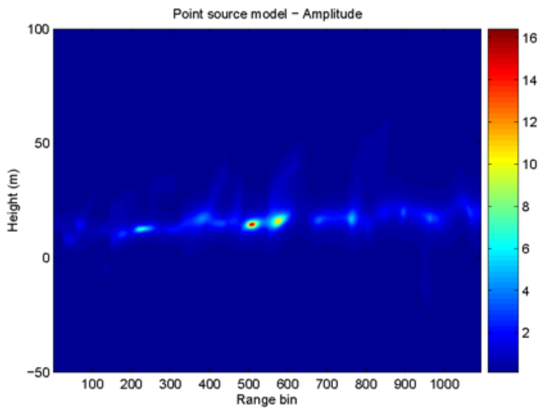

Figure 1.30: Tomo image with MUSIC, relative az. bin 177.

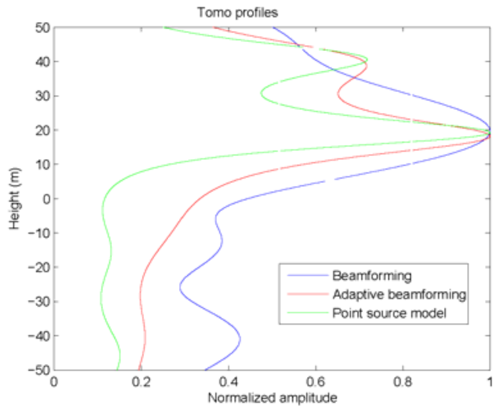

Figure 1.31: Tomo profiles, rg. bin 570, relative az. bin 177.

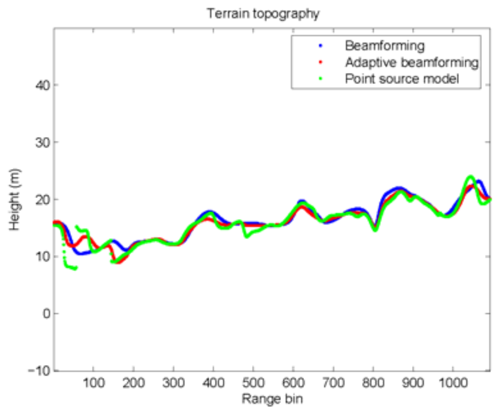

Figure 1.32: Terrain topography, relative az. bin 177.

10.2.1.3 Range line #3

This subsection shows the results obtained with the tomographic processing of the range line in correspondence of the third corner reflector (absolute az. bin 4769); the full resolution and the satellite resolution images portion for this case are reported in Figures 1.33 and 1.34 respectively (rg. bin from 1 to 1100, az. bin 4600 to 5000, absolute coordinates). Figure 1.35 reports the PSF calculate on this range line (relative azimuth bin 169); the sidelobe profile is quite regular, and does not exhibit particularly strong sidelobes, except for the second sidelobe and a sidelobe arising between 90 m and 100 m in height in near range.

Figures 1.36-1.38 show the tomographic images obtained at the selected azimuth bin. In this case, the forest contribution is too weak to be generally clearly detected. By visual inspection of the Capon or MUSIC tomographic images, we can affirm that a possible forest is present e.g. between range bin 700 and range bin 800. Another possible canopy is individuated by the power contribution at a few meter in heights between range bin 300 and 400. In the range interval between bin 550 and 700, Capon finds some other power contributions above or below the ground layer. However, these contributions are not confirmed by MUSIC, as a consequence they could be associated to some residual miscalibration.

Finally, Figure 1.39 shows the terrain topography extracted with the three tomographic processors with the dominant peak method.

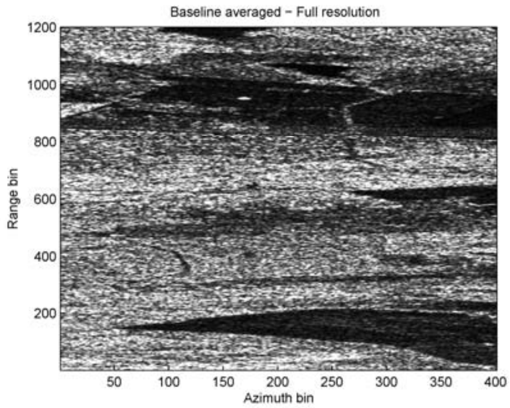

Figure 1.33: SAR image for the third analyzed range line, full resolution.

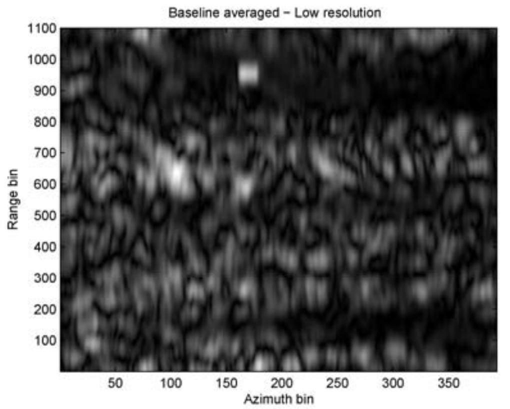

Figure 1.34: SAR image for the third analyzed range line, satellite resolution.

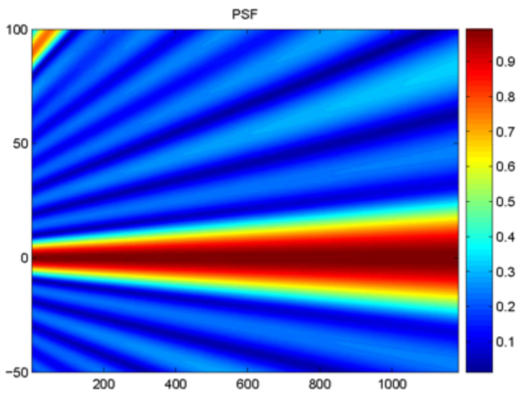

Figure 1.35: Nominal height PSF calculated for the range line #3.

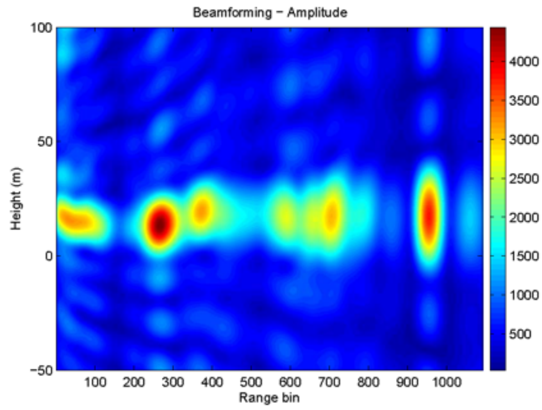

Figure 1.36: Tomo image with beamforming, relative az. bin 169.

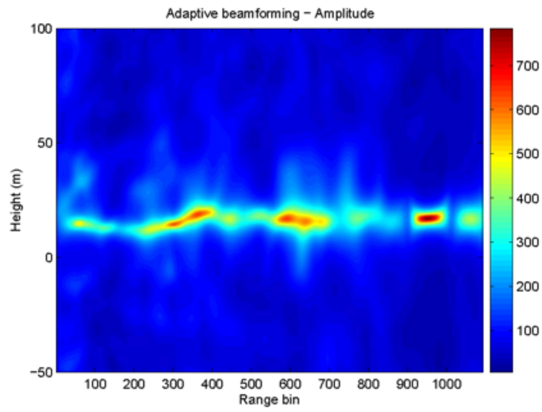

Figure 1.37: Tomo image with Capon, relative az. bin 169.

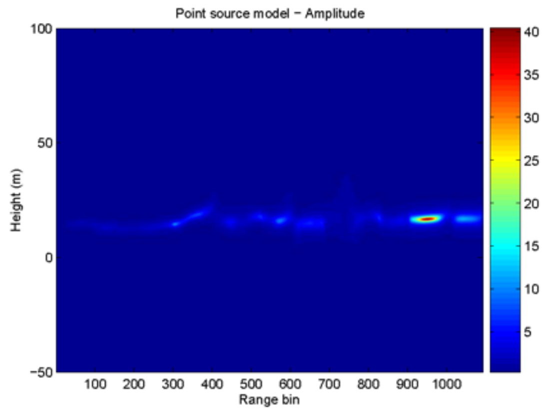

Figure 1.38: Tomo image with MUSIC, relative az. bin 169.

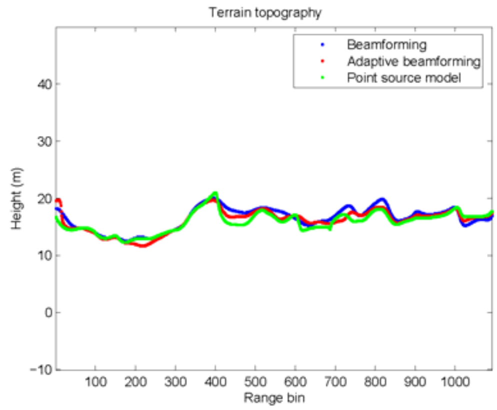

Figure 1.39: Terrain topography, relative az. bin 169.

10.2.2 HV polarization

Differently from HH polarization, in HV polarization the expected main power contribution is no more given by the ground layer. As a consequence, HV polarization is more suitable for the observation of the forest canopy layer. The analyzed image portions and range lines are again those selected for the analysis in the HH polarization (see Figure 1.9). The following images are still all obtained by processing the 9 selected images re-calibrated with the sparse grid recalibration strategy.

10.2.2.1 Range line #1

Figure 1.40 shows the MB coherent average of the selected portion of full resolution images with azimuth bin spanning from 860 to 1460 and the range bin from 0 to 1200 (absolute coordinate); Figure 1.41 shows its low resolution version after range-azimuth filtering. As expected, the low HV scattering from the corner reflector becomes very low in the low resolution image; moreover, as it will be showed in the following, the highest pixel amplitudes are due more to scattering from canopy rather than scattering from the double bounce trunks-terrain.

The first analyzed range line is located again at the relative azimuth bin 454. The tomographic images are reported in Figures 1.42-1.44. By comparing them with the analogous for HH polarization, it is apparent that the corner reflector (rg. bin 3030) gives very low bakscattered power, and it is not visible in the tomo images. Moreover, differently from HH polarization, from these images (in particular Capon) it is clear the presence, together with some ground scattering, of an intense canopy contribution in a large area especially starting from range bin 600, which extends up to an height of nearly 40 m. This is reasonable, since the terrain topography in HH polarization shows a mean height of about 10-15 m in that region, as a consequence the canopy layer extends for about 25-30 m above the ground centroid, as expected from this kind of forest. Figure 1.45 reports the tomo profiles extracted at range bin 753 at this range bin; it is apparent the presence of a canopy dominant peak located around 23 m height.

In Figure 1.46 the position of the dominant peaks in height is reported as a function of the range bin. Globally, the resulting curves are very different from the dominant peak profiles in HH, due to the change of scattering mechanism. In particular, this difference is accentuated in the area around the corner reflector and the canopy area mentioned before. It is thus confirmed that Hv polarization is not well suited for terrain topography extraction, especially if the dominant peak method is employed. Finally, Figure 1.46 shows the result of the double peak extraction, which in general are very similar to those of the dominant peak method, except for some isolated points.

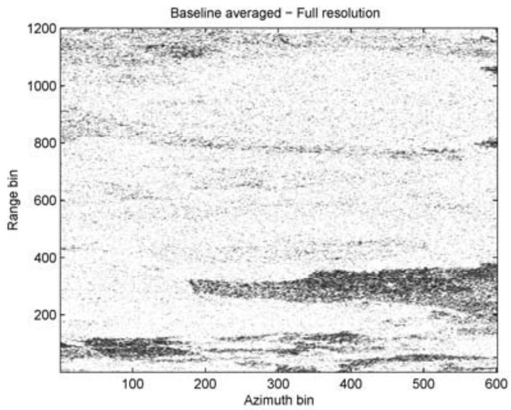

Figure 1.40: SAR image for the first analyzed range line, full resolution.

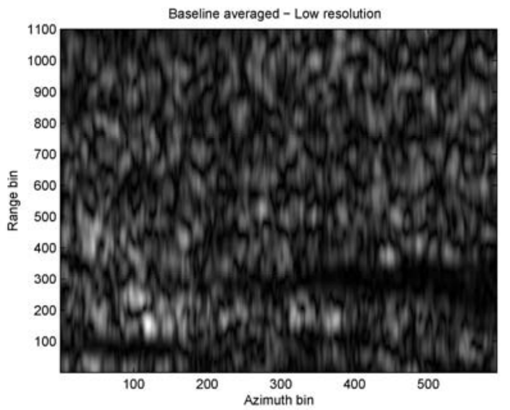

Figure 1.41: SAR image for the first analyzed range line, satellite resolution.

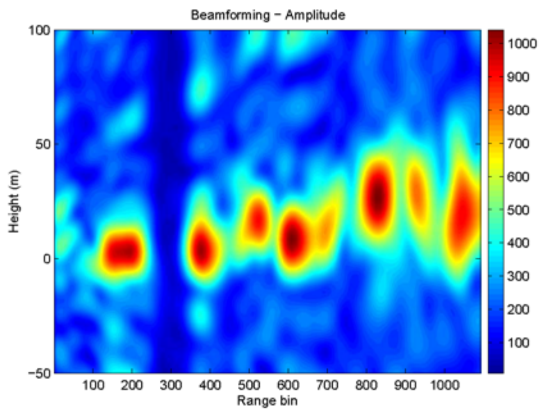

Figure 1.42: Tomo image with beamforming, relative az. bin 454.

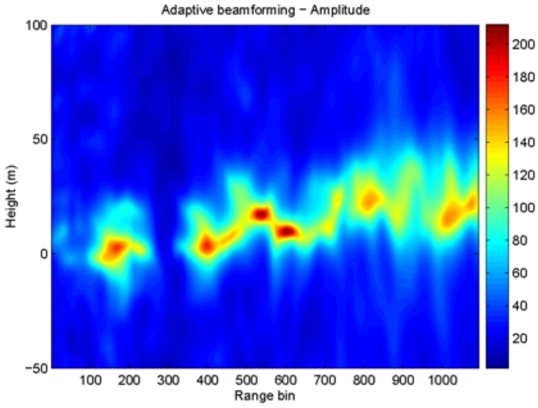

Figure 1.43: Tomo image with Capon, relative az. bin 454.

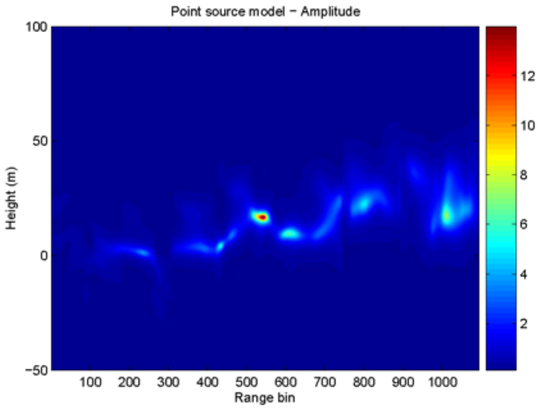

Figure 1.44: Tomo image with MUSIC, relative az. bin 454.

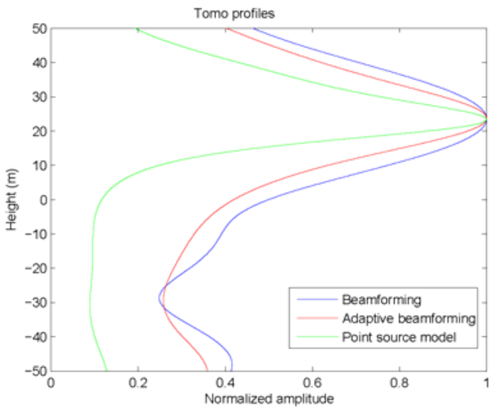

Figure 1.45: Tomo profiles, rg. bin 753, relative az. bin 454.

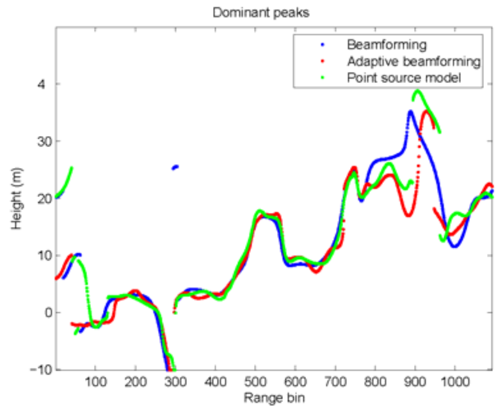

Figure 1.46: Dominant peak extraction, relative az. bin 454.

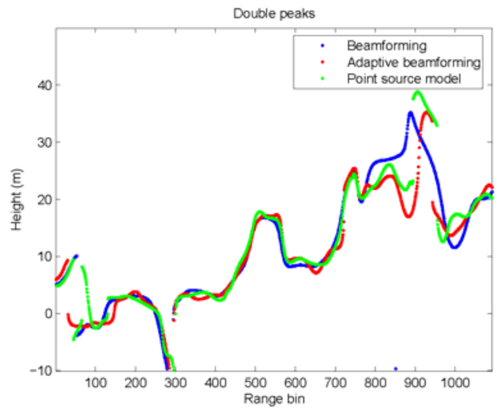

Figure 1.47: Double peaks method, relative az. bin 454.

10.2.2.2 Range line #2

Figures 1.48 and 1.49 report the full resolution and satellite resolution images, for the same cut selected in HH polarization. Again, the natural corner reflector (point-like scatterer) disappears after the resolution reduction in HV polarization.

The tomo images are shown in Figures 1.50-1.52; again, it is apparent the presence of a quite intense forest layer, even if Capon may be affected by miscalibration residuals because of the presence of some spectral components for negative heights, in particular between range bins 800 and 900. Moreover, between range bin 300 and 400 it is possible to separate two peaks with Capon and MUSIC; as can be inferred from Figure 1.53, showing the position of the dominant peaks in height as a function of the range bin, the dominant peak is that of canopy.

10.2.2.3 Range line #3

Figures 1.54 and 1.55 report the full resolution and satellite resolution images, for the same cut selected in HH polarization. We observe once again that the corner reflector shows a very low intensity in both images.

The tomo images are shown in Figures 1.56-1.58. The presence of the canopy is apparent before about range bin 800; however, as shown in Figure 1.59, in this range line the dominant peak is at the terrain level, although influenced by the presence of the scattering layer above. Notice that Capon suffers again from possible miscalibration residuals (see around range bin 250).

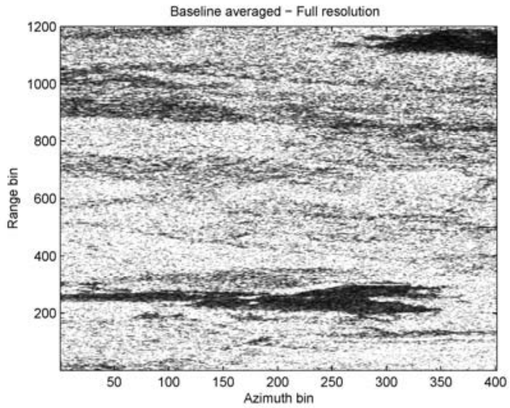

Figure 1.48: SAR image for the second analyzed range line, full resolution.

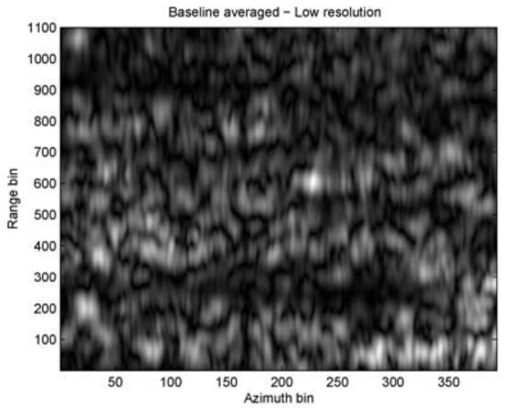

Figure 1.49: SAR image for the second analyzed range line, satellite resolution.

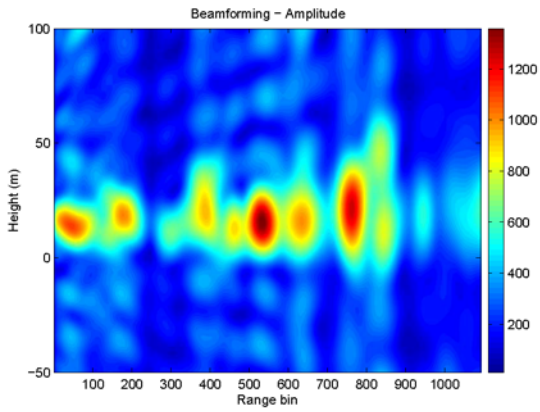

Figure 1.50: Tomo image with beamforming, relative az. bin 234.

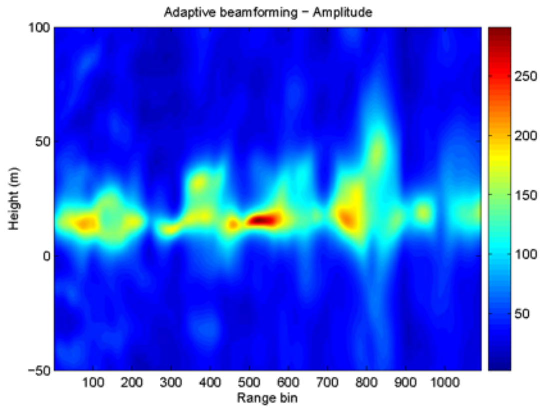

Figure 1.51: Tomo image with Capon, relative az. bin 234.

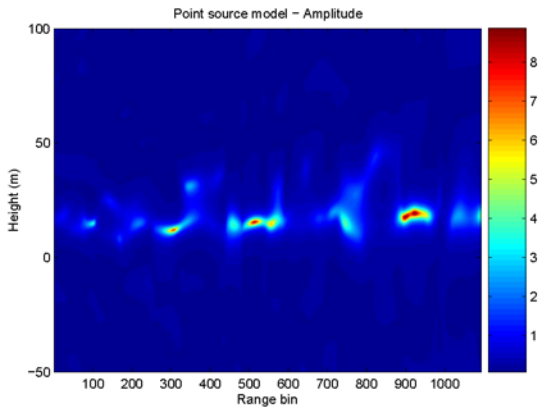

Figure 1.52: Tomo image with MUSIC, relative az. bin 234.

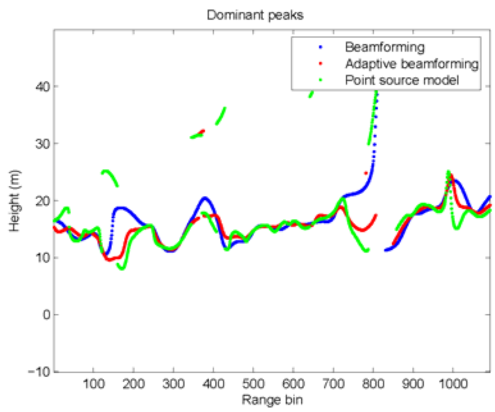

Figure 1.53: Dominant peak extraction, relative az. bin 234.}

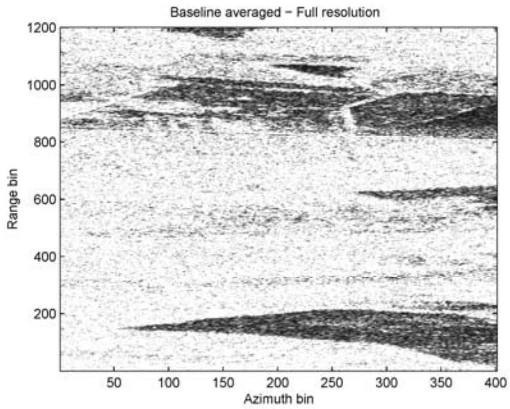

Figure 1.54: SAR image for the third analyzed range line, full resolution.

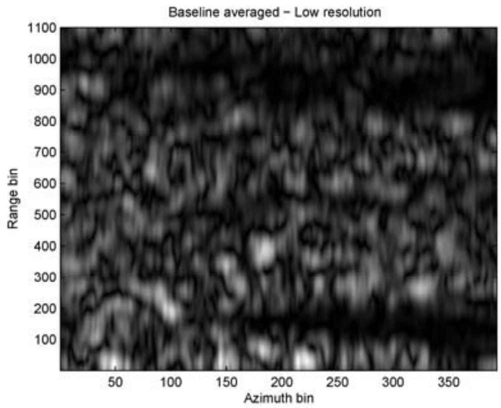

Figure 1.55: SAR image for the third analyzed range line, satellite resolution.

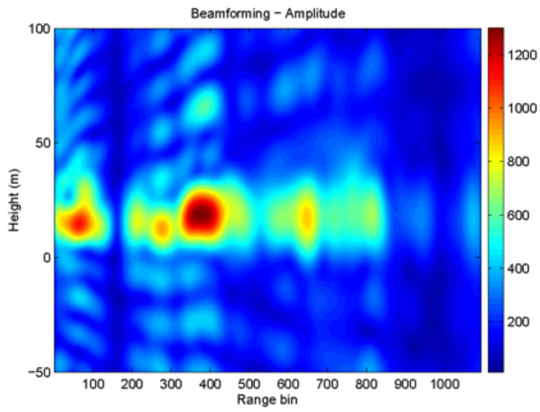

Figure 1.56: Tomo image with beamforming, relative az. bin 169.

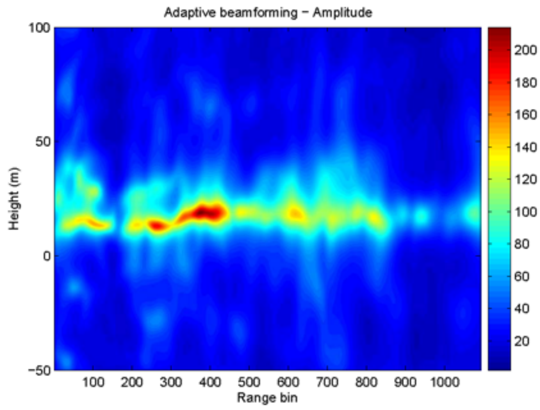

Figure 1.57: Tomo image with Capon, relative az. bin 169.

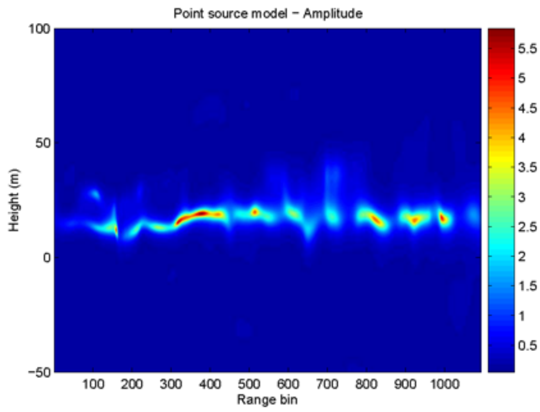

Figure 1.58: Tomo image with MUSIC, relative az. bin 169.

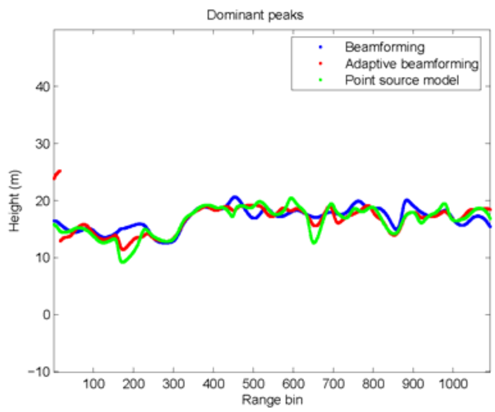

Figure 1.59: Dominant peak extraction, relative az. bin 169.

10.3 DEM extraction

As already seen for the three range lines, the tomographic processing can be used to extract a DEM of the terrain also when is covered by canopy. HH polarization is more suited than HV for this purpose.

In this section, we report results of HH DEM extraction over an area, extending the previous results. In our analysis, the DEM extraction has been performed by means of the Capon spectral estimator. The DEM regards a portion of the image around the first corner reflector (range bins 100-1100, azimuth bins 1095-1733, absolute coordinates), which is reported in Figure 1.60 for the dominant peak method. This area is centered on the first corner reflector range line, and comprehends the image portion seen before. The estimation has been performed in azimuth every half of the tomographic resolution cell, i.e. every 25 m in azimuth then it has been oversampled to maintain the same bin grid in the final product. The DEM obtained is regular. This DEM has been compared with some tomographic sections extracted at some azimuth bin, and it has been verified that it apparently tracks the terrain contribution. The DEM obtained with the double peak method is shown in Figure 1.61. It does not present particular differences, except for a very small area centered on relative azimuth bin 319 and range bin of about 620. In that point, the lower height peak of the estimated Capon spectrum corresponds to a residual sidelobe.

Figures 1.62 and 1.63 shows the HH DEM extracted with both methods, but considering a larger area (both in range and azimuth, range bins 1-1100, azimuth bins 500-2500, absolute coordinates) which contains the area previously analyzed. Again, we observe that they do not present noticeable differences for the most part of them. However, due again to the influence of residual sidelobes, some anomalies are observed in the DEM extracted with the double peak method, in particular between the relative azimuth bins 1500-2000 and the range bins 1-400. However, it is expected that the double peak method can exhibit its advantages with highly sloping forested terrain HH data, where the terrain double bounce is not the dominant scattering mechanism (or with HV data). By visual inspection, a qualitative comparison of the trends of the extracted DEM with the DTM extracted from LIDAR data, accounting for the different reference height, has shown a reasonable agreement.

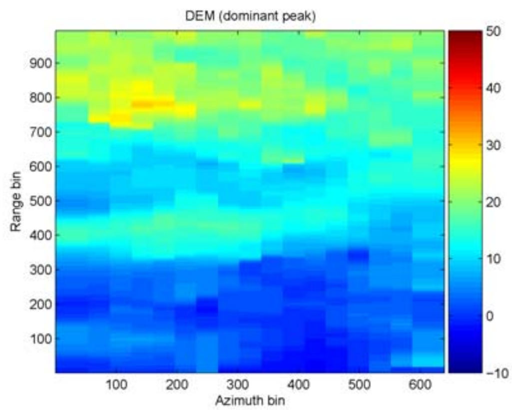

Figure 1.60: DEM extracted from HH polarization, dominant peak method (range bins 100-1100, azimuth bins 1095-1733, absolute coordinates).

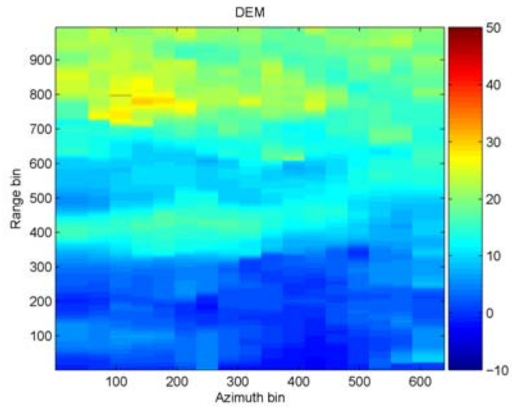

Figure 1.61: DEM extracted from HH polarization, double peak extraction method (range bins 100-1100, azimuth bins 1095-1733, absolute coordinates).

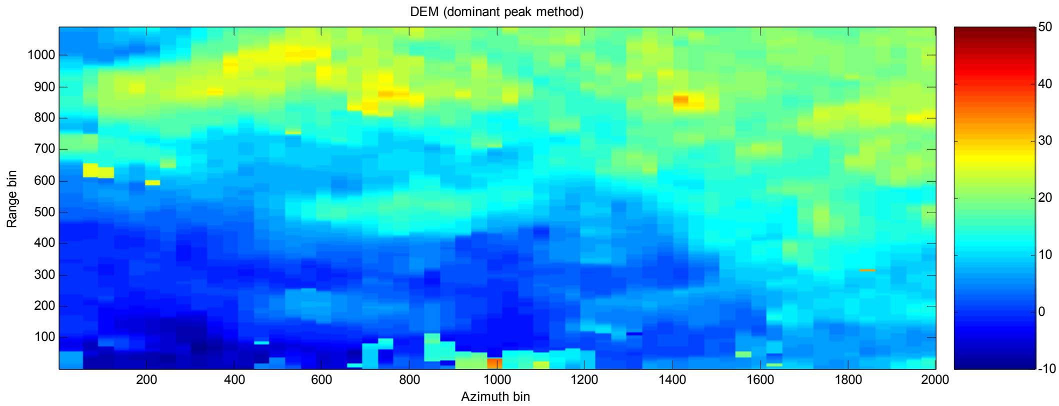

Figure 1.62: DEM extracted from HH polarization, dominant peak method (range bins 1-1100, azimuth bins 500-2500, absolute coordinates).

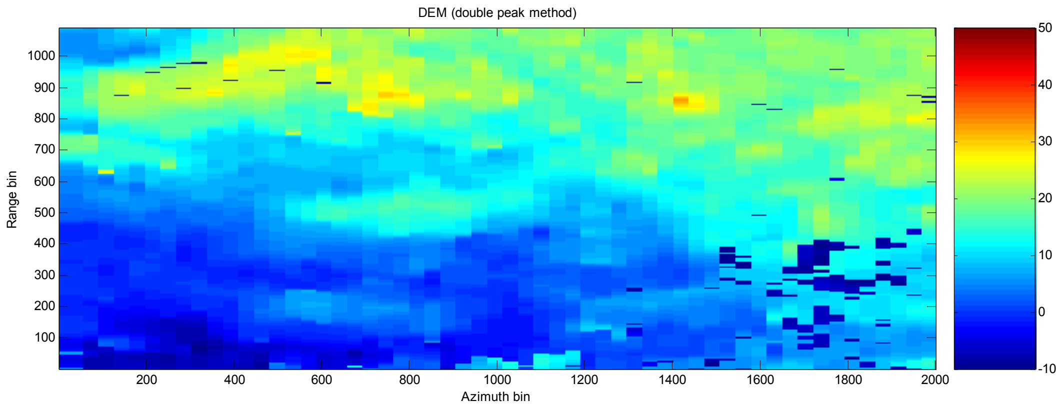

Figure 1.63: DEM extracted from HH polarization, double peak extraction method (range bins 1-1100, azimuth bins 500-2500, absolute coordinates).

10.4 Coherent Layer Cancellation

10.4.1 Theoretical background

The proposed processing chain to perform coherent layer cancellation (and possible subsequent band synthesis on the remaining layer) is reported in Figure 2.1 [3]. After the already mentioned classical pre-processing procedures on the SAR images (in particular deramping), a general tomographic calibration is performed to identify the typical height separation of the layers and their thickness, possibly coupling this analysis with a priori information; the separation and thickness information will be exploited together with the tomographic produced terrain DEM in the design of the coefficients used in the cancellation step. Then, it is possible to perform layer cancellation and possibly band synthesis. In this report, we focus on the cancellation part.

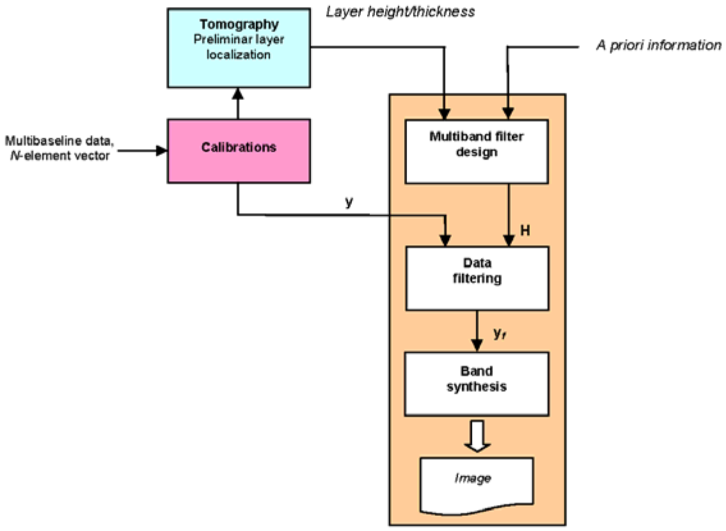

Figure 2.1: Overall processing chain for layer cancellation and band synthesis.

To cancel one of the scattering layers while preserving the coherent structure of the MB signal components from the other layer, we can resort to a deterministic technique by using a multiband filter, i.e. a filter with a spatial pass band centered around the height of the layer of interest and a stop band to reject the other layer [3]. It is worth noting that the possible non-uniformity of the N spatial samples (non-uniform baselines) makes the filtering quite atypical; moreover, a moving window processing of a short data sequence (e.g. $N = 9$) would be subject to transient effects on the filtered data and height array resolution loss. For this reason, we resort to matrix filters, that corresponds to linear non-stationary filters. The filtered MB data is given by

$$\mathbf{y}_c = \mathbf{H}\mathbf{y} \tag{1.1}$$

where $\mathbf{H}$ is the matrix which performs the desired filtering. Notice that $\mathbf{y}_c$ and $\mathbf{y}$ can have a different number of elements, and no assumptions have been made about the spatial uniformity of the samples (neither for $\mathbf{y}$ or $\mathbf{y}_c$). The matrix filter is designed according to the least squares problem

$$\mathbf{H} = \arg\min_{\mathbf{H}} \left(\int_{S_1} \left\| \mathbf{a}_V(h) - \mathbf{H}\mathbf{a}(h) \right\|_F^2 dh + \int_{S_0} \left\| \mathbf{H}\mathbf{a}(h) \right\|_F^2 dh \right). \qquad (1.2)$$

where $\mathbf{a}_V(h)$ is the steering vector corresponding to the (generally virtual) baseline distribution chosen for the output spatial samples $\mathbf{y}_c$, S_1 is the interval of heights of the pass band, and S_0 the interval of heights of the stop band. So doing, spatial harmonics corresponding to scatterers in stop band will be canceled or attenuated, while spatial harmonics corresponding to scatterers in pass band will be left almost undistorted. The solution to the minimization problem (2.2) can be found in closed form using conventional rules for the overdetermined equation systems. As an example, by imposing the condition on S_1, the solution is easily obtained by discretizing the height interval of interest and it assumes the following form [4]:

$$\mathbf{H}_1 = \mathbf{A}_V \mathbf{A}^H \left(\mathbf{A}\mathbf{A}^H \right)^{-1}, \qquad (1.3)$$

where $\mathbf{A}_V = \left[\mathbf{a}_V(h_1) \;\; \mathbf{a}_V(h_2) \;\; \cdots \;\; \mathbf{a}_V(h_s) \right]$, $\mathbf{A} = \left[\mathbf{a}(h_1) \;\; \mathbf{a}(h_2) \;\; \cdots \;\; \mathbf{a}(h_s) \right]$, and $h_1,\ldots,h_s$ are s heights contained in the interval S_1. Moreover, to avoid possible ill-conditioning of the solution and sensitivity to noise and miscalibration, in the derivation of the solution a regularization term can be added. It is worth noting that the output of the coherent layer canceller is a MB data set that might be used for other applications in addition to band synthesis.

Figure 2.2 reports the filter response calculated as the baseline averaged output power when the input MB signal is originated by a point-like scatterer, as a function of the height of the latter (expressed in resolution units), expressed in dB. This response has been calculated for the baselines [0 10 21.5 28 39 51 58.5 71.5 80] whose PSF approximates that obtained on the first corner reflector (see Figure 1.15(b)). The baselines chosen for the output are the same as the input data. Stop band and pass band have been set according to a typical scenario as seen in the simulated (and real data) tomographies of the previous sections. The filter response is almost flat and equal to about 0 dB in pass band, and attenuates 18 dB or more in stop band, for the chosen regularization term. Out of these two bands, it attenuates nearly 5 dB, thus sensitivity to noise and out of band components is sufficiently low in the scenario under analysis.

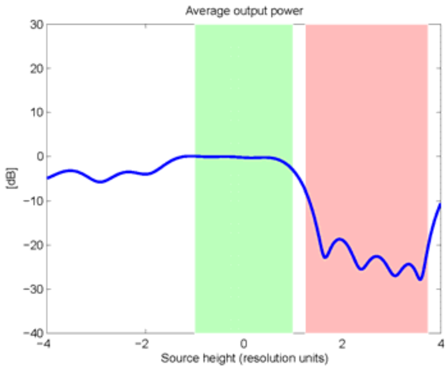

Figure 2.2: Matrix filter response for a typical scenario, calculated for a non-uniform baseline configuration whose PSF resembles the PSF on the first corner reflector.
Red stripe: stop band; green stripe: pass band.

10.5 Simulated analysis

To test the cancellator under controlled conditions, Figures 2.3 and 2.4 report two simulated realizations of the beamforming and the Capon spectra ($M = 32$ looks), respectively, before and after cancellation of the canopy layer in the data, for the near range case, with a distance between canopy and ground centroids of 23 m. The pass band has been set 20 m large, centered around zero height; the stop band has been chosen 25 meter large, centered around 23 m, as in Figure 2.2. The results obtained are very satisfactory. It is apparent also a non-linear radiometric effect of Capon. In fact, after cancellation, the remaining peak is more powerful than before the cancellation.

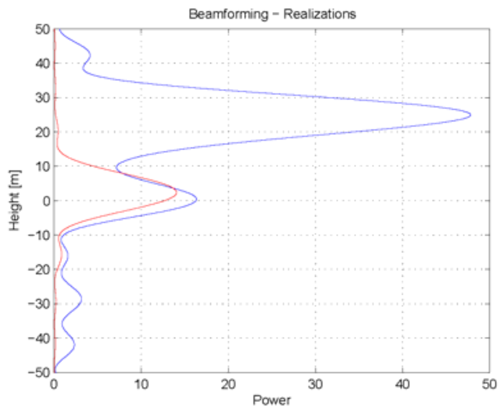

Figure 2.3: Realization of beamforming spectrum, canopy centroid 23 m. Blue curve: before cancellation; red curve: after cancellation.

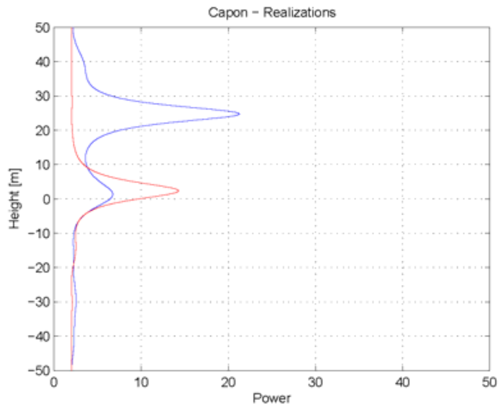

Figure 2.4: Realization of Capon spectrum, canopy centroid 23 m.
Blue curve: before cancellation; red curve: after cancellation.

10.6 Real data analysis

10.6.1 Range line #1

For the real data analysis, in this section we focus on the results of the cancellation for the range line #1. The objective is the cancellation of the forest layer, in order to retrieve MB data with the ground layer component only in order to possibly perform a subsequent band synthesis. In this framework, HV data are more interesting since they are more sensible to the canopy layer scattering. Here we report also the results obtained with HH data, because they are a good test for judging the behavior of the cancellation step.

The pass and stop band largeness and separation has been set according to general information derived from the real data tomographic profiles extracted in the previous section. In particular, the terrain layer largeness as seen from the radar with the limited slant-range resolution has been derived from the Capon tomo images in HH, whereas the canopy layer largeness has been deduced from the tomo profiles in HV where the canopy only was detected. This information was also compared and coupled with typical a priori information used in the definition of the simulated scenarios, and expected variations for different look angles were also considered. From this investigation, we deduced two possible settings, depending on near range or far range operations respectively:

- pass band 20 m, stop band 25 m, separation between centroids 24 m (in the following denoted as Filter 1);
- pass band 17 m, stop band 20 m, separation between centroids 20 m (Filter 2).

From a filter design point of view, Filter 1 is to be preferred since it has larger bandwidths. The pass band centroid is automatically derived from the terrain topography extracted with HH data. Once the pass band centroid is set, pass band and stop band are set according to the previous parameters relatively to it. As a consequence, the matrix filter is designed pixel by pixel.

10.6.1.1 HH polarization

Figure 2.5 reports the tomo images extracted with Capon in correspondence of the range line on the first corner, before and after cancellation with both filters, with HH data. Even if the canopy is not strongly visible with HH data, the tomo images obtained from the data after cancellation do not present anymore those flat spectral portion characteristic of the presence of a canopy. Moreover, the remaining ground layer image after cancellation is very similar to the same layer before cancellation; as a consequence, the matrix filter has not introduced any sensible alteration of the MB signal components in the pass band. It is also worth noting that employing Filter 1 or Filter 2 is not essential for the final tomo result, even if in terms of bandwidths Filter 1 would be better matched for near range and Filter 2 for far range.

Figure 2.6 reports the MB averaged SAR images around the first corner reflector (clearly visible), in gray level and false color, before and after cancellation with Filter 1. Both images have the same amplitude scale. After canopy layer cancellation, the image features remain almost unaltered, since the main contribution comes from the terrain. However, after cancellation the image has slightly lower amplitudes, as it is reasonable because of the cancellation of one layer.

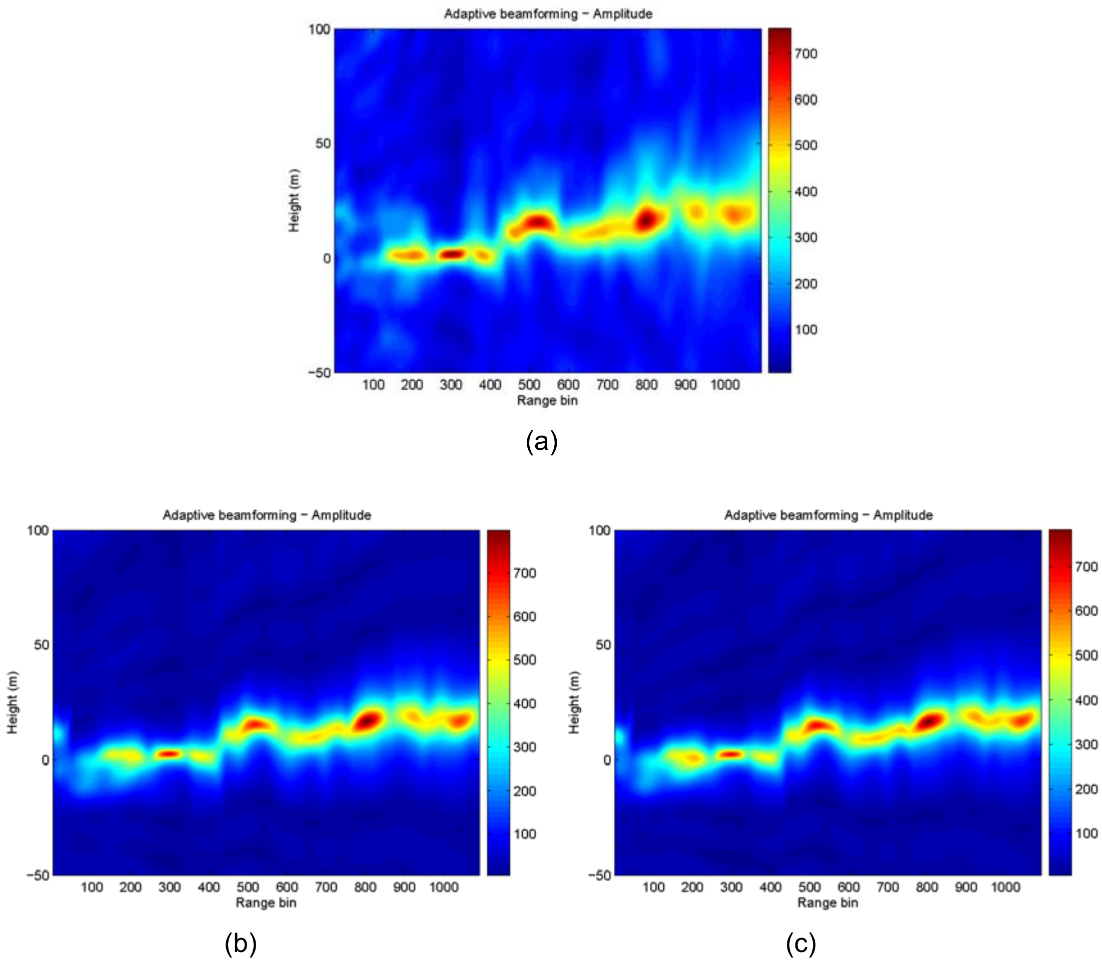

Figure 2.5: Capon tomo images for the first analyzed range line, HH polarization, before and after cancellation with the two filters. (a) Before cancellation; (b) After cancellation, Filter 1; (c) After cancellation, Filter 2

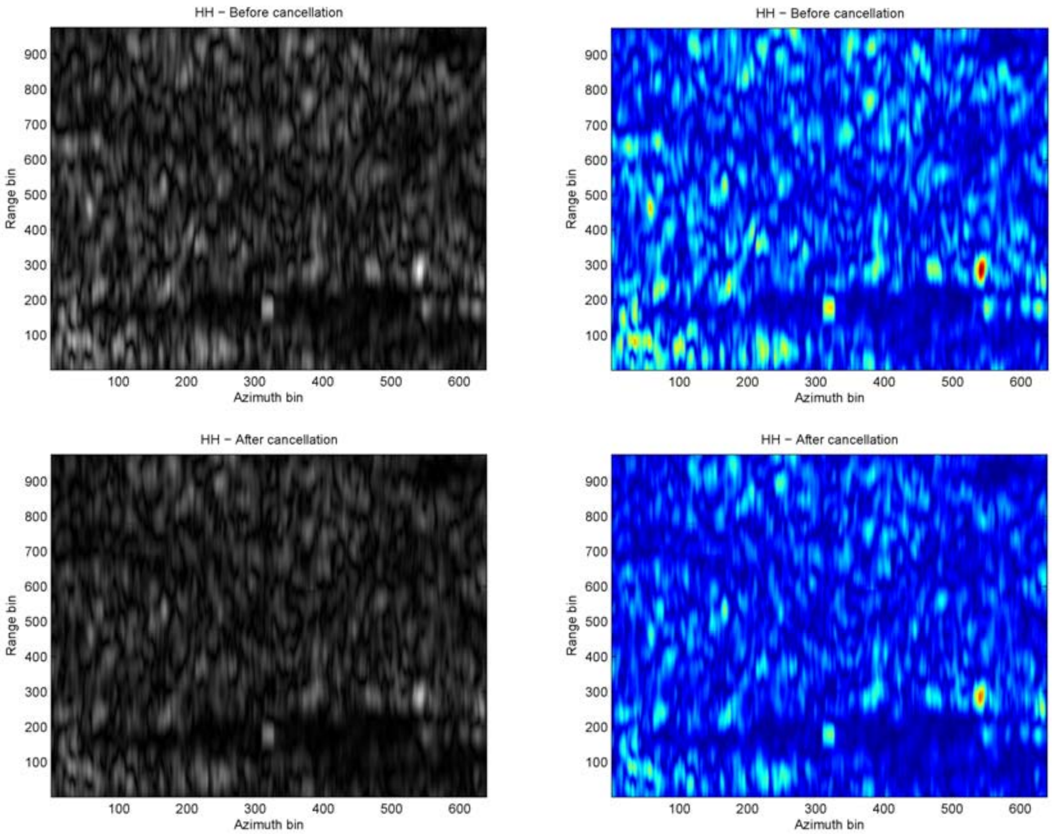

Figure 2.6: SAR images for the first analyzed range line, HH polarization, before and after cancellation with the Filter 1. (a) Before cancellation, gray level map; (b) before cancellation, false color map; (c) after cancellation, gray level map; (d) after cancellation, false color map.

10.6.1.2 HV polarization

The same analysis has been carried out also in HV polarization over the same image portion, with the pass band centroid still derived from HH terrain tomography. The Capon tomographic images before and after cancellation are reported in Figure 2.7. Both filters are efficient in canceling the canopy layer; this is particularly visible in far range, where the canopy is more intense. Globally, the remaining terrain layer behaves in height as seen in HH polarization. However, a double peaked feature appears in near range (around range bin 150) and around range bins 600. This structure is more evident in the second zone with Filter 2. To give a possible explanation to this phenomenon, the use of the statistical simulator could be of some help. In Figure 2.8, it is reported a realization of the Capon spectrum before and after cancellation. In this simulation, we considered three scatterering layers: two compact layers at 0 m and -3 m in height (unresolved), and a canopy layer at 23 m. The filter has been designed according to the Filter 2 specifications, with the pass band centroid set at 0 m. It is apparent that after the canopy cancellation, the weaker peak (corresponding to the two peaks of the compact scatterers unresolved) is splitted into two peaks about 10 meter distant between each other. This situation is very similar to what happens with the real data. As a consequence, the splitting of the terrain peak into two peaks in the tomographic image after cancellation could be due to the presence of two near peaks which where unresolved before cancellation. Operating on data in which one of the layers has been already canceled by the matrix filter exploiting a priori information, Capon could better exploit its degrees of freedom to resolve the other two layers. The presence of these two near peaks could be connected to the multilooking operation: the multilooking could have involved resolution cells where the ground layer was at slightly different heights. However, the observed peak splitting might be also originated by distortions caused by the matrix filter.

Figure 2.9 reports the same SAR images reported in Figure 2.6 around the first corner reflector (not visible here), HV polarization, in gray level and false color, before and after cancellation with Filter 1. Both images have the same amplitude scale. The difference between the images before and after cancellation is significant here as expected, since the canopy layer is strong in HV polarization.

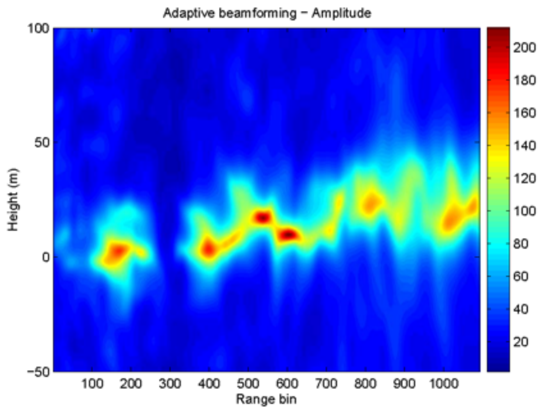

(a)

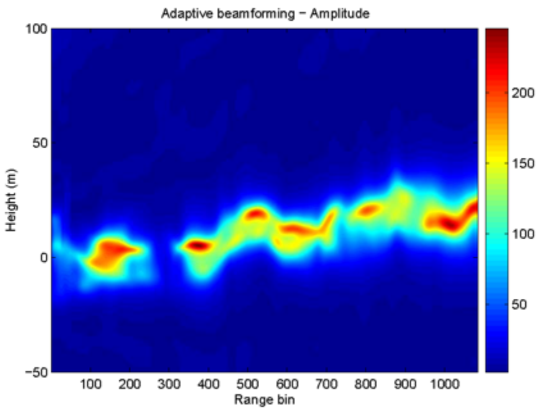

(b)

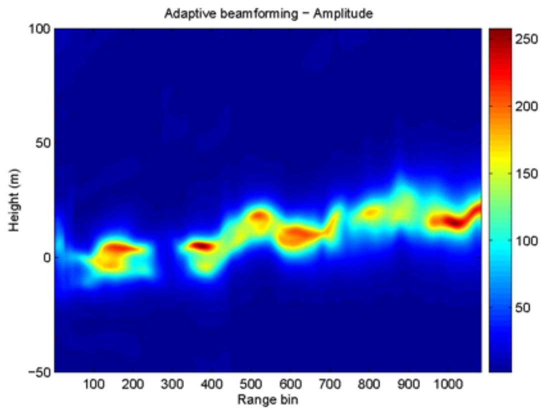

(c)

Figure 2.7: Capon tomo images for the first analyzed range line, HV polarization, before and after cancellation with the two filters. (a) Before cancellation; (b) After cancellation, Filter 1; (c) After cancellation, Filter 2.

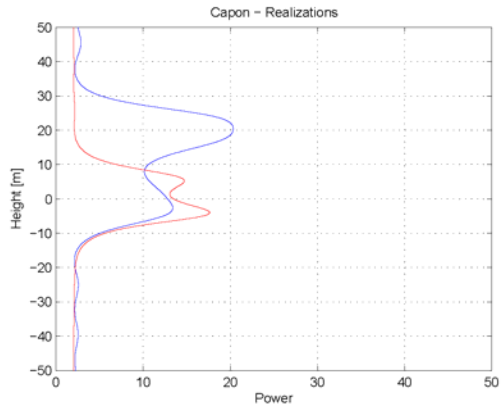

Figure 2.8: Realization of Capon spectrum, canopy centroid 23 m, two compact scatterers at 0 m and -3 m. Blue curve: before cancellation; red curve: after cancellation.

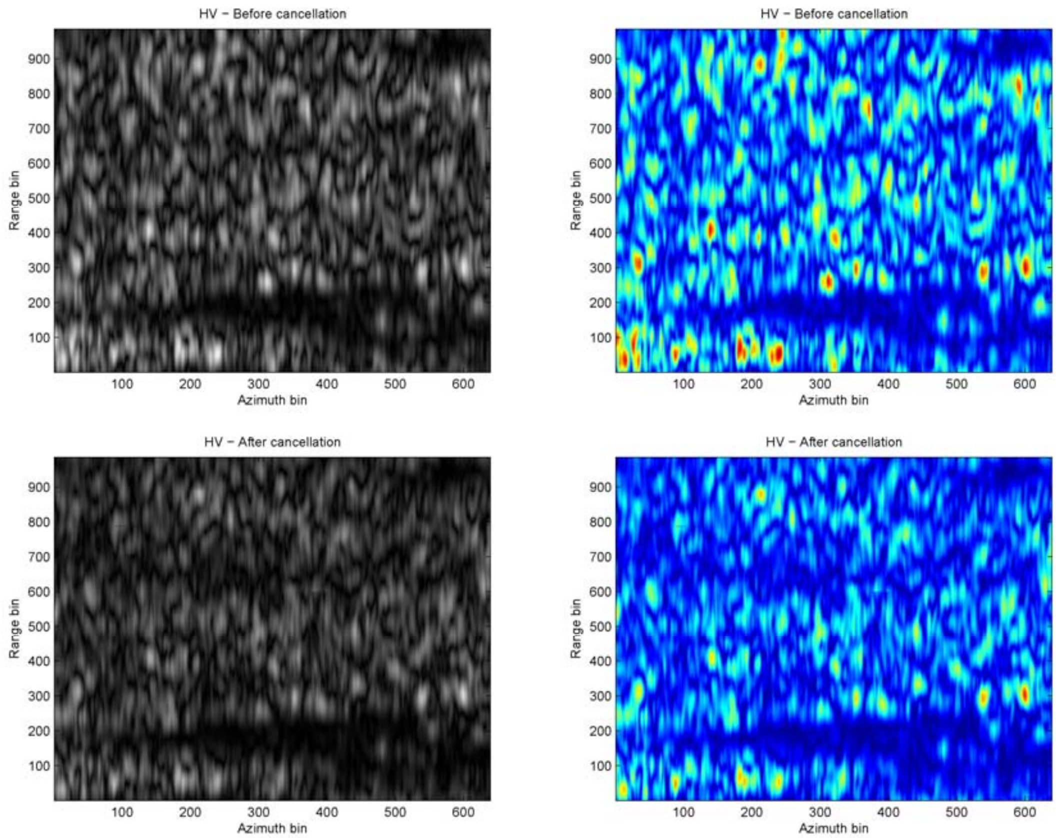

Figure 2.9: SAR images for the first analyzed range line, HV polarization, before and after cancellation with the Filter 1. (a) Before cancellation, gray level map; (b) before cancellation, false color map; (c) after cancellation, gray level map; (d) after cancellation, false color map.

10.6.2 Range line #2

10.6.2.1 HH polarization

Figure 2.10 reports the Capon tomographic images resulting after the cancellation with both filters performed along the range line containing the point-like scatterer. The original tomographic image before cancellation of Figure 1.29 is reported for comparison. We observe that both filters can provide an efficient cancellation of the canopy layer. A common feature of the tomo images after cancellation is the arise of light isolated power contributions below the remaining ground layer, which could be due to possible slight distorsions introduced by the filter.

10.6.2.2 HV polarization

Figure 2.11 shows the resulting tomo images after cancellation performed over the same range line with both filters, performed on HV data. It is apparent the great efficiency of the filter in canceling the canopy layer. We observe again light isolated power contributions arising below the terrain layer, even if at a lower extent.

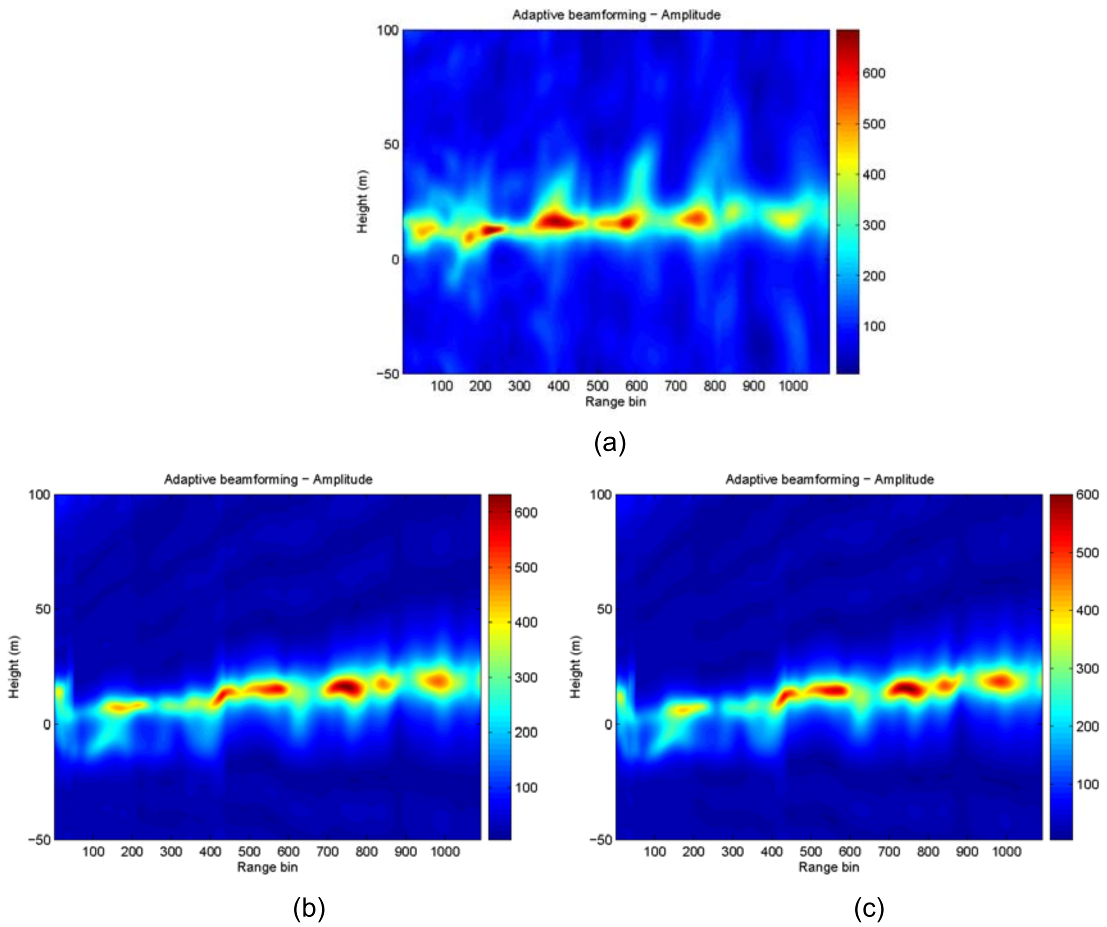

Figure 2.10: Capon tomo images for the second analyzed range line, HH polarization, before and after cancellation with the two filters. (a) Before cancellation; (b) After cancellation, Filter 1; (c) After cancellation, Filter 2

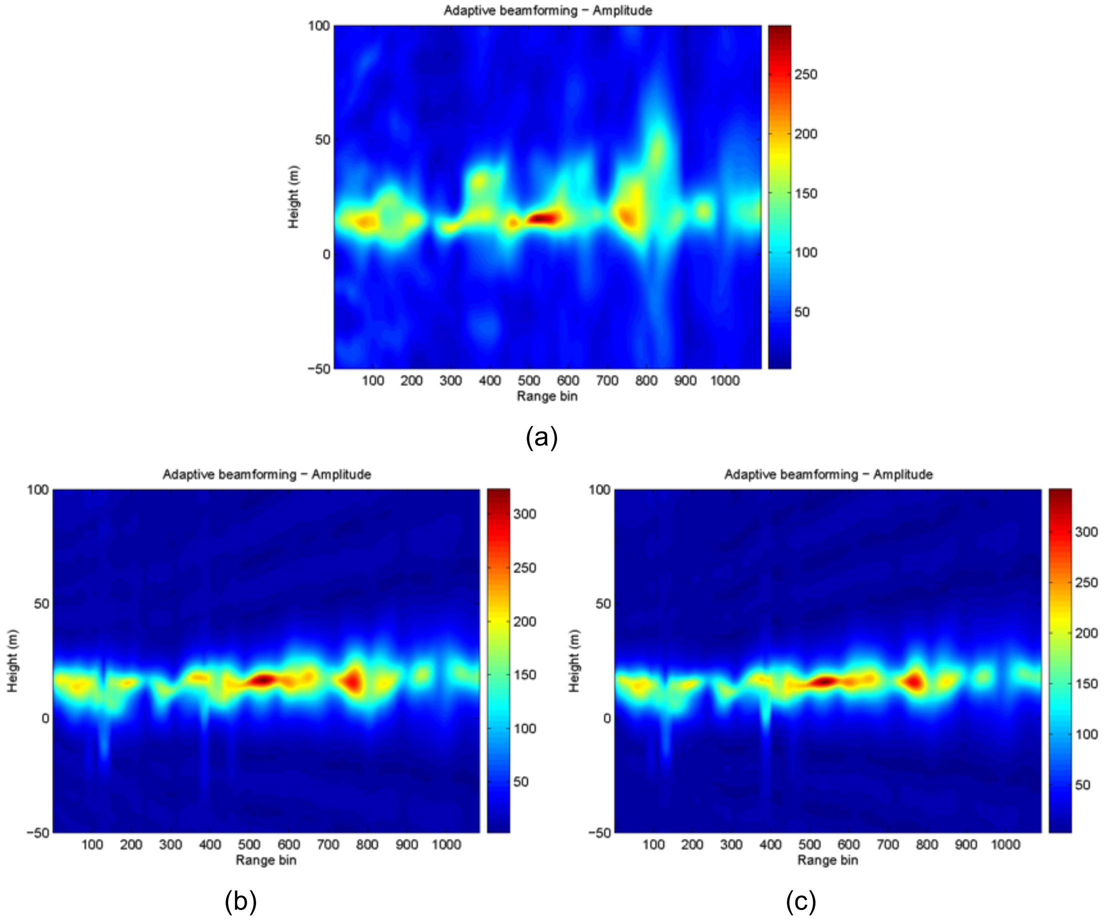

Figure 2.11: Capon tomo images for the second analyzed range line, HV polarization, before and after cancellation with the two filters. (a) Before cancellation; (b) After cancellation, Filter 1; (c) After cancellation, Filter 2

10.6.3 Range line #3

10.6.3.1 HH and HV polarizations

Figure 2.12 reports the Capon tomographic images resulting from the cancellation on HH data with both filters, performed along the range line containing the third corner reflector, whereas Figure 2.13 shows the same tomographic images obtained by canceling on the HV data. Again, both filters demonstrate their efficiency in canceling the canopy layer, without noticeable differences. Again, some slightly arised features can be individuated below the ground layer.

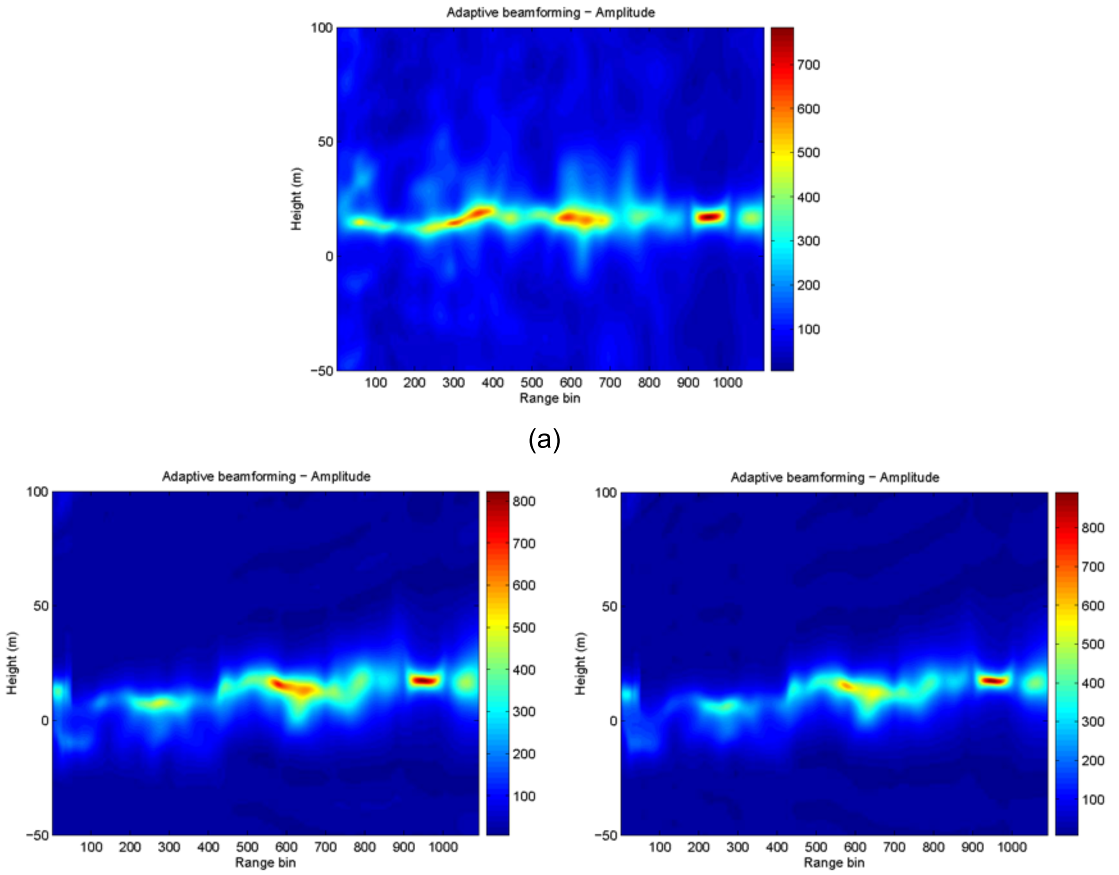

(a)

(b) (c)

Figure 2.12: Capon tomo images for the third analyzed range line, HH polarization, before and after cancellation with the two filters. (a) Before cancellation; (b) After cancellation, Filter 1; (c) After cancellation, Filter 2.

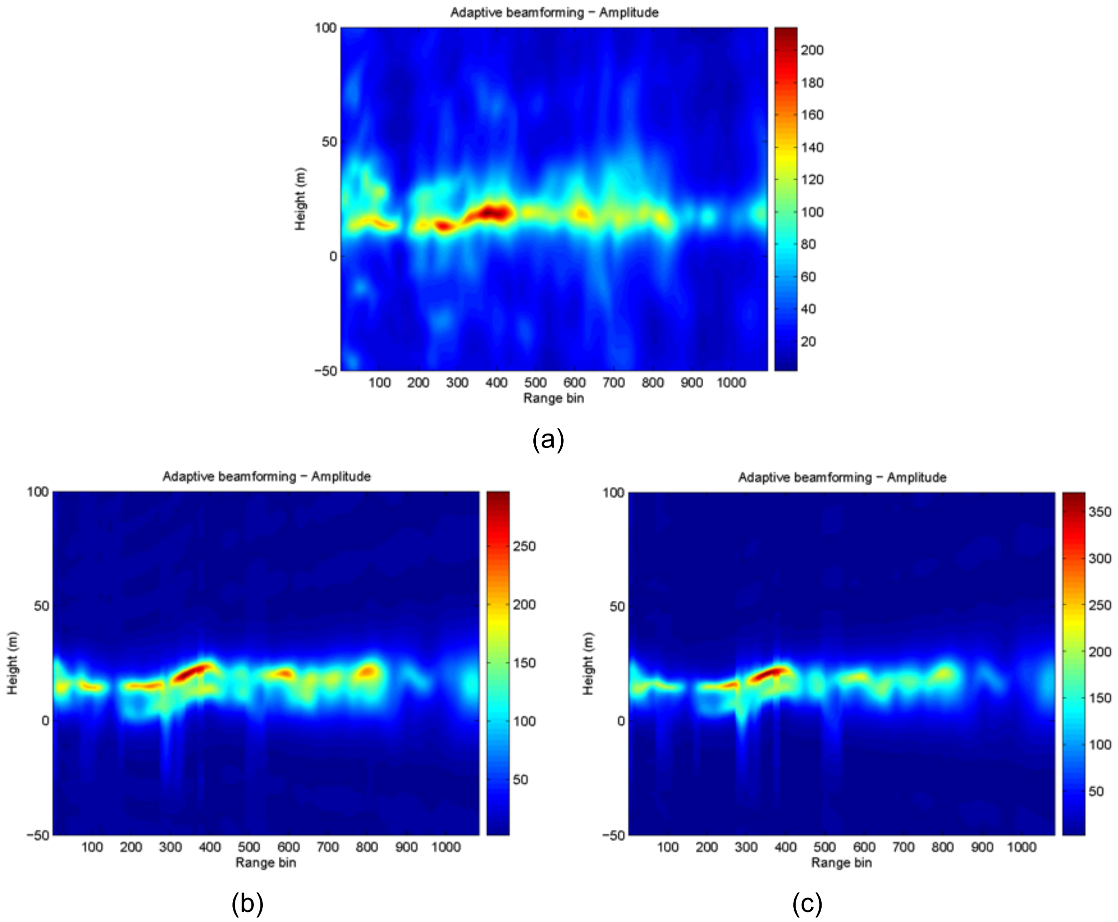

Figure 2.13: Capon tomo images for the third analyzed range line, HV polarization, before and after cancellation with the two filters. (a) Before cancellation; (b) After cancellation, Filter 1; (c) After cancellation, Filter 2.

10.6.4 Range line #2, HV polarization, other results

Additional tests with a small portion of the SAR image are carried out again centered around range line #2 by exploiting all the available satellite bandwidth. In Figure 2.14, the SAR image is reported as corresponding to the previous tests in 2.3.2, but for azimuth 3571-3784 (absolute coordinates), corresponding to the central portion of the previous test area (one third along the azimuth; conversely, little more range bins are considered, 1 to 1166). The corresponding image for all the available satellite bandwidth is shown in Figure 2.15. By applying a plain band synthesis processing, matched to a fixed height plane approximately corresponding to the terrain heights for near range and with no equalization, the synthetic band image shown in Figure 2.16 is obtained, where the resolution gain is apparent compared to Figure 2.15. After tomographic processing exploiting all the available satellite bandwidth and the coherent layer cancellation, applying again the plain band synthesis processing the synthetic band image achieved after cancellation is shown in Figure 2.17. The band synthesis result looks still reasonable. The accuracy can be improved of the automatic pass band centroid setting derived from the HH extracted terrain topography. Large differences with the band synthesis before cancellation are not visible, possibly due to the HV canopy layer scattering which is anyway not dominant, and is less resolvable from the terrain layer in the tomographic and cancellation processing conditions of these additional tests.

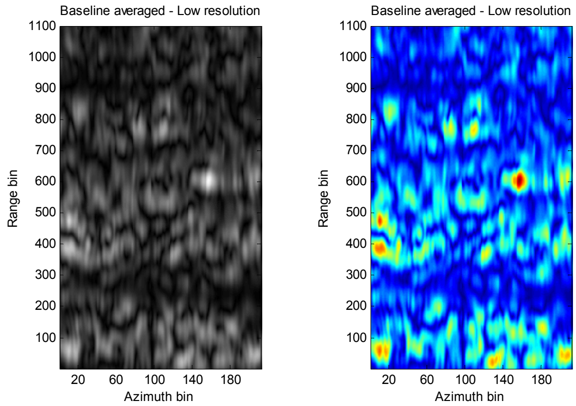

(a) (b)

Figure 2.14: SAR image for the second analyzed range line, HV polarization, before cancellation, normalized amplitudes. (a)gray level map; (b) false color map.

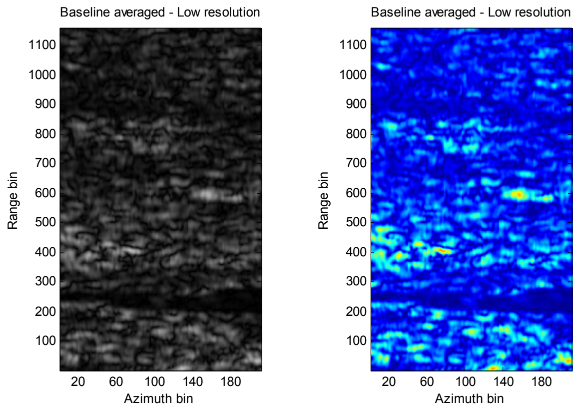

(a) (b)

Figure 2.15: SAR image for the second analyzed range line, HV polarization, before cancellation, normalized amplitudes, additional test. (a) gray level map; (b) false color map.

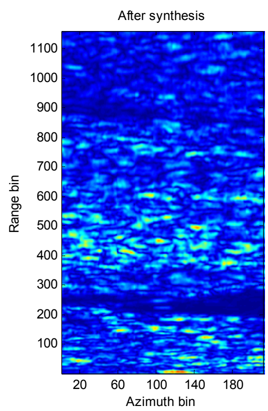

Figure 2.16: Synthetic band image for the second analyzed range line, HV polarization, before cancellation, normalized amplitudes, additional test.

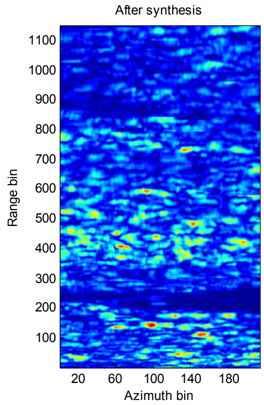

Figure 2.17: Synthetic band image for the second analyzed range line, HV polarization, after cancellation, normalized amplitudes, additional test.

10.7 Conclusions

First P-band real data experiments with the developed techniques show that adaptive Capon spatial spectral estimation can be a powerful and flexible method for tomographic processing, together with MUSIC, offering both superresolution and low sidelobes. Subcanopy terrain topography can be also derived from the tomographic images. Coherent layer cancellation with the deterministic multiband matrix filter driven by the derived topography can cancel the canopy contribution in the MB data set. However, slight enlargements of the satellite bandwidth may be beneficial. It is expected that multibaseline SAR tomography can be useful especially for highly sloping forested terrains and arid zones subsurface remote sensing.

10.8 References

1. F. Lombardini, A. Reigber, "Adaptive Spectral Estimators for Multibaseline SAR Tomography with Airborne L-Band Data," *Proc. 2003 IEEE Int. Geosci. and Remote Sensing Symp.*, Tolouse, France, July 2003.
2. F. Gini, F. Lombardini, M. Montanari, "Layover Solution in Multibaseline SAR Interferometry," *IEEE Trans. on Aerospace and Electronic Systems*, Vol. 38, No. 4, pp. 1344-1356, 2002.
3. F. Lombardini, M. Pardini, "Multibaseline Improvement of SAR Range Resolution in a Two-layer Scenario: Sample Analytical Results," Internal Report, University of Pisa, Feb. 2007.
4. F. Lombardini, M. Pardini, F. Gini, "Sector Interpolation for 3D SAR Imaging with Baseline Diversity Data," *Proc. 2007 IEEE Waveform Diversity and Design Conference*, Pisa, Italy, June 2007.